POLYPUBLIE
Polytechnique Montréal

POLYTECHNIQUE MONTRÉAL
UNIVERSITÉ D'INGÉNIERIE

Titre: Title:	Dynamique particulaire dans des lits fixes et rotatifs
Auteur: Author:	Olivier Dubé
Date:	2013
Type:	Mémoire ou thèse / Dissertation or Thesis
Référence: Citation:	Dubé, O. (2013). Dynamique particulaire dans des lits fixes et rotatifs [Thèse de doctorat, École Polytechnique de Montréal]. PolyPublie. https://publications.polymtl.ca/1128/

Document en libre accès dans PolyPublie
Open Access document in PolyPublie

URL de PolyPublie: PolyPublie URL:	https://publications.polymtl.ca/1128/
Directeurs de recherche: Advisors:	François Bertrand, & Jamal Chaouki
Programme: Program:	Génie chimique

Ce fichier a été téléchargé à partir de PolyPublie, le dépôt institutionnel de Polytechnique Montréal
This file has been downloaded from PolyPublie, the institutional repository of Polytechnique Montréal

https://publications.polymtl.ca

UNIVERSITÉ DE MONTRÉAL

DYNAMIQUE PARTICULAIRE DANS DES LITS FIXES ET ROTATIFS

OLIVIER DUBÉ

DÉPARTEMENT DE GÉNIE CHIMIQUE

ÉCOLE POLYTECHNIQUE DE MONTRÉAL

THÈSE PRÉSENTÉE EN VUE DE L'OBTENTION

DU DIPLÔME DE PHILOSOPHIAE DOCTOR

(GÉNIE CHIMIQUE)

AVRIL 2013

© Olivier Dubé, 2013.

UNIVERSITÉ DE MONTRÉAL

ÉCOLE POLYTECHNIQUE DE MONTRÉAL

Cette thèse intitulée:

DYNAMIQUE PARTICULAIRE DANS DES LITS FIXES ET ROTATIFS

présentée par : DUBÉ Olivier

en vue de l'obtention du diplôme de : Philosophiae Doctor

a été dûment acceptée par le jury d'examen constitué de :

M.FRADETTE Louis, Ph.D., président

M.BERTRAND François, Ph.D., membre et directeur de recherche

M.CHAOUKI Jamal, Ph.D., membre et codirecteur de recherche

M.HENRY Olivier, Ph.D., membre

M.ROY Shantanu, Ph.D., membre

Celui qui a besoin d'un protocole n'ira jamais loin; les génies lisent peu, pratiquent beaucoup et se font d'eux-mêmes.

Denis Diderot

Rien de grand ne s'est accompli dans le monde sans passion.

Georg Wilhelm Friedrich Hegel

DÉDICACE

À qui de droit

REMERCIEMENTS

Je tiens tout d'abord à remercier mes directeurs de thèse, François Bertrand et Jamal Chaouki, pour m'avoir permis de réaliser ce travail au sein de leur groupe de recherche. Leur support, leurs encouragements, leurs critiques ainsi que leur disponibilité ont été des plus appréciés au cours de ces longues années.

J'aimerais également remercier Mark Ackley et Cem Celik de PRAXAIR Inc ainsi que François Chouinard de TEVA/Ratiopharm sans qui une grande partie de cette thèse n'aurait tout simplement pas pu être réalisée.

Je remercie aussi particulièrement Jocelyn et Jonathan, deux collègues devenus de très bons amis, sans qui cette expérience n'aurait pas été aussi divertissante et enrichissante. J'aimerais aussi remercier Ebrahim, Hamed, Alexandre, Majid, Vincent, Isabelle, Marc, ainsi que tous les membres de l'URPEI, pour les nombreuses discussions qui m'ont permis de faire avancer ma pensée, que ce soit sur ma thèse ou la vie en général. Je remercie également tous les membres du département de génie chimique, particulièrement Diane, Lyne, Louise, Jean, Yazid, Carole, Gino, Martine, et Robert.

Je tiens également à souligner le soutien de l'équipe du réacteur nucléaire Slowpoke de l'École, Cornelia Chilian, Rahma Kada, Greg Kennedy et Jean St-Pierre. Un grand merci à vous pour votre aide et pour avoir répondu à mes nombreuses demandes d'activation.

Finalement, je tiens à remercier chaleureusement ma femme ainsi que mes parents, mes frères, ma sœur et toute ma belle-famille pour leur écoute et les innombrables fois où leur aide a été plus qu'indispensable. Un merci spécial à Angy, bima'anno halla' seret docteur, sar dawré ta'ellik : Attends, je t'explique!

La thèse a été financée par une bourse de doctorat (ES-D) du conseil de recherche en sciences naturelles et génie (CRSNG).

Toutes les simulations réalisées pour cette thèse ont été rendues possibles grâce aux ressources informatiques de Calcul Canada.

RÉSUMÉ

Les matériaux particulaires sont couramment employés dans une grande variété d'industries (pharmaceutique, alimentaire, céramique, polymère, chimique, métallurgique, traitement des déchets, etc.) où ils sont soumis à un large éventail d'opérations unitaires (p.ex. mélange, réduction de taille, séchage, réaction chimique). Les écoulements particulaires peuvent être regroupés selon trois régimes: quasi-statique, dense ou rapide. Les régimes quasi-statiques et rapides sont ceux qui ont été le plus souvent étudiés. L'étude des écoulements particulaires denses est plus complexe étant donné que ce régime regroupe une grande variété d'écoulements où la contribution relative des contraintes dues à la friction et aux collisions à l'écoulement est inconnue. Cette thèse propose donc de caractériser les écoulements denses en lits fixes et rotatifs.

Les lits particulaires fixes sont utilisés lors de procédés catalytiques hétérogènes et pour la purification de gaz. Bien qu'il s'agisse de lits fixes, plusieurs événements font en sorte que les particules peuvent se déplacer. L'écoulement en lit fixe de particules sphériques pouvant survenir lors de la pré-purification de l'air réalisée dans un réacteur à flux radial (RFR) à l'aide d'un procédé d'adsorption par oscillations thermiques (TSA) est étudié. Ce type de procédé a été sélectionné étant donné sa grande popularité industrielle. Les parois soutenant le lit fixe peuvent se contracter et/ou se dilater suite aux importantes différences de température entre les différentes phases d'opération du procédé TSA. Ces mouvements de parois sont susceptibles d'endommager les particules du lit fixe, entraîner la création de vides locaux, provoquer la ségrégation de particules ainsi que mélanger les adsorbants. Tout cela peut évidemment avoir des conséquences sur l'uniformité de l'écoulement du gaz à travers le lit fixe ainsi que sur le rendement et l'efficacité du procédé. Il est donc nécessaire d'évaluer l'effet d'une contraction et d'une expansion thermique cyclique des murs d'un RFR utilisé pour la pré-purification de gaz sur un lit particulaire fixe. À cette fin, la méthode des éléments discrets (DEM) a été employée puisque les techniques de mesure expérimentale perturbatrices ou non-perturbatrices ne sont pas facilement applicables à l'étude de ce genre d'écoulement.

Les cylindres rotatifs, aussi appelés fours rotatifs, sont couramment utilisés dans une grande variété de procédés industriels étant donné leur grande simplicité d'opération, leur efficacité adéquate de transfert de masse et de chaleur ainsi que leur capacité à traiter des matières premières hétérogènes. La compréhension fondamentale des phénomènes qui se produisent à l'intérieur de cylindres rotatifs est essentielle pour concevoir et opérer de manière optimale ce genre d'équipement. De très nombreuses études ont tenté d'élucider les mystères de l'écoulement granulaire à l'intérieur de cylindres rotatifs. Cependant, la grande majorité d'entre elles se sont limitées au cas de particules sphériques. Pourtant, comme il a été mentionné, un des avantages des cylindres rotatifs est de pouvoir traiter une matière première ayant une large distribution de taille et/ou de forme. Il s'avère donc nécessaire de caractériser la dynamique de particules non-sphériques à l'intérieur d'un cylindre rotatif. Dans ce cas-ci, une approche expérimentale a été employée puisque les méthodes de simulations numériques comme la DEM ne sont pas parfaitement adaptés pour étudier la dynamique de particules non-sphériques. La technique de suivi de particules radioactives (RPT) est, à cet égard, appropriée pour effectuer cette étude. Dans le cadre de cette thèse, des comprimés pharmaceutiques sont choisis pour représenter les particules non-sphériques. Cependant, leur utilisation comme traceur pour la RPT implique que la source d'émission de rayons gamma n'est pas ponctuelle. De ce fait, une plus grande incertitude quant à la reconstruction de la position du traceur est attendue. Par conséquent, il est nécessaire de développer une stratégie d'optimisation permettant d'identifier un positionnement optimal des détecteurs à scintillation pour la technique de suivi de particules radioactives pour ainsi minimiser l'erreur commise par à l'utilisation d'une source non-ponctuelle.

La première partie de cette thèse présente l'évaluation de l'effet, sur un lit particulaire fixe, d'une contraction et d'une expansion thermique cyclique des murs d'un RFR utilisé pour la pré-purification de gaz à l'aide de la DEM. Il s'agit de la première étude réalisée sur ce genre d'écoulement. La précision du modèle DEM construit a été évaluée en utilisant les valeurs expérimentales de porosité d'un lit fixe, les valeurs analytiques de pression prédites par la théorie de Janssen ainsi que les valeurs expérimentales de pression mesurée aux parois du lit fixe d'une unité commerciale de pré-purification de l'air. L'utilisation de la DEM dans le cadre de cette étude a permis d'évaluer la dispersion particulaire pouvant survenir à l'interface des adsorbants composant le lit fixe. Cette mesure peut permettre d'évaluer la qualité du lit fixe après plusieurs

années d'utilisation. Il est important de noter que le modèle DEM développé ne considère pas l'effet du gaz circulant à travers le lit fixe de même que les changements au niveau des propriétés particulaires pouvant survenir en cours de cycle. Néanmoins, les résultats obtenus avec le modèle montrent que la DEM est un outil utile pour l'étude de ce type de dynamique lente, à condition qu'une calibration minutieuse ait été préalablement réalisée.

La seconde partie de cette thèse présente la stratégie d'optimisation développée pour identifier un positionnement optimal des détecteurs à scintillation. Celle-ci utilise une méthode de recherche directe à maillage adaptatif (MADS) comme algorithme d'optimisation ainsi que la résolution des détecteurs comme fonction-objectif. La validation et l'application de cette stratégie a permis de démontrer que celle-ci permet l'identification d'une configuration optimale des détecteurs qui est propre à l'objectif de l'étude ainsi qu'aux conditions expérimentales. Elle peut donc facilement être appliquée à d'autres types d'études que celle réalisée dans le cadre de cette thèse.

Finalement, la troisième partie de cette thèse présente la caractérisation de la dynamique de particules non-sphériques à l'intérieur d'un cylindre rotatif. Les données recueillies ainsi que les observations réalisées en laboratoire permettent de supposer que les particules non-sphériques s'écoulent selon une orientation préférentielle. Cette dernière semble être une des raisons pouvant expliquer les différences observées entre certaines particules non-sphériques et les particules sphériques. Le mélange et la ségrégation à l'intérieur d'un cylindre rotatif de particules de formes similaires mais de tailles différentes ainsi que de masses similaires mais de formes différentes a aussi été étudiés. Une ségrégation radiale traditionnelle, où les particules petites ou denses se retrouvent au centre de l'écoulement alors que les grosses et légères se retrouvent en périphérie, a été observée dans la plupart des cas. Une ségrégation radiale inverse a toutefois été observée dans le cas où de grosses particules longues et plates étaient mélangées à de petites particules denses. Dans ce cas-ci, les petites particules denses se sont retrouvées en périphérie de l'écoulement plutôt que dans le centre. Les résultats obtenus ont permis pour la première fois de mettre en évidence l'effet que peut avoir la forme de la particule sur la dynamique, le mélange et la ségrégation de celle-ci.

ABSTRACT

Particulate materials (also referred as granular materials) are widely used in a great variety of industries (pharmaceutical, food processing, ceramic, polymer, chemical, metallurgical, waste treatment) where they are subjected to a wide range of operations (e.g. mixing, size reduction, drying, chemical reaction). Granular flow can be grouped into three regimes: quasi-static, dense or fast. The quasi-static and rapid granular flows have been studied the most. The study of dense granular flows is more complex since this regime includes a broad range of flows where the relative contribution of frictional and collisional stresses is unknown. Hence, this thesis proposes to characterize the dense granular flows occurring in fixed and rotating beds.

Fixed beds are mostly used in heterogeneous catalytic processes or for gas purification. Even though they are considered fixed, several factors can induce particles motion. The flow of spherical particles that could occur during air pre-purification using a thermal swing adsorption (TSA) process in a radial flow reactor (RFR) is studied. This type of process was selected due to its wide industrial use. When a RFR is used in conjunction with a thermal swing regeneration step, the reactor mechanical components (e.g. reactor vessel) contract and expand because of substantial temperature differences between the different operating phases. The axial and/or radial relative motions between the vessel walls and the bed of adsorbents can damage the adsorbents bed by breaking the particles, creating voids, inducing particle settling and promoting mixing of layered adsorbents. All of this will inevitably affect flow uniformity as well as process efficiency. It is thus needed to study the effect of this cyclic expansion and contraction of the RFR vessels on the fixed bed. The discrete element method was used to conduct this investigation as most experimental measurement techniques, whether they are invasive or non-invasive, are either not readily applicable or extremely costly to implement in this situation.

Rotating drums, also referred as rotary kiln, are widely used to process granular materials in a great variety of industries due to their adequate mixing and heat transfer efficiency as well as their ability to handle heterogeneous feedstock. Understanding the phenomena occurring inside rotating drums at a fundamental level is essential for optimal design and operation of this

equipment. A considerable amount of experimental work has been performed in order to elucidate the behavior of granular flow inside a rotating drum. However, a majority of these investigations have involved spherical or nearly spherical particles. Yet, as was previously mentioned, one advantage of rotating drums is their ability to handle varied feedstocks, i.e. granular material having a wide distribution of size, density, shape, roughness or else. It is therefore necessary to characterize the dynamics of non-spherical particles inside a rotating drum. In this case, an experimental approach was used since the numerical methods like the DEM are not well suited for studying dynamics of non-spherical particles. The radioactive particle tracking (RPT) technique is appropriate to carry out this investigation. In the context of this thesis, pharmaceutical tablets were used to represent non-spherical particles. However, the use of a large pharmaceutical tablet as a tracer particle in the RPT technique implies that the source of the gamma rays emission is no longer a point source. Therefore, a greater uncertainty in the reconstruction of the tracer particle trajectory is expected. Hence, it is needed to develop an optimization strategy to find an optimal set of positions for the scintillation detectors used in the RPT technique in order to minimize the error introduced by the use of a non-point source.

The first part of this thesis presents an evaluation of the effect, on a bed of adsorbents, of a cyclic thermal expansion and contraction of the vessels of a RFR used for gas pre-purification using the DEM. This is the first reported study of granular flow of this kind. The accuracy of the DEM-based model was assessed using experimental values of bed porosity, analytical values of predicted wall pressure based on Janssen’s theory, and experimental values of wall pressure measured during the operation of a full-scale unit. In this study, the use of DEM simulations enabled the computation of a dispersion coefficient at the interface of the adsorbents. This dispersion coefficient could be used to assess the fixed bed quality after several years of use. It must be noted that the DEM-based model developed does not consider the effect of the circulating gas and the changes in particle properties likely to occur in the course of a cycle. Nevertheless, the results obtained with the proposed model show that the DEM is a valuable tool for the investigation of such slow dynamical processes, provided a careful calibration is done

The second part of this thesis presents the optimization strategy developed to determine an optimal set of scintillation detector positions and orientations. This strategy uses a mesh adaptive direct search (MADS) optimization algorithm and the detectors resolution as an objective function. The results of this work showed that the optimal positioning found by the optimization strategy is sensitive to both the objectives of the study and the experimental conditions. It can therefore be easily applied to studies different from the one conducted in this thesis.

Finally, the third part of this thesis presents the characterization of the dynamics of non-spherical particles in a rotating drum. The data collected and the observations made in the laboratory showed that non-spherical particles tend to flow with a preferred spatial orientation. This preferred spatial orientation can be one of the reasons that could explain the differences observed between the flow of spherical and non-spherical particles. Mixing and segregation of bi-disperse mixtures of mono-shaped tablets and bi-disperse mixtures of bi-shaped tablets were also investigated. A traditional core segregation pattern, where the smaller/denser particles are found in the center of the bed while the larger/lighter particles are found on the outside, was observed in most cases. However, a reverse core segregation pattern was observed when long and large particles were mixed with small compact particles. In this case, the smaller/denser particles were found on the outside of the bed instead of in the center. The results obtained with this investigation are of interest in that they highlight for the first time the effect that the shape of a particle may have on flow dynamics as well as on mixing and segregation inside a rotating drum.

TABLE DES MATIÈRES

DÉDICACE IV

REMERCIEMENTS V

RÉSUMÉ VII

ABSTRACT X

TABLE DES MATIÈRES XIII

LISTE DES TABLEAUX XVII

LISTE DES FIGURES XIX

LISTE DES SIGLES ET ABRÉVIATIONS XXIV

INTRODUCTION 1

CHAPITRE 1 REVUE DE LA LITTÉRATURE 5

1.1 Écoulements particulaires denses 5

1.1.1 Lits particulaires fixes 7

1.1.2 Lits particulaires rotatifs 11

1.2 Méthodes expérimentales de caractérisation des écoulements particulaires 14

1.2.1 Méthodes perturbatrices 14

1.2.2 Méthodes non-perturbatrices 15

1.3 Modélisation des écoulements particulaires 19

1.3.1 Approches continues 20

1.3.2 Modèles discrets 21

CHAPITRE 2 ORGANISATION DE LA THÈSE 27

CHAPITRE 3 MÉTHODOLOGIE 30

3.1 Dynamique particulaire dans des lits fixes 30

3.1.1 Calibration du modèle 30

3.1.2 Dimensionnement des domaines de calcul 34

3.1.3 Spécification du cycle d'expansion et de contraction 35

3.1.4 Planification des simulations numériques 36

3.2 Optimisation du positionnement des détecteurs de la technique de suivi de particules radioactives 37

3.2.1 Identification de l'algorithme d'optimisation approprié 37

3.2.2 Validation, évaluation et application de la stratégie d'optimisation 38

3.3 Dynamique particulaire dans des lits rotatifs 39

3.3.1 Fabrication des particules non-sphériques 39

3.3.2 Planification d'expériences 44

CHAPITRE 4 SIMULATION PAR ÉLÉMENTS DISCRETS DE LA DYNAMIQUE D'ADSORBANTS DANS UN RÉACTEUR À FLUX RADIAL UTILISÉ POUR LA PRÉ-PURIFICATION DE GAZ 47

4.1 Présentation du premier article 47

4.2 Discrete Element Simulation of the Dynamics of Adsorbents in a Radial Flow Reactor Used for Gas Prepurification 47

4.2.1 Abstract 47

4.2.2 Introduction 48

4.2.3 Methodology 51

4.2.4 Results and discussion 66

4.2.5 Conclusion 85

4.2.6 Acknowledgments 86

4.2.7 References 86

CHAPITRE 5 OPTIMISATION DU POSITIONNEMENT DES DETECTEURS POUR LA TECHNIQUE DE SUIVI DE PARTICULE RADIOACTIVE 91

5.1 Présentation du second article 91

5.2 Optimization of Detector Positioning in the Radioactive Particle Tracking Technique 91

5.2.1 Abstract 91

5.2.2 Introduction 92

5.2.3 RPT basics 97

5.2.4 Optimization strategy 100

5.2.5 Results and discussion 109

5.2.6 Conclusion 130

5.2.7 Acknowledgements 132

5.2.8 References 132

CHAPITRE 6 DYNAMIQUE DE PARTICULES NON-SPHÉRIQUES DANS UN CYLINDRE ROTATIF 138

6.1 Présentation de l'article 138

6.2 Dynamics of Non-Spherical Particles in a Rotating Drum 138

6.2.1 Abstract 138

6.2.2 Introduction 139

6.2.3 Methodology 141

6.2.4 Results and discussion 148

6.2.5 Conclusion 182

6.2.6 Acknowledgements 182

6.2.7 References 183

CHAPITRE 7 DISCUSSION GÉNÉRALE 188

7.1 Écoulements particulaires denses dans un lit fixe 188

7.2 Écoulements particulaires non-sphériques denses dans un cylindre rotatif 190

CONCLUSION ET RECOMMANDATIONS 193

BIBLIOGRAPHIE 196

LISTE DES TABLEAUX

Tableau 1-1 Caractéristiques des régimes d'écoulement à l'intérieur de cylindres rotatifs.....13

Tableau 3-1 Spécifications des domaines de simulation.....35

Tableau 3-2 Planification des simulations DEM.....37

Tableau 3-3 Seconde formulation 41

Tableau 3-4 Troisième formulation.....42

Tableau 3-5 Propriétés des comprimés 44

Tableau 3-6 Planification des expériences RPT.....46

Table 4-1 Particle properties for the DEM-based model 57

Table 4-2 Computational domain specifications.....61

Table 5-1 Summary of systems studied using the RPT technique.....93

Table 5-2 Factors affecting the quality of RPT data 96

Table 5-3 Parameters of the optimization strategy.....110

Table 5-4 Domains of the R and θ variables 111

Table 5-5 Optimization results for three, four and six detectors.....112

Table 5-6 Domains of variables z and θ 116

Table 5-7 Comparison of the average objective function values for the reference case and both optimization tests. Ten and four runs were performed for the first and second tests respectively.....124

Table 5-8 CPU time required to reach convergence for all the optimization tests of this study..129

Table 5-9 Breakdown of the computational time.....130

Table 6-1 Tablet composition 144

Table 6-2 Tablet properties 146

Table 6-3 Design of experiments 147

Table 6-4 Definition of the variables used 149

Table 6-5 Primary observations 151

Table 6-6 Values of the active layer thickness α_0 based on the turning point line 165

Table 6-7 Values of the active layer thickness δ_0 based on the yield line 168

Table 6-8 Blend characteristic ratios.....175

Table 6-9 Axial dispersion coefficient 181

LISTE DES FIGURES

Figure 1-1 Classification des écoulements selon le Groupement De Recherche Milieux Divisés: a) cisaillement entre plans b) cisaillement annulaire c) chute verticale d) plan incliné e) tas f) cylindre rotatif. Adapté de GDR MiDi (2004). 6

Figure 1-2 Étapes de a) adsorption et b) désorption du cycle TSA. Adapté de Ruthven (1984). 8

Figure 1-3 Représentation schématique d'un a) réacteur axial et d'un b) réacteur à flux radial contenant deux types d'adsorbants. 10

Figure 1-4 Schéma de l'écoulement particulaire dense pouvant survenir dans le cas de lits fixes contenu dans un a) réacteur axial et un b) réacteur à flux radial. 11

Figure 1-5 Régimes d'écoulement particulaire à l'intérieur de cylindres rotatifs: a) avalanche, b) roulement, c) déferlement et d) centrifuge. Adapté de Meier (2007). 12

Figure 1-6 Montage expérimental RPT typique. Adapté de Doucet et al. (2008). 18

Figure 1-7 Représentation schématique de a) la DEM (adapté de Bouffard (2012)) et b) un modèle de force de type ressort-amortisseur (adapté de Cundall et Strack (1979)). 22

Figure 3-1 Photographies a) des particules d'alumine et b) des zéolites synthétiques de type X (« molecular sieve ») utilisées ainsi que c) les distributions granulométriques de chacun. ... 31

Figure 3-2 Exemple de la mesure d'une particule en chute libre réalisée à l'aide d'une caméra haute vitesse. 32

Figure 3-3 Appareil servant à la mesure d'angles de talus des adsorbant [a) et b)] ainsi qu'un exemple d'angle de talus obtenu pour c) les particules d'alumine et d) les zéolites synthétiques de type X. 33

Figure 3-4 Représentation schématique du RFR: a) vue de face, b) vue de haut et c) domaine de simulation DEM. 34

Figure 3-5 Spécifications du cycle de TSA: a) évolution de la température aux parois internes et externes du RFR, b) variations de rayon correspondantes aux changements de température et c) mouvements des murs simulés à l'aide de la DEM. 36

Figure 3-6 Formes des comprimés produit avec la seconde formulation: a) pomme, b) diamant et c) capsule. 41

Figure 3-7 Formes et dimensions des comprimés produits avec la troisième formulation. 43

Figure 4-1 Particle size distributions of the two adsorbents. 55

Figure 4-2 Schematic of the RFR: a) front view, b) top view) and c) the DEM simulation domain. 59

Figure 4-3 Original temperature cycle (a) and corresponding radius change (b). 63

Figure 4-4 Adapted wall motion cycle for the DEM simulations. 64

Figure 4-5 Stability criterion vs wall cycle frequency. 66

Figure 4-6 Bed porosity with respect to bed height for a) domain A, b) domain B and c) DEM packed bed after filling for domain B (particles are colored by size). 67

Figure 4-7 Normal and shear stress values for computational domains a) A and b) B. 70

Figure 4-8 Mobilized friction in computational domain A. 72

Figure 4-9 Comparison of wall pressure for different values of the wall-particle friction coefficient. 73

Figure 4-10 Relationship between the macroscopic (μ_w) and microscopic friction (μ_{pw}) coefficients. 74

Figure 4-11 Normal pressure evolution a) for the full-scale unit and b) the DEM simulations. ... 76

Figure 4-12 Wall maximum pressure evolution. 77

Figure 4-13 Comparison over one single cycle of (a-c-e) experimental data and (b-d-f) DEM simulation results: a) and b) radius change, c) and d) compression/expansion velocity and e) and f) normal pressure. 79

Figure 4-14 Evolution of the molecular sieve surface concentration near the initial position of the interface. 82

Figure 4-15 Molecular sieve concentration on specific cross-section planes located at specific distance from the initial positioning of the interface 83

Figure 4-16 a) Radial (Dxx) and b) axial (Dyy) dispersion coefficients. 84

Figure 5-1 Typical RPT setup. Sodium iodide (NaI) scintillation detectors are strategically placed around the system of interest. They are connected to amplifiers/discriminators for signal adjustments. The latter are connected to high-speed counter cards which transfer the information to a data acquisition system. 94

Figure 5-2 Schematic representation of the accuracy (A) and precision (P) of the RPT technique in the case of a) a single detector (AS, PS), b) multiple detectors (AM, PM) and c) multiple optimized detectors (AO, PO). 101

Figure 5-3 a) Counts and resolution for b) the nodes of a 2D plane surrounding a scintillation detector. 102

Figure 5-4 Optimization strategy algorithm. 106

Figure 5-5 Schematic representation of a) the resolution computation and b) the weight computation. 108

Figure 5-6 a) Objective function evolution with respect to the number of NOMAD evaluations for ten runs of the optimization strategy and b) probability distribution of θ for one hundred runs of the optimization strategy and three detectors. 113

Figure 5-7 Evolution of the maximum resolution and minimum sensitivity for the circular geometry as the number of detectors increases. 115

Figure 5-8 Reference configurations a) A b) B and c) C, and results obtained by the optimization procedure using as the objective function d) $\max\left(w^n\sigma_T^n\right)$ (configuration D) and e) $\max\left(w^n\sigma_z^n\right)$ (configuration E). 117

Figure 5-9 Objective function evolution with the number of NOMAD evaluations for ten runs of the optimization strategy using a) the first objective function $\left(\max\left(w^n\sigma_T^n\right)\right)$ and b) the second objective function $\left(\max\left(w^n\sigma_z^n\right)\right)$ 118

Figure 5-10 Cumulative distribution function of a) the overall radial resolution and b) the overall axial resolution. 119

Figure 5-11 Schematic representation of the partially filled horizontal cylinder: a) side view, b) top view and variable domain for the first optimization test and c) top view and variable domain for the second optimization test. 122

Figure 5-12 Three-dimensional representation of a) the reference configuration F, and the optimal configuration found by b) the first optimization test (configuration G) and c) the second optimization test (configuration H). 123

Figure 5-13 Cumulative distribution function of variable θ for the first optimization test.....125

Figure 5-14 Evolution of the maximum resolution and minimum sensitivity for the partially filled horizontal cylinder as the number of detectors increases.....126

Figure 5-15 Cumulative distribution function of a) the overall radial resolution and b) the overall axial resolution. 127

Figure 5-16 Schematic representation of a) the large non-spherical tracer particle as well as b) the side view and c) top view for the five known locations tested. 128

Figure 5-17 Mean error in the reconstruction of the fixed position of both tracer particle: 3mm glass bead (GB) and large non-spherical particle (NS).....128

Figure 6-1 Schematic representation of the five tablets used in this study.....145

Figure 6-2 a) Cross-section view of the rotating drum and b) a close-up on the active layer 149

Figure 6-3 Typical velocity field for a) tablet E and b) blend AE (at 10RPM) 152

Figure 6-4 Streamwise velocity profiles at x=0 for a) the individual tablets and c) the different blends, and transverse velocity profiles at x=0 for b) the individual tablets and d) the different blends.....155

Figure 6-5 Streamwise velocity profiles for a) tablet C and c) blend AE, and transverse velocity profiles for b) tablet C and d) blend AE, at x = 0m, ±0.04m and ±0.08m 156

Figure 6-6 Streamwise velocity profiles along the bed free surface for a) the individual tablets and b) the different blends, and the scaled streamwise velocity profiles along the bed free surface for c) the individual tablets and d) the different blends.....157

Figure 6-7 Normalized streamwise velocity profiles at the bed surface for a) the individual tablets and b) the different blends, and under the bed surface for c) tablet C and d) tablet D. 160

Figure 6-8 Normalized active layer depth profile $\alpha(x)/\alpha_0$ for tablets D and E, and 6mm glass bead 163

Figure 6-9 Mean residence time in cells of the Eulerian grid used for a) tablet B and b) tablet D. 170

Figure 6-10 Residence times in the active and passive layers for all the tablets and blends tested. The symbols correspond to experimental data. 174

Figure 6-11 Values of (a and c) the occupancy and (b and d) the location probability for blends AE, AE*, BC and the 5-6 mm glass beads. For a) and b), the smaller particle was used as a tracer. For c) and d), the larger particle was used as a tracer. 177

Figure 6-12 Values of a) the occupancy and b) the location probability for blends CD and CE. 179

Figure 6-13 Evolution of D_{axial} with respect to the active layer depth (ξ_0) 180

Figure 7-1 Comparaison des champs de vitesse obtenus à l'aide d'un positionnement a) non-optimal et b) optimal pour le comprimé A. 191

LISTE DES SIGLES ET ABRÉVIATIONS

APB	Annular packed bed
ASU	Air separation unit
CDF	Cumulative distribution function
CFD	Dynamique des fluides computationnelle / Computational fluid dynamics
CoR	Coefficient de restitution / Coefficient of restitution
DEM	Méthode des éléments discrets / Discrete element method
GDR MiDi	Groupement De Recherche Milieux Divisés
LBM	Méthode de Lattice-Botlzmann
LIF	Fluorescence par lumière induite
MADS	Méthode de recherche directe à maillage adaptatif / Mesh adaptive direct search method
MCC	Cellulose microcristalline
MCNP5	Monte Carlo N Particle Code Version 5
MRI	Imagerie par résonnance magnétique / Magnetic resonance imaging
NIR	Spectroscopie proche infra-rouge
NOMAD	C++ implementation of the MADS algorithm
PBM	Modélisation par bilan de population
PEPT	Suivi de particule par émission de positron / Positron emission particle tracking
PIV	Vélocimétrie par imagerie de particules / Particle imaging velocimetry
PPU	Pre-purification unit
PSD	Distribution granulométrique / Particle size distribution
PTV	Vélocimétrie par suivi de particules / Particle tracking velocimetry

RFBR	Radial flow fixed bed reactor
RFR	Réacteur à flux radial / Radial flow reactor
RPM	Rotation par minute / Rotation per minute
RPT	Suivi de particules radioactives / Radioactive particle tracking
TSA	Adsorption par Oscillations Thermiques / Thermal Swing Adsorption

INTRODUCTION

La science des matériaux particulaires (aussi appelés matériaux granulaires) intéresse une multitude de disciplines de recherche, allant de l'astrophysique à la géophysique et les sciences de l'environnement, en passant par les procédés industriels. De plus, les matériaux particulaires sont couramment employés dans une grande variété d'industries (pharmaceutique, alimentaire, céramique, polymère, chimique, métallurgique, traitement des déchets, etc.) où ils sont soumis à un large éventail d'opérations unitaires (p.ex. mélange, réduction de taille, séchage, réaction chimique) à des fins de transformation en divers produits intermédiaires ou terminaux.

L'étude des écoulements particulaires n'est pas une mince entreprise. Dans son édition spéciale du 125e anniversaire, la revue *Science* a identifié la question des écoulements granulaires comme l'une des 125 plus importantes questions toujours en attente de réponse (Collection of authors, 2005). Plusieurs raisons expliquent la complexité propre à ce genre de matériaux. Tout d'abord, l'étude du comportement d'une seule particule et de son interaction avec une autre ne permet pas d'avoir un aperçu du comportement macroscopique d'un système complet ou de la dynamique d'écoulement des particules (Juarez, 2009; Meier, 2007). Les patrons de ségrégation obtenus à l'intérieur d'un système particulaire composé de différents types de particules en sont un exemple. Les liens entre les propriétés microscopiques (i.e. à l'échelle de la particule) et les propriétés macroscopiques (i.e. pour un ensemble de particules) ne sont pas encore totalement établis. De plus, tout dépendant des conditions environnantes, les matériaux particulaires peuvent présenter des caractéristiques qui sont spécifiques aux gaz, aux solides ou aux liquides. De surcroît, leur nature opaque entraîne des limitations majeures quant à leur caractérisation expérimentale. Finalement, ils sont difficiles à modéliser puisque l'ensemble des éléments du système particulaire doit être intégré au modèle, augmentant ainsi significativement la complexité du modèle mathématique (Doucet, 2008).

Les écoulements particulaires peuvent être regroupés selon trois régimes: quasi-statique, dense ou rapide. Les régimes quasi-statiques et rapides sont ceux qui ont été le plus souvent étudiés

(Meier, 2007). Dans le premier cas, l'écoulement est dominé par les contraintes de friction entre les particules alors que celles-ci subissent des contacts prolongés (Herminghaus, 2005; Savage, 1984). La mécanique des sols ainsi que les modèles de plasticité sont souvent employés pour décrire ces écoulements (GDR MiDi, 2004; Nedderman, 2005). Dans le second cas, les particules interagissent par le biais de collisions binaires brèves. Une théorie cinétique s'apparentant à la théorie cinétique des gaz a été développée pour décrire ce régime (Campbell, 1990, 2006; Savage, 1984). L'étude des écoulements particulaires denses est plus complexe étant donné que ce régime regroupe une grande variété d'écoulements où la contribution relative des contraintes dues à la friction et aux collisions à l'écoulement est inconnue.

En ce qui a trait au régime dense, le Groupement de Recherche Milieux Divisés (GDR MiDi) a regroupé les écoulements particulaires denses les plus étudiés selon deux catégories : les écoulements confinés et de surface (GDR MiDi, 2004). Les procédés ayant recours à des écoulements particulaires entrant dans l'une ou l'autre de ces catégories sont nombreux. Cette thèse s'intéresse spécifiquement aux cas d'écoulements confinés à l'intérieur de lits fixes et d'écoulements de surface à l'intérieur de cylindres rotatifs.

D'une part, les lits particulaires fixes sont utilisés lors de procédés catalytiques hétérogènes et pour la purification de gaz. Bien qu'il s'agisse de lits fixes, plusieurs événements font en sorte que les particules peuvent se déplacer. Le passage d'un fluide à travers le lit particulaire peut être une de ces raisons. Cependant, d'autres phénomènes indirects peuvent entraîner un mouvement particulaire non-désiré. Le cas de la pré-purification de l'air réalisée à l'aide d'un procédé cyclique d'adsorption par oscillations thermiques (« thermal swing adsorption », TSA) en est un parfait exemple. Des colonnes d'adsorption composées de lits fixes d'adsorbants sont généralement employées dans ce type de procédé. Ces dernières servent à retirer de l'air les impuretés tels l'eau, le dioxyde de carbone, les oxydes nitreux, les hydrocarbures légers, ou autres produits, pour qu'il puisse ensuite être acheminé à une unité de séparation cryogénique servant à la séparation de l'oxygène et de l'azote. Ces impuretés sont retirées de manière sélective par différents adsorbants spécifiques à certaines impuretés suite au passage de l'air à travers le lit fixe ordonné. L'ordre dans lequel les impuretés sont retirées est important. Ainsi, le

mélange des différents adsorbants doit absolument être évité. Suite aux importantes différences de température entre les différentes phases d'opération du procédé TSA, les parois soutenant le lit fixe peuvent se contracter et/ou se dilater (Ackley, Celik, Nowobilski, & Schneider, 2012; Libal, Fierlbeck, & Von Gemmingen, 1998). Ces mouvements de parois sont susceptibles d'endommager les particules du lit fixe, entraîner la création de vides locaux, provoquer la ségrégation de particules ainsi que mélanger les adsorbants à leurs interfaces. Tout cela peut évidemment avoir des conséquences sur l'uniformité de l'écoulement du gaz à travers le lit fixe ainsi que sur le rendement et l'efficacité du procédé. Aucune étude n'a examiné l'effet de tels phénomènes de transfert thermique sur la structure d'un lit fixe ainsi que sur la dynamique des particules le constituant.

D'autre part, les cylindres rotatifs, aussi appelés fours rotatifs, sont couramment utilisés dans une grande variété de procédés industriels, notamment pour le traitement thermique de rejets solides ou la production de ciment, étant donné leur grande simplicité d'opération, leur efficacité adéquate de transfert de masse et de chaleur (Descoins, Dirion, & Howes, 2005) ainsi que leur capacité à traiter des matières premières hétérogènes (Boateng, 1998). La compréhension fondamentale des phénomènes qui se produisent à l'intérieur de cylindres rotatifs est essentielle pour concevoir et opérer de manière optimale ce genre d'équipement (Heydenrych, Greeff, Heesink, & Versteeg, 2002; Khakhar, McCarthy, Shinbrot, & Ottino, 1997; Mellmann, 2001). Ainsi, la caractérisation de l'écoulement particulaire est d'une importance primordiale. Bien que les cylindres rotatifs représentent une géométrie relativement simple, l'écoulement granulaire survenant à l'intérieur est complexe (Boateng, 1998; Ding, Forster, Seville, & Parker, 2002a; Ndiaye, Caillat, Chinnayya, Gambier, & Baudoin, 2010). De plus, si les particules composant le lit réagissent et/ou subissent un changement de forme ou de taille en cours d'opération, comme dans des applications de pyrolyse, combustion, frittage ou réduction de taille, le problème devient beaucoup plus complexe puisque de nouveaux phénomènes affectant la dynamique particulaire peuvent survenir. Une quantité considérable d'études ont été réalisées afin d'élucider les mystères de l'écoulement granulaire à l'intérieur de cylindres rotatifs. Cependant, la grande majorité d'entre elles se sont limitées au cas de particules sphériques. Pourtant, comme il a été mentionné, un des avantages des cylindres rotatifs est de pouvoir traiter une matière première ayant une large distribution de taille et/ou de forme. Il est connu depuis un certain temps déjà que la forme

des particules affecte leurs propriétés dynamiques (Ridgway & Rupp, 1971). Plus spécifiquement, le comportement des particules non-sphériques diffère de celui de particules sphériques par leur efficacité de compactage, leur résistance au cisaillement, leur dilatation sous l'effet de cisaillement, leur transfert de quantité de mouvement entre la translation et la rotation d'une particule ainsi que leur capacité à bloquer l'écoulement (Cleary, 2010).

L'objectif général de la présente thèse est de caractériser la dynamique particulaire pour des écoulements denses en lits fixes et rotatifs. Un phénomène de transfert thermique est à l'origine de l'écoulement de particules sphériques dans les lits fixes. Les lits rotatifs sont pour leur part composés de particules non-sphériques.

CHAPITRE 1 REVUE DE LA LITTÉRATURE

Ce chapitre présente une brève revue de la littérature où il sera, entre autres, question des écoulements particulaires denses ainsi que des méthodes de caractérisation expérimentale et de modélisation des écoulements particulaires.

1.1 Écoulements particulaires denses

Tel que mentionné précédemment, les écoulements particulaires denses sont regroupés en deux catégories : les écoulements confinés et de surface (GDR MiDi, 2004). L'ensemble des écoulements confinés contient, entre autres, les écoulements par cisaillement entre plans (« plane shear »), par cisaillement annulaire (« annular shear ») et en chute verticale (« vertical-chute ») tandis que l'ensemble des écoulements de surface intègre les écoulements le long de plans inclinés (« inclined plane »), les écoulements de tas (« heap flow »), ainsi que ceux se produisant à l'intérieur de cylindres rotatifs. Ces écoulements sont représentés à la Figure 1-1. Les écoulements de surface sont en fait gouvernés principalement par la force de gravité. Pour tous ces types d'écoulements, les particules ont la possibilité de se mélanger ou même de ségréger.

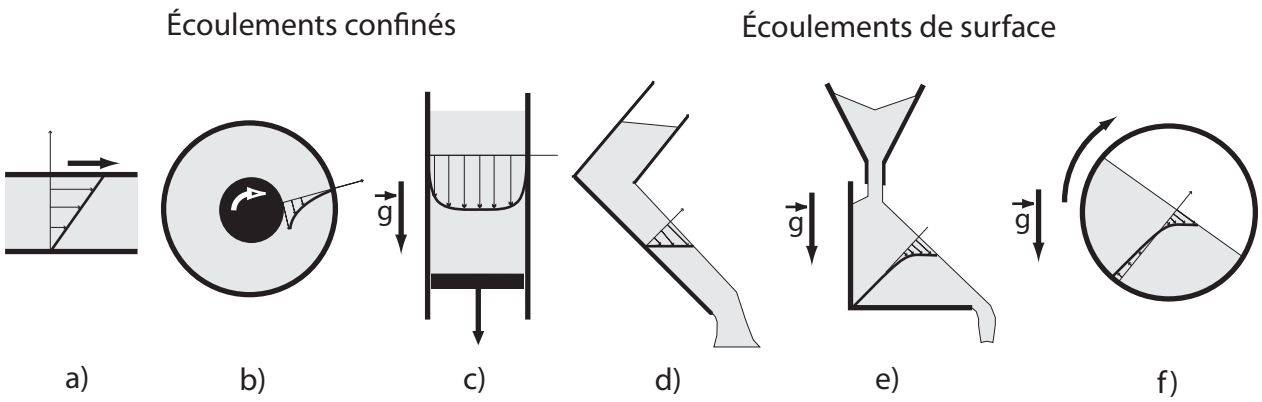

Figure 1-1 Classification des écoulements selon le Groupement De Recherche Milieux Divisés: a) cisaillement entre plans b) cisaillement annulaire c) chute verticale d) plan incliné e) tas f) cylindre rotatif. Adapté de GDR MiDi (2004).

Lacey (1954) a identifié trois mécanismes principaux de mélange particulaire soit les mélanges par convection, diffusion ou cisaillement. Le mélange par convection est défini comme le déplacement de groupes de particules d'un endroit à l'autre. Le mélange par diffusion fait référence au réarrangement particulaire se déroulant à l'échelle de quelques particules. Comme il a été noté par Lemieux (2006), l'utilisation du terme diffusion pour qualifier un mécanisme de mélange particulaire est un abus de langage. Le terme dispersion est plus approprié et est employé dans cette thèse. Finalement, le mélange par cisaillement consiste en l'échange de particules entre deux couches de particules en mouvement et est difficilement dissociable du mélange par dispersion (Berthiaux, 2002). Dans le cas de cylindres rotatifs, il est globalement reconnu que le mélange se produisant selon l'axe de rotation du cylindre (i.e. mélange axial) est purement dispersif alors que celui se déroulant sur une section transversale du cylindre (i.e. mélange radial) est en fait une combinaison de mélange convectif et dispersif (Elperin & Vikhansky, 1998; Gray, 2001; Khakhar, 2011; Khakhar, McCarthy, Shinbrot, et al., 1997; Rao, Bhatia, & Khakhar, 1991). Dans le cas de lits fixes où des contractions/expansions des parois sont responsables de l'écoulement particulaire, le mélange est plutôt de nature dispersive.

La manipulation de matériaux particulaires dont les constituants possèdent des propriétés physiques ou physico-chimiques différentes entraîne généralement la ségrégation de ceux-ci, à

plus ou moins grande vitesse (Ottino & Khakhar, 2000). Harnby et al. (1992) mentionnent que les principales propriétés responsables de la ségrégation sont, par ordre d'importance, les différences de taille, de morphologie et de densité. L'ensemble des conditions et propriétés pouvant affecter la ségrégation complexifie grandement l'étude de ce phénomène. De plus, il est pratiquement impossible d'établir des règles infaillibles prédisant l'occurrence de la ségrégation. L'ampleur et la structure de la ségrégation obtenue dépendent de nombreux paramètres comprenant l'origine du mouvement particulaire (ex. vibrations, écoulement), la géométrie du système ainsi que les propriétés des particules (Khakhar, 2011). Les phénomènes de ségrégation due à la taille et à la densité sont ceux qui ont été le plus fréquemment étudiés (Jain, Ottino, & Lueptow, 2005). La ségrégation due à la forme particulaire n'a été étudiée que par Makse et al. (1997) dans le cas d'écoulements de tas. Cependant, le patron de ségrégation observé n'était pas spécifique à la forme des particules utilisées mais dépendait plutôt de la différence entre les angles de repos des particules utilisées. L'étude de l'effet de la forme particulaire sur la ségrégation est ardue puisqu'il est difficile de développer un contexte expérimental où l'effet de la forme est discriminé des autres facteurs pouvant affecter la ségrégation.

Cette thèse a pour objet la dynamique particulaire à l'intérieur de lits fixes où un phénomène de transfert thermique est responsable du mouvement ainsi qu'à l'intérieur de cylindre rotatif où le lit particulaire est composé de particules non-sphériques, les deux prochaines sections traiteront donc respectivement de ces aspects.

1.1.1 Lits particulaires fixes

Étant donné sa grande utilité et sa popularité industrielle, le cas de la pré-purification de l'air réalisée à l'aide d'un procédé cyclique d'adsorption par oscillations thermiques (TSA) est idéal pour étudier la dynamique particulaire pouvant survenir à l'intérieur de lits fixes (Hidano, Nakamura, & Kawai, 2011). Comme il a été souligné, ce type d'écoulement particulaire n'a jamais été étudié auparavant. Cette section se contente donc de présenter sommairement les

particularités de la pré-purification de l'air à l'aide d'un procédé de TSA ainsi que les raisons pouvant expliquer la présence d'un mouvement particulaire au sein du lit fixe.

La première étape du cycle TSA consiste en la pressurisation du lit à l'aide du gaz qui sera ensuite passé à travers le lit pour que les contaminants puissent être adsorbés. Puis, le lit est dépressurisé et alimenté avec un gaz de régénération chauffé à contre-courant afin de permettre la désorption des contaminants, régénérant ainsi les adsorbants. Finalement, le lit est alimenté avec un gaz de refroidissement pour l'amener à son état thermique initial. Les deux principales étapes du cycle TSA, soit l'adsorption et la désorption sont présentées à la Figure 1-2. Un cycle TSA s'étale généralement sur plusieurs heures (Ruthven, 1984). Les températures nécessaires pour la régénération des adsorbants sont relativement élevées, variant entre 150°C et 300°C, et dépendent du type d'adsorbant utilisé de même que des impuretés à retirer (Hidano et al., 2011; Kalbassi & Golden, 1999; Ko, Kim, Moon, & Choi, 2002; Kumar & Dissinger, 1986; Ruthven, 1984).

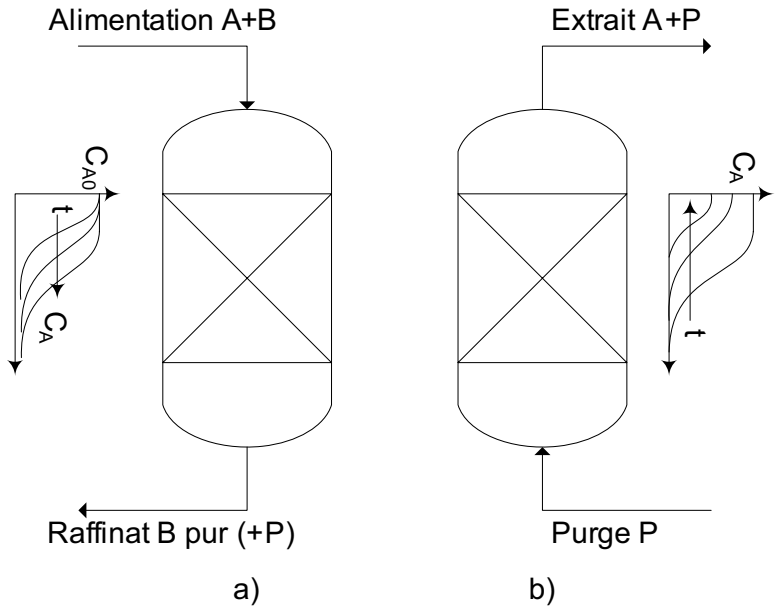

Figure 1-2 Étapes de a) adsorption et b) désorption du cycle TSA. Adapté de Ruthven (1984).

Un réacteur à lit fixe axial (Figure 1-3a) est généralement employé pour pré-purifier de l'air à l'aide d'un procédé de TSA. Le terme axial fait référence au fait que le gaz passe à travers le lit

fixe selon l'axe du cylindre composant le réacteur. Dans ce genre de réacteur, au minimum deux types différents d'adsorbants sont empilés axialement. La première couche est généralement composée d'alumine activée, servant à retirer l'eau de l'air, alors que la deuxième couche est composée de zéolites synthétiques de type X, permettant de retirer le dioxyde de carbone et d'autres contaminants mineurs (Ackley et al., 2012; Hidano et al., 2011; Kalbassi & Golden, 1999; Kumar, Huggahalli, & Bülow, 2002). Ces deux types d'adsorbants présentent des propriétés physiques et des granulométries généralement significativement différentes. Les réacteurs à flux radial (RFR) (Figure 1-3b) sont aussi fréquemment utilisés pour ce type de procédé (Ackley, Celik, Nowobilski, & Schneider, 2011; Libal et al., 1998). Dans de tels réacteurs, l'air circule radialement à travers le lit fixe, ce qui implique que les adsorbants sont aussi empilés de cette manière. Comparés aux réacteurs à lit fixe axial, ces derniers présentent comme avantage de nécessiter une perte de charge moins grande pour l'opération, d'augmenter la surface de circulation du gaz et de permettre un débit de gaz plus élevé. La plupart des études sur ce type de réacteur se sont concentrées sur l'uniformité de la distribution du gaz le long de la hauteur du lit puisque leur efficacité ainsi que leur rentabilité dépendent essentiellement de cet aspect (Celik & Ackley, 2012; Heggs, Ellis, & Ismail, 1995a, 1995b; Kareeri, Zughbi, & Al-Ali, 2006; Lobanov & Skipin, 1986; Ponzi & Kaye, 1979).

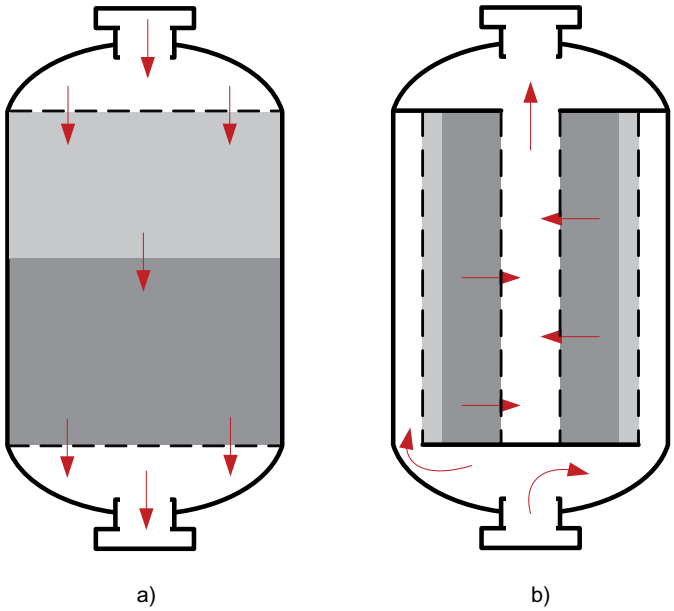

Figure 1-3 Représentation schématique d'un a) réacteur axial et d'un b) réacteur à flux radial contenant deux types d'adsorbants.

En raison des avantages techniques que présentent les RFR, l'utilisation de ces derniers pour des procédés d'adsorption à grande échelle est fortement favorisée. Cependant, lorsque ce réacteur est utilisé en combinaison avec un procédé impliquant de larges oscillations thermiques comme le TSA, ses composantes mécaniques, dont les parois retenant le lit d'adsorbants, se contractent et se dilatent (Ackley et al., 2012; Libal et al., 1998). Ceci engendre inévitablement un mélange des adsorbants à leur interface et peut aussi entraîner la ségrégation de ceux-ci. Après plusieurs cycles, le mélange et la ségrégation des adsorbants peuvent être tels que l'uniformité de distribution du gaz d'alimentation ainsi que l'efficacité et le rendement du procédé en sont significativement affectés. Le type d'écoulement particulaire dense confiné dont il est question dans cette thèse n'entre pas dans une des catégories répertoriées par le GDR Midi (Figure 1-1) et est schématisé à la Figure 1-4.

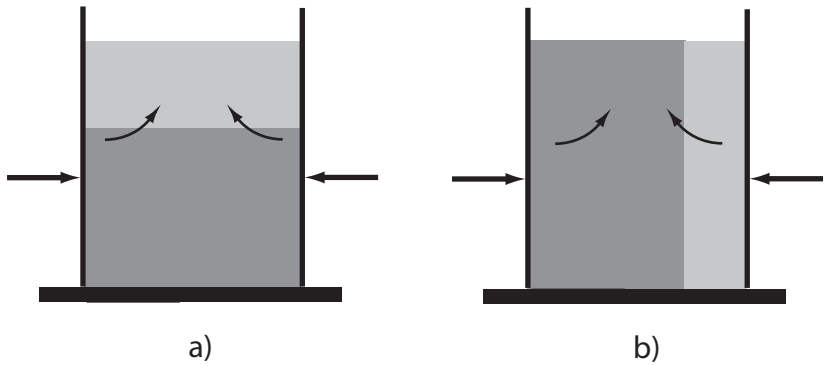

Figure 1-4 Schéma de l'écoulement particulaire dense pouvant survenir dans le cas de lits fixes contenu dans un a) réacteur axial et un b) réacteur à flux radial.

1.1.2 Lits particulaires rotatifs

La dynamique particulaire à l'intérieur de cylindres rotatifs a été considérablement étudiée principalement à cause du grand nombre d'applications ayant recours à ce type d'équipement mais aussi parce que, utilisés comme modèle expérimental, les cylindres rotatifs présentent un écoulement ne possédant essentiellement que deux dimensions, amenant ainsi de nombreuses simplifications.

Le régime d'écoulement particulaire prenant place à l'intérieur de cylindres rotatifs peut être classifié selon quatre catégories : avalanche/affaissement (« avalanching/slumping »), roulement (« rolling »), déferlement (« cataracting ») et centrifuge (« centrifugating ») (Figure 1-5) (Ottino & Khakhar, 2000). Pour certains auteurs (Henein, Brimacombe, & Watkinson, 1983; Mellmann, 2001), le régime de type roulement inclut le régime appelé cascade (« cascading »). Le régime obtenu dépend du nombre de Froude (Fr), représentant le ratio entre les forces inertielles et la force gravitationnelle, et obtenu par :

$$Fr = \frac{\omega^2 R}{g} \tag{1.1}$$

où ω est la vitesse de rotation angulaire du cylindre, R le rayon du cylindre et g l'accélération gravitationnelle.

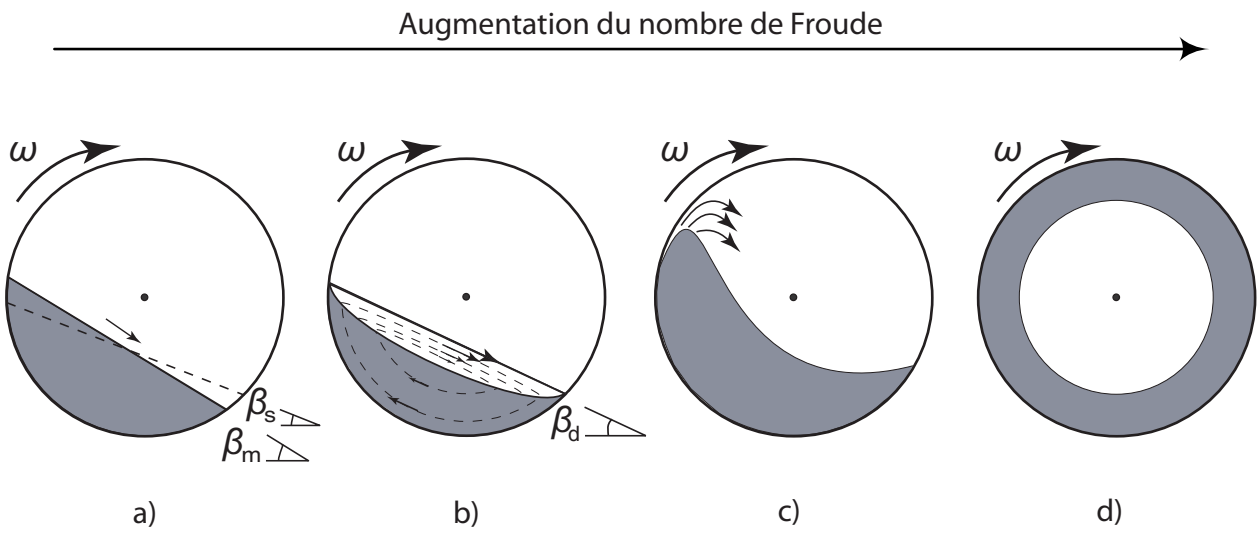

Figure 1-5 Régimes d'écoulement particulaire à l'intérieur de cylindres rotatifs: a) avalanche, b) roulement, c) déferlement et d) centrifuge. Adapté de Meier (2007).

Les valeurs du nombre de Froude correspondant à la transition entre les différents régimes dépendent des propriétés particulaires (taille, forme, coefficient de friction), du niveau de remplissage, de la vitesse de rotation angulaire ainsi que du ratio entre la taille des particules et la taille du cylindre (Henein et al., 1983; Mellmann, 2001). Le Tableau 1-1 présente les caractéristiques propres à chacun des régimes d'écoulement ainsi que les plages du nombre de Froude correspondantes à chacun (Brucks, Arndt, Ottino, & Lueptow, 2007; Henein et al., 1983; Meier, 2007; Mellmann, 2001). Le régime d'écoulement de type roulement est celui le plus souvent utilisé pour opérer les cylindres rotatifs puisqu'il permet un meilleur mélange des particules et donc un meilleur transfert de masse et de chaleur à l'intérieur du cylindre (Fantozzi, Colantoni, Bartocci, & Desideri, 2007; S. Q. Li, Chi, Li, Yan, & Cen, 2002; Liu, Specht, Gonzalez, & Walzel, 2006).

Tableau 1-1 Caractéristiques des régimes d'écoulement à l'intérieur de cylindres rotatifs

Régime	**Nombre de Froude**	**Caractéristiques**
Avalanche	$10^{-5} < Fr < 10^{-3}$	Avalanche sporadique des particules à la surface du lit.
Roulement	$10^{-4} < Fr < 10^{-1}$	Couche mince, appelée couche active, à la surface du lit où les particules s'écoulent rapidement.
Déferlement	$10^{-1} < Fr < 1$	Détachement des particules à la surface du lit en amont de l'écoulement.
Centrifuge	$Fr > 1$	Les particules sont centrifugées et adhèrent à la paroi du cylindre rotatif.

Des phénomènes de ségrégation radiale et axiale peuvent survenir à l'intérieur des cylindres rotatifs si des particules de différentes densités et/ou tailles sont utilisées. Dans un régime de roulement, la ségrégation radiale se produit essentiellement dans la couche active suite à la percolation de petites particules à travers les interstices entre les grosses particules ou par une différence de densité entre les particules légères et lourdes (Khakhar, Orpe, & Hajra, 2003). Le patron de ségrégation radiale traditionnellement observé est celui où les particules petites ou denses se retrouvent au centre de l'écoulement alors que les grosses et légères se retrouvent en périphérie (Alizadeh, Dubé, Bertrand, & Chaouki, 2013; Jain et al., 2005; Meier, 2007). Il est aussi possible d'obtenir un patron de ségrégation inversé, c'est-à-dire un patron où les petites particules se retrouvent en périphérie et les grosses particules se retrouvent au centre, suite à l'augmentation de la vitesse de rotation du cylindre (Nityanand, Manley, & Henein, 1986). Différentes formes de patrons de ségrégation, comme la présence de stries radiales, peuvent aussi être obtenues pour divers types de particules, de ratios de la taille des particules sur la taille du cylindre, de niveaux de remplissage, de vitesses de rotation ainsi que de combinaisons de taille et de densité (Jain et al., 2005; Khakhar, Orpe, & Ottino, 2001a). La ségrégation radiale est généralement très rapide et peut survenir à l'intérieur d'une ou deux rotations du cylindre (Meier, 2007). La ségrégation axiale fait quant à elle référence à l'apparition de bandes riches en un type de particules après quelques centaines de rotations du système (Meier, 2007). Cependant, ces

bandes de ségrégation ne contiennent pas nécessairement qu'un seul type de particule; elles peuvent aussi faire l'objet de ségrégation radiale traditionnelle et ainsi contenir un cœur plus riche que la périphérie en un type de particules (Hill, Caprihan, & Kakalios, 1997; Meier, 2007). La plupart des études mentionnent que la ségrégation axiale peut être attribuée à une différence d'angle de repos des particules du système (Das, Khakhar, & Bhatia, 1991; Hill & Kakalios, 1994, 1995; Zik, Levine, Lipson, Shtrikman, & Stavans, 1994). Toutefois, des résultats obtenus par Hill et al. (1997) suggèrent que la ségrégation axiale ne peut être exclusivement expliquée par une différence d'angle de repos. Chen et al. (2010) mentionnent que l'écoulement axial des particules peut aussi être responsable de l'apparition de ségrégation axiale.

1.2 Méthodes expérimentales de caractérisation des écoulements particulaires

Les méthodes expérimentales de caractérisation des écoulements granulaires sont nombreuses et variées. La qualité et la quantité d'informations qu'elles permettent d'obtenir varient aussi grandement d'une méthode à une autre. Lemieux (2006) a classé les méthodes les plus couramment employées selon leur caractère perturbateur et non-perturbateur. Le choix d'une méthode dépend essentiellement des objectifs de l'étude (dynamique, mélange, ségrégation, dispersion, etc.), des propriétés particulaires ainsi que du système particulaire à caractériser.

1.2.1 Méthodes perturbatrices

Une méthode dont l'utilisation entraîne une modification de l'écoulement particulaire ou bien de la structure du lit granulaire est dite perturbatrice. Les techniques de solidification du lit particulaire (Brone, Alexander, & Muzzio, 1998; Wightman & Muzzio, 1998), les méthodes de prélèvements avec sondes voleuses (Lemieux, Bertrand, Chaouki, & Gosselin, 2007; Muzzio, Robinson, Wightman, & Dean, 1997; Perrault, Bertrand, & Chaouki, 2010) ainsi que les mesures réalisées à l'aide de fibres optiques (Boateng & Barr, 1997; Pugsley et al., 2003) sont toutes des

méthodes perturbatrices. Ces méthodes présentent l'avantage de pouvoir être appliquées facilement ainsi que d'être peu coûteuses, étant donné qu'elles requièrent une instrumentation généralement moins sophistiquée. Cependant, leur caractère perturbateur est un inconvénient majeur pour l'étude de la dynamique d'écoulement particulaire. La mesure peut ne pas représenter exactement les conditions normales de l'écoulement.

1.2.2 Méthodes non-perturbatrices

Les méthodes non-perturbatrices peuvent être classées selon leur nature intrusive ou non-intrusive. Une méthode est dite intrusive si un contact avec les particules est nécessaire pour en évaluer la composition. Selon Lemieux (2006), la spectroscopie proche infrarouge (NIR) (Arratia et al., 2006), la fluorescence par lumière induite (LIF) (Lai et al., 2001) ainsi que l'effusivité (Leonard, Bertrand, Chaouki, & Gosselin, 2008) sont des exemples de méthodes intrusives. Le principal inconvénient de ces méthodes est de ne pouvoir analyser que la surface des écoulements. Ainsi, dans le cas d'un écoulement où il y a présence de ségrégation, les mesures obtenues par ces méthodes ne sont pas représentatives de l'ensemble de l'écoulement.

À l'opposé, les méthodes non-intrusives sont celles qui ne nécessitent pas de contact avec les particules pour en caractériser l'écoulement. Chaouki et al. (1997) présentent une revue détaillée des différentes techniques tomographiques et vélocimétriques non-invasives utilisées pour la caractérisation d'écoulements poly-phasiques. Seules les techniques fréquemment employées pour étudier les écoulements particulaires denses sont discutées ici. Ainsi, il est question des techniques de vélocimétrie par imagerie de particules (PIV) ou par suivi de particules (PTV), d'imagerie par résonnance magnétique (MRI), de suivi de particules par émission de positrons (PEPT) et de suivi de particules radioactives (RPT).

Les techniques de PTV/PIV sont celles les plus souvent employées pour l'étude de la dynamique particulaire. Contrairement à la majorité des méthodes non-perturbatrices, celles-ci sont

relativement simples à appliquer et utiliser. L'instrumentation nécessaire est aussi disponible à coût abordable. Ces techniques ont notamment été utilisées pour étudier l'écoulement se produisant à l'intérieur de cylindres rotatifs par, entre autres, Alexander et al., (2002) Jain et al. (2002) ainsi que Orpe et Khakhar (2007). Récemment, Chung et al. (2010) ont adapté la PTV au cas de particules non-sphériques, permettant ainsi la détermination des vitesses de translation et de rotation de ces dernières. Malheureusement, ces techniques ne peuvent que quantifier l'écoulement à la surface libre des particules ou sous la surface si le montage expérimental est constitué de parois transparentes. Cependant, dans ce cas, l'écoulement particulaire mesuré est affecté par la présence de ces parois et la mesure réalisée peut ne pas être représentative de l'écoulement prenant place loin des parois (Alizadeh, Bertrand, & Chaouki, 2013).

La technique de MRI utilise l'émission de fréquences radio et un champ magnétique pour faire interagir les spins de noyaux atomiques des molécules hydrogénées et ainsi obtenir des profils de vitesse et de concentration (Leonard, 2005). Cette technique a notamment été appliquée à l'étude d'écoulements particulaires à l'intérieur de cylindres rotatifs (Kawaguchi, Tsutsumi, & Tsuji, 2006; Nakagawa, Altobelli, Caprihan, Fukushima, & Jeong, 1993) et de lits fluidisés (Kawaguchi, 2010). L'instrumentation sophistiquée nécessaire à cette méthode et l'opération de l'équipement peuvent s'avérer très coûteuses (Kawaguchi, 2010). De plus, la taille ainsi que le type de systèmes particulaires pouvant être étudiés par cette méthode sont grandement limités par l'instrumentation nécessaire et la sensibilité de cette dernière aux conditions environnantes (Kawaguchi, 2010).

La PEPT suit le mouvement d'un traceur radioactif grâce à la détection simultanée de paires de rayons gamma colinéaires ayant une énergie de 511keV et émis suite à la collision entre un positron et un électron. Les radio-isotopes utilisés pour cette technique sont généralement le ^{18}F, le ^{61}Cu ou le ^{66}Ga et le marquage radioactif d'une particule au radio-isotope désiré s'effectue à l'aide d'un cyclotron, soit par activation directe, transfert d'ions ou bien par modification de surface (Parker & Fan, 2008). La technique de fabrication et d'activation du traceur dépend fortement de la composition ainsi que de la taille de ce dernier. La taille des traceurs utilisés est généralement de l'ordre de quelques millimètres. Elle peut aussi être inférieure à 1000 μm si les

propriétés du traceur permettent le marquage du traceur par transfert d'ions. La PEPT a été appliquée avec succès, entre autres, à l'étude de la dynamique particulaire à l'intérieur de cylindres rotatifs (Ingram, Seville, Parker, Fan, & Forster, 2005; Parker, Dijkstra, Martin, & Seville, 1997), de mélangeurs en V (Kuo, Knight, Parker, & Seville, 2005) et de lits fluidisés (Van de Velden, Baeyens, Seville, & Fan, 2008). Les récents développements de la PEPT se sont concrétisés au niveau de la création d'algorithmes permettant de reconstruire les trajectoires de plusieurs traceurs utilisés simultanément (Yang, Fan, Bakalis, Parker, & Fryer, 2008; Yang et al., 2007) ainsi que de la conception de nouvelles caméras modulaires (Leadbeater, Parker, & Gargiuli, 2011; Parker et al., 2008). Malheureusement, l'instrumentation nécessaire à la PEPT est complexe et très dispendieuse (Chaouki et al., 1997). De plus, le type de caméra utilisée limite grandement la taille des systèmes qui peuvent être étudiés grâce à cette méthode ainsi que les vitesses de particules pouvant être mesurées. Finalement, des complications de nature réglementaire ainsi que des coûts élevés reliés à la production et au transport des radio-isotopes limitent davantage l'utilisation de la PEPT, notamment dans le cas où un accélérateur cyclotron n'est pas disponible sur place.

La RPT est une technique permettant de suivre un traceur radioactif grâce à la détection de rayons gamma (Figure 1-6). Contrairement à la PEPT, ces derniers n'ont pas à être colinéaires pour pouvoir reconstruire la trajectoire du traceur. La RPT utilise plutôt une relation phénoménologique pour relier le nombre de rayons gamma reçus et effectivement comptés par un détecteur à scintillations à la position du traceur radioactif (Knoll, 2000; Larachi, Kennedy, & Chaouki, 1994; Tsoulfanidis, 2011). La redondance introduite par l'utilisation de plusieurs détecteurs permet de localiser le traceur radioactif avec une grande précision. Contrairement à la PEPT, la RPT est une méthode basée sur l'atténuation des rayons gamma dans le système à l'étude. Ainsi, les frontières de ce dernier de même que les interfaces de matières doivent être connues pour pouvoir appliquer la technique. Les principaux radio-isotopes utilisés sont le ^{46}Sc, le ^{198}Au et, plus récemment, le ^{24}Na (Alizadeh, Dubé, et al., 2013; Godfroy, Larachi, Kennedy, Grandjean, & Chaouki, 1997; S. Roy, Larachi, Al-Dahhan, & Dudukovic, 2002). La taille des traceurs utilisés est généralement de l'ordre de quelques millimètres. Tout comme la PEPT, la RPT a été employée avec succès, pour étudier, entre autres, la dynamique particulaire à l'intérieur de cylindres rotatifs (Alizadeh, Dubé, et al., 2013; Sheritt, Chaouki, Mehrotra, & Behie, 2003),

de mélangeurs en V (Doucet, Bertrand, & Chaouki, 2008) et de lits fluidisés (Larachi, Chaouki, & Kennedy, 1995; Upadhyay & Roy, 2010). Les plus récents développements réalisés au niveau de cette technique ont consisté à étendre la méthode pour pouvoir considérer des systèmes ayant des frontières mobiles irrégulières (Doucet, Bertrand, et al., 2008) et à intégrer le code *Monte Carlo N Particle Version 5* (MCNP5) à l'algorithme de la RPT pour ainsi pouvoir considérer davantage de phénomènes d'interactions entre la matière et les rayons gamma (Mosorov & Abdullah, 2011). La RPT a l'avantage d'être moins dispendieuse que la PEPT et la MRI. De plus, elle n'est pas limitée par la taille du système auquel elle peut être appliquée. Cependant, la considération des surfaces particulaires irrégulières et variantes dans le temps n'est pas simple. De plus, l'incertitude quant aux résultats obtenus avec la RPT pour l'étude de systèmes hautement hétérogènes possédant une structure interne variable peut être grande, voire inacceptable. Aussi, la RPT requiert une étape de calibration pour mesurer l'atténuation des rayons gamma dans la matière. Cette calibration doit idéalement être réalisée dans des conditions identiques à celles dans lesquelles la mesure sera réalisée. Ceci peut nuire sensiblement à l'application de la RPT.

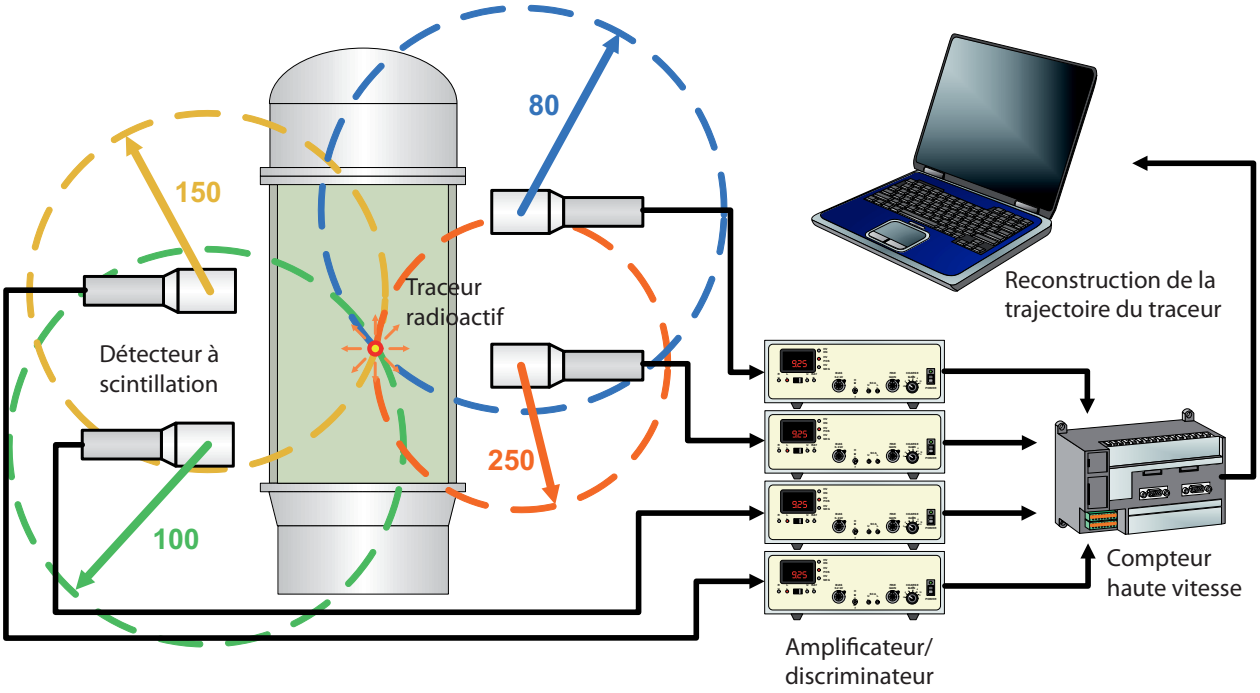

Figure 1-6 Montage expérimental RPT typique. Adapté de Doucet et al. (2008).

En résumé, les méthodes non-perturbatrices non-invasives sont idéales pour étudier les écoulements particulaires denses. Cependant, elles requièrent généralement une instrumentation plus sophistiquée et dispendieuse, les rendant ainsi plus difficiles à appliquer et utiliser. Il est important de mentionner que dans le cas des méthodes utilisant des particules traceurs, celles-ci doivent absolument présenter des propriétés identiques (taille, forme, densité, surface, etc.) à celles des particules à l'étude. Cette contrainte est souvent très difficile à surmonter (Bridgwater, 1995). De plus, dans le cas de la RPT et de la PEPT, une reconstruction précise de la trajectoire du traceur n'est souvent possible que si la portion du traceur émettrice de rayons gamma est petite, idéalement ponctuelle. L'utilisation de traceurs de l'ordre du centimètre ne permet souvent pas d'obtenir des résultats d'une qualité satisfaisante.

1.3 Modélisation des écoulements particulaires

Les modèles numériques permettant de simuler des écoulements particulaires sont classés selon leur nature continue ou discrète. L'utilisation de l'une ou l'autre de ces méthodes dépend en fait de l'application étudiée. Il est fréquent qu'une compréhension complète d'un écoulement particulaire passe par une utilisation complémentaire de ces deux types de méthodes (McCarthy, Khakhar, & Ottino, 2000; Meier, 2007).

Meier (2007) mentionne qu'il est souvent préférable d'utiliser une méthode de modélisation discrète lorsque les interactions particule-particule affectent grandement l'écoulement, qu'il y a présence de forces à long rayon d'action (i.e. cohésion), que les propriétés de surface des particules telle la rugosité sont importantes ou que les couches d'écoulements ne sont pas simplement connectées, comme dans le cas où l'écoulement est causé par les pales d'un mélangeur. À l'inverse, une approche continue est envisageable lorsque les interactions entre les particules sont moins importantes ou, par exemple, lorsque l'effet de la géométrie d'un système sur l'écoulement particulaire est étudié.

1.3.1 Approches continues

Les modèles continus sont composés d'une série d'équations différentielles partielles constitutives, représentant la conservation de quantités clés, tels la masse, le moment et l'énergie, ainsi que des conditions limites (Cleary, 2008). Ces modèles sont généralement beaucoup moins exigeants au niveau computationnel que les modèles discrets.

La théorie cinétique des gaz est un exemple de modèle continu qui a été modifié pour ainsi être appliqué aux écoulements particulaires rapides (Campbell, 2006). Malheureusement, les études ont montré que ce type de modèle n'est utile que dans le cas d'écoulements dilués de particules sphériques ayant un coefficient de restitution supérieur à 0.9 et respectant l'hypothèse du chaos moléculaire de Boltzmann (i.e. aucune corrélation entre les positions et les vitesses des particules qui entreront en contact) (Campbell, 2006). Ce type de modèle n'est donc pas approprié pour modéliser la dynamique particulaire d'écoulements denses comme ceux considérés dans cette thèse.

Une des grandes difficultés rencontrées lors de l'élaboration d'un modèle continu pour la simulation d'écoulements denses consiste à identifier la contribution relative des contraintes de friction et de contact à l'écoulement (Meier, 2007). Le modèle nommé JFP proposé par Jop et al. (2006) ainsi que les approches de profondeur moyenne utilisant des bilans de masse et de quantité de mouvement (Khakhar, Orpe, Andresen, & Ottino, 2001; Savage & Hutter, 1989) sont des exemples d'approches continues qui ont été développées. Ces dernières ont été appliquées à des écoulements denses le long de plans inclinés et/ou à l'intérieur de cylindres rotatifs (Ding, Seville, Forster, & Parker, 2001; Gray, 2001; Khakhar, 2011; Khakhar, McCarthy, Shinbrot, et al., 1997).

1.3.2 Modèles discrets

Les modèles discrets simulent le déplacement de chacune des particules d'un système et appliquent un traitement particulier en cas de collisions particulaires (Bertrand, Leclaire, & Levecque, 2005). Ces modèles peuvent essentiellement être regroupés selon deux catégories : probabiliste ou déterministe. Les modèles probabilistes se basent sur un générateur de nombres aléatoires pour simuler le déplacement des particules alors que les modèles déterministes utilisent la force totale agissant sur la particule pour la déplacer (Bertrand et al., 2005). Cette section traite exclusivement de la méthode discrète la plus utilisée, soit la méthode des éléments discrets (DEM).

La DEM est une méthode lagrangienne déterministe qui calcule les interactions entre les éléments d'un système ainsi qu'entre ces éléments et leur environnement (Langston, Al-Awamleh, Fraige, & Asmar, 2004). Originalement introduite par Cundall et Strack (1979), la DEM consiste en l'application de la deuxième loi de Newton à chacune des particules d'un système pour ainsi simuler leurs déplacements. Conséquemment, un bilan de force et de quantité de mouvement est réalisé sur chacune des particules :

$$m\frac{d^2\vec{x}}{dt^2} = m\vec{g} + \sum\left(\vec{F_n} + \vec{F_t}\right) \tag{1.2}$$

$$I\frac{d\vec{\omega}}{dt} = \sum\left(\vec{T} + \vec{M}\right) \tag{1.3}$$

où $\vec{x}$, m, I, $\vec{\omega}$ sont respectivement le vecteur position, la masse, le moment d'inertie et le vecteur de vitesse angulaire d'une particule, $\vec{g}$ l'accélération gravitationnelle, $\vec{T}$ le couple et $\vec{M}$ le couple de friction de roulement. Sous sa plus simple application, la DEM intègre les forces gravitationnelles $\left(m\vec{g}\right)$ ainsi que celles de contacts particule-particule et particule-paroi, exprimées en composantes normales $\left(\vec{F_n}\right)$ et tangentielles $\left(\vec{F_t}\right)$. Il est à noter que diverses forces hydrodynamiques (p.ex. poussée d'Archimède, force de traînée) ou non-hydrodynamiques (p.ex. forces cohésives capillaires ou colloïdales) peuvent être intégrées au bilan de force. Lors de

simulations DEM, les particules sont considérées comme étant des solides viscoélastiques. La déformation particulaire engendrée suite à un contact est représentée par un chevauchement particulaire. Un modèle de force de contact (aussi appelé relation force-déplacement) permet de relier les composantes normales et tangentielles des forces de contact au chevauchement particulaire. Des exemples de contact particule-particule ainsi que de modèle de force de contact sont présentés à la Figure 1-7. Une analyse exhaustive des différents modèles de force développés pour la DEM a été réalisée par Di Renzo et Di Maio(2004), Zhu et Yu (2006) et Thornton et al. (2011, 2013).

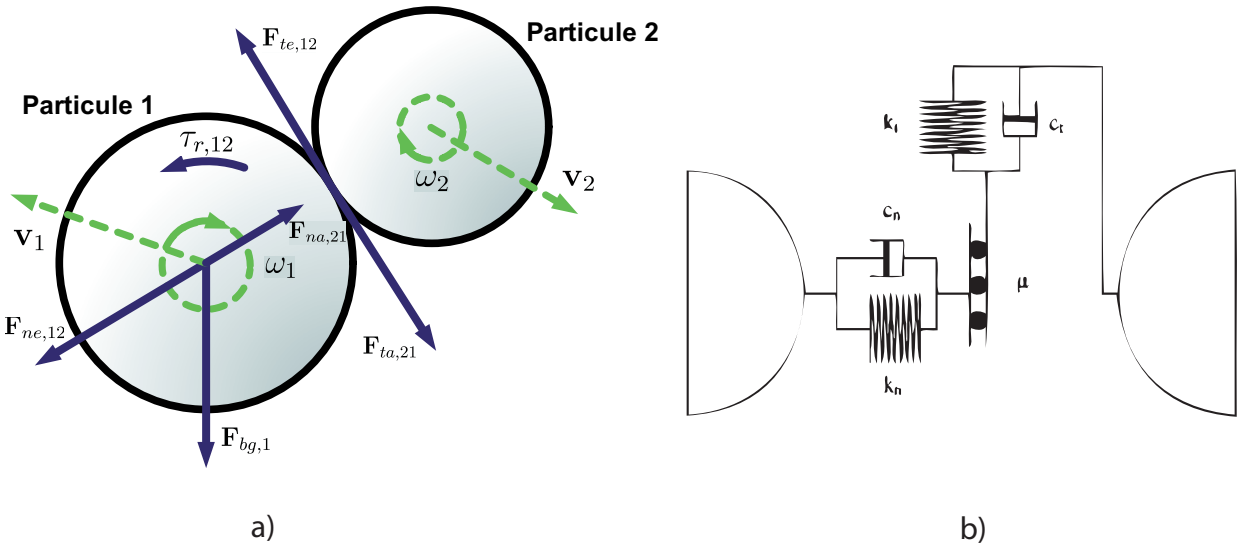

Figure 1-7 Représentation schématique de a) la DEM (adapté de Bouffard (2012)) et b) un modèle de force de type ressort-amortisseur (adapté de Cundall et Strack (1979)).

La DEM est basée sur l'idée qu'en prenant un pas de temps assez faible, qui est généralement de l'ordre de 10^{-6}s, les perturbations dues aux contacts ne se propageront pas au-delà des particules directement voisines (Cundall & Strack, 1979; Mack, Langston, Webb, & York, 2011). Ainsi, le pas de temps adéquat pour la réalisation de simulations DEM dépend des propriétés particulaires. Le choix de celui-ci est une étape critique et a été le sujet de nombreuses publications (Doucet, 2008; Y. Li, Xu, & Thornton, 2005; O'Sullivan & Bray, 2004). Une itération typique de l'algorithme de la DEM consiste à 1) déplacer les murs de la géométrie, 2) détecter et résoudre les contacts particule-particule ainsi que particule-paroi et 3) intégrer l'équation de Newton pour

ensuite déplacer les particules (Leclaire, 2004). L'étape consistant en la détection des contacts est la plus importante et la plus exigeante en termes de temps calcul possédant un ordre variant entre $O(N \log N)$ et $O(cN)$, où N est le nombre total de particules simulées et c (Munjiza, Latham, & John, 2003; Perkins & Williams, 2001; Williams, Perkins, & Cook, 2004) est une constante. L'efficacité au niveau de l'utilisation du temps calcul et, dans une moindre mesure, l'exactitude des résultats de simulations DEM dépendent aussi de la méthode d'intégration numérique utilisée pour intégrer l'équation de Newton. Étant donné la grande variété de méthodes disponibles, plusieurs études se sont penchées sur les performances et les conséquences de ces dernières (Fraige & Langston, 2004; Kruggel-Emden, Stepanek, & Munjiza, 2011; Kruggel-Emden, Sturm, Wirtz, & Scherer, 2008; Rougier, Munjiza, & John, 2004).

La DEM a été utilisée pour étudier une grande variété de procédés particulaires. Pour n'en nommer que quelques-uns, elle a notamment été appliquée avec succès pour étudier le remplissage, le stockage et la décharge de particules à l'intérieur de trémies (Balevicius, Sielamowicz, Mroz, & Kacianauskas, 2011; Goda & Ebert, 2005; Gonzalez-Montellano, Ramirez, Gallego, & Ayuga, 2011; Ketterhagen, Curtis, Wassgren, & Hancock, 2009; Masson & Martinez, 2000) ainsi que le mélange et la ségrégation particulaire à l'intérieur de mélangeurs à tambour (Lemieux et al., 2007; Sudah, Arratia, Alexander, & Muzzio, 2005) ou de cylindres rotatifs (Rapaport, 2007).

La capacité de la DEM à prédire ou reproduire des phénomènes granulaires réalistes ainsi que des propriétés et paramètres d'écoulements particulaires repose essentiellement sur une mesure méticuleuse des propriétés particulaires, une sélection rigoureuse du modèle de force de contact approprié et surtout, une vérification et/ou une validation expérimentale du modèle utilisé (Balevicius et al., 2011; Gonzalez-Montellano et al., 2011). Les propriétés physiques des particules peuvent être évaluées à l'aide de mesures expérimentales à l'échelle de la particule ou bien par une calibration utilisant des simulations DEM auxiliaires simples permettant la discrimination de l'effet d'une propriété spécifique. Cependant, l'incorporation des propriétés physiques réelles, tels les coefficients de friction et d'amortissement de même que la dureté, à l'intérieur des modèles de force, rend fréquemment instable les simulations DEM et/ou en fausse

les résultats. Deux raisons peuvent en partie expliquer ces difficultés. Premièrement, les propriétés particulaires mesurées expérimentalement ne sont pas celles qui doivent être utilisées dans les modèles de force. Par exemple, les coefficients de friction mesurés à l'aide d'une cellule de cisaillement de type Jenike ne correspondent pas aux coefficients de friction d'interaction particule-particule se retrouvant dans les modèles de force mais sont en fait des coefficients de friction d'assemblage de particules. Deuxièmement, malgré le fait que les véritables propriétés particulaires soient incorporées aux modèles de forces, une stabilisation de la simulation ne peut être obtenue qu'en la ralentissant significativement (i.e. en diminuant le pas de temps). Cependant, les ressources computationnelles ainsi que le temps disponible pour réaliser les simulations DEM sont souvent limités. Il est parfois impossible de ralentir suffisamment les simulations pour permettre l'obtention de résultats probants à l'intérieur d'un délai raisonnable. Étant donné les limitations et les difficultés inhérentes associées aux modèles de forces ainsi qu'à leurs paramètres, de nombreux chercheurs se résignent alors à calibrer ces derniers selon leurs besoins, les ressources disponibles et l'application souhaitée. Cette technique de calibration « fit-for-purpose » présente l'avantage de permettre l'obtention de résultats rapidement, donnant ainsi une idée générale de la dynamique particulaire simulée. Toutefois, elle a comme inconvénients d'être spécifique à l'application développée, donc difficilement généralisable, et de ne pas permettre une validation exhaustive du modèle DEM. Dans le meilleur des cas, elle n'en permettra qu'une vérification limitée. Dans cet ordre d'idées, il est important de mentionner qu'il est pratique courante d'utiliser une valeur anormalement basse pour représenter la dureté des particules (module de Young), permettant ainsi d'augmenter significativement le pas de temps des simulations (Gonzalez-Montellano, Ramirez, Fuentes, & Ayuga, 2012).

La grande majorité des simulations DEM utilisent des particules de formes sphériques non-cohésives. L'incorporation de la non-sphéricité au sein de la DEM fait surgir de nombreuses difficultés supplémentaires. En plus de nécessiter des temps de calculs prolongés, plusieurs complications surgissent au niveau de la représentation mathématique exacte d'une forme arbitraire, des algorithmes de détection de contacts entre particules, de l'identification rigoureuse du point de contact, du calcul du chevauchement ainsi que de l'orientation de la normale de contact et finalement, de la résolution de l'équation du moment angulaire nécessaire pour déterminer l'orientation propre de la particule (Hogue, 1998; Jia & Williams, 2001; Langston et

al., 2004; J. Li, Langston, Webb, & Dyakowski, 2004; Peters & Dziugys, 2002; Wachs, Girolami, Vinay, & Ferrer, 2012). De nombreuses approches sont proposées dans la littérature pour intégrer la forme particulaire aux simulations DEM. En effet, des assemblages de sphères (Langston et al., 2004; Song, Turton, & Kayihan, 2006), des polyèdres (Fraige, Langston, & Chen, 2008; Hart, Cundall, & Lemos, 1988), des ellipsoïdes (X. Lin & Ng, 1995), des superquadriques (Cleary, 2008), des représentations par fonction discrète (Hogue, 1998; Williams & O'Connor, 1995) ainsi que des méthodes probabilistes (Dubé, Chaouki, & Bertrand, 2012; Jin, Xin, Zhang, & Sun, 2011) peuvent être employés pour représenter la forme d'une particule en DEM. Cependant, la grande majorité de ces approches n'ont malheureusement jamais fait l'objet d'une validation rigoureuse et exhaustive. Une simple vérification sommaire et qualitative est généralement réalisée. Par exemple, Wachs et al. (2012) ont intégré une nouvelle approche pour la simulation DEM de particules ayant une forme arbitraire convexe mais ont seulement pu comparer les résultats de leur approche à des expériences impliquant des particules sphériques. Pour leur part, Kodam et al. (2010) ont développé les algorithmes de contact nécessaires pour la simulation DEM de cylindres mais ils ont seulement évalué leur modèle en le comparant à des données expérimentales des angles de repos dynamiques à l'intérieur de cylindre rotatif ainsi que des hauteurs de remplissage. Les lacunes au niveau de la validation des modèles DEM non-sphériques proviennent en grande partie du fait qu'il est difficile de créer un contexte expérimental, facilement reproductible numériquement, où l'effet de la forme particulaire est discriminé des autres facteurs influençant la dynamique, et où une technique de mesure adéquate, permettant une quantification détaillée de la dynamique particulaire, peut être appliquée.

De nombreux groupes de recherches à travers le monde tentent de corriger, adapter et améliorer les modèles DEM actuels en se basant sur les plus récents avancements scientifiques au niveau de la physique particulaire de même qu'en employant divers artifices numériques, computationnels et logiciels. En plus de tous les travaux concernant le traitement de la forme particulaire présentement en cours, plusieurs groupes œuvrent activement, entre autres, à l'incorporation de modèles de cohésion particulaire (S. Li, Marshall, Liu, & Yao, 2011; Mishra, Thornton, & Bhimji, 2002), à l'adaptation des programmes DEM aux environnements massivement parallèles (Longmore, Marais, & Kuttel, 2013; Radeke, Glasser, & Khinast, 2010) ou à l'implantation de phénomènes de transfert thermique (Chaudhuri, Muzzio, & Tomassone, 2010; Figueroa, Vargas,

& McCarthy, 2010; Zhang, Zhou, Xing, & Muhlhaus, 2011). Parallèlement, afin de pouvoir prendre en considération une autre phase que celle du solide (i.e. les particules) ou bien de tout simplement accélérer les simulations, plusieurs essaient de combiner la DEM à d'autres méthodes de simulation numérique tels la dynamique des fluides computationnelle (CFD) (Fries, Antonyuk, Heinrich, Dopfer, & Palzer, 2013; Shi, Vargas, & McCarthy, 2008), les chaînes de Markov (Doucet, Hudon, Bertrand, & Chaouki, 2008; Tjakra, Bao, Hudon, & Yang, 2013), la méthode de Lattice-Botlzmann (LBM) (Feng, Han, & Owen, 2010; Monitzer, 2012) ou les bilans de population (PBM) (Bouffard, Bertrand, & Chaouki, 2012; Freireich, Li, Litster, & Wassgren, 2011), développant ainsi des approches multi-échelles.

CHAPITRE 2 ORGANISATION DE LA THÈSE

Il a été démontré au Chapitre 1 que l'étude des écoulements particulaires est complexe. Une panoplie d'approches expérimentales et/ou numériques peuvent être utilisées pour réaliser ce genre d'étude. Le choix de l'approche dépend des propriétés des particules, du système particulaire étudié ainsi que des objectifs de l'étude.

La pré-purification de l'air réalisée à l'aide d'un procédé cyclique d'adsorption par oscillations thermiques (TSA) est le cas idéal pour étudier l'écoulement particulaire pouvant survenir à l'intérieur de lits fixes. L'écoulement particulaire à l'intérieur d'un réacteur à flux radial (RFR) est étudié puisque, comme il a été mentionné à la Section 1.1.1, l'utilisation de ce type de réacteur est fortement favorisée. Les techniques de mesures expérimentales perturbatrices ou non-perturbatrices ne sont pas facilement applicables à l'étude de ce genre d'écoulement ou peuvent être très coûteuses à implanter. La nature du système (colonne d'adsorption) et des particules le composant (adsorbants quasi-sphériques) favorisent l'utilisation d'une méthode numérique. Dans ce cas-ci, il est attendu que les interactions entre les particules ainsi que leurs propriétés affecteront grandement la nature de l'écoulement simulé. Ainsi, la méthode des éléments discrets (DEM) est une méthode numérique de prédilection pour réaliser cette étude. Cependant, puisque les propriétés particulaires sont importantes, il est essentiel de ne pas tenter d'accélérer la DEM en modifiant ces dernières. Le modèle DEM développé doit être calibré et vérifié avec soin.

Dans le cas d'écoulements particulaires de lits rotatifs composés de particules non-sphériques, les méthodes de simulations numériques comme la DEM, tel que souligné dans la Section 1.3.2, ne sont pas parfaitement adaptés pour étudier la dynamique de particules non-sphériques étant donné leurs lacunes au niveau de la vérification et/ou de la validation des modèles. Il est donc préférable de développer une approche expérimentale. Pour ce faire, il est nécessaire d'identifier une technique d'investigation expérimentale appropriée ainsi que de choisir des particules non-sphériques adaptées à cette technique. Parmi l'ensemble des méthodes décrites à la Section 1.2, la

technique de suivi de particules radioactives (RPT) est une technique appropriée pour effectuer cette étude. Dans le cadre de cette thèse, des comprimés pharmaceutiques ont été retenus pour représenter les particules non-sphériques. Ce type de matériaux a essentiellement été choisi pour trois raisons. Premièrement, il est facile, dans une certaine mesure, d'en contrôler la composition. Conséquemment, un composé produisant un radio-isotope pouvant être utilisé avec la RPT peut être introduit dans le mélange servant à la fabrication des comprimés. Deuxièmement, la masse et la taille de chacun des comprimés peuvent être rigoureusement contrôlées lors de leur fabrication. Finalement, des poinçons et des matrices de formes et de tailles variées sont largement disponibles. Cependant, l'utilisation de comprimés pharmaceutiques comme traceurs pour la RPT implique que la source d'émission de rayons gamma n'est pas ponctuelle. De ce fait, une plus grande incertitude quant à la reconstruction de la position du traceur est attendue. Par conséquent, il est nécessaire de développer une méthode permettant de minimiser l'erreur commise par l'utilisation d'une source non-ponctuelle.

Ainsi, les objectifs spécifiques de cette thèse sont:

1. Évaluer à l'aide de la méthode des éléments discrets l'effet d'une contraction et d'une expansion thermique cyclique des murs d'un réacteur à flux radial utilisé pour la pré-purification de gaz sur un lit particulaire fixe;
2. Développer une stratégie d'optimisation permettant d'identifier un positionnement optimal des détecteurs à scintillation pour la technique de suivi de particules radioactives;
3. Caractériser la dynamique de particules non-sphériques à l'intérieur d'un cylindre rotatif.

L'atteinte de chacun de ces objectifs spécifiques est présentée dans les Chapitres 4, 5 et 6, correspondant en fait aux trois articles scientifiques issus de cette thèse.

Le Chapitre 4 traite donc de la modélisation DEM de la dynamique particulaire à l'intérieur d'un RFR utilisé pour la pré-purification de gaz. Les véritables propriétés particulaires sont intégrées au modèle DEM. Après avoir assuré une vérification détaillée du modèle, ce dernier est utilisé

pour mesurer la dispersion particulaire survenant à l'interface de deux types d'adsorbants couramment utilisés pour la pré-purification de l'air.

Le Chapitre 5 présente la stratégie d'optimisation permettant d'identifier un positionnement optimal des détecteurs de la RPT. La stratégie développée est validée et ensuite appliquée dans des cas de figure intéressants pour le génie chimique. Les forces ainsi que les limites de la stratégie sont présentées à travers ces applications. Cette étape d'optimisation de la technique de RPT est essentielle pour pouvoir étudier la dynamique de grosses particules non-sphériques à l'intérieur de cylindres rotatifs.

Le Chapitre 6 discute de la dynamique de particules non-sphériques à l'intérieur d'un cylindre rotatif. Plus spécifiquement, ce chapitre traite de la modélisation du temps de résidence des particules, du mélange et de la ségrégation de particules de formes et/ou de tailles différentes ainsi que de la dispersion axiale des particules. Tout au long de ce chapitre, le comportement des particules non-sphériques testées est comparé à celui de particules sphériques.

La thèse se termine par une discussion générale (Chapitre 7) présentant les principales avancées réalisées dans le cadre de cette thèse et par la présentation de recommandations pour des travaux futurs (dernier chapitre).

CHAPITRE 3 MÉTHODOLOGIE

Ce chapitre présente sommairement la méthodologie employée pour atteindre les objectifs spécifiques de cette thèse. Davantage de détails et de justifications sont présentés dans les chapitres propres à chaque article.

3.1 Dynamique particulaire dans des lits fixes

Pour évaluer l'effet d'une contraction et d'une expansion thermique cyclique des murs d'un réacteur à flux radial utilisé pour la pré-purification de gaz sur un lit particulaire fixe à l'aide de la méthode des éléments discrets (DEM), il est nécessaire de calibrer le modèle DEM, de dimensionner le domaine de simulation, d'élaborer un cycle d'expansion et de contraction des murs ainsi que de planifier les simulations numériques à réaliser.

3.1.1 Calibration du modèle

Les deux types d'adsorbants généralement utilisés pour la pré-purification de l'air, soit de l'alumine activée et des zéolites synthétiques de type X, appelés « molecular sieve », constituent des particules sphériques et sont utilisés pour cette étude. Des photos de ces deux types d'adsorbants ainsi que les distributions granulométriques (PSD) sont présentées à la Figure 3-1. Il est à noter que la PSD a été fournie par PRAXAIR Inc et est directement implantée dans le modèle DEM.

a)

b)

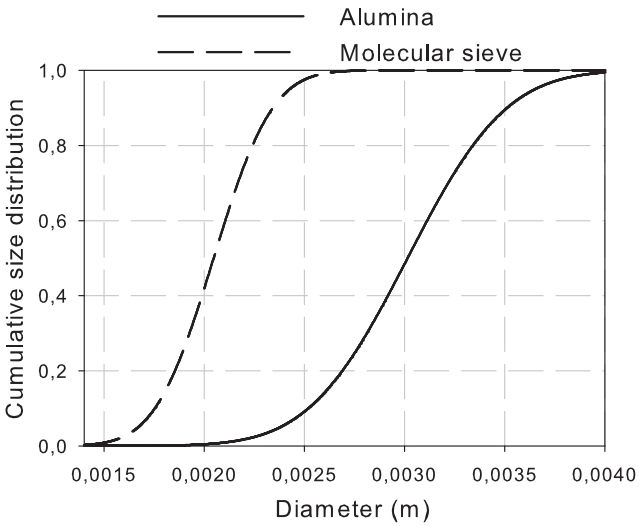

c)

Figure 3-1 Photographies a) des particules d'alumine et b) des zéolites synthétiques de type X (« molecular sieve ») utilisées ainsi que c) les distributions granulométriques de chacun.

Les trois principales propriétés particulaires à intégrer au modèle DEM sont le module de Young, le coefficient d'amortissement et le coefficient de friction. Les valeurs de module de Young de chaque adsorbant sont mesurées expérimentalement à l'aide d'une méthode de contacts par ultrasons (Akseli & Cetinkaya, 2008; C. Li & Cetinkaya, 2006). Quant aux coefficients d'amortissement et de friction à intégrer au modèle DEM, ils sont mesurés et calibrés à l'aide d'expériences auxiliaires permettant de discriminer leurs effets.

Ainsi, les coefficients d'amortissement sont évalués à l'aide des coefficients de restitution (CoR) mesurés expérimentalement suite à un impact normal sur une plaque d'acier d'une particule en chute libre. Pour mesurer les CoR, les expériences de chute libre sont filmées à l'aide d'une caméra haute vitesse utilisant une fréquence d'enregistrement de 120 images par seconde. Un exemple de ce type d'expérience est présenté à la Figure 3-2. Ces expériences sont ensuite reproduites numériquement à l'aide de la DEM en faisant varier le coefficient d'amortissement utilisé dans le modèle. Une courbe de calibration du CoR numérique en fonction du coefficient d'amortissement est obtenue, permettant ainsi d'identifier la valeur du coefficient d'amortissement correspondant à la valeur du CoR mesurée expérimentalement.

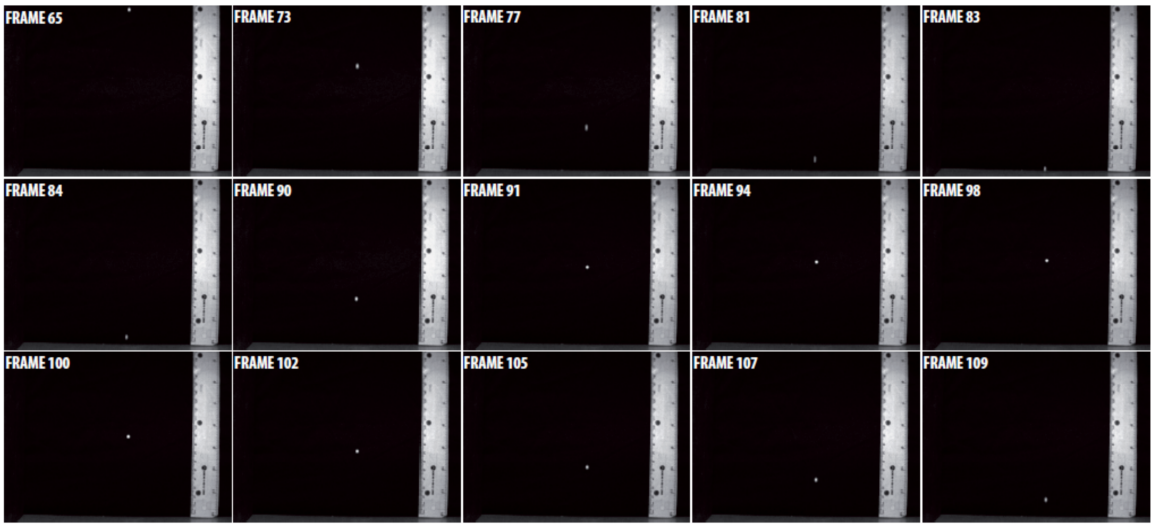

Figure 3-2 Exemple de la mesure d'une particule en chute libre réalisée à l'aide d'une caméra haute vitesse.

Les coefficients de friction sont quant à eux étalonnés à l'aide de mesures d'angle de talus d'un tas de particules. L'appareil servant à réaliser ces mesures est illustré à la Figure 3-3. Pour réaliser ces mesures, l'appareil est d'abord rempli de particules (Figure 3-3a). L'angle de talus se forme suite à la création d'ouvertures de chaque côté de l'appareil (Figure 3-3b). Un exemple d'angle de talus obtenu pour chacun des adsorbants est présenté à la Figure 3-3c et d. Encore une fois, ces expériences sont reproduites numériquement à l'aide de la DEM en faisant varier les

coefficients de friction utilisés dans le modèle. Les valeurs des coefficients de friction appropriées sont celles permettant de reproduire avec le plus d'exactitude les expériences.

a)

b)

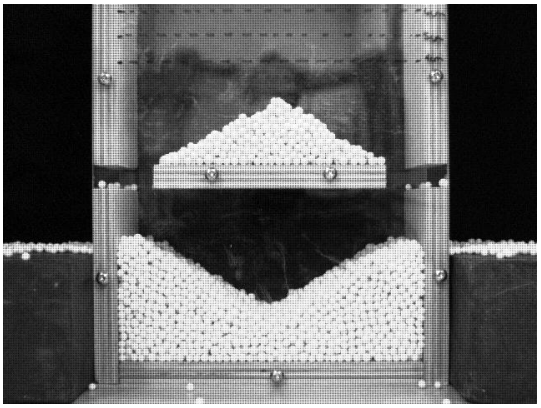

c)

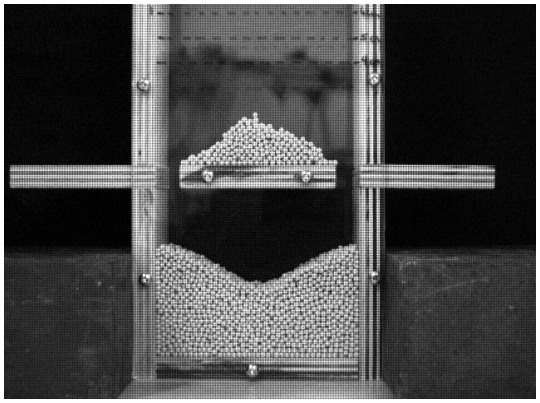

d)

Figure 3-3 Appareil servant à la mesure d'angles de talus des adsorbant [a) et b)] ainsi qu'un exemple d'angle de talus obtenu pour c) les particules d'alumine et d) les zéolites synthétiques de type X.

3.1.2 Dimensionnement des domaines de calcul

Dans un réacteur à flux radial (RFR) (Figure 3-4a), le gaz à traiter est alimenté au lit fixe par le canal annulaire en phase d'adsorption et par le tube intérieur en phase de régénération. La simulation DEM d'une unité de taille industrielle n'est pas possible étant donné le nombre de particules impliquées. Une petite section du réacteur est donc simulée. Cette dernière est représentée à la Figure 3-4b et c. Des conditions périodiques sont imposées dans le sens de la largeur du domaine pour ainsi éviter que des effets de parois affectent la dynamique particulaire. Pour compléter cette étude, deux domaines de simulation sont utilisés. Les spécifications de chaque domaine sont détaillées dans le Tableau 3-1. Le premier domaine (A) est utilisé pour vérifier le modèle DEM alors que le deuxième domaine (B) est utilisé pour étudier la dynamique particulaire à l'interface d'adsorbants. Il faut noter que pour des raisons de stabilité numérique, la partie supérieure du lit d'adsorbants est une surface libre.

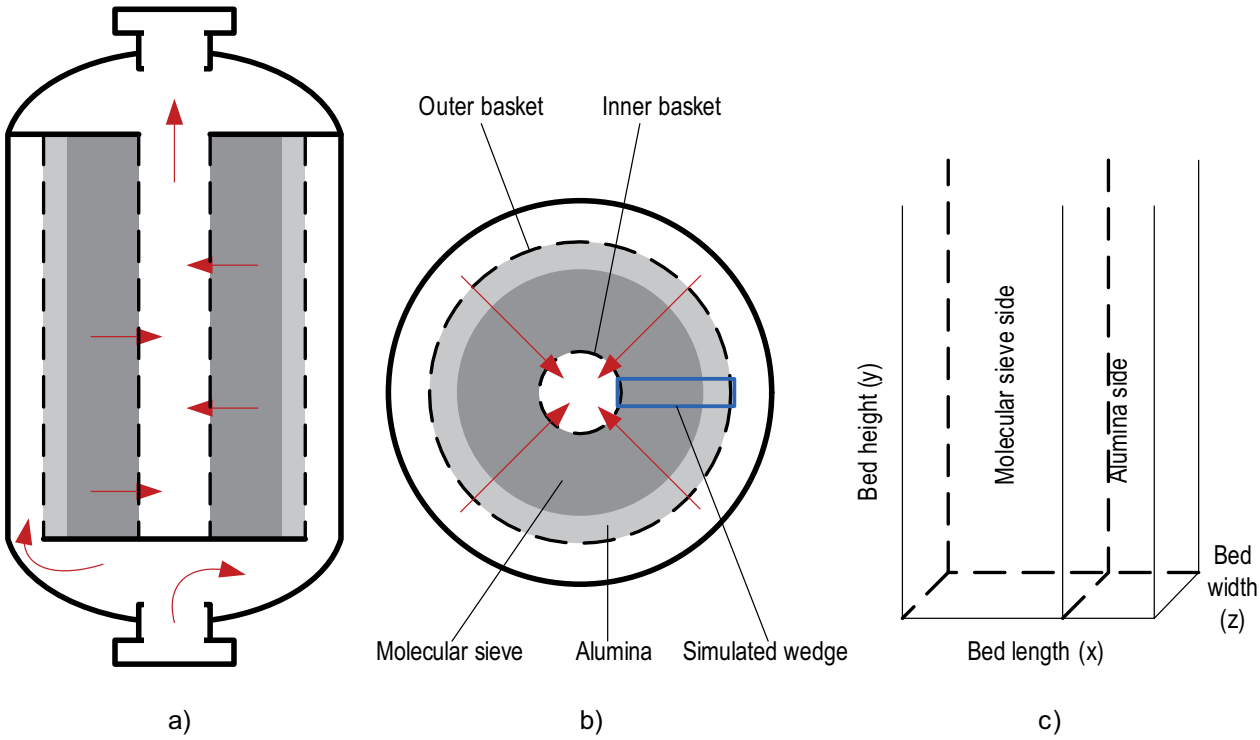

Figure 3-4 Représentation schématique du RFR: a) vue de face, b) vue de haut et c) domaine de simulation DEM.

Tableau 3-1 Spécifications des domaines de simulation

Domaine	**Dimensions (m)**		**Nombre de particules (Fraction volumique)**		**#Cœurs CPU**
			Alumine	**Zéolite synthétique de type X (« Molecular sieve »)**	
A	Longueur	0.16	222 925 (1)	0 (0)	16
	Hauteur	1.28			
	Largeur	0.025			
B	Longueur	0.32	51 467 (0.24)	547 513 (0.76)	48
	Hauteur	0.64			
	Largeur	0.025			

3.1.3 Spécification du cycle d'expansion et de contraction

La Figure 3-5a présente l'évolution de la température mesurée aux parois interne et externe d'une unité commerciale d'adsorption par oscillations thermiques (TSA). Ces données sont une gracieuseté de PRAXAIR Inc. À l'aide du coefficient de dilatation thermique linéaire du matériau constituant les parois du réacteur, il est possible d'évaluer l'expansion et la contraction attendues en cours de cycle (Figure 3-5b). Puisqu'aucun changement de température ne se produit durant la première moitié du cycle, cette portion de cycle peut être éliminée des simulations DEM. Ainsi, le véritable cycle simulé est celui présentée à la Figure 3-5c.

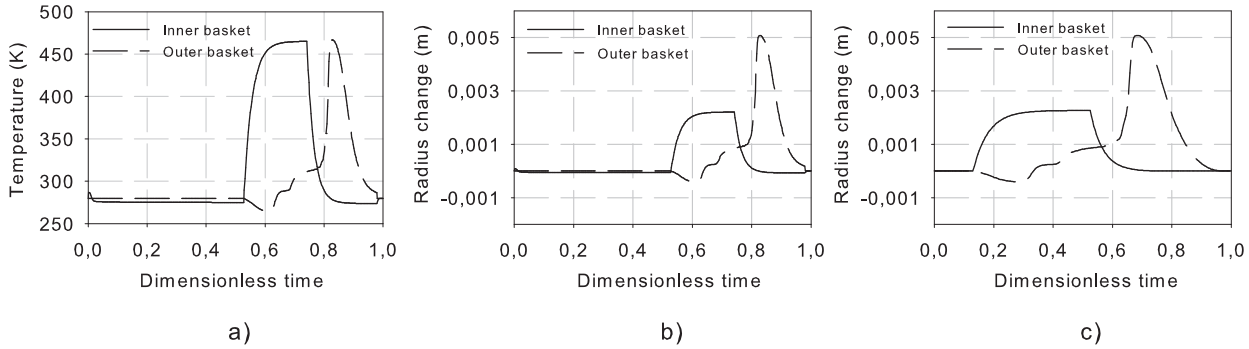

Figure 3-5 Spécifications du cycle de TSA: a) évolution de la température aux parois internes et externes du RFR, b) variations de rayon correspondantes aux changements de température et c) mouvements des murs simulés à l'aide de la DEM.

3.1.4 Planification des simulations numériques

Comme il a été mentionné à la Section 1.1.1, un cycle de TSA s'étend généralement sur plusieurs heures. Évidemment, la simulation DEM d'un cycle réel n'est pas possible. Il faut donc déterminer une fréquence de cycle appropriée. Une borne supérieure de 2Hz pour la fréquence peut être identifiée. Davantage de détails concernant cette borne supérieure sont présentés à la Section 4.2.3.2.5. Des fréquences de 0.5Hz, 1.0Hz et 2.0Hz sont testées. Les simulations numériques réalisées à l'aide de chacun des domaines sont présentées au Tableau 3-2. Ces simulations sont effectuées sur le serveur de calcul haute performance Mammouth-Série II de l'Université de Sherbrooke.

Tableau 3-2 Planification des simulations DEM

Domaine	Objectif de la simulation	Fréquence de cycle
A	Vérification du modèle	0.5Hz
A	Vérification du modèle	1.0Hz
A	Vérification du modèle	2.0Hz
B	Dynamique particulaire	1.0Hz

3.2 Optimisation du positionnement des détecteurs de la technique de suivi de particules radioactives

Cette section décrit la méthodologie employée pour développer la stratégie d'optimisation nécessaire à l'identification d'un positionnement optimal des détecteurs de la technique de suivi de particules radioactives (RPT). Cette méthodologie consiste en la sélection d'un algorithme d'optimisation adéquat ainsi qu'en la détermination des cas tests permettant de valider, évaluer la performance et, finalement, appliquer la stratégie d'optimisation.

3.2.1 Identification de l'algorithme d'optimisation approprié

La fonction-objectif permettant d'identifier un positionnement optimal des détecteurs de la RPT dépend de l'objectif de l'expérience réalisée. Cependant, il est évident que celle-ci est, d'une manière ou d'une autre, liée à la relation phénoménologique reliant le nombre de comptes reçus par un détecteur à la position du traceur radioactif. Puisque cette relation est évaluée grâce à une méthode de Monte Carlo (Larachi et al., 1994), il est impossible d'obtenir une évaluation précise des dérivées de la fonction-objectif. La composante stochastique de cette relation garantit également que la fonction-objectif est non-lisse. De plus, deux évaluations successives de la

fonction-objectif produisent deux résultats généralement différents. Il est donc nécessaire d'identifier une classe d'algorithme d'optimisation qui est capable de composer avec les particularités de la fonction-objectif.

L'éventail de méthodes d'optimisation disponibles pour résoudre des problèmes d'ingénierie est extrêmement large. Audet et al. (2008) a dressé une liste exhaustive des algorithmes les plus utilisés pour résoudre des problèmes issus de l'ingénierie chimique. Tel que mentionné, la plupart de ces algorithmes doivent être adaptés lorsque la fonction-objectif est non-lisse, d'autres ont besoin de relaxation pour évaluer la fonction-objectif aux frontières du domaine d'optimisation, d'autres ne sont pas en mesure de traiter des problèmes possédant un domaine de solution non-convexe, d'autres nécessitent un réglage intensif de leurs paramètres pour pouvoir être efficace et d'autres ne présentent pas des propriétés de convergence théorique rigoureuses. Une classe de méthode peut cependant être utilisée dans le cas de problèmes non-dérivables, non-linéaires, non-convexes ou déconnectés. Il s'agit de la méthode de recherche directe (Lewis, Torczon, & Trosset, 2000) dont l'utilisation est ici fortement favorisée. Dans le cadre de cette thèse, NOMAD, une implémentation C++ de la méthode de recherche directe à maillage adaptatif (MADS), est sélectionné pour optimiser le positionnement des détecteurs (Abramson et al., 2012; Le Digabel, 2011).

3.2.2 Validation, évaluation et application de la stratégie d'optimisation

La stratégie d'optimisation développée doit tout d'abord être validée à l'aide d'un système dont le positionnement optimal des détecteurs est connu. Pour ce faire, un système bidimensionnel constitué d'un cercle de 0.10m de rayon est utilisé. Il est évident que dans ce cas précis, l'agencement optimal pour les détecteurs consiste à les disposer aussi près que possible du système et à les répartir uniformément autour de celui-ci. La stratégie d'optimisation est testée avec 3, 4 et 6 détecteurs à scintillations.

Une fois validée, la performance de la stratégie d'optimisation est évaluée à l'aide du système le plus fréquemment étudié avec la RPT soit une colonne cylindrique verticale pouvant correspondre à un lit fluidisé, une colonne à bulles ou autre. Dans ce cas-ci, la colonne présente une hauteur de 0.61m et un rayon de 0.075m. Étant donné la taille limitée du système, la stratégie d'optimisation est testée avec seulement six détecteurs à scintillations.

Finalement, la stratégie d'optimisation est appliquée au système pour lequel cette dernière a été développée : un cylindre rotatif horizontal partiellement rempli possédant un rayon de 0.127m et une longueur de 0.381m. La stratégie d'optimisation est testée avec le même nombre de détecteurs à scintillation qui est utilisé pour réaliser l'expérimentation, soit dix détecteurs.

3.3 Dynamique particulaire dans des lits rotatifs

Pour être en mesure de caractériser la dynamique de particules non-sphériques à l'intérieur d'un cylindre rotatif il faut d'abord concevoir et fabriquer les particules non-sphériques et ensuite, planifier les expériences à réaliser.

3.3.1 Fabrication des particules non-sphériques

L'élément le plus facile à introduire dans la fabrication de comprimés pharmaceutiques pouvant produire un radio-isotope adéquat pour la RPT est le sodium (Na). Sous le flux de neutrons du réacteur nucléaire SLOWPOKE de l'École Polytechnique de Montréal, le sodium (Na) se transforme en ^{24}Na et émet deux rayons gamma de haute énergie (1.368 et 2.754 MeV). Il faut noter que la demi-vie du ^{24}Na est relativement courte à seulement 14.95 heures. La quantité de sodium à introduire à l'intérieur de la matrice des comprimés est dictée par un seul critère : un comprimé introduit dans le réacteur nucléaire doit atteindre un niveau d'activité de 60 μCi (2.22 MBq) en moins de 20 minutes. Cette limite de temps est extrêmement importante pour éviter

tout changement au niveau des propriétés physiques du comprimé lors de son activation. Les poudres organiques, principaux constituants des comprimés pharmaceutiques, sont affectées par une exposition prolongée au flux de neutrons ainsi que par la température régnant aux alentours du cœur du réacteur.

Trois formulations différentes ont été testées pour fabriquer les comprimés. La première formulation utilise un mélange de cellulose microcristalline (MCC), de lactose monohydrate et de sel, qui est d'abord granulé à l'aide d'un procédé d'extrusion-sphéronisation, et ensuite comprimé, en y ajoutant du mannitol, à l'aide d'une presse à comprimés. Malheureusement, l'utilisation de ces granules n'a pas permis la production de comprimés ayant des propriétés physiques adéquates (i.e. une dureté élevée et une faible friabilité) pour répondre aux objectifs de l'étude. La seconde formulation, présentée au Tableau 3-3, utilise un mélange de MCC, mannitol, sel micronisé et de MgSt qui est directement comprimé à l'aide d'une presse. Trois types de comprimés, illustrés à la Figure 3-6, présentant une dureté et friabilité adéquates, ont été fabriqués à l'aide de ce mélange en utilisant une presse à comprimé 10-stations PICCOLA® (Riva, Aldershot, Hampshire, Angleterre). Les résultats d'expériences utilisant ces comprimés ont d'ailleurs fait l'objet d'une présentation lors du 8th World Congress of Chemical Engineering (Dubé, Bouffard, Legros, Bertrand, & Chaouki, 2009). Malheureusement, cette formulation s'est également avérée inadéquate pour plusieurs raisons. Tout d'abord, le chlore (Cl) contenu dans le sel produit du ^{38}Cl lors du passage du comprimé dans le réacteur nucléaire. Malgré que cet isotope ait une courte demi-vie (i.e. 37 minutes), sa présence nuit de manière substantielle au déroulement des expériences RPT. Ensuite, la présence de sel dans la matrice des comprimés les rendent extrêmement sensibles à l'humidité ambiante, diminuant ainsi significativement leur durée de vie.

Tableau 3-3 Seconde formulation

Composé **(Provenance)**	**Concentration**
Cellulose microcristalline **(Avicel® PH-200, FMC, Philadelphie, Pennsylvanie, États-Unis)**	29.5%
Mannitol **(Pearlitol® 200 SD, Roquette, Waterloo, Ontario, Canada)**	29.5%
Sel micronisé	40%
Stéarate de magnésium monohydrate **(Peter-Greven Fett-Chemie GmbH, Bad Münstereifel, Allemagne)**	1%

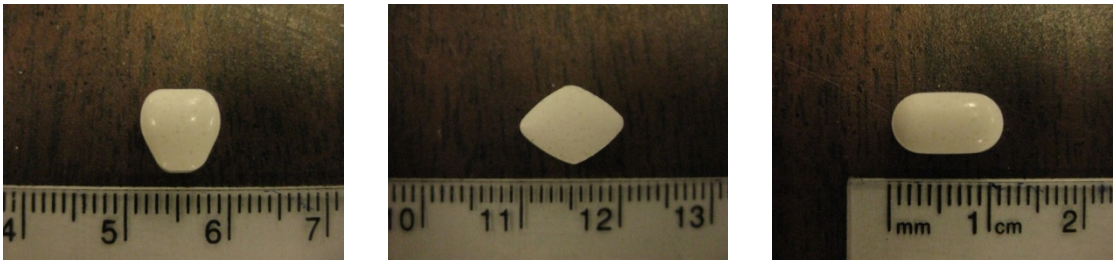

a) b) c)

Figure 3-6 Formes des comprimés produit avec la seconde formulation: a) pomme, b) diamant et c) capsule.

Finalement la troisième formulation, détaillée au Tableau 3-4, est grandement inspirée de la seconde formulation et est celle qui a été utilisée pour compléter la recherche. Dans celle-ci, le

sel est remplacé par du bicarbonate de soude et le mannitol par un de grade plus fin, améliorant ainsi significativement les propriétés de compaction du mélange. Des comprimés de cinq formes différentes ont été fabriqués à l'aide de cette formulation et sont présentés à la Figure 3-7. Ces derniers ont été produits à l'aide d'une presse à comprimés 10-stations KORSCH XL100 (KORSCH America Inc., South Easton, Massachusetts, États-Unis) opérée à une vitesse de 60RPM.

Tableau 3-4 Troisième formulation

Composé (Provenance)	**Concentration**
Cellulose microcristalline (Avicel® PH-200, FMC, Philadelphie, Pennsylvanie, États-Unis)	29.75%
Mannitol (Pearlitol® 100 SD, Roquette, Waterloo, Ontario, Canada)	29.75%
Bicarbonate de soude (Arm&Hammer®, Church and Dwight Co., Ewing, New Jersey, États-Unis)	40%
Stéarate de magnésium monohydrate (Peter-Greven Fett-Chemie GmbH, Bad Münstereifel, Allemagne)	0.5%

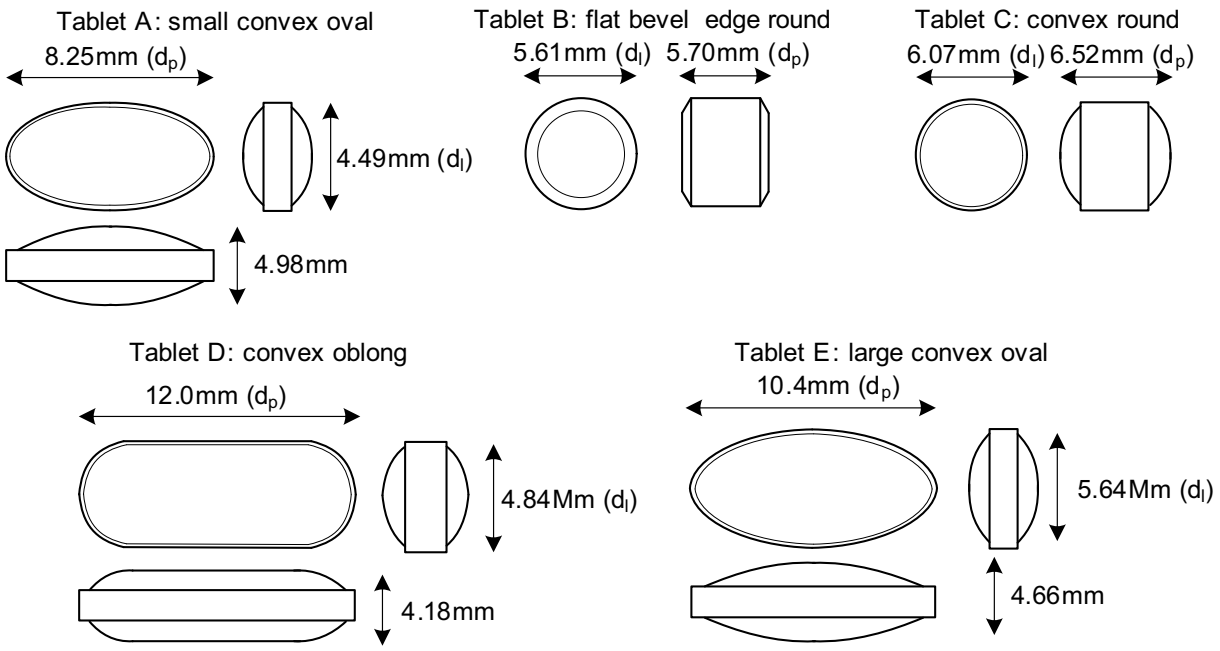

Figure 3-7 Formes et dimensions des comprimés produits avec la troisième formulation.

Pour améliorer les propriétés mécaniques des comprimés et prolonger leur durée de vie, un enrobage 2% massique de mélange polymérique Opadry® II-rouge (Colorcon®, West Point, Pennsylvanie, États-Unis) a été appliqué à l'aide d'une turbine perforée Vector LCDS (Freund-Vector Co., Marion, Iowa, États-Unis). Les propriétés des comprimés sont présentées au Tableau 3-5.

Tableau 3-5 Propriétés des comprimés

Comprimé	A	B	C	D	E
Masse (mg)	206.8 ± 2.1	219.8 ± 3.0	276.1 ± 3.7	280.1 ± 3.3	284.4 ± 3.1
Volume (mm^3)	147.2 ± 0.4	139.0 ± 0.8	169.0 ± 1.6	181.9 ± 1.3	220.9 ± 1.6
Surface (mm^2)	162.6 ± 0.5	143.2 ± 0.6	157.6 ± 1.1	176.1 ± 0.7	195.5 ± 1.3
Densité particulaire (mg/mm^3)	1.40 ± 0.01	1.58 ± 0.02	1.63 ± 0.02	1.54 ± 0.02	1.29 ± 0.01
Densité apparente (kg/m3)	1072 ± 3	1035 ± 3	1029 ± 2	968 ± 2	1031 ± 6
Sphéricité	0.83	0.91	0.94	0.88	0.90
Rapport d'aspect	1.84	1.02	1.07	2.48	1.84

3.3.2 Planification d'expériences

L'étude de la dynamique des particules non-sphériques s'est effectuée dans un cylindre rotatif fait entièrement en acrylique, possédant une longueur interne de 0.3556m et un rayon interne de 0.2413m. Un volume de remplissage de 35 % a été utilisé pour l'ensemble des expériences. La majorité d'entre elles ont été réalisées à une vitesse de rotation du cylindre de 10RPM. Cette vitesse a été sélectionnée pour maximiser la quantité de données récoltées lors d'expériences RPT, tout en se maintenant dans le régime d'écoulement de type « roulement », le régime de prédilection pour l'opération des fours rotatifs. Chaque expérience a duré 180 minutes et a utilisé une période d'échantillonnage de 10ms. Dix détecteurs à scintillations ont été utilisés pour suivre la trajectoire du traceur radioactif et ceux-ci ont été placés suivant les recommandations issues de l'atteinte du second objectif spécifique de cette thèse.

La planification d'expériences complète est présentée au Tableau 3-6. Les cinq types de comprimés ont été testés individuellement. Par la suite, des mélanges de comprimés de formes similaires mais de tailles différentes ainsi que de formes différentes mais de masses similaires ont

été testés. Ces deux types de mélange ont été sélectionnés pour représenter le cas où des changements de taille et de forme se produisent en cours d'opération. La concentration de chaque type de comprimé dans chacun des mélanges a été choisie pour représenter une situation où seulement une faible fraction du contenu subit un changement de forme et/ou de taille. Ainsi, 85vol% du mélange est constitué du plus gros comprimé et 15vol% du plus petit comprimé. Les expériences E, BC.B et CD.C ont été répétées pour évaluer la variation des résultats due à l'instrument de mesure.

Tableau 3-6 Planification des expériences RPT

Type	Identification de l'expérience	Spécification du mélange	Vitesse de rotation (RPM)	Particule traceur
Mono-disperse	A	100vol% A	10	A
	B	100vol% B	10	B
	C	100vol% C	10	C
	D	100vol% D	10	D
	E	100vol% E	10	E
	GB6	100vol% 6mm	10	6mm
Bi-disperse	AE.A	15vol% A	10	A
	AE.E	85vol% E		E
	AE.A*	15vol% A	5	A
	AE.E*	85vol% E		E
	BC.B	15vol% B	10	B
	BC.C	85vol% C		C
	CD.C	15vol% C	10	C
	CD.D	85vol% D		D
	CE.C	15vol% C	10	C
	CE.E	85vol% E		E
	GB56.5	15vol% 5mm	10	5mm
	GB56.6	85vol% 6mm		6mm

CHAPITRE 4 SIMULATION PAR ÉLÉMENTS DISCRETS DE LA DYNAMIQUE D'ADSORBANTS DANS UN RÉACTEUR À FLUX RADIAL UTILISÉ POUR LA PRÉ-PURIFICATION DE GAZ

4.1 Présentation du premier article

Accepté pour publication dans *Adsorption* le 30 avril 2013.

Auteurs : Olivier Dubé, Mark Ackley, Cem Celik, Jamal Chaouki, François Bertrand.

Ce chapitre présente l'évaluation, à l'aide de la méthode des éléments discrets, de l'effet d'une contraction et d'une expansion thermique cyclique des murs d'un réacteur à flux radial utilisé pour la pré-purification de gaz sur un lit particulaire fixe

4.2 Discrete Element Simulation of the Dynamics of Adsorbents in a Radial Flow Reactor Used for Gas Prepurification

4.2.1 Abstract

Radial flow reactors (RFR) are used in thermal swing adsorption (TSA) processes for gas prepurification. The aim of this work is to show the validity of the discrete element method (DEM) to simulate the effect of thermal expansion and contraction cycles occurring in such processes on the packed bed of RFR reactors. Both mono-layered and bi-layered packed beds of adsorbents are investigated. A DEM-based model of a full-scale size unit was developed, the parameters of which were calibrated by means of particle-scale experimental measurements and simple auxiliary DEM simulations. The DEM-based model used is isothermal and the thermal

expansion and contraction phenomena are modelled through the displacement of the inner and outer walls of the computational domain. First, the accuracy of this model is assessed using analytical values of the static wall pressure (i.e. with no wall motion) as well as experimental measurements of the dynamic wall pressure (i.e. with wall motion) of a bi-layered bed. Next, simulation results for a few process cycles in the case of a bi-layered packed bed indicates that little mixing occurs at the interface between the two types of adsorbents. To our knowledge, this is the first time that simulation is used to investigate the behavior of the packed bed of a RFR in a TSA process. The results obtained with the proposed model show that the DEM is a valuable tool for the investigation of such slow dynamical processes, provided a careful calibration is done.

4.2.2 Introduction

Nitrogen and oxygen are the most common and extensively used industrial gases with applications in various process industries like petrochemical, metal, food, etc. They are typically produced using a cryogenic air separation unit (ASU) in which air is cooled, liquefied and separated using a distillation process. A pre-purification unit (PPU) is needed prior to cryogenic ASU to remove air impurities and contaminants such as water, carbon dioxide, nitrous oxide, light hydrocarbons, etc. Thermal swing adsorption (TSA) is commonly used for air pre-purification and is the technology of choice prior to cryogenic distillation (Kumar & Deng, 2006). In an optimized TSA PPU, a typical axial packed bed reactor is filled with layers of at least two different adsorbents. The first layer is usually made of activated alumina, to remove water from the gas feed, and the second one is commonly made of a synthetic zeolite X material (NaX type like 13X molecular sieve), to remove carbon dioxide and other minor contaminants (Ackley et al., 2012; Hidano et al., 2011; Kalbassi & Golden, 1999; Kumar et al., 2002). TSA processes are normally operated on a cyclic basis (Ruthven, 1984; Seader & Henley, 1998). The cycle involves the basic steps of 1) pressurizing the bed with feed gas, 2) passing the pressurized feed stream through the bed of adsorbents (adsorption of contaminants), 3) depressurizing the bed, 4) passing a heated regenerating gas counter-currently to the normal feed direction (desorption of contaminants) and 5) passing a cooling gas through the bed to bring it back to its initial thermal state. The regeneration part of the process usually adopts the thermal pulse concept

wherein a heat front or wave is created and it moves forward and causes a fraction of the bed to heat up entirely to the hot regeneration temperature. The cool purge is then initiated and the effect is to begin cooling the hot portion of the bed while simultaneously carrying forward the previously stored heat into the remaining forward part of the bed to complete the desorption of contaminants. Regeneration temperatures in a TSA PPU are sufficiently high, ranging typically from 150°C to 300°C, and depend on the adsorbents used and the components to be desorbed (Hidano et al., 2011; Kalbassi & Golden, 1999; Ko et al., 2002; Kumar & Dissinger, 1986; Ruthven, 1984).

The annular packed bed (APB), also called radial flow reactor (RFR) or radial flow fixed bed reactor (RFBR), is generally used for heterogeneous catalytic processes and gas purification systems (Heggs, Ellis, & Ismail, 1994; Kareeri et al., 2006). The main advantages of RFR over traditional axial flow packed bed reactors are the lower pressure drop needed for operation, the increased flow area and the higher flow rate that can be achieved. Many studies of RFR have mainly focused on gas stream uniform distribution over the active material bed height since process efficiency as well as profitability of RFR largely depend on this aspect (Celik & Ackley, 2012; Heggs et al., 1995a, 1995b; Kareeri et al., 2006; Lobanov & Skipin, 1986; Ponzi & Kaye, 1979). Kareeri et al. (2006) and Lobanov and Skipin (1986) showed that low bed porosity improves flow distribution. They also insisted on proper active material loading so that tight packing of active material is maintained throughout operation.

Due to the aforementioned technical advantages of RFR, there is great benefit to use this configuration for full-scale adsorption processes. However, when RFR is used in conjunction with a thermal swing regeneration step, the reactor mechanical components (e.g. reactor vessel) contract and expand because of the substantial temperature differences between the different operating phases (Ackley et al., 2012; Libal et al., 1998). The axial and/or radial relative motions between the vessel walls and the bed of adsorbents can be the source of induced thermal loads. It can also damage the adsorbent bed by breaking the particles, creating voids, inducing particle settling and promoting mixing of layered adsorbents. All of this will inevitably affect flow uniformity as well as process efficiency.

While limited, previous RFR studies have solely focused on the gas phase. Using experiments, phenomenological numerical models or computational fluid dynamics (CFD), flow direction, configuration and distribution as well as reaction conversion and selectivity in isothermal, incompressible and steady-state conditions have been investigated. No study has explored the effect of a TSA cyclic process on the particles constituting the packed bed of a RFR. Experimental investigation of particle dynamics is extremely tedious, particularly in the case of a TSA process in a RFR. Most experimental measurement techniques, whether they are invasive (e.g. sampling technique, fiber optics) or non-invasive (e.g. tomography or velocimetry techniques), are either not readily applicable or extremely costly to implement. Also, each measurement technique provides only a limited amount of information on particle behavior.

The discrete element method (DEM) is a powerful numerical simulation technique internationally recognized and used to gain valuable insight into static or dynamic behaviour of granular materials. First introduced by Cundall and Strack (1979), the DEM consists of simulating the motion of each individual particle using Newton's second law of motion. Even if the particles are considered rigid, they are allowed to overlap so as to mimic particle deformation occurring during contact. A contact model (force-displacement law) is used to relate the contact force between the particles to their overlap. DEM has been used to study a wide variety of granular processes. To name just a few, it has been successfully used to investigate discharge of silos (Balevicius et al., 2011; Gonzalez-Montellano et al., 2011; Ketterhagen et al., 2009), pressure and shear exerted by stored materials (Goda & Ebert, 2005; Masson & Martinez, 2000), granular mixing and segregation inside pharmaceutical blenders (Lemieux et al., 2007; Sudah et al., 2005) or cylindrical tumblers (Rapaport, 2007). DEM capability of predicting realistic granular phenomena as well as flow parameters and properties are only achievable through meticulous identification of material properties, careful selection of an appropriate contact model and, most importantly, experimental verification and/or validation of the DEM-based model used (Balevicius et al., 2011; Gonzalez-Montellano et al., 2011). Material physical properties can be evaluated by experimental measurement of a property at the particle scale or by calibration using simple auxiliary DEM simulations discriminating the effect of a specific property.

In this study, the effect of cyclic thermal expansion and contraction of the vessel of a RFR, used in a TSA process for air pre-purification, on mono- and bi-layered packed beds of adsorbents is investigated using the DEM. A simplified DEM-based model of a full-scale unit is created. The DEM model is carefully calibrated using both experimental measurements and auxiliary DEM simulations. Then, the model is assessed using a mono-layered packed bed computational domain. To complete its assessment, the model is compared against analytical and experimental data of a full-scale size unit for verification and validation. A specific wall motion cycle, representing one temperature cycle of a TSA process, was considered for the simulations. Wall pressures are investigated over the course of many cycles. Finally, the DEM-based model is applied in a bi-layered packed bed computational domain in order to investigate adsorbent migration. The results obtained with the proposed model show the usefulness of the DEM for investigating slow dynamical processes.

4.2.3 Methodology

4.2.3.1 Discrete element method

The DEM is based on a force and momentum balance on each particle. For this study, it is written as:

$$m\frac{d^2\vec{x}}{dt^2} = m\vec{g} + \sum\left(\overrightarrow{F_n} + \overrightarrow{F_t}\right) \tag{4.1}$$

$$I\frac{d\vec{\omega}}{dt} = \sum\left(\vec{T} + \overrightarrow{M}\right) \tag{4.2}$$

where $\vec{x}$, m, I and $\vec{\omega}$ denote the position vector, mass, moment of inertia and angular velocity vector of a particle. These equations are solved using a half-step leapfrog Verlet (HSLV) integration scheme (Fraige & Langston, 2004). The forces involved in this model are the gravitational force $\left(m\vec{g}\right)$ and the inter-particle contact forces decomposed into normal $\left(\overrightarrow{F_n}\right)$ and

tangential components $\left(\overrightarrow{F_t}\right)$. Drag and buoyant forces are neglected due to the low density of the fluid phase (air) and cohesion forces are also neglected because of the particle sizes, which are in the order of a few millimeters. $\vec{T}$ and $\overrightarrow{M}$ are the torque and rolling friction torque. They are given by:

$$\vec{T} = \vec{r} \times \overrightarrow{F_t} \tag{4.3}$$

$$\overrightarrow{M} = -\mu_r \left\| \overrightarrow{F_n} \right\| \frac{\vec{\omega}}{\left\| \vec{\omega} \right\|} \tag{4.4}$$

where $\vec{r}$ is the vector from the center of a particle to the contact point and μ_r is the coefficient of rolling resistance and has length units. To account for the elastic *(el)* and dissipation *(dis)* forces, the normal and tangential components of the contact forces are modeled using a generalized spring-dashpot model:

$$\begin{aligned} \overrightarrow{F_n} &= \overrightarrow{F_n^{el}} + \overrightarrow{F_n^{dis}} \\ &= k_n \delta_n^{\frac{3}{2}} \vec{n} + \gamma_n \delta_n^{\frac{1}{2}} \overrightarrow{v_n} \end{aligned} \tag{4.5}$$

$$\begin{aligned} \overrightarrow{F_t} &= \overrightarrow{F_t^{el}} + \overrightarrow{F_t^{dis}} \\ &= k_t \vec{\delta_t} + \gamma_t \overrightarrow{v_t} \end{aligned} \tag{4.6}$$

where $\vec{n} = \frac{\vec{r}}{\left\| \vec{r} \right\|}$, δ_n and $\vec{\delta_t}$ are respectively the normal deformation and vector of tangential deformation, and $\overrightarrow{v_n}$ and $\overrightarrow{v_t}$ are the normal and tangential components of the relative velocities between the particles in contact. $\overrightarrow{F_n^{el}}$ is evaluated with the Hertz theory while $\overrightarrow{F_n^{dis}}$ is evaluated with the Tsuji model (Tsuji, Tanaka, & Ishida, 1992). The tangential deformation vector is given by:

$$\vec{\delta_t} = \min\left(\int_0^{t_c} \overrightarrow{v_t}(t')dt', \delta_{t,\max} \frac{\overrightarrow{v_t}}{\left\| \overrightarrow{v_t} \right\|} \right) \tag{4.7}$$

where t_c is the contact lifetime. The maximum tangential deformation is given by:

$$\delta_{t,\max} = \mu \frac{(2-\nu)}{2(1-\nu)} \delta_n \tag{4.8}$$

where ν is the Poisson ratio and μ is the dynamic friction coefficient. Constants k_n, k_t, γ_n and γ_t are given by:

$$k_n = -\frac{4}{3}\sqrt{R^*}E^* \tag{4.9}$$

$$\gamma_n = -c_n \left(6m^* E^* \sqrt{R^*}\right)^{\frac{1}{2}} \tag{4.10}$$

$$k_t = -\mu_s \left[1 - \left(1 - \frac{\left\|\vec{\delta_t}\right\|}{\delta_{t,\max}}\right)^{\frac{3}{2}}\right] \frac{\left\|\overrightarrow{F_n^{el}}\right\|}{\left\|\vec{\delta_t}\right\|} \tag{4.11}$$

$$\gamma_t = -c_t \left(6\mu_s m^* \left\|\overrightarrow{F_n^{el}}\right\| \frac{\sqrt{1 - \left\|\vec{\delta_t}\right\| / \delta_{t,\max}}}{\delta_{t,\max}}\right)^{\frac{1}{2}} \tag{4.12}$$

where, for a contact between particles i and j, R^* is the reduced radius $\left(\frac{1}{R^*} = \frac{1}{R_i} + \frac{1}{R_j}\right)$, E^* is the effective Young's modulus $\left(\frac{1}{E^*} = \frac{1}{E_i} + \frac{1}{E_j}\right)$, m^* is the geometric mean mass $\left(\frac{1}{m^*} = \frac{1}{m_i} + \frac{1}{m_j}\right)$, μ_s is the static friction coefficient, and c_n and c_t are the normal and tangential damping constants, respectively. The Coulomb criterion $\left\|\vec{F_t}\right\| \le \mu \left\|\vec{F_n}\right\|$ arises naturally as $\left\|\vec{\delta_t}\right\| \le \delta_{t,\max}$.

4.2.3.2 Simulation specifications

4.2.3.2.1 Particle properties

Two types of adsorbents are used to carry out this study: activated alumina and molecular sieve. They each represent a specific layer of adsorbent typically used in a TSA PPU. The ability of a DEM model to simulate a physical phenomenon relies mainly on the particle properties used in the contact force model. They need to be precisely measured or, at least, properly calibrated. The calibration of a parameter must be done in such a way that the effect of this particular parameter is discriminated from the effect of the other parameters. In this study, the particle parameters are set using a mix of direct measurement and calibration methods. The particles density, Young's modulus and Poisson ratio presented in Table 4-1 were experimentally measured and incorporated directly into the DEM-based model.

Spherical particles were used to model the adsorbents since their sphericity is greater than 0.90. The particle porosity is 0.32-0.35 and 0.42-0.46 for the sieve and alumina particles, respectively. The Young's modulus is one of the most important parameters of a DEM model. If proper pressure measurements are to be obtained using the DEM, its value must be measured with great accuracy. The Young's modulus values were determined using a contact ultrasonic measurement method (Akseli & Cetinkaya, 2008; Cetinkaya, 2009; C. Li & Cetinkaya, 2006). The Young's modulus determined for the activated alumina of the present study is consistent with that obtained for the similar alumina beads (catalyst support) using the single particle contact deformation method (Couroyer et al., 1999).

The specific particle size distribution (PSD) of each adsorbent is also integrated into the DEM-based model. Figure 4-1 displays the respective PSD.

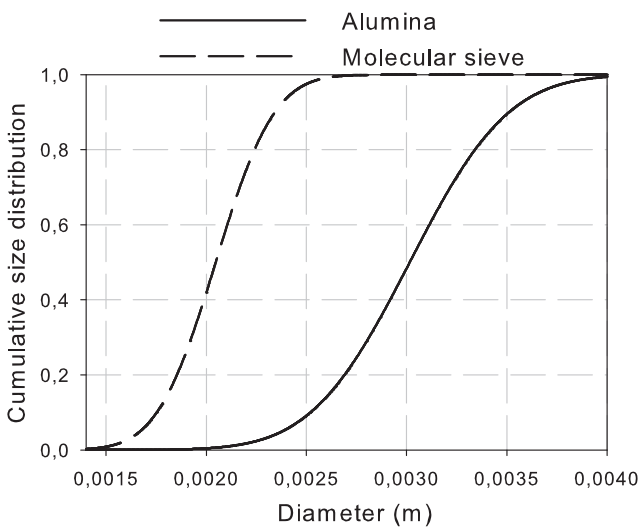

Figure 4-1 Particle size distributions of the two adsorbents.

The damping coefficients for the DEM-based model were calibrated using experimental measurements similar to the ones performed by Sondergaard et al. (1990). In these experiments, the coefficients of restitution (CoR) of each adsorbent type were measured following their impact on a horizontal steel plate after a free fall under gravity. Particles were dropped from a height of 208 mm as many times as needed to have 50 valid trials for each particle type. Since neither type of adsorbents is perfectly spherical, only the trials that resulted in a close to 90-degree rebound with respect to the surface were considered. Particle free falls were recorded by means of a high-speed camera at a frame rate of 120 fps. The normal CoR values of the alumina and molecular sieve adsorbents were measured at 0.68 ± 0.02 and 0.72 ± 0.01, respectively. The same free fall experiment was simulated using the DEM-based model with a varying normal damping factor (c_n) in order to obtain a calibration curve. Normal damping factors of 0.135 and 0.110 for the alumina and molecular sieve adsorbents best fitted the experimental CoR values. The same value of the normal damping factor was used for the particle-particle and particle-wall interactions. Also, like in previous work presented by Zhou et al. (1999) and Landry et al. (2004), it was assumed that the value of the tangential damping factor was the same as the normal one.

The friction coefficients for the DEM-based model were calibrated using experimental measurements of the angle of repose of a heap of particles. The same experiments as the ones

described in Zhou et al. (2002) were carried out. The angles of repose were measured at 27.7°±1.7° for the alumina particles and at 30.8°±2.5° for the molecular sieve particles. After these trials, a complete numerical design of experiments (DOE) was performed to identify two friction factors (i.e. the particle-particle friction factor $\left(\mu_{pp}\right)$ and the particle-particle rolling friction factor$\left(\mu_{r,pp}\right)$). It was found that, for both types of particles, $\mu_{pp} = 0.1335$ and $\mu_{r,pp} = 0.05$ provided the best fit with the experimental data. Simulated angles of repose of 27.0° and 28.4° were obtained for the alumina and molecular sieve particles, respectively. Following Zhou et al. (1999; 2001; 2002), the values of the corresponding particle-wall friction $\left(\mu_{pw}\right)$ and rolling friction $\left(\mu_{r,pw}\right)$ coefficients were set to $\mu_{pw} = 1.5\mu_{pp}$ and $\mu_{r,pw} = 2\mu_{r,pp}$.

Table 4-1 presents a summary of the particle properties used in the DEM simulations.

Table 4-1 Particle properties for the DEM-based model

	Properties	Value	
		Alumina	Molecular sieve
Particle-particle interaction	Density $\left(\rho, kg/m^3\right)$	1130	1060
	Young's modulus $\left(E, GPa\right)$	9.02	3.57
	Poisson ratio $\left(\nu\right)$	0.2	0.3
	Normal damping coefficient $\left(c_{n,pp}\right)$	0.135	0.110
	Tangential damping coefficient $\left(c_{t,pp}\right)$	0.135	0.110
	Static friction coefficient $\left(\mu_{s,pp}\right)$	0.1335	0.1335
	Dynamic friction coefficient $\left(\mu_{pp}\right)$	0.1335	0.1335
	Rolling friction coefficient $\left(\mu_{r,pp}, m\right)$	0.05	0.05
Particle-wall interaction	Normal damping coefficient $\left(c_{n,pw}\right)$	0.135	0.110
	Tangential damping coefficient $\left(c_{n,pw}\right)$	0.135	0.110
	Static friction coefficient $\left(\mu_{s,pw}\right)$	0.2	0.2
	Dynamic friction coefficient $\left(\mu_{pw}\right)$	0.2	0.2
	Rolling friction coefficient $\left(\mu_{r,pw}, m\right)$	0.1	0.1

4.2.3.2.2 Simulation time-step

The value of the simulation time step should be a trade-off between numerical errors and stability, computational time and contact mechanics. Regarding the contact mechanics criterion, it was previously reported that, in the case of a model using non-linear springs (e.g. Hertzian dynamics), the critical time step $\left(\Delta t_c\right)$ should be a fraction of the Rayleigh wave propagation time (Y. Li et al., 2005). The Rayleigh time $\left(t_R\right)$ is defined as (Johnson, 1985):

$$t_R = \frac{\pi \overline{R}}{\beta}\sqrt{\frac{\rho}{G}} \tag{4.13}$$

where $\overline{R}$ is the mean particle radius and G the particle shear modulus given by:

$$G = \frac{E}{2(1+\nu)} \tag{4.14}$$

Finally, β is approximated by (Y. Li et al., 2005):

$$\beta = 0.8766 + 0.163\nu \tag{4.15}$$

Li et al. (2005) and Gonzalez-Montellano et al. (2011) both used 20% of the Rayleigh time as the simulation time step. Unfortunately, even the use of a fraction of the critical time step may sometimes yield numerically unstable results. In order to minimize the computational time, one must consider how the DEM software is programmed. In this study, a custom-made DEM program developed at Ecole Polytechnique de Montreal was used (Bertrand et al., 2005). This program is based on parallel programming and computing as well as other efficient data structures to reduce computational time significantly, especially when a large number of particles are simulated (Leclaire, 2004). The fact that these data structures (e.g. list of neighboring particles) are shared by the processors (or cores) involved in a simulation and the use of an inappropriate time step may render a DEM simulation unstable. In particular, it was observed that updating these data structures at every N iterations, which entails the exchange of information between cores, may speed up the simulation significantly while preserving the accuracy of the solution. For this study, preliminary investigations revealed that the use of a 3.5×10^{-8} second time step with $N = 50$ required less computational time than the use of a 2.5×10^{-7} second time step, corresponding to $0.2t_R$, with an update of the data structures at every iteration $(N = 1)$. It should be noted that the DEM simulations performed for this study are extremely CPU intensive. It is also worth mentioning that it is common practice to use an abnormally low value of the Young's modulus in order to increase the time step (see equation (4.13)) and reduce significantly the computational time (Gonzalez-Montellano, Ramirez, et al., 2012). This strategy is useful especially when only flow patterns are of interest. However, it cannot be applied here since studies of pressure measurements as well as particle dynamics are investigated.

4.2.3.2.3 Simulation domain

A schematic of the RFR is shown at Figure 4-2. The air to be treated enters from the bottom of the unit and is fed to the radial packing through the annular channel during the adsorption phase and through the inner pipe during regeneration. In this configuration, the axial flow directions in the annular channel and in the inner pipe are the same. This configuration is identical to the "RZ arrangement" from Heggs et al. (1994) and the so-called "Cp z-flow" from Kareeri et al. (2006).

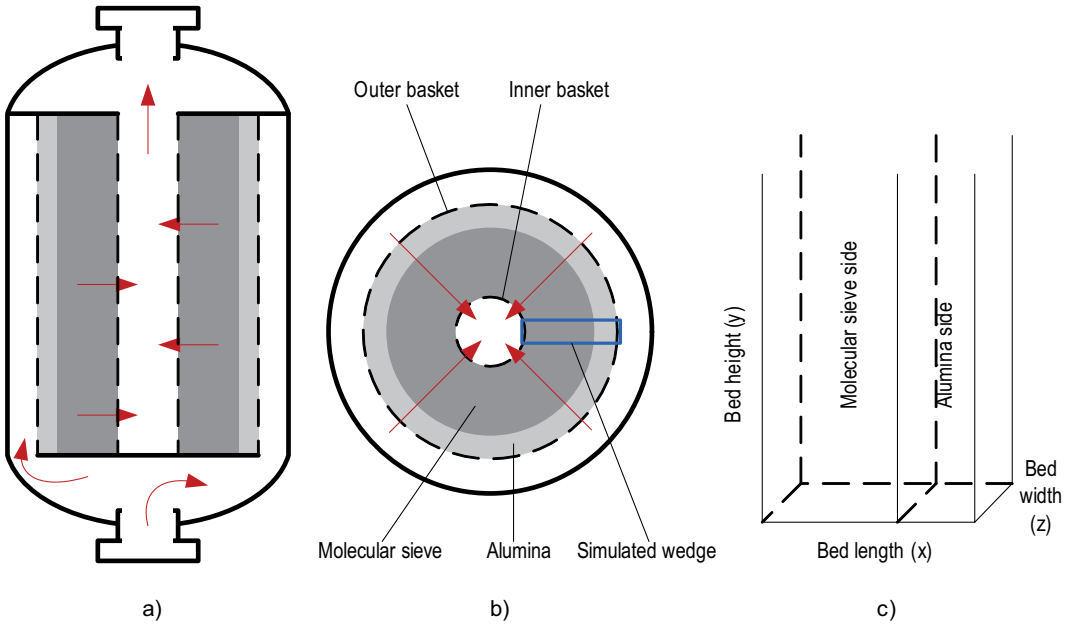

Figure 4-2 Schematic of the RFR: a) front view, b) top view) and c) the DEM simulation domain.

Because of the large amount of particles in the reactor, the value of the simulation time step and the computational resources available, a simulation of the whole reactor would be computationally out of reach. Therefore, a small volume element of this reactor, the shape of which represents a "wedge", such as the one identified in Figure 4-2b, is used as the computational domain. The wedge is represented by a rectangle in the figure due to the large bed length to bed width ratio. Periodic boundary conditions are imposed on both sides along the width direction, which means that one particle flowing out of one side re-enters into the domain through the opposite side. It has been previously reported that the simulation domain size in the

direction of the periodic boundary conditions should at least be five times the particle diameter in order to have no significant effect on the numerical results (Bertrand, Gange, Desaulniers, Vidal, & Hayes, 2004). Also, Landry et al. (2004) showed that a width of $2\bar{d}$ ($\bar{d}$ being the particles mean diameter) represents the transition from a 2D-like behavior to a 3D-like behavior. Here, the largest particle has a 4mm diameter, so a 25mm width is used. Such a scaled portion of the reactor is justified because it is axisymmetric and because of the occurrence of mainly radial dominated transfer mechanisms in the case of the radial expansion and contraction of the vessel.

To carry out this study, two computational domains are used. The specifications of each domain are presented in Table 4-2. The first computational domain (A) is used to calibrate and assess the DEM-based model. It serves to investigate the wall pressure evolution over the course of many wall motion cycles. For this part of the study, only alumina particles are considered since they are harder than the molecular sieve particles. For this domain, the height of the bed is emphasized and its length is compromised, which is justified by the fact that some relief in wall pressure is expected near the free surface. In other words, the use of a higher bed reduces the effect of the walls near the free surface. The second computational domain (B) contains both types of adsorbents and is used to study particle dynamics and mixing of the adsorbents at their interface (Figure 4-2c). Here bed length is emphasized and the bed height is compromised because the length is the main direction along which mixing takes place when the walls are moved. The use of a shorter bed results in a larger effect of the free surface upon mixing, which can be viewed as a conservative strategy as less intense mixing is expected further away from the free surface. It should be noted that the top of the adsorbent bed is also a free surface in the full-scale unit. There is no horizontal plate at the top of the reactor and particles therein are free to move upward during wall motion.

Table 4-2 Computational domain specifications

Domain	Dimensions (m)		Number of particles (Volume fraction)		#Cores
			Alumina	Molecular sieve	
A	Length	0.16	222 925 (1)	0 (0)	16
	Height	1.28			
	Width	0.025			
B	Length	0.32	51 467 (0.24)	547 513 (0.76)	48
	Height	0.64			
	Width	0.025			

The simulations of this work were done using a parallel implementation of the DEM based on the MPI library. All computations were performed using between 16 and 48 cores (Table 4-2) of the Compute Canada Mammouth supercomputer. The average computational time was in the order of 600 hours for one second of simulated time.

4.2.3.2.4 Reactor filling

The computational domain is filled using a technique called “en masse” filling. With this technique, all particles are generated at the same time. They are loosely and evenly spread over the computational domain. They are then allowed to settle under gravity. Even though this technique is frequently used to save computational time (Gonzalez-Montellano, Ramirez, et al., 2012), it is used here for another important reason. During the filling process, the larger the height of the bed, the larger the velocities of the particles impacting its surface. These large particle velocities help to create a uniform tight packing, which is essential for a realistic simulation of the packed bed of a RFR. To fill two layers of particles in domain B, a zero thickness virtual wall is placed between the two types of adsorbents during the settling process. This wall is used to prevent any mixing of the adsorbents during the initial filling step. The two

respective subdomains corresponding to each type of adsorbent are then clearly defined. Once the filling phase is complete, the virtual wall is removed and the particles are again allowed to settle in order to fill the voids that may have been created by the presence of this virtual wall.

4.2.3.2.5 Wall motion

The DEM-based model is isothermal. The thermal expansion and contraction phenomena occurring in a TSA process are taken into account in the DEM-based model through the implementation of the corresponding wall motion. A typical temperature cycle of a full-scale unit TSA process is shown in Figure 4-3a. Using the coefficient of thermal expansion of the materials used to build the RFR baskets, the corresponding radius change cycles for a full-scale unit are obtained (Figure 4-3b).

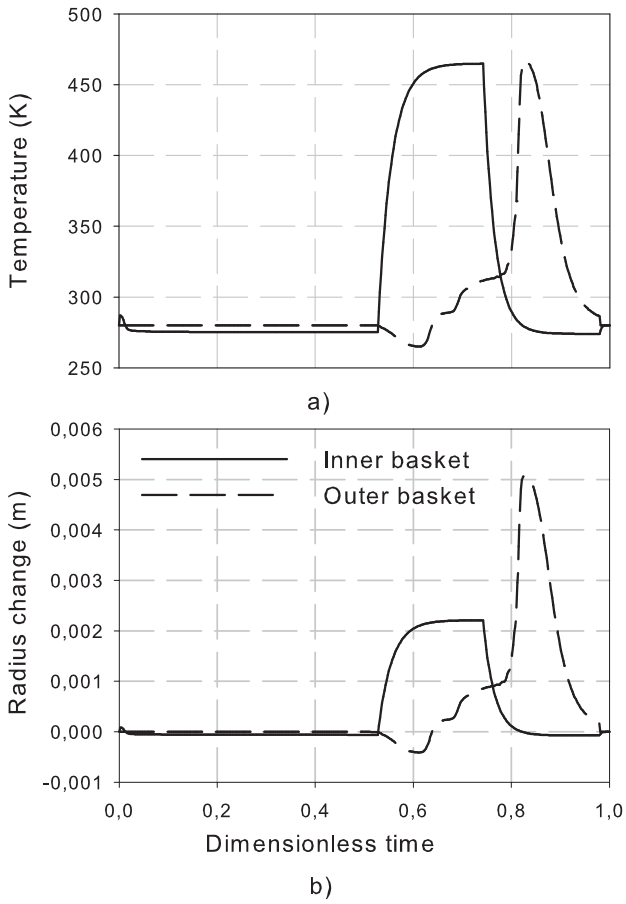

Figure 4-3 Original temperature cycle (a) and corresponding radius change (b).

TSA cycles usually last many hours (Ruthven, 1984). The DEM simulation of such a long process is not feasible due to the small time step required. Some modifications must then be made to the original cycle so that it can be simulated using the DEM. It can be noticed that no temperature change occurs for approximately 50% of the cycle. To save computational time, this portion of the cycle is removed for both baskets. To make sure that the particle dynamics is not affected significantly by this removal, a small portion of inactivity must be kept so that the energy gained during a cycle has time to dissipate before a new cycle begins. Figure 4-4 compares the original wall motion cycle and the one that was used for the DEM simulations. It must be mentioned that the radius change is not scaled down and corresponds to the wall motion occurring in the full-scale unit. Here again, such a strategy is deemed conservative as less mixing is then expected further away from the free surface.

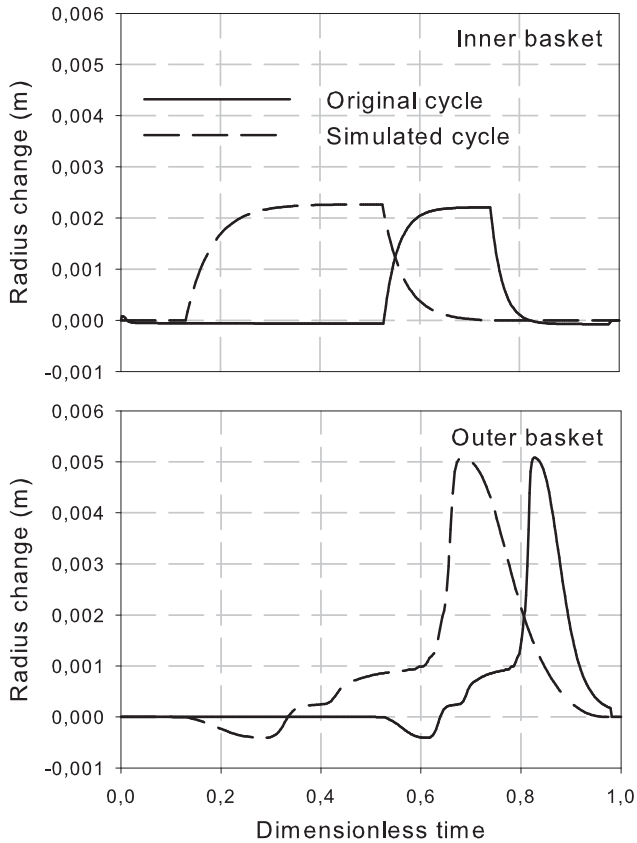

Figure 4-4 Adapted wall motion cycle for the DEM simulations.

Finally, a cycle frequency needs to be chosen for the simulations. Similar to the compromises made in the selection of the time step, the cycle frequency should be a trade-off between numerical stability, computational time and accurate prediction of the real TSA process. In fact, an adequate frequency is the one that allows the DEM-based model to simulate both dynamically and accurately a full-scale unit. Preliminary trial simulations revealed that it is possible to identify an upper bound for the wall cycle frequency. In order for the simulation to be stable, it was found that the following criterion should hold:

$$\frac{\delta_{n,\max}}{V_{wall,\max}} > t_R \tag{4.16}$$

where t_R is defined in equation (4.13) and $\delta_{n,\max}$ is the normal overlap experienced by the smallest particle of the system following a normal impact with a wall velocity $V_{wall,\max}$, which corresponds to the maximum wall velocity attained for a specific wall cycle frequency. In other words, the characteristic impact time $\left(\frac{\delta_{n,\max}}{V_{wall,\max}}\right)$ inherent to the wall cycle frequency f should be higher than the characteristic time associated with the model (i.e. the Rayleigh wave propagation time t_R). The maximum wall velocity is linearly proportional to the wall cycle frequency:

$$V_{wall,\max} = kf \tag{4.17}$$

where k is a proportionality constant, which is equal to 24.5m/cycle for the wall motion cycle displayed in Figure 4-4. The stability criterion for the wall cycle frequency then becomes:

$$\frac{\delta_{n,\max}}{kft_R} > 1 \tag{4.18}$$

Figure 4-5 shows the relationship between this criterion and the wall cycle frequency. It can readily be noticed that, in order for the simulation to be stable, the wall cycle frequency should be lower than 2Hz. Frequencies of 0.5, 1 and 2Hz were used for the DEM simulations of this work. The results are compared to experimental data measured on a full-scale unit in the next section.

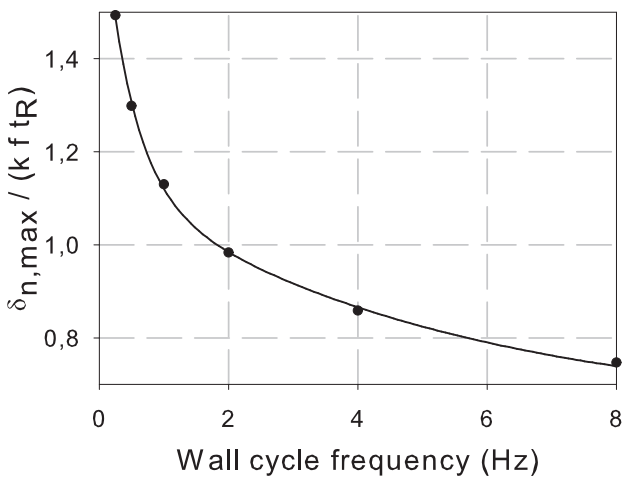

Figure 4-5 Stability criterion vs wall cycle frequency.

4.2.4 Results and discussion

4.2.4.1 Model assessment

The DEM-based model is assessed by comparing bed porosity as well as static and dynamic wall pressures to both analytical and experimental results.

4.2.4.1.1 Bed porosity

If reliable numerical results are to be obtained from DEM simulations of a TSA process, the packed bed resulting from the filling process must have a porosity close to the one measured in a full-scale unit. RFR are filled using a dense loading technique that generates a uniformly tight packed bed (Schneider, Smolarek, Ackley, & Nowobilski, 1999). Kareeri et al. (2006) and Heggs et al. (1995a) respectively used bed porosity values of 0.3 and 0.4 to conduct their investigations. Most DEM studies have reported values varying between 0.38 and 0.42 after the filling process (Balevicius et al., 2011; J. W. Landry, Grest, Silbert, & Plimpton, 2003).Figure 4-6 displays bed

porosities of the two computational domains after settling. A uniform porosity of 0.367 is observed for the alumina layer in both cases, and a value of 0.360 is obtained for the molecular sieve particles layer in computational domain B. The lower bed porosity obtained here can be attributed to the high polydispersity as well as the high impact velocities of the particles. Bed porosities of 0.35 for alumina and 0.34 for molecular sieve were measured experimentally. These differences between the DEM results and the experimental data are deemed reasonable.

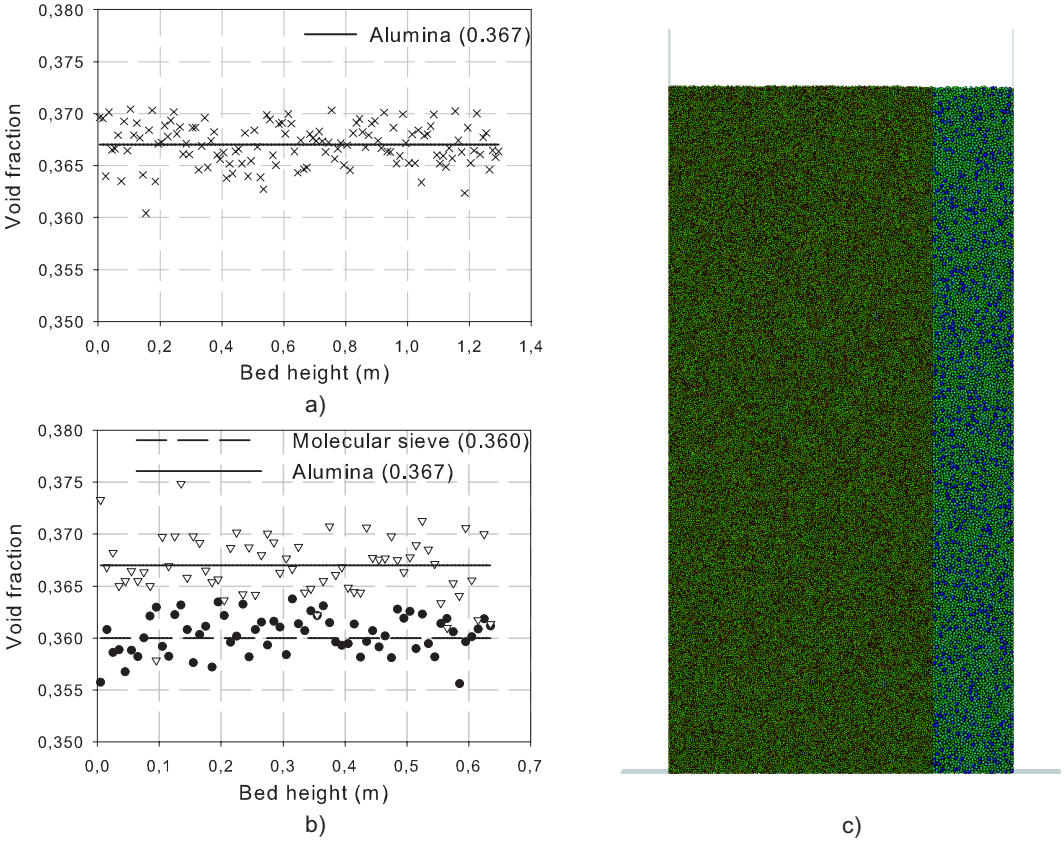

Figure 4-6 Bed porosity with respect to bed height for a) domain A, b) domain B and c) DEM packed bed after filling for domain B (particles are colored by size).

4.2.4.1.2 Static stress analysis (no wall motion)

The wall pressure and shear stress computed by the DEM with no wall motion are compared to values predicted by Janssen's analysis. Janssen's analytical solution for wall normal pressure (σ_n) and wall shear stress (τ_w) is given by (Nedderman, 2005):

$$\sigma_{xx} = \sigma_n = \frac{\gamma D_H}{4\mu_w}\left[1 - e^{\left(-\frac{4\mu_w K y}{D_H}\right)}\right] \tag{4.19}$$

$$\tau_w = \mu_w \sigma_n \tag{4.20}$$

where

$$\gamma = \rho_b g = \rho_p g\left(1-\varepsilon\right) \tag{4.21}$$

In these equations, γ is the weight of the granular material, ρ_b the bulk density, ρ_p the particle density, μ_w the friction coefficient between the bulk of particles and the wall, $K = \frac{1-\sin\phi}{1+\sin\phi}$ the Janssen constant and y the depth below the top surface of the bed. In this study, for comparison purposes, the internal friction angle ϕ is approximated using $\phi = \tan^{-1}\mu_{pp}$. The hydraulic diameter (D_H) is defined as:

$$D_H = \frac{4A}{P} \tag{4.22}$$

where A and P are respectively the cross-sectional area and the perimeter. It can be shown that, in the case of infinite parallel twin walls separated by a distance b, which applies to computational domains A and B, the hydraulic diameter is simply:

$$D_H = 2b \tag{4.23}$$

Note that Janssen's formulation for an annular bed is identical to the one presented here. Indeed, the hydraulic diameter of an annular bed with a distance b between the walls of two concentric cylinders is:

$$2b = \left(D_O - D_I\right) \tag{4.24}$$

where D_O and D_I are the external and internal diameters of the annular bed.

A comparison of the wall pressure and shear stress values from the DEM simulations and Janssen's equations (4.19) and (4.20) using the particle properties of Table 4-1 are presented in Figure 4-7. A quantitative match is obtained for the computational domain B while, for the taller computational domain A, an overshoot of the normal stress when the depth becomes twice as large as the bed hydraulic diameter is observed. This overshoot has been reported before in different circumstances (Balevicius et al., 2011; J. W. Landry et al., 2003). Two explanations for this overshoot in the case of the taller domain can be given.

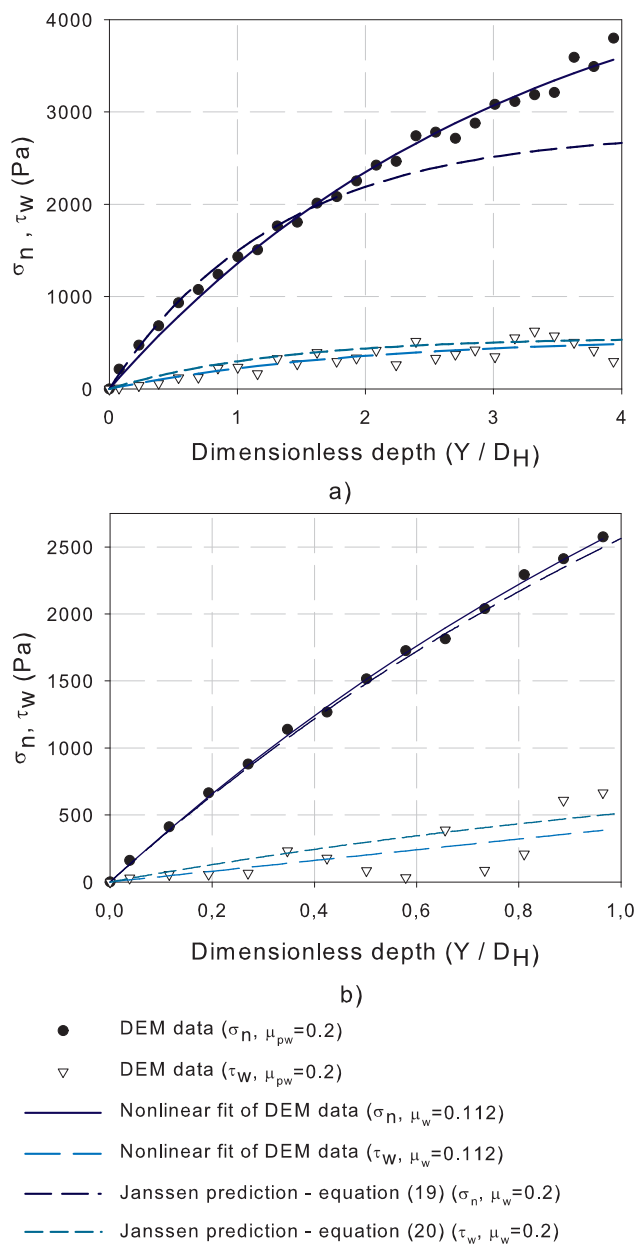

Figure 4-7 Normal and shear stress values for computational domains a) A and b) B.

The first possible explanation is related to the hypothesis made in Janssen's original analysis, which relies on three main assumptions: a) the stresses are uniform across any horizontal section of the material, b) the vertical and horizontal stresses are the dominant ones, and c) the forces in play are at incipient failure on the basis of the Coulomb yield criterion (James W. Landry et al., 2004; Nedderman, 2005). The mobilized friction (μ_m), corresponding to the ratio of tangential

forces to normal forces (Gonzalez-Montellano, Gallego, Ramirez-Gomez, & Ayuga, 2012), was computed to verify the last assumption. As can be seen in Figure 4-8, the mobilized friction is always lower than the particle-wall friction $(\mu_{pw} = 0.2)$ used for the simulations. Just like in the work of Gonzalez-Montellano et al. (2012) and Landry et al. (2004), a region at the top of the bed $\left(Y / D_H \to 0\right)$ having a significantly low μ_m is observed. It indicates that this region of the bed is far away from the Coulomb yield value; the walls support less stress so a hydrostatic stress profile is obtained. As for the rest of the bed, a mean value 0.16 is obtained for μ_m. This value is lower than $\mu_w\left(0.2\right)$, which partially explains why a larger hydrostatic region is predicted by the DEM. Gonzalez-Montellano et al. (2012) studied in detail the effect of the "en masse" filling technique and concluded that this technique indeed reduces mobilization of friction. They specified that this filling technique could potentially lead to errors when predicting the wall pressures that develop during the filling of a silo. It must be noted that an incomplete development of friction is expected with the DEM since friction is mobilized by both the particle interactions and the particle shape (Hartl & Ooi, 2008). In particular, the representation of the granular material by perfect spheres contributes to the decrease in friction mobilization. This means that the third assumption from Janssen's original analysis does not seem to apply in DEM simulations, which would explain the discrepancies between the numerical results and the analytical data. On the other hand, note that the depth-independent region of the normal stress profile, as obtained from Janssen's analysis, has still not been reached in the simulation. Consequently, it is possible that, with a taller bed, a quantitative agreement for the maximum normal stress would be obtained, like in Landry et al. (2003). Moreover, Figure 4-7 shows that Janssen's equation best approximates the DEM data with a value of $\mu_w = 0.112$. This is lower than the value of μ_m, 0.16, obtained from Figure 4-8 as discussed above. Therefore, this first explanation alone cannot elucidate completely why there is an overshoot in normal pressure in Figure 4-7.

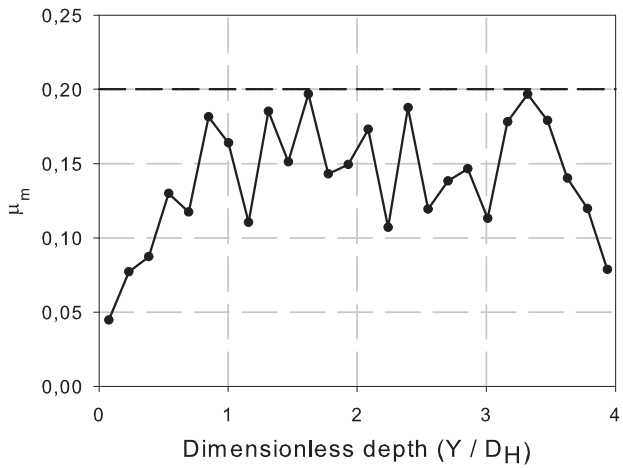

Figure 4-8 Mobilized friction in computational domain A.

The second possible explanation is related to the parameters used in equation (4.19). The nonlinear fits displayed in Figure 4-7 were obtained after applying a nonlinear least-square regression to determine values for coefficients μ_w and K. A quasi-identical value for K (0.71 instead of 0.76) and a much lower value for μ_w (0.112 instead of 0.2 (from Table 4-1) are obtained. The coefficient μ_w used in Janssen's formulation should be the coefficient of friction between the bulk of particles and the wall (macroscopic friction) while the one used in the DEM-based model is the particle-wall interaction coefficient of friction (microscopic friction). Ketterhagen et al. (2009) presented a relationship between the macroscopic wall friction angle and the particle-wall friction coefficient for particles used in the simulation of a Schulze ring shear tester. This relationship indicates that, if the particles are allowed to rotate, the macroscopic friction can be significantly lower than the microscopic friction. Consequently, the lower values of the normal stress predicted by the Janssen's model could simply be explained by the inappropriate higher friction factor used in equation (4.19). To confirm this, three additional simulations were performed. They consist of varying the particle-wall friction coefficient $\left(\mu_{pw}\right)$ and filling domain A with a larger amount of particles (360 000), in order to have a taller bed and thus get closer to the asymptotic behavior and increase friction mobilization. Values of 0.1, 0.2 and 0.4 for μ_{pw} were tested. Figure 4-9 presents the wall pressure profiles obtained with the

DEM-based model as well as the ones yielded by the Janssen's formulation when μ_{pw} is directly used in equation (4.19).

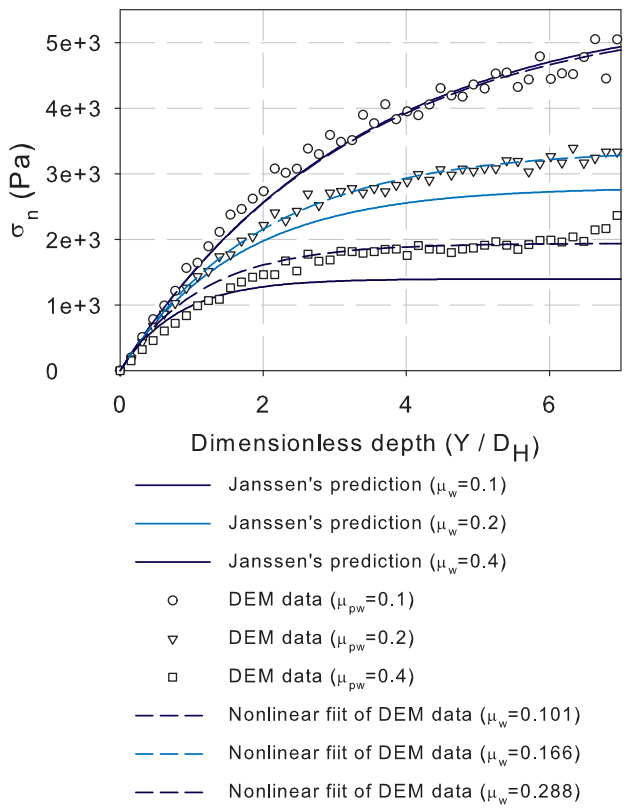

Figure 4-9 Comparison of wall pressure for different values of the wall-particle friction coefficient.

It can be observed that the agreement between the DEM results and Janssen's formulation is excellent when μ_{pw} is low, the discrepancies getting larger as μ_{pw} increases. Figure 4-10 shows the relationship between the macroscopic friction coefficient μ_w and the particle-wall friction coefficient μ_{pw} found by Ketterhagen et al. (2009) as well as the results obtained with the three DEM simulations. For the latter, the macroscopic friction coefficient μ_w corresponds to the value for which the DEM results best fit Janssen's formulation in Figure 4-9. It can be noticed that the numerical results comply with those of Ketterhagen et al. (2009).

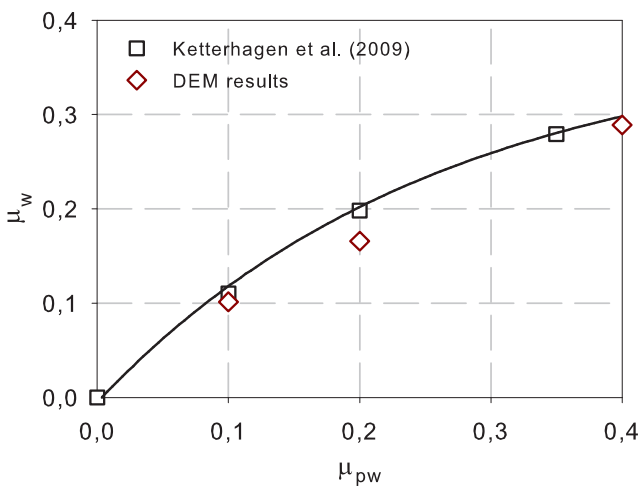

Figure 4-10 Relationship between the macroscopic (μ_w) and microscopic friction (μ_{pw}) coefficients.

It must be recalled that, for the simulation of the shorter domain A, a value of $\mu_w = 0.112$ was found for $\mu_{pw} = 0.2$ (Figure 4-7). This value of μ_w is well below the one found (0.166) with the taller bed (Figure 4-10). This variation may indeed be attributed to the different bed heights used in the simulations of domain A. It also suggests that the two explanations proposed here for the overshoot in normal pressure (Figure 4-7a) are plausible. Further investigation would be required to fully identify the sources of these discrepancies.

4.2.4.1.3 Dynamic stress analysis (with wall motion)

As was previously mentioned, a DEM simulation of the real experimental cycle, which is in the order of many hours, is not feasible. A much higher cycle frequency must then be chosen, which must however be such that the DEM-based model can yield numerical results that are phenomenologically accurate. One way to assess the reliability of the DEM-based model under dynamic conditions is to compare the numerical and experimental normal wall pressure values

over the course of many cycles using the computational domain A. As already mentioned, the bed height is emphasized and the bed length is compromised in this computational domain, which is justified by the fact that some relief in wall pressure is expected near the free surface of the bed. The normal pressures for the full-scale unit and the DEM simulations are presented at Figure 4-11. More precisely, experimental data for 10 cycles of the full-scale unit as well as 9, 7 and almost 4 cycles of DEM simulations with 2Hz, 1Hz and 0.5Hz cycle frequencies, respectively, are shown. Pressures in the full-scale unit were measured using load cells (Stellar Technology, Amherst, NY) mounted at various heights to the walls of both the inner and outer baskets. There was no significant variation in wall pressure with respect to height for the number of cycles compared.

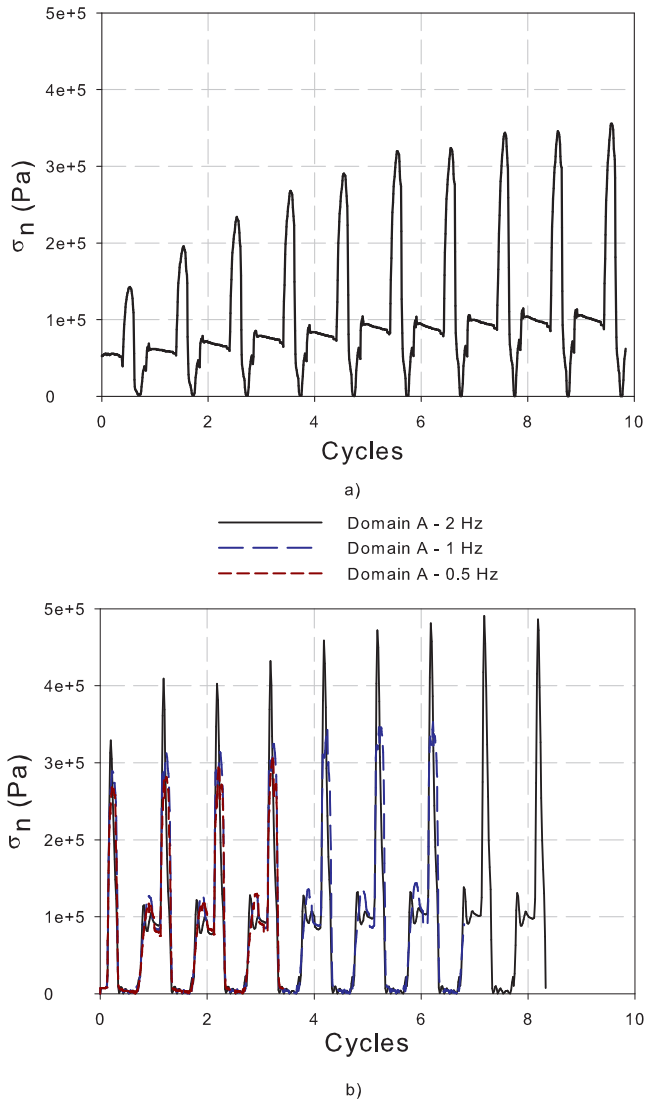

Figure 4-11 Normal pressure evolution a) for the full-scale unit and b) the DEM simulations.

It can be readily noticed that a qualitative agreement between the numerical results and the experimental data is obtained. In all cycles, a maximum normal pressure peak is obtained followed by a drastic drop to zero. The pressure then levels off to an intermediate value before the beginning of the next cycle. Figure 4-12 displays the maximum pressure evolution in all cases and a progressive increase is observed. The increase is smoother with the DEM and a 0.5Hz or 1Hz frequency than with both the DEM and a 2Hz frequency and the full-scale unit. It can also be noticed that the curves corresponding to the DEM simulation with a 1Hz cycle and the full-scale unit level off to similar values around 3.5×10^5 Pa. The simulation results with a 0.5Hz frequency

also indicate a similar trend after 4 cycles. On the other hand, the DEM simulation with a 2Hz frequency overestimates the normal pressure measured in the full-scale unit after 9 cycles by more than 10 kPa. In fact, while the maximum pressure curve at this frequency follows a trend similar to the experimental curve, the results of Figure 4-12 reveal that reducing the frequency from 2Hz to 1Hz and 0.5Hz improves the asymptotic behavior significantly. As mentioned before, the wall cycle frequency should be strictly lower than 2Hz. When analyzing the results of this figure, one should also keep in mind that the walls of the full-scale unit are elastic while the DEM-based model assumes rigid wall conditions. Note that the progressive increase in stress is a manifestation of thermal racking (Nedderman, 2005). One observation here is that, by accounting for these thermal changes by means of radial expansion and contraction, the DEM is able to reproduce this phenomenon. To our knowledge, it is the first time that this phenomenon can be predicted using the DEM.

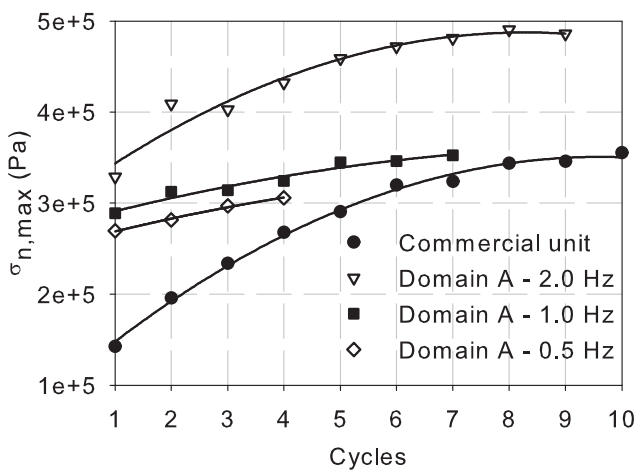

Figure 4-12 Wall maximum pressure evolution.

The accuracy of the DEM-based model cannot be assessed rigorously by comparing only the maximum value of the normal stress. Since particle dispersion is going to be evaluated below, the evolution of the numerical pressure with respect to the bed length should also match the one measured on the full-scale unit. The fact that the real reactor is much larger and the real cycle time is much longer does not allow a priori for a direct comparison. However, a closer look at the time variation of the compression/expansion speed of the granular bed for the full-scale unit and

the DEM simulation reveals that it is possible to identify three similar characteristic phases within one single cycle. To identify these phases, the compression/expansion speed $(v_{c/e})$ is introduced:

$$v_{c/e} = \frac{\Delta R_{t^* + \Delta t^*} - \Delta R_{t^*}}{\Delta t^*} \tag{4.25}$$

where ΔR is the bed length (i.e. the difference between the outer basket and inner basket positions) and t^* is the cycle time. A negative value of $v_{c/e}$ implies that the granular bed is being compressed while a positive value implies that it is expanding. These characteristic phases are clearly identified in Figure 4-13. A detailed evolution of the normal pressure over the course of a single cycle (cycle 8 for the full-scale unit and cycle 6 for the DEM simulation with a 1Hz frequency) is also presented in this figure.

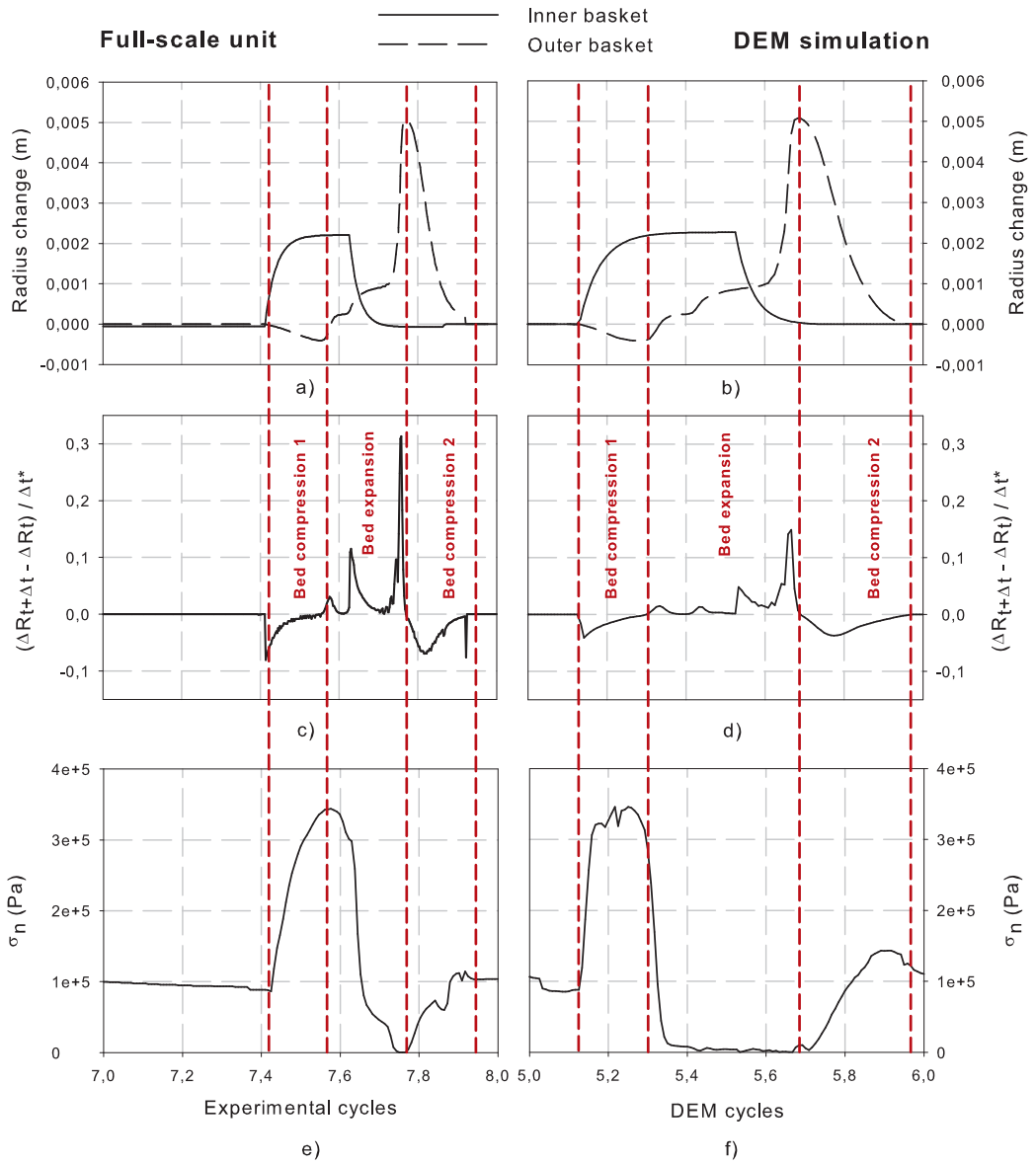

Figure 4-13 Comparison over one single cycle of (a-c-e) experimental data and (b-d-f) DEM simulation results: a) and b) radius change, c) and d) compression/expansion velocity and e) and f) normal pressure..

At the end of the first compression phase, both bed lengths are reduced by approximately 2.5mm (Figure 4-13a and b). Since the bed is smaller than its initial length, a maximum pressure peak is expected in this phase. This can indeed be seen in both the experimental and the numerical cases. However, the maximum pressure peak is obtained at the end of the first compression phase in the

full-scale unit while it is obtained in the middle of this phase for the DEM simulation. Nevertheless, it can be noticed that the intensity of these peaks is similar.

At the end of the expansion phase, both beds are 5mm longer than at the beginning of the cycle. It is expected that the normal pressure reaches zero in both cases. This is exactly what can be noticed in Figure 4-13e and f. However, the decrease in pressure in the DEM simulation is faster and sharper than in the full-scale unit. Also, the time that the simulated pressure spent near the 0Pa value is longer. This is due to the discrete nature of the wall motion. The first step of a DEM iteration consists of moving the walls. Then, the particle-particle and particle-wall contacts are detected and solved. The particles are moved by integrating Newton's second law only at the end of the iteration. So, if the bed is expanding, since the particles are not moved immediately, the number of contacts detected at the walls will diminish greatly and can even be zero. This explains the near-zero values of the wall pressure in the DEM simulation during the expansion phase.

In the last compression phase, both beds get compressed until their initial lengths are regained. For this reason, during this phase, the pressure is expected to steadily increase and level off to the value it had at the beginning of the cycle. It can be noticed in Figure 4-13e and f that the pressure increase is slightly higher in the DEM simulation than in the full-scale unit, although, at the end of the cycle, a similar wall pressure is obtained in both cases.

In summary, good quantitative agreement between the experimental data and the numerical results was achieved in the different phases of the TSA cycle when a 1Hz frequency is used for the simulation. These pressure results altogether show that the DEM-based model used in this work is accurate enough to predict the granular behavior in a RFR.

4.2.4.2 Investigation of particle dynamics

Particle dynamics and, in particular, mixing of the molecular sieve and alumina particles at their interface was simulated with the calibrated DEM-based model. The simulation domain B was considered for this part of the study. The goal was to derive a particle dispersion coefficient that could be used to predict the long-time mixing behavior of the particles. As already mentioned, the bed length is emphasized and the bed height is compromised in this computational domain because the bed length is the main direction along which mixing takes place when the walls are moved. The domain walls were moved with a 1Hz frequency. Figure 4-14 displays the evolution of the “surface” concentration of molecular sieve particles for 10 cycles near the initial position of the interface. It represents the fraction of molecular sieve particles (the surface occupied by the molecular sieve particles divided by the surface occupied by all the particles) on a cross-section plane covering the entire domain height. This figure clearly shows that the concentration of molecular sieve particles left of the initial position of the interface decreases with time, which indicates that alumina particles are migrating into this region. Quite obviously, a similar phenomenon occurs right of this interface, where the concentration of alumina particles diminishes with time owing to the migration of molecular sieve particles into this region.

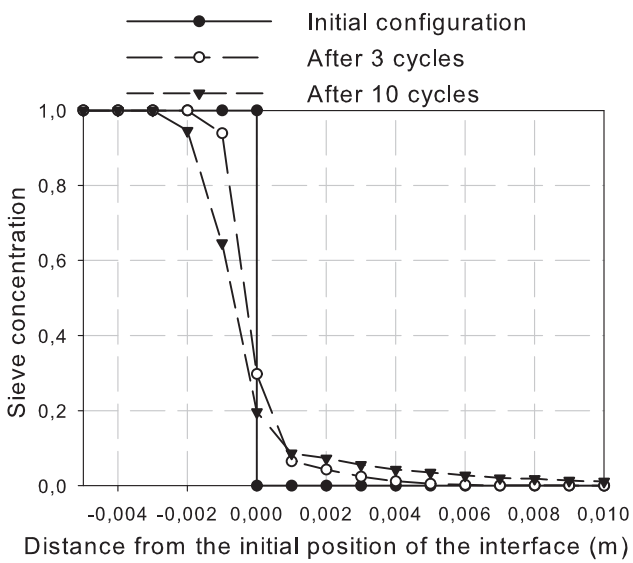

Figure 4-14 Evolution of the molecular sieve surface concentration near the initial position of the interface.

The evolution of the molecular sieve concentration over the course of 10 cycles on cross-section planes on both side of the initial interface and that are 1mm and 5mm away from it are presented in Figure 4-15. It can be noticed that the decrease in sieve concentration 1mm left of the interface is sharper than the increase 1mm right this interface. This is explained by the smaller average size of the molecular sieve particles. Also, no change in the molecular sieve concentration 5mm left of the interface can be observed while some changes are noticeable 5mm right of this interface. Again, this is a direct consequence of the size differences between the two particle types. Since the bed of particles is slightly denser on the molecular sieve side and since the alumina particles are bigger on average than the molecular sieve ones, these alumina particles are expected to be hampered and slowed down significantly. Nevertheless, some particle migration is observed.

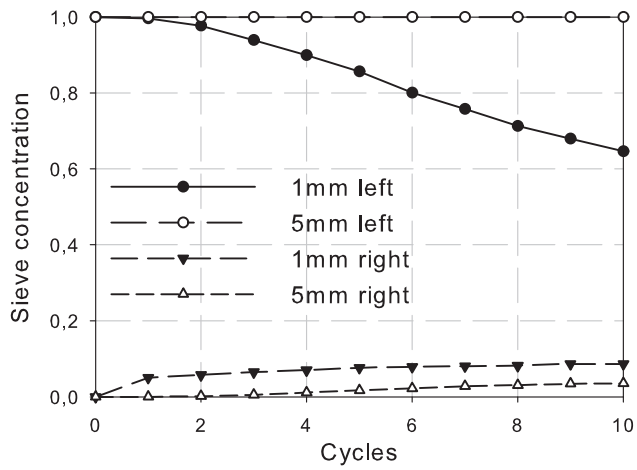

Figure 4-15 Molecular sieve concentration on specific cross-section planes located at specific distance from the initial positioning of the interface.

To quantify the extent of the particle migration, a dispersion coefficient (Einstein, 1905) was computed as:

$$D_{xx} = \frac{\sigma_x^2}{2t} = \frac{\sum_{i=1}^{N}\left(\Delta x_i - \Delta\bar{x}\right)^2}{2\left(N-1\right)t} \tag{4.26}$$

In this expression, t stands for the time in cycle units, Δx is the particle displacement along the radial direction (perpendicular to the interface), $\Delta\bar{x}$ the mean particle displacement and N the number of particles in a rectangular box circumscribing the interface. Figure 4-16a shows that the dispersion coefficients in the x-direction for both particle types decrease rather rapidly initially, but then level off to values around $1\text{x}10^{-8}$ m^2/cycle for the alumina particles and $2\text{x}10^{-8}$ m^2/cycle for the molecular sieve particles. The difference between the two coefficients is likely due to the fact that the alumina particles are larger than the molecular sieve particles, thereby reducing their mobility near the interface. The higher value of the dispersion coefficients observed in the first few cycles can be attributed to the free space at the interface, which is due to the removal of the invisible wall used during the filling process to prevent the two types of particles from mixing. The dispersion coefficients in the y-direction (Figure 4-16b) exhibit the same behaviour as in the x-direction except that they level off to the same value ($1\text{x}10^{-8}$ m^2/cycle). It must be noted that, since the motion of the simulated walls is more intense than that in the full-scale unit because of

the differences in the temperature cycles, the computed dispersion coefficients represent an upper bound.

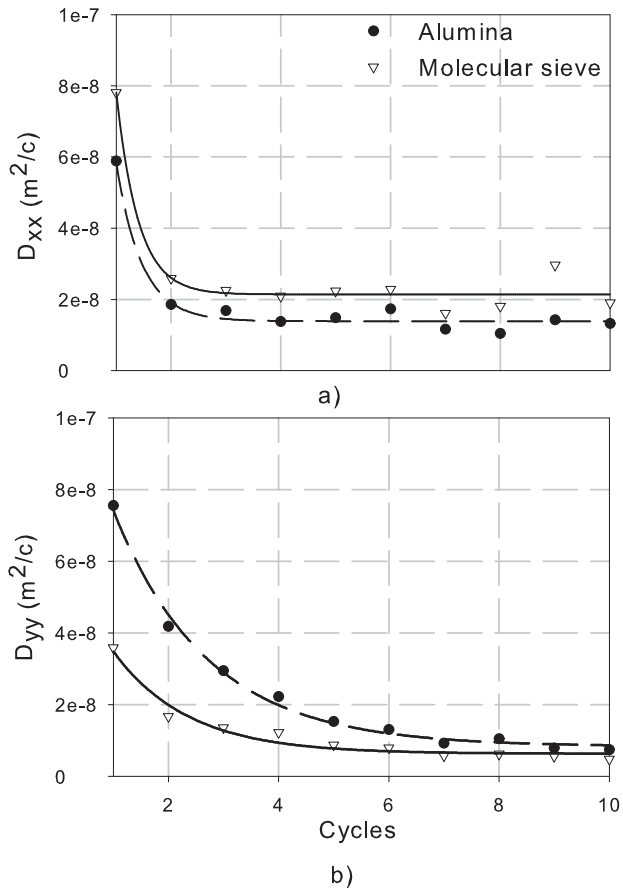

Figure 4-16 a) Radial (Dxx) and b) axial (Dyy) dispersion coefficients.

These dispersion coefficients could be used in a transient diffusion equation to predict the extent of mixing occurring at the interface of a full-scale size RFR. It is known that particle mixing can have a significant deteriorative effect on the reactor efficiency. In this way, the dispersion coefficients could also be used to set an upper limit for the bed operation lifetime. Nevertheless, the results obtained here indicate that particle motion across the interface is relatively slow.

4.2.5 Conclusion

A DEM-based model was successfully applied to study the dynamics of adsorbents used in the RFR of a TSA process. The thermal swing cycle was simulated by a corresponding wall motion cycle in the DEM. It was shown that, if the model is properly calibrated using a mix of direct measurements of particle properties and simple auxiliary simulations, it can predict phenomenologically the granular flow behavior in a full-scale unit. The accuracy of the DEM-based model was assessed using experimental values of bed porosity, analytical values of predicted wall pressure based on Janssen's theory, and experimental values of wall pressure measured during the operation of a full-scale unit. Qualitatively and quantitatively good agreement was obtained for porosity as well as static (i.e. with no wall motion) and dynamic (i.e. with wall motion) wall pressure. It was noticed that, in the case of a tall computational domain, the DEM yielded wall pressure values that exceed the values predicted by Janssen's analysis. Further investigation would be required to clearly identify the cause of this discrepancy. Moreover, the dynamic pressure obtained by the DEM simulation was observed to comply well with every phase of a full-scale unit cycle. The DEM-based model was also able to reproduce the thermal racking phenomenon occurring is this type of reactor. Finally, the dispersion of particles during many wall motion cycles was investigated using the simulation of a packed bed containing layers of alumina and molecular sieve particles. While the corresponding dispersion coefficients indicate that little mixing occurs at the adsorbent interface, they show that mixing could potentially affect the efficiency of the reactor in the long run.

To our knowledge, this is the first time that simulation is used to investigate the behavior of the packed bed of a RFR in a TSA process. The results obtained with the proposed model show that the DEM is a valuable tool for the investigation of such slow dynamical processes, provided a careful calibration is done.

4.2.6 Acknowledgments

The financial support of the Natural Sciences and Engineering Research Council of Canada (NSERC) and PRAXAIR Inc. is gratefully acknowledged. All simulations were made possible thanks to the computational resources of Compute Canada.

4.2.7 References

Ackley, M.W., Celik, C.E., Nowobilski, J.J., Schneider, J.S.: Radial flow reactor. US 8,101,133 B2, January 24, 2012

Akseli, I., Cetinkaya, C.: Drug tablet thickness estimations using air-coupled acoustics. International Journal of Pharmaceutics 351(1–2), 165-173 (2008)

Balevicius, R., Sielamowicz, I., Mroz, Z., Kacianauskas, R.: Investigation of wall stress and outflow rate in a flat-bottomed bin: A comparison of the DEM model results with the experimental measurements. Powder Technology 214(3), 322-336 (2011)

Bertrand, F., Gange, T., Desaulniers, E., Vidal, D., Hayes, R.E.: Simulation of the consolidation of paper coating structures: Probabilistic versus deterministic models. Computers and Chemical Engineering 28(12), 2595-2604 (2004)

Bertrand, F., Leclaire, L.A., Levecque, G.: DEM-based models for the mixing of granular materials. Chemical Engineering Science 60, 2517-2531 (2005)

Celik, C.E., Ackley, M.W.: Radial bed vessels having uniform flow distribution. US 8,313,561 B2, November 20, 2012

Cetinkaya, C.: Accoustic Measurement of Young's Modulus and Poisson's Ratio for Adsorbents Beads. In: unpublished Praxair Project Progress Report (375-35322), Clarkson University. (2009)

Couroyer, C., Ning, Z., Ghadiri, M., Brunard, N., Kolenda, F., Bortzmeyer, D., Laval, P.: Breakage of macroporous alumina beads under compressive loading: Simulation and experimental validation. Powder Technology 105, 57-65 (1999)

Cundall, P.A., Strack, O.D.L.: Discrete Numerical Model for Granular Assemblies. Geotechnique 29(1), 47-65 (1979)

Einstein, A.: Motion of suspended particles on the kinetic theory. Annalen der Physik 17(3), 549-560 (1905)

Fraige, F.Y., Langston, P.A.: Integration schemes and damping algorithms in distinct element models. Advanced Powder Technology 15(2), 227-245 (2004)

Goda, T.J., Ebert, F.: Three-dimensional discrete element simulations in hoppers and silos. Powder Technology 158(1-3), 58-68 (2005)

Gonzalez-Montellano, C., Gallego, E., Ramirez-Gomez, A., Ayuga, F.: Three dimensional discrete element models for simulating the filling and emptying of silos: Analysis of numerical results. Computers and Chemical Engineering 40, 22-32 (2012a)

Gonzalez-Montellano, C., Ramirez, A., Fuentes, J.M., Ayuga, F.: Numerical effects derived from en masse filling of agricultural silos in DEM simulations. Computers and Electronics in Agriculture 81, 113-123 (2012b)

Gonzalez-Montellano, C., Ramirez, A., Gallego, E., Ayuga, F.: Validation and experimental calibration of 3D discrete element models for the simulation of the discharge flow in silos. Chemical Engineering Science 66(21), 5116-5126 (2011)

Hartl, J., Ooi, J.Y.: Experiments and simulations of direct shear tests: Porosity, contact friction and bulk friction. Granular Matter 10(4), 263-271 (2008)

Heggs, P.J., Ellis, D.I., Ismail, M.S.: Modelling of fluid-flow distributions in annular packed beds. Gas separation & purification 8(4), 257-264 (1994)

Heggs, P.J., Ellis, D.I., Ismail, M.S.: Evaluation of pressure profiles and overall pressure drop for flow through annular packed bed configurations. Gas Separation & Purification 9(3), 171-171 (1995a)

Heggs, P.J., Ellis, D.I., Ismail, M.S.: Prediction of flow distributions and pressure changes in multi-layered annular packed beds. Gas Separation & Purification 9(4), 243-243 (1995b)

Hidano, T., Nakamura, M., Kawai, M.: Pre-purification unit of cryogenic air separation unit, hydrocarbon adsorbent, and method of pre-treating feed air. US 7,931,736 B2, April 26, 2011

Johnson, K.L.: Contact mechanics. Cambridge University Press, Cambridge [Cambridgeshire] ; New York (1985)

Kalbassi, M.A., Golden, T.C.: Purification of gases using solid adsorbents. US 5,855,650, January 5, 1999

Kareeri, A.A., Zughbi, H.D., Al-Ali, H.H.: Simulation of flow distribution in radial flow reactors. Industrial and Engineering Chemistry Research 45, 2862-2874 (2006)

Ketterhagen, W.R., Curtis, J.S., Wassgren, C.R., Hancock, B.C.: Predicting the flow mode from hoppers using the discrete element method. Powder Technology 195(1), 1-10 (2009)

Ko, D., Kim, M., Moon, I., Choi, D.: Analysis of purge gas temperature in cyclic TSA process. Chemical Engineering Science 57(1), 179-195 (2002)

Kumar, R., Deng, S.: Trace carbon monoxide and hydrogen conversion prior to cryogenic distillation of air. Adsorption 12(5-6), 361-373 (2006)

Kumar, R., Dissinger, G.R.: Nonequilibrium, Nonisothermal Desorption of Single Adsorbate by Purge. Industrial & Engineering Chemistry, Process Design and Development 25(2), 456-464 (1986)

Kumar, R., Huggahalli, M., Bülow, M.: Thermal swing adsorption process. US 6,432,171 B1, August 13, 2002

Landry, J.W., Grest, G.S., Plimpton, S.J.: Discrete element simulations of stress distributions in silos: Crossover from two to three dimensions. Powder Technology 139(3), 233-239 (2004)

Landry, J.W., Grest, G.S., Silbert, L.E., Plimpton, S.J.: Confined granular packings: structure, stress, and forces. Physical Review E (Statistical, Nonlinear, and Soft Matter Physics) 67(4), 41303-41301 (2003)

Leclaire, L.-A.: Parallélisation de la méthode des éléments discrets appliquée aux écoulements granulaires (Parallelization of the discrete element method applied to granular flows). Mémoire de maîtrise (Ecole polytechnique de Montréal), (2004)

Lemieux, M., Bertrand, F., Chaouki, J., Gosselin, P.: Comparative study of the mixing of free-flowing particles in a V-blender and a bin-blender. Chemical Engineering Science 62(6), 1783-1802 (2007)

Li, C., Cetinkaya, C.: Frequency domain thickness measurement approach for microscale multilayered structures. IEEE Transactions on Instrumentation and Measurement 55(1), 206-211 (2006)

Li, Y., Xu, Y., Thornton, C.: A comparison of discrete element simulations and experiments for 'sandpiles' composed of spherical particles. Powder Technology 160(3), 219-228 (2005)

Libal, K., Fierlbeck, W., Von Gemmingen, U.: Adsorption reactor solid cage walls - for minimal erosion of contained solids during adaptation to temp. change by inherent expansion of the walls. US 5,827,485, October 27, 1998

Lobanov, E.L., Skipin, Y.A.: Increasing the Operating Efficiency of Radial Reactors in Reforming. Chemistry and Technology of Fuels and Oils 22(5-6), 275-278 (1986)

Masson, S., Martinez, J.: Effect of particle mechanical properties on silo flow and stresses from distinct element simulations. Powder Technology 109(1-3), 164-178 (2000)

Nedderman, R.M.: Statics and kinematics of granular materials, Digitally printed 1st pbk. ed. Cambridge University Press, Cambridge, UK ; New York (2005)

Ponzi, P.R., Kaye, L.A.: Effect of Flow Maldistribution on Conversion and Selectivity in Radial Flow Fixed-Bed Reactors. AIChE Journal 25(1), 100-108 (1979)

Rapaport, D.C.: Radial and axial segregation of granular matter in a rotating cylinder: a simulation study. Physical Review E (Statistical, Nonlinear, and Soft Matter Physics) 75(3), 31301-31301 (2007)

Ruthven, D.M.: Principles of adsorption and adsorption processes. Wiley, New York (1984)

Schneider, J.S., Smolarek, J., Ackley, M.W., Nowobilski, J.J.: Assembly and method for loading particles into a vessel. US 5,836,362-A, November 17, 1998

Seader, J.D., Henley, E.J.: Separation process principles. John Wiley & Sons, New York ; Toronto (1998)

Sondergaard, R., Chaney, K., Brennen, C.E.: Measurements of solid spheres bouncing off flat plates. Journal of Applied Mechanics, Transactions ASME 57(3), 694-699 (1990)

Sudah, O.S., Arratia, P.E., Alexander, A., Muzzio, F.J.: Simulation and experiments of mixing and segregation in a tote blender. AIChE Journal 51(3), 836-844 (2005)

Tsuji, Y., Tanaka, T., Ishida, T.: Lagrangian numerical simulation of plug flow of cohesionless particles in a horizontal pipe. Powder Technology 71(3), 239-250 (1992)

Zhou, Y.C., Wright, B.D., Yang, R.Y., Xu, B.H., Yu, A.B.: Rolling friction in the dynamic simulation of sandpile formation. Physica A: Statistical Mechanics and its Applications 269(2), 536-553 (1999)

Zhou, Y.C., Xu, B.H., Yu, A.B., Zulli, P.: Numerical investigation of the angle of repose of monosized spheres. Physical Review E - Statistical, Nonlinear, and Soft Matter Physics 64(2 I), 213011-213018 (2001)

Zhou, Y.C., Xu, B.H., Yu, A.B., Zulli, P.: An experimental and numerical study of the angle of repose of coarse spheres. Powder Technology 125(1), 45-54 (2002)

CHAPITRE 5 OPTIMISATION DU POSITIONNEMENT DES DETECTEURS POUR LA TECHNIQUE DE SUIVI DE PARTICULE RADIOACTIVE

5.1 Présentation du second article

Soumis à *Applied Radiation and Isotopes* en avril 2013.

Auteurs : Olivier Dubé, David Dubé, Jamal Chaouki, François Bertrand.

Ce chapitre présente la stratégie d'optimisation qui a été développée pour identifier un positionnement optimal des détecteurs à scintillation pour la technique de suivi de particules radioactives.

5.2 Optimization of Detector Positioning in the Radioactive Particle Tracking Technique

5.2.1 Abstract

The Radioactive Particle Tracking (RPT) technique is a non-intrusive experimental velocimetry and tomography technique extensively applied to the study of hydrodynamics in a great variety of systems. In this technique, arrays of scintillation detectors are used to track the motion of a single radioactive tracer particle emitting isotropic γ-rays. This work describes and applies an optimization strategy developed to find an optimal set of positions for the scintillation detectors used in the RPT technique. This strategy employs the overall resolution of the detectors as the objective function and a Mesh Adaptive Direct Search (MADS) algorithm to solve the

optimization problem. More precisely, NOMAD, a C++ implementation of the MADS algorithm is used. First, the optimization strategy is validated using simple cases with known optimal detector configurations. Next, it is applied to a three-dimensional axisymmetric system (i.e. a vertical cylinder, which could represent a fluid bed, bubble column, riser or else). The results obtained using the optimization strategy are in agreement with what was previously recommended by Roy et al. (2002) for a similar system. Finally, the optimization strategy is used for a system consisting of a partially filled cylindrical tumbler. The application of insights gained by the optimization strategy is shown to lead to a significant reduction in the error made when reconstructing the position of a tracer particle. The results of this work show that the optimization strategy developed is sensitive to both the type of objective function used and the experimental conditions. The limitations and drawbacks of the optimization strategy are also discussed.

5.2.2 Introduction

5.2.2.1 Background

Radioactive particle tracking (RPT) is a non-intrusive experimental velocimetry and tomography technique extensively applied for the study of hydrodynamics in a great variety of systems. Ever since it was first introduced by Lin et al. (1985), RPT has been successfully used to investigate a wide range of reactors involving single or multiphase flow. A thorough summary of previously studied systems is presented in Table 5-1.

Table 5-1 Summary of systems studied using the RPT technique

System	Phase(s) in play	Researchers
Bubble column		
	Gas-liquid	(Devanathan, Moslemian, & Dudukovic, 1990; Salierno et al., 2012)
Cylindrical tumbler		
	Solid	(Alizadeh, Dubé, et al., 2013; Sheritt et al., 2003)
Fluidized bed		
	Gas-solid	(Bhusarapu, Al-Dahhan, & Dudukovic, 2006; Khanna, Pugsley, Tanfara, & Dumont, 2008; Mabrouk, Chaouki, & Guy, 2007; Tamadondar, Azizpour, Zarghami, Mostoufi, & Chaouki, 2012)
	Gas-solid-solid	(K. Kiared, Larachi, Chaouki, & Guy, 1999; Lefebvre, Guy, & Chaouki, 2007a, 2007b; Upadhyay & Roy, 2010)
	Gas-liquid	(K. Kiared, Larachi, Cassanello, & Chaouki, 1997)
	Gas-solid-liquid	(M. Cassanello, Larachi, Marie, Guy, & Chaouki, 1995; M. C. Cassanello, Fraguio, Larachi, & Chaouki, 2006; Fraguio, Cassanello, Larachi, & Chaouki, 2006; Fraguio, Cassanello, Larachi, Limtrakul, & Dudukovic, 2007; Karim Kiared, Larachi, Guy, & Chaouki, 1997; Larachi, Cassanello, Chaouki, & Guy, 1996; Larachi, Cassanello, Marie, Chaouki, & Guy, 1995; Larachi, Chaouki, et al., 1995; Larachi et al., 1994)
Riser		
	Gas-solid	(S. Roy et al., 2002)
	Liquid-solid	(S. Roy, Chen, Kumar, Al-Dahhan, & Dudukovic, 1997; S. Roy, Kemoun, Al-Dahhan, & Dudukovic, 2005)
Spouted bed		
	Gas-solid	(M. Cassanello, Larachi, Legros, & Chaouki, 1999; Djeridane, Larachi, Roy, Chaouki, &

		Legros, 1998; Larachi, Grandjean, & Chaouki, 2003; D. Roy, Larachi, Legros, & Chaouki, 1994)
V-blender		
	Solid	(Doucet, Bertrand, et al., 2008)

The concepts behind RPT are rather simple: using an array of scintillation detectors, it is possible to track the motion of a single radioactive tracer particle, emitting isotropic γ-rays, by counting the number of these γ-rays received by each detector during a sample time period. The position of the tracer particle in time can be reconstructed using a rigorous phenomenological relation which correlates the number of photons received and effectively counted by a detector and the position of the emitting source. Figure 5-1 presents a typical RPT experimental setup.

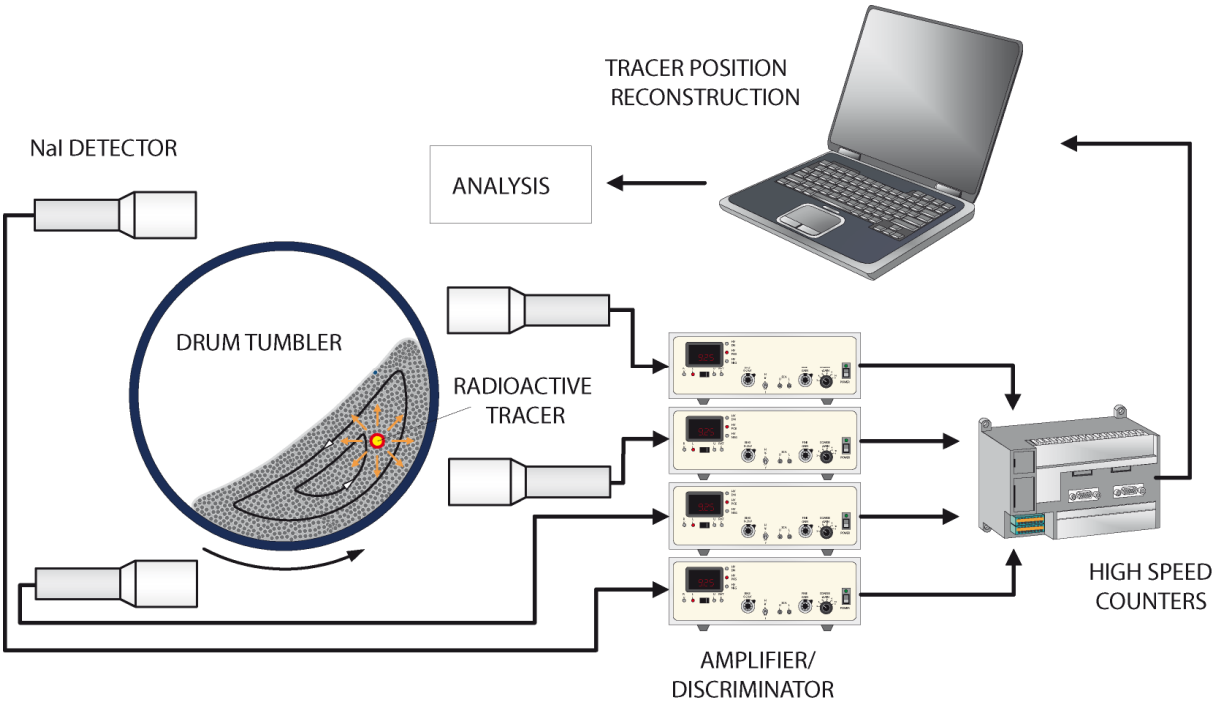

Figure 5-1 Typical RPT setup. Sodium iodide (NaI) scintillation detectors are strategically placed around the system of interest. They are connected to amplifiers/discriminators for signal adjustments. The latter are connected to high-speed counter cards which transfer the information to a data acquisition system.

The latest progress achieved in the field of RPT has been on extending the traditional RPT in order to take into account systems with irregular moving boundaries (Doucet, Bertrand, et al., 2008), as well as on integrating into an RPT program and applying the so-called Monte Carlo N-Particle code version 5 (MCNP5) (Mosorov & Abdullah, 2011). MCNP5 is an internationally recognized code to analyze neutron and γ-ray transport, developed and maintained by the Los Alamos National Laboratory ("MCNP User Manual, Version 5," 2003). It has the advantage over current traditional RPT codes to treat a wider range of γ-ray interactions and transport phenomena.

5.2.2.2 Motivation

Even though the experimental application of the RPT technique is rather straightforward, obtaining highly reliable and quality data may prove to be extremely difficult. Several factors will inevitably affect the gathered data and/or the efficiency of the tracer particle position reconstruction step. Such factors can be organized into two categories; they are either related to the RPT technique hardware or the experimental setup and conditions. More specifically, the hardware of the RPT technique refers to the tracer particle and the data acquisition system, which includes the scintillation detectors, the amplifiers/discriminators as well as the high-speed counters. Table 5-2 presents some of these factors.

Table 5-2 Factors affecting the quality of RPT data

Hardware	
Tracer particle	Isotope type Strength (activity) Size Shape
Scintillation detectors	Crystal size Crystal shape Crystal material General conditions: • Age • Defects • Damages
Experimental setup and conditions	
Setup	Number of available detectors Maximum number of detectors that can be used Detector position
Conditions	Sampling time Inhomogeneous media Flow regime

Tracer particle strength and isotope type as well as detector crystal size, shape and material are all important factors that were extensively studied by Roy et al. (2002). Their impact on the RPT technique resolution and sensitivity as well as their optimal choices are thoroughly analyzed and well explained in that paper. The effect of the sampling time was also studied by Godfroy et al. (1997) and Mostoufi et al. (2003).

Using a numerical analysis, Roy et al. (2002) also presented guidelines and analyzed practical scenarios to help position detectors efficiently. The optimum hardware was chosen to perform their analysis, which they restricted to a system consisting of an ideal axisymmetric geometry (i.e. vertical cylinder) as well as a limited set of detector configurations. However, several reasons can explain why the optimal hardware cannot be used in practice. Such reasons may be related, for instance, to the specific objectives of the study to be carried out (Alizadeh, Dubé, et

al., 2013) or the hydrodynamics to be captured (Dubé, Alizadeh, Chaouki, & Bertrand, 2013). To our knowledge, the impact of the experimental setup and conditions on detector positioning has never been thoroughly studied.

In this article, a numerical optimization strategy to determine an optimal set of detector positions and orientations, given a set of constraints or specifications that are either related to the detectors, tracer particle and/or experimental setup, is presented and applied. In the next section, the concepts behind RPT are briefly presented. The optimization strategy (i.e. the objective function, the optimization algorithm and its implementation) is then described in detail followed by a verification and validation of this strategy using test cases with known analytical solutions. The optimization program is also tested in a case similar to the one discussed by Roy et al. (2002). Finally, the strategy is applied in a situation where experimental conditions influence detector positioning. The limitations and drawbacks of the optimization strategy are discussed through these applications.

5.2.3 RPT basics

The fundamentals of the RPT are recalled here.

5.2.3.1 Phenomenological model

For a nonparalyzable counting system, the phenomenological relation between the number of gamma ray photons received and effectively counted by a scintillation detector and the position of the emission source is given by (Knoll, 2000; Tsoulfanidis, 2011):

$$C\left(\vec{x}\right) = \frac{T\nu A\phi\xi\left(\vec{x}\right)}{1+\tau\nu A\phi\xi\left(\vec{x}\right)} \tag{5.1}$$

where T is the sampling period (s), ν the number of distinct energy γ-rays emitted by the source, A the activity of the source (Bq), τ the detector dead-time (s), ξ the detector absolute efficiency, C the number of photons counted by the detector and $\vec{x}$ the position of the emission source (m). ϕ is the fraction of the energy spectrum captured by the detector. Its value depends on the settings of the signal discriminator and is equal to the peak-to-total ratio only if the full-energy peak of the source is considered. The detector absolute efficiency (ξ) is given by:

$$\xi\left(\vec{x}\right)=\oiint_{\Omega}\rho_m\left(\vec{r}\right)\rho_d\left(\vec{r}\right)\left(\frac{\vec{r}d\vec{A}}{\left\|\vec{r}\right\|^3}\right) \tag{5.2}$$

where $\vec{r}$ is the vector starting from $\vec{x}$ and pointing in the direction of the detector surface, $d\vec{A}$ the normal vector of an element of area on the detector surface, Ω the solid angle subtended by the radiation and ρ_d and ρ_m the probability functions of the γ-ray interaction with the detector crystal and the phases present inside the system, respectively. These functions depend on the distance travelled by the γ-rays inside the detector and the matter as well as the energy of the emission. The detector efficiency can be rigorously evaluated using a Monte Carlo technique developed by Beam et al. (1978). This technique consists of tracking a large number of photon histories starting from the emission at the source up to the absorption within the detector. Using this technique, the equation to evaluate the detector efficiency is:

$$\xi\left(\vec{x}\right)=\lim_{n\to\infty}\frac{1}{n}\sum_{k=1}^{n}\Omega^k e^{-\mu_m l_m^k}\left(1-e^{-\mu_d l_d^k}\right) \tag{5.3}$$

where n is the number of photons emitted towards the detector, Ω^k the solid angle fraction of the kth photon, μ_d and μ_m the coefficients of total linear attenuation in the detector crystal and matter, respectively, and finally, l_d^k and l_m^k the lengths travelled by the kth photon inside the detector crystal and the matter, respectively. In other words, the detector efficiency is equivalent to a solid angle weighted by the probability that the γ-rays do not interact with the matter yet do interact with the detector crystal. Previous studies have suggested that a thousand photon histories are sufficient for a good approximation of the detector efficiency (Godfroy et al., 1997;

Larachi et al., 1994). In a typical RPT experiment, μ_m, τ and ϕ are all found using a calibration procedure while μ_d is taken from the literature.

5.2.3.2 Reconstruction algorithm

In order to reconstruct the tracer particle trajectory, a tetrahedral mesh of the studied system is first created. Then, using the phenomenological relation (Equation (5.1)), a theoretical count rate is associated with all nodes $P(x, y, z)$ of the mesh, for all detectors. These are known as detector count dictionaries. Using the experimental data collected (i.e. the count rate received by each detector), a search through all nodes is conducted in order to find the node P that satisfies:

$$\min_{P} \sum_{d=1}^{D} \left(\frac{C_d^m - C_d\left(P(x, y, z)\right)}{C_d^m + C_d\left(P(x, y, z)\right)} \right)^2 \tag{5.4}$$

where C_d^m and $C_d\left(P(x, y, z)\right)$ are respectively the experimental and theoretical count rates, and D is the total number of detectors. A further refining of the solution is performed by searching within each tetrahedron containing the node P found previously for a position $\vec{x}$ that satisfies:

$$\min_{\vec{x}} \sum_{d=1}^{D} \left(\frac{C_d^m - C_d\left(\vec{x}\right)}{C_d^m + C_d\left(\vec{x}\right)} \right)^2 \tag{5.5}$$

The values of $C_d\left(\vec{x}\right)$ are obtained by a linear interpolation using the computed values at the nodes of the corresponding tetrahedron. The positions $\vec{x}$ tested in this last minimization step are generated using an appropriate optimization algorithm.

5.2.4 Optimization strategy

The objective is to find the optimal position and orientation of a set of detectors given specific experimental conditions and/or restrictions. To achieve this goal, a suitable objective function and algorithm must be chosen.

5.2.4.1 Objective function

Like any experimental measurement technique, it is desirable to optimize its accuracy and precision. The RPT accuracy is partially associated with the phenomenological model used to link the tracer particle position to the measured counts of the detectors. This part of the accuracy essentially depends on the appropriateness of the model parameters (Equation (5.1)) as well as the computation of the detector efficiency (Equation (5.3)). It is generally recognized that, given the right parameters and a sufficient amount of photon histories, the model will be accurate. However, because of the probabilistic nature of the emission and counting processes, a single tracer particle position will result in a distribution of counts recorded. When the tracer particle position is reconstructed using a single measurement value of the count rate, it is assumed that this value corresponds to the mean value of the count distribution that would be recorded if multiple measurements were available. As can be seen in Figure 5-2a, if the measured count (C_M) is greater than the true mean corresponding to the real tracer particle position (C_T), a tracer particle position closer to the detector will be found.

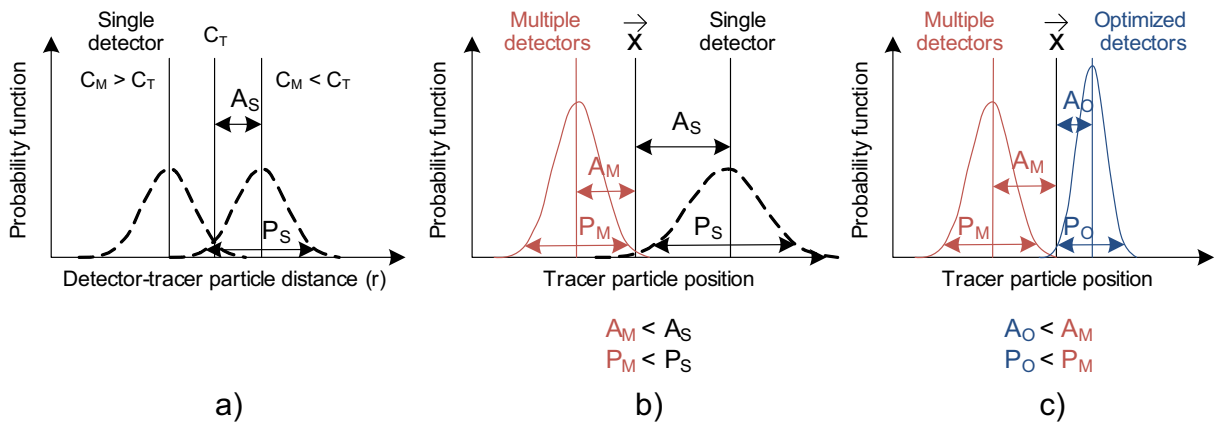

Figure 5-2 Schematic representation of the accuracy (A) and precision (P) of the RPT technique in the case of a) a single detector (AS, PS), b) multiple detectors (AM, PM) and c) multiple optimized detectors (AO, PO).

The statistical nature of the emission and counting processes is then responsible for the existence of a sphere of uncertainty surrounding the reconstructed position of the tracer particle. This sphere of uncertainty, which can also be viewed as the minimum distance that must exist between two neighboring positions of the tracer particle so that a detector can discriminate one from the other, is defined as the detector radial resolution (σ_r) (S. Roy, 2000). The RPT overall resolution can be reduced by purposely adding redundancy in the determination of the tracer particle position (i.e. by increasing the number of detector used) (see Figure 5-2b). In this study, it is supposed that the RPT overall resolution can also be further enhanced with an optimal configuration of detectors (see Figure 5-2c). From Figure 5-2, it is clear that the detector resolution gives an indication about both the precision (i.e. the degree to which repeated measurements of the tracer particle position under identical conditions give the same value) and the accuracy (i.e. the degree of closeness of the measurements of the tracer particle position to its true value) of the RPT technique. The finer the detector resolution is, the more accurate and precise the technique will be. It then follows that the objective function to solve the optimization problem at hand should ideally depend on the detector resolution.

In order to derive a relation for the detector radial resolution, Equation (5.1) needs to be reformulated. Lin et al. (1985) first approximated the relation between the number of counts recorded and the tracer particle position with:

$$C = C(r) \tag{5.6}$$

where

$$r = \sqrt{(x - x_0)^2 + (y - y_0)^2 + (z - z_0)^2} \tag{5.7}$$

is the distance between the tracer particle position (x, y, z) and the geometric center of the detector crystal (x_0, y_0, z_0). Figure 5-3a presents a graph of C for the distances r associated with the nodes of Figure 5-3b.

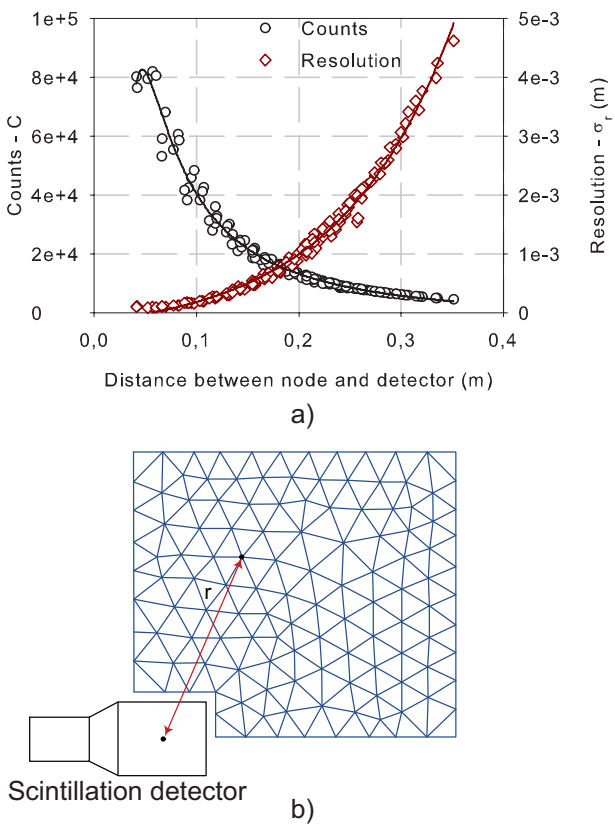

Figure 5-3 a) Counts and resolution for b) the nodes of a 2D plane surrounding a scintillation detector.

Using the error propagation formula, it can then be shown that:

$$\sigma_C = \frac{dC}{dr}\sigma_r \Rightarrow \sigma_r = \sigma_C \frac{dr}{dC} \tag{5.8}$$

where σ_C is the error associated with the count measurement. It corresponds to the standard deviation of the measured counts. Given that the counting process follows a Poisson distribution, the standard deviation in counts is simply the square root of the mean value of counts (Knoll, 2000). Roy et al. (2002) also established that the resolution in specific directions x, y, and z are given by:

$$\sigma_x = \sigma_C \frac{dx}{dC};\ \sigma_y = \sigma_C \frac{dy}{dC};\ \sigma_z = \sigma_C \frac{dz}{dC} \tag{5.9}$$

For reasons that will be explained in a subsequent section, it is desirable to evaluate the resolution in a specific direction using a function of the radial resolution. Using Equations (5.8) and (5.9), it can be shown that:

$$\sigma_x = \frac{\sigma_r}{\cos\alpha};\sigma_y = \frac{\sigma_r}{\cos\beta};\sigma_z = \frac{\sigma_r}{\cos\gamma} \tag{5.10}$$

where $\cos\alpha$, $\cos\beta$ and $\cos\gamma$ are the direction cosines of the vector $\vec{r} = (x - x_0)\vec{i} + (y - y_0)\vec{j} + (z - z_0)\vec{k}$.

If multiple detectors are used, since the set of counts for all these detectors can be considered as independent measurements having unequal errors, the overall radial resolution σ_T can be obtained by:

$$\frac{1}{\sigma_T^2} = \sum_{d=1}^{D} \frac{1}{\sigma_{r,d}^2} \tag{5.11}$$

where D is the total number of detectors and $\sigma_{r,d}$ is the radial resolution of detector d as calculated by Equation (5.8). Similarly, the overall resolution in specific direction x, y or z is obtained by Equation (5.11) and the appropriate axial resolution $(\sigma_{x,d}, \sigma_{y,d}\ or\ \sigma_{z,d})$ instead of the

radial resolution $\left(\sigma_{r,d}\right)$. The choice of the objective function depends on the problem. In this work, two objective functions were used and are presented in Section 5.2.5.

5.2.4.2 Optimization algorithm

5.2.4.2.1 Description

Several factors restrict the choice of the appropriate optimization algorithm to solve this optimization problem. Due to the phenomenological model (Equation (5.1)) and its stochastic component (i.e. the Monte Carlo technique used), it is not possible to have an accurate estimation of the objective function derivatives. Its stochastic component also means that the objective function will lack smoothness. Moreover, two successive evaluations of the objective function will generally provide two different results. It is also expected that the objective function contains many local optima. Finally, as will be shown in a later section, the evaluation of the objective function for a single set of detector positions is computationally expensive. The optimization technique must then be able to search efficiently through a large region of possible solutions in order to find an optimal set of detector positions. The spectrum of readily available optimization methods to solve engineering problem is wide. Audet et al. (2008) presented a concise listing of the most popular and common ones used for chemical engineering applications. Unfortunately, as they mention, some of these optimization algorithms need to be adapted when dealing with nonsmooth functions, require a special procedure to evaluate the objective function at the domain boundaries, cannot treat problems with non-convex domains, require an intensive parameter tuning step to be efficient, or do not present rigorous theoretical convergence properties (Audet et al., 2008). However, one class of optimization methods, the direct search methods, can handle non-differentiable, non-linear, non-convex or disconnected problems (Lewis et al., 2000).

For all the above reasons, a direct search method was favored for this study. More precisely, a non gradient-based iterative Mesh Adaptive Direct Search (MADS) algorithm was used to solve

the optimization problem. This type of algorithm is used for minimizing a nonsmooth function $f:\mathbb{R}^n \to \mathbb{R} \cup \{+\infty\}$ under general nonsmooth constraints and essentially consists of three steps: 1) search, 2) poll and 3) update (Audet & Dennis, 2006). At the beginning of the algorithm, an initial mesh M_0 of size Δ_0^m representing a discretization of the solution domain and a feasible initial solution $x_0 \in \mathbb{R}^n$ are specified. Then, the algorithm uses a finite strategy to generate a list of trial points lying on the current mesh M_k of size Δ_k^m, seeking for a better incumbent solution, i.e. $x_{k+1} \in \Omega$ with $f_\Omega(x_{k+1}) < f_\Omega(x_k)$ (Step 1). If the search step fails to find an improved mesh point, the poll step is invoked (Step 2). In this step, the objective function f_Ω is evaluated at neighboring trial points lying on a frame P_k of size Δ_k^P. The frame is built in a way that $\Delta_k^m \le \Delta_k^P$. For this study, the poll directions are generated according to the ORTHOMADS instantiation of the MADS algorithm (Abramson, Audet, Dennis, & Le Digabel, 2009). They are orthogonal and deterministic thereby ensuring a better reproducibility of the algorithm as well as minimizing the risk of having a large unexplored region of possible solutions. Finally, for the last step, if the search and poll step fails to find a better solution, the mesh size is reduced and step 1 is performed again from the current incumbent solution x_k. However, if either the search or poll step is successful, the mesh size is increased and step 1 is performed again from the new incumbent solution x_{k+1}. It must be noted that the optimization mesh and frame are only conceptual and are not actually constructed. More details about the MADS algorithm can be found in Audet and Dennis Jr. (2006), Abramson et al. (2009) and Audet et al. (2010).

5.2.4.2.2 Implementation in RPT software

NOMAD, a C++ implementation of the MADS algorithm (Abramson et al., 2012; Le Digabel, 2011), is used in this study. It is directly integrated into the RPT software developed at Ecole Polytechnique de Montreal. Figure 5-4 presents the algorithm of the entire optimization strategy.

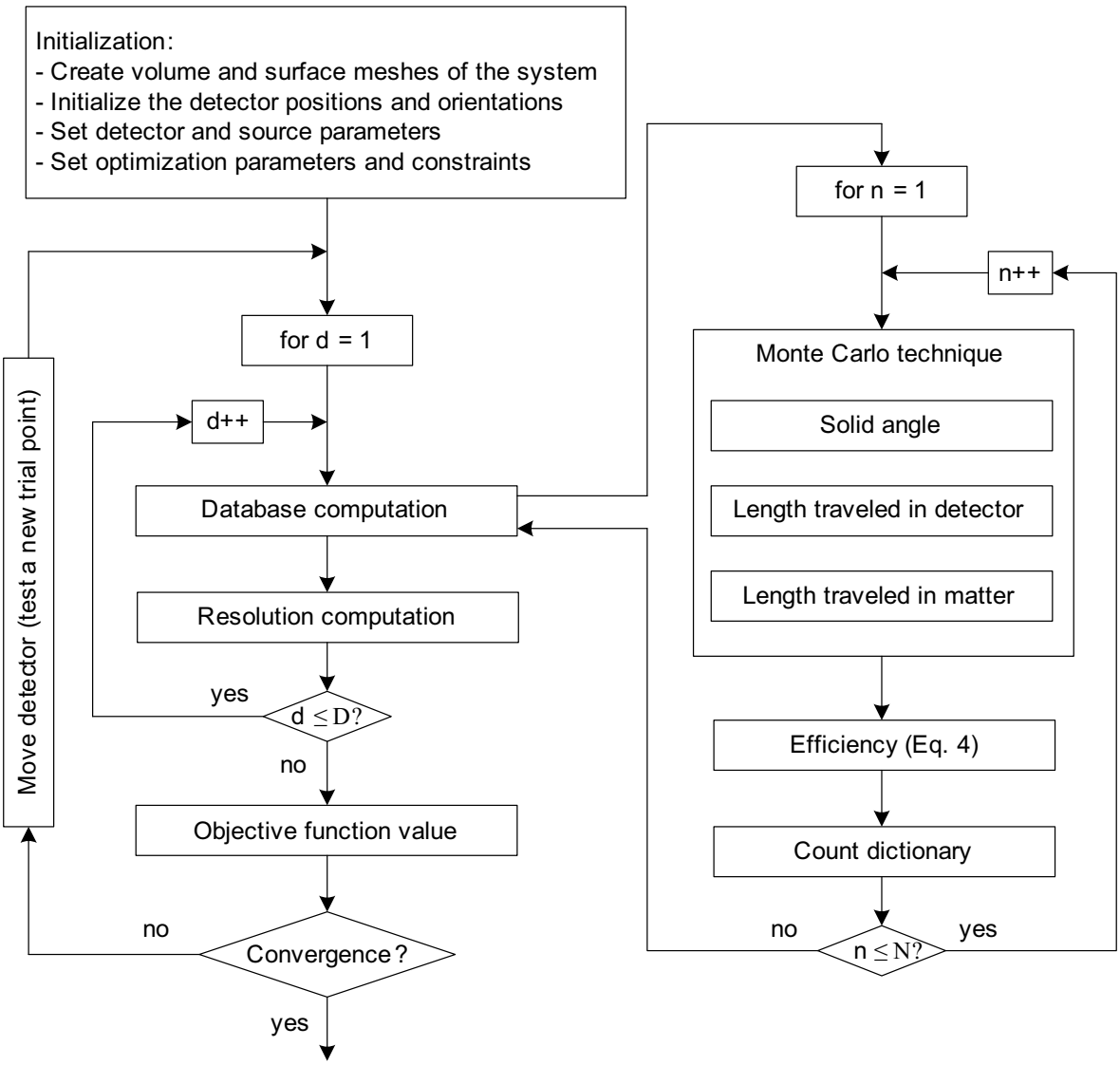

Figure 5-4 Optimization strategy algorithm.

During the initialization phase, a tetrahedral mesh of the geometry is created, the initial positions and orientations of the detectors are specified and the parameters for the detectors (i.e. the dead-time (τ) and the photopeak-to-total ratio (ϕ)), the source (i.e. activity (A), coefficient of linear attenuation in the crystal (μ_d) and the matter (μ_m) and the number of γ-rays emitted (ν)), the experiment (i.e. the sampling period (T)) as well as those for the optimization algorithm (e.g. optimization constraints, convergence criteria, search direction specifications, etc.) are set. The

optimization constraints are also defined. In this study, they are mainly related to the positions of the detectors and are problem-dependent. These constraints are the following:

- no detectors can be oriented in such a way that γ-rays would enter through the back of the crystal;
- the minimum distance between a detector and the geometry must be higher or equal to the saturation length of a detector;

It must be noted that no restriction on the overlapping of detectors is imposed. There is no need to do so since overlapping detectors are never part of an optimal configuration. If the optimization is truly capable of finding an optimal configuration, it should never converge to a solution in which detectors overlap.

The specifications of the initialization phase are passed along to NOMAD. For a given set of detector positions and orientations, the databases related to each detector are computed. It consists of computing the efficiencies as well as the count dictionaries for every node n of the geometry and for all detectors d, using the Monte Carlo technique previously described. Using this information, NOMAD computes the overall resolution (Equation (5.11)) on every node. Then, the objective function is evaluated. If the convergence criterion has not been reached, a new trial point, issued from a list of trial points generated by NOMAD, is tested. This corresponds to moving the detectors. If the convergence criterion has been reached, NOMAD stops and gives the optimal set of detector positions and orientations found. It must be noted that, for all the applications considered in this work, no explicit convergence criterion was used, and NOMAD stopped as soon as the mesh size reached a minimum value $\left(\Delta_k^m \leq \Delta_{\min}^m\right)$.

5.2.4.3 Numerical computation of the objective function

The detector resolution is computed for every node of the volumetric mesh of the geometry created in the initialization phase of the strategy. Figure 5-5a displays an example of such computation.

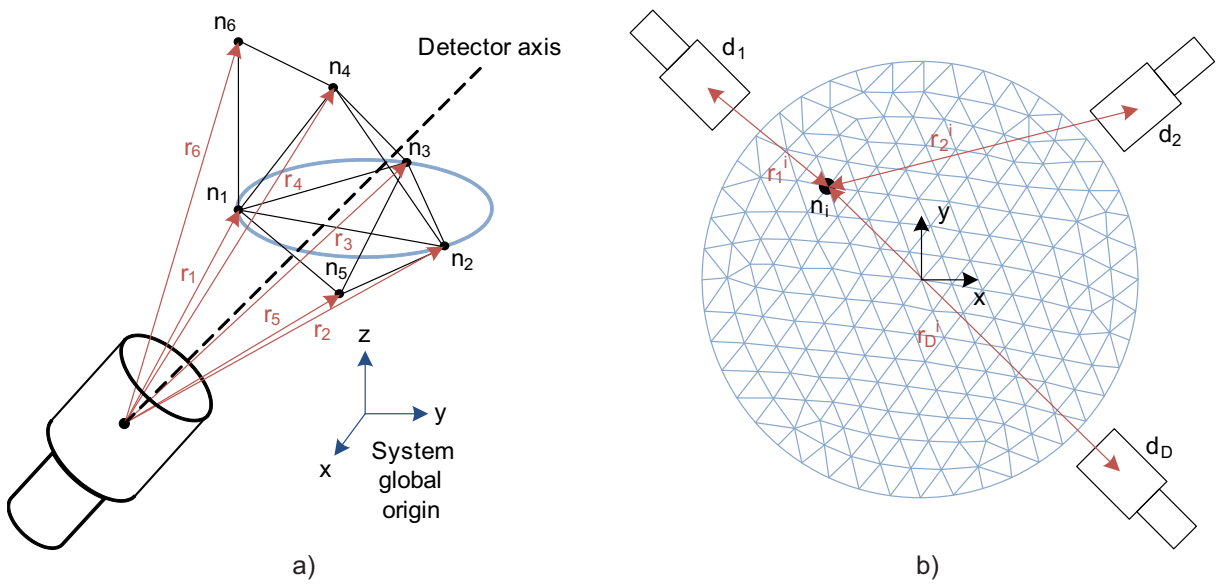

Figure 5-5 Schematic representation of a) the resolution computation and b) the weight computation.

For every detector d and for every neighboring node j of a node n, the radial resolution is approximated using the following relation:

$$\sigma_{r,d}^{nj} = \sqrt{C_n} \frac{|r_j - r_n|}{|C_j - C_n|} \tag{5.12}$$

The node radial resolution $\sigma_{r,n}^{d}$ is taken as the mean of the resolutions between node n and its neighbors:

$$\sigma_{r,d}^{n} = \frac{1}{m} \sum_{j=1}^{m} \sigma_{r,d}^{nj} \tag{5.13}$$

where m is the total number of neighboring nodes. Note that the node resolutions in specific directions x, y and z can be obtained using Equation (5.10), which brings into play the node radial resolution $\sigma_{r,n}^{d}$. The node overall resolution is then obtained using Equation (5.11):

$$\left(\frac{1}{\sigma_T^n}\right)^2 = \sum_{d=1}^{D} \left(\frac{1}{\sigma_{r,d}^n}\right)^2 \tag{5.14}$$

where D is the total number of detectors. In order to help the optimization strategy discriminate an optimal set of detector positions from non-optimal ones, it was decided to add a weight to the computed node overall resolutions. Ultimately, it is best that all nodes can be adequately reached by a sufficient amount of detectors. Since the resolution is mainly a function of the distance between the detectors and the tracer particle (Figure 5-3a), the use of weights based on this distance is natural. Figure 5-5b presents a schematic representation that explains how weights were calculated.

More precisely, the mean distance of node n from the D detectors is calculated as:

$$\overline{r^n} = \frac{1}{D}\sum_{d=1}^{D} r_d^n \tag{5.15}$$

Then, the weight w_n to apply on the overall resolution of node n is defined as:

$$w^n = \frac{\overline{r^n}}{\frac{1}{N}\sum_{i=n}^{N}\overline{r^n}} \tag{5.16}$$

where N is the total number of nodes. Clearly, this weight increases the overall resolution of poorly reached nodes and reduces the overall resolution of the strongly reached ones.

5.2.5 Results and discussion

The proposed optimization strategy is first assessed using a simple case with known optimal detector configurations. Next, it is applied to a three-dimensional axisymmetric vertical cylinder, which could represent a fluid bed, bubble column, riser or else. Finally, the optimization strategy is tested for a more complex system consisting of a partially filled cylindrical tumbler. All the parameters used to obtain the results presented in this section are shown in Table 5-3. It must be mentioned that the value chosen for μ_m is representative of the attenuation measured in systems filled with 3mm glass beads used in combination with a tracer particle made of scandium-46.

Table 5-3 Parameters of the optimization strategy

	Parameters	Value
Source	Nature	Scandium
	Number of γ-rays (ν)	2
	Energy of γ-rays	889 and 1120 keV
	Coefficient of total linear attenuation - crystal (μ_d)	21.477m^{-1}
	Coefficient of total linear attenuation - matter (μ_m)	10m^{-1}
	Activity (A)	2 000 000 Bq (54 μCi)
	Photopeak-to-total ratio (ϕ)	0.4
Detector	Crystal type	Sodium Iodide (NaI)
	Crystal length	7,62cm (3inches)
	Crystal diameter	7,62cm (3inches)
	Dead-time (τ)	1x10^{-5}s
	Sampling time (T)	1s

5.2.5.1 Assessment and validation of the optimization strategy

A two-dimensional circular geometry having a 0.10m radius and a 0.014m triangular mesh size (i.e. 208 nodes) is used to assess and validate the optimization strategy (see Figure 5-5b). It is known that, in this case, the optimal arrangement for the detectors is to put them as close as possible to the geometry and distribute them evenly around it. Therefore, the angle between each detector should be $360/D$. The optimization strategy is assessed with three, four and six detectors. The initial position of all detectors is the same; they are placed at a distance of 0.15m from the center of the geometry and at a counterclockwise 180° angle (θ) from the x-positive axis (see Figure 5-5b). Given the nature of this system, the optimization is done in cylindrical coordinates and the detectors are allowed to move in r and θ, r being the distance from the center of a detector crystal to the center of the geometry. The domains for each of these variables are specified in Table 5-4.

Table 5-4 Domains of the R and θ variables

Variable	Domain
R	$[0.110m,\ 0.200m]$
θ	$[0°,\ 360°[$

It must be mentioned that periodic boundary conditions are used for θ. Moreover, the geometry is considered empty since it is two-dimensional. Consequently, the length l_m traveled by a photon does not need to be computed by the Monte Carlo technique and is set to zero. In other words, there is no attenuation of the γ-rays inside the geometry.

The objective function used in this case is simply:

$$\max_n \left(w^n \sigma_T^n \right) \tag{5.17}$$

In other words, the optimization strategy seeks to minimize the maximum weighted overall resolution. It can already be noticed that an infinite number of solutions exist. While the angles at which the detectors are placed by the optimization strategy are not unique, the optimal angle between each pair of consecutive detectors should be $360/D$.

Table 5-5 displays the results obtained for three, four and six detectors. More precisely, the number of NOMAD evaluations needed to reach the convergence criterion, the final value of the objective function, the distance of each detector to the center of the geometry (R) and the angles (θ_{ij}) between the pairs of consecutive detectors i and j are presented. In all three cases, the results are for ten runs of the optimization strategy and the uncertainties are the standard deviations.

Table 5-5 Optimization results for three, four and six detectors

Number of detectors	3	4	6
Number of NOMAD evaluations	422 ± 27	539 ± 40	875 ± 68
Objective function value	$3.87\text{x}10^{-4} \pm 3\text{x}10^{-6}$	$3.00\text{x}10^{-4} \pm 3\text{x}10^{-6}$	$2.57\text{x}10^{-4} \pm 4\text{x}10^{-6}$
Distance from the geometry (R)	R_1= 0.1118 ± 0.0025m R_2= 0.1129 ± 0.0029m R_3= 0.1114 ± 0.0028m	R_1= 0.1117 ± 0.0028m R_2= 0.1122 ± 0.0027m R_3= 0.1115 ± 0.0022m R_4= 0.1120 ± 0.0020m	R_1= 0.1115 ± 0.0023m R_2= 0.1125 ± 0.0026m R_3= 0.1113 ± 0.0020m R_4= 0.1118 ± 0.0021m R_5= 0.1121 ± 0.0027m R_6= 0.1116 ± 0.0029m
Angle between two consecutive detectors	θ_{12}=120.5 ± 2.3° θ_{23}=119.1 ± 2.0° θ_{31}=120.4 ± 2.2°	θ_{12}=90.2 ± 2.4° θ_{23}=89.6 ± 2.8° θ_{34}=90.8 ± 2.6° θ_{41}=89.4 ± 2.1°	θ_{12}=53.3 ± 14.2° θ_{23}=54.9 ± 12.0° θ_{34}=53.0 ± 12.6° θ_{45}=67.3 ± 15.7° θ_{56}=54.5 ± 15.8° θ_{61}=67.0 ± 14.6°

It is noteworthy that, in all cases, the optimization strategy invariably brings the detectors close to the geometry, less than 3mm $\left(R = 0.113m\right)$ from its boundary $\left(R_{\min} = 0.110m\right)$, corresponding to the saturation length of the detector. This result complies with the graph of Figure 5-3a.

A closer look at the evolution of the objective function value with respect to the number of NOMAD evaluations performed for ten runs of the strategy in the case of three detectors is displayed in Figure 5-6a. One can notice that the objective function value levels off after approximately 150 NOMAD evaluations. This means that, even though the strategy needs 422 ± 27 NOMAD evaluations to reach the convergence criterion $\left(\Delta_k^m \leq \Delta_{\min}^m\right)$, less than half of these iterations would suffice to find an optimal configuration for the detectors. This is likewise observed in the case of four and six detectors. Figure 5-6b presents the probability of finding a detector in a particular range of θ, in the case of a three-detector optimization. To obtain this figure, the optimization strategy was launched one hundred times. It can be observed that each

detector has comparable probabilities of being anywhere around the domain. Again, similar results were obtained in the case of four and six detectors.

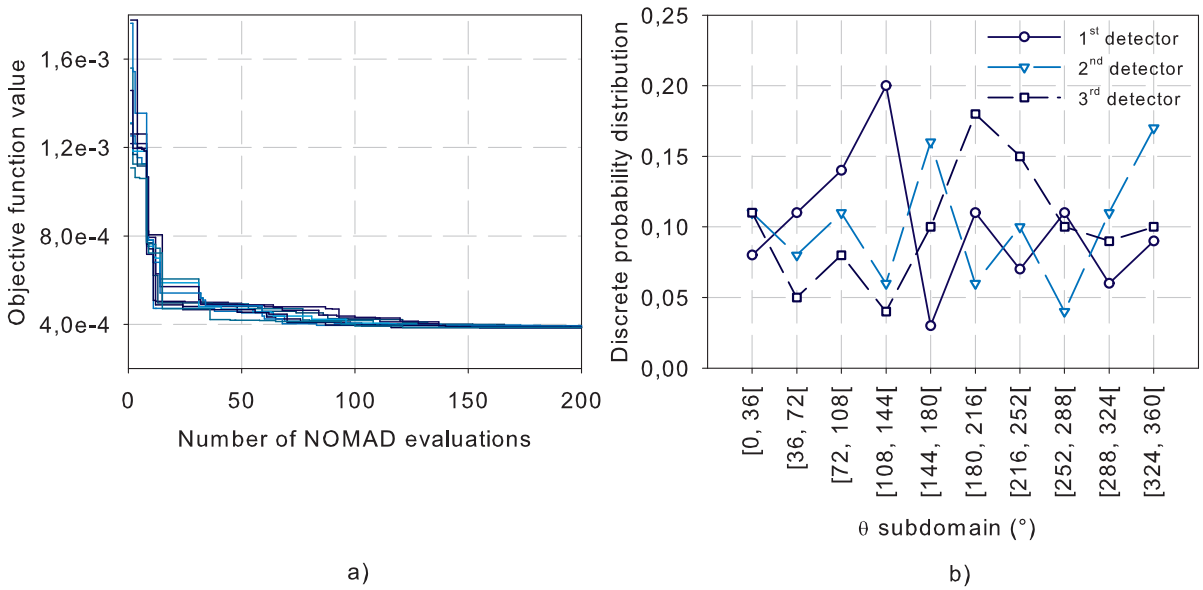

Figure 5-6 a) Objective function evolution with respect to the number of NOMAD evaluations for ten runs of the optimization strategy and b) probability distribution of θ for one hundred runs of the optimization strategy and three detectors.

In the case of three and four detectors, the angles between two consecutive detectors are very close to $360/D$, the errors varying between 2° and 3° (Table 5-5). However, the optimization procedure is less efficient when six detectors are involved, with angles between 53° and 67°, and an uncertainty between 12° and 16°. This can be explained by Figure 5-7, which displays the evolution of the maximum overall resolution with respect to the number of detectors. The optimal configuration for the detectors was used to compute this quantity and each point represents the mean value obtained following ten runs of the database computation part of the optimization strategy. Not surprisingly, the maximum overall resolution converges to zero if an infinite number of detectors is used because of the presence of a convergent series in Equation (5.14). Most importantly, one may notice that, above four detectors, the maximum overall resolution stops decreasing significantly with a further increase in the number of detectors. This loss of

sensitivity of the objective function, combined with the use of a Monte Carlo technique to compute the count dictionaries, means that it will become increasingly difficult for the optimization algorithm to find an optimal configuration as the number of detectors increases. This behaviour, which is due to the fact that the objective function only depends on the overall resolution, is an important limitation of the optimization strategy.

In order to grasp a better understanding of the RPT performance, one has to take into account both the overall resolution and the sensitivity in the system as well as the way the data are post-processed.

The sensitivity corresponds to the fractional change in counts C that will be registered following a small change in the tracer particle position. For a single detector, it is given by (S. Roy, 2000):

$$S_r = \frac{1}{C}\frac{dC}{dr} = \frac{d\ln C}{dr} \tag{5.18}$$

When N detectors are used, the overall sensitivity S_T is obtained with the following relation:

$$S_T^2 = \sum_{d=1}^{N} S_{r,d}^2 \tag{5.19}$$

As shown in Figure 5-7, , the minimum overall sensitivity continues to increase significantly with an increase in the number of detectors. This suggests that it would be better to use as many detectors as possible for an RPT experiment, even though the resolution stops decreasing significantly after a certain amount of detectors. However, one should keep in mind that the RPT data are generally analyzed by projecting the tracer particle trajectory on an Eulerian grid that is either two-dimensional or three-dimentional. The number of times that the tracer particle is found in each cell of the grid and the resulting mean velocity vectors can then be computed. To ensure that statistically reliable results are obtained, the grid size and the total experimental time are chosen in order to have between 200 and 1200 tracer particle occurrences in each cell. The practical consequence of these choices is that the overall sensitivity becomes irrelevant since it concerns the variation of the number of counts with respect to a change in position that is much smaller than the grid size. This means that equally good results can be obtained using fewer

detectors. In other word, a large number of detectors is not needed to ensure the convergence of the velocity field. The sensitivity curve presented in Figure 5-7 is therefore less important than the resolution curve when analyzing RPT results. Consequently, the objective function underlying limitation is adequate for the determination of an optimal number of detectors to be used for a specific RPT experiment.

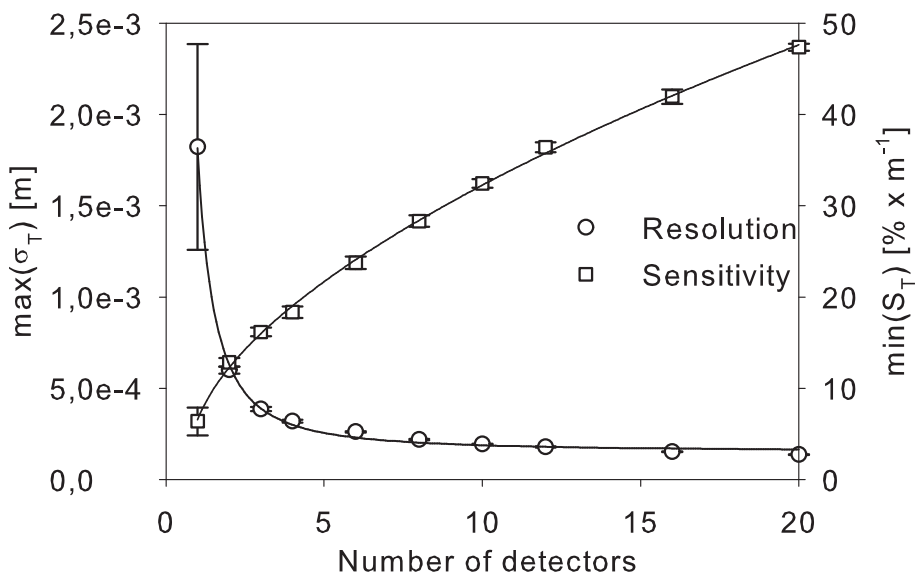

Figure 5-7 Evolution of the maximum resolution and minimum sensitivity for the circular geometry as the number of detectors increases.

5.2.5.2 Application of the optimization strategy to a three-dimensional axisymmetric system

The optimization strategy is next considered for the most frequently studied system using RPT: a vertical cylindrical column that can represent a fluid bed, bubble column, riser or else. In this study, the column has a 0.61m height, a 0.075m radius and is discretized by means of a tetrahedral mesh size of 0.015m (i.e. 3010 nodes). Given the limited size of this system, the

optimization is performed on the position and orientation of 6 detectors. Since the geometry is a vertical cylinder, the optimization is again realized in cylindrical coordinates. The optimized variables for each detector are the angular position θ and height z. The distance R, corresponding in this case to the distance between the geometrical center of the detector crystal to the central axis and the vertical cylinder, is not considered since the results presented in Section 5.2.5.1 showed that the optimization strategy invariably converges to its lowest value (i.e. the detector is as close as possible to the geometry). The domain of each variable is specified in Table 5-6.

Table 5-6 Domains of variables z and θ

Variable	Domain
z	$[-0.30m,\ 0.30m]$
θ	$[0°,\ 360°[$

Periodic boundary conditions are again used for θ. At the beginning of the optimization procedure, all the detectors have the same position and orientation; they are placed at a distance of 0.085m from the column axis, an angle θ of 180° and a height z of 0m. For this particular optimization, two objective functions are tested. The first one is the same as in the previous section, $\max_n\left(w^n\sigma_T^n\right)$, and the second one is:

$$\max_n\left(w^n\sigma_z^n\right) \tag{5.20}$$

With the second objective function, the optimization strategy attempts to minimize the maximum weighted axial resolution. This objective function is tested since many researchers have reported poor axial resolution and poor quality results in the direction of the cylinder axis (Godfroy et al., 1997; Larachi et al., 1994; Mostoufi et al., 2003).

5.2.5.2.1 Reference configurations

To evaluate the performance of the optimization strategy, reference detector configurations, which are deemed potentially adequate for RPT experiments, are introduced. They are presented in Figure 5-8 and are similar to those studied by Roy et al. (2002).

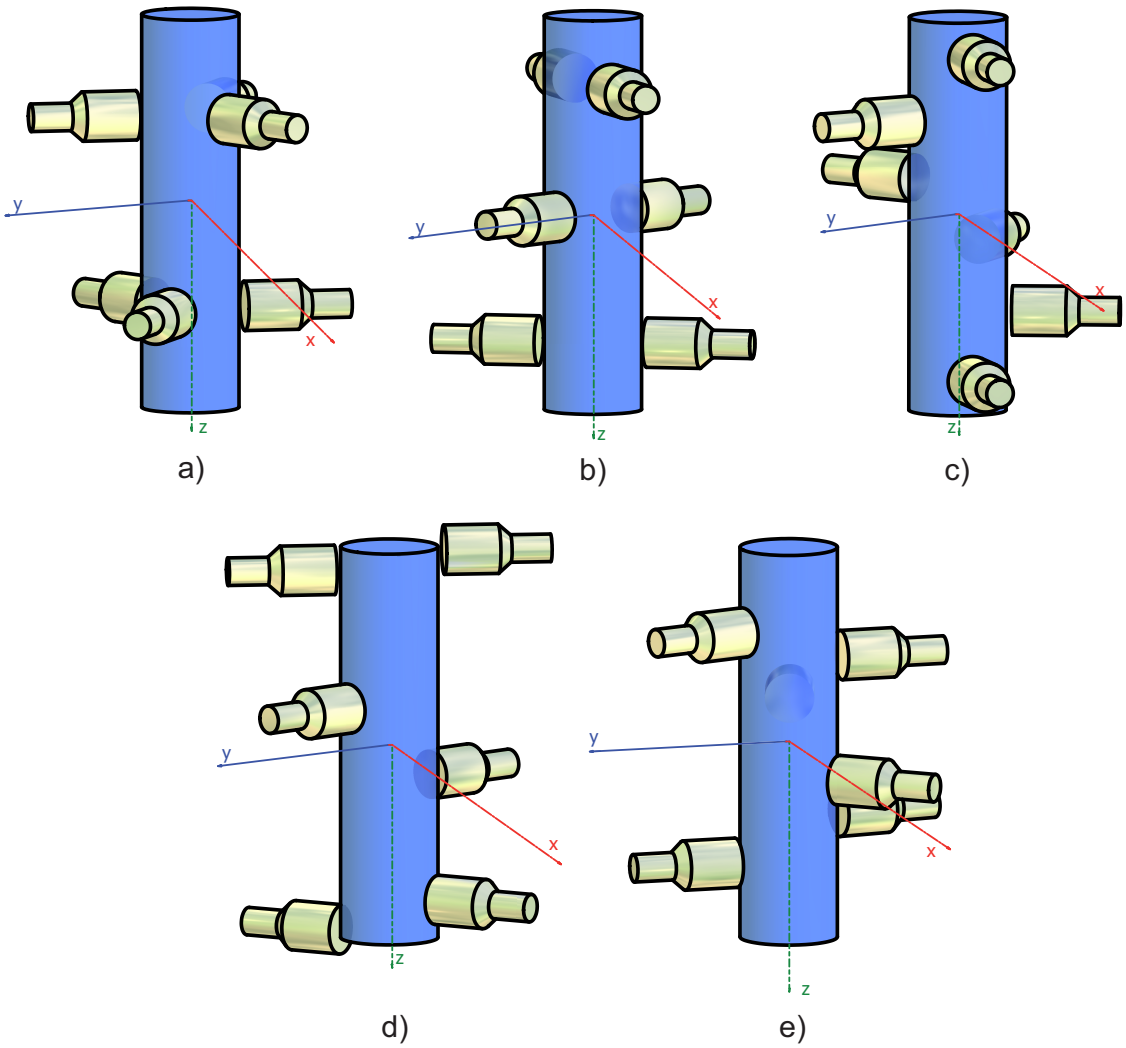

Figure 5-8 Reference configurations a) A b) B and c) C, and results obtained by the optimization procedure using as the objective function d) $\max\left(w^n\sigma_T^n\right)$ (configuration D) and e) $\max\left(w^n\sigma_z^n\right)$ (configuration E).

The performance of the optimization strategy will be evaluated by comparing the results to these reference configurations.

5.2.5.2.2 Optimization results

Figure 5-9 shows the evolution of both objective functions with the number of NOMAD evaluations performed for ten runs of the optimization strategy in each case. It can be readily observed that, for these objective functions, the optimization strategy invariably converges to a configuration having a lower objective function value than any of the reference cases. It took 1540 ± 144 evaluations and 1541 ± 127 evaluations, when using the first and second objective function respectively, for the optimization procedure to reach the convergence criterion. However, it took only 640 ± 198 and 680 ± 169 evaluations in each case to find an optimal configuration.

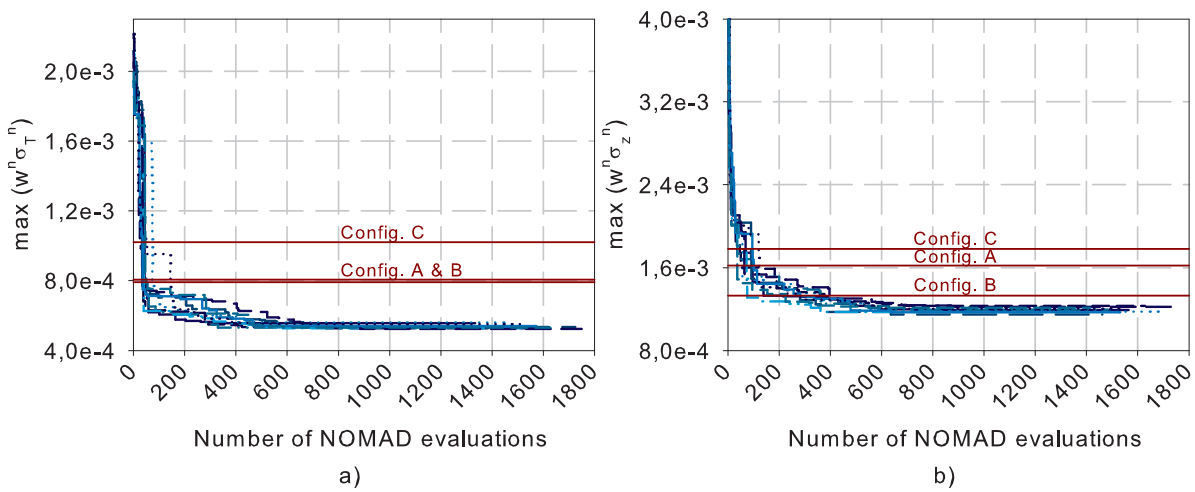

Figure 5-9 Objective function evolution with the number of NOMAD evaluations for ten runs of the optimization strategy using a) the first objective function $\left(\max\left(w^n\sigma_T^n\right)\right)$ and b) the second objective function $\left(\max\left(w^n\sigma_z^n\right)\right)$.

In order to gain a better understanding of the system overall radial and axial resolutions, the cumulative distribution function (CDF) of the corresponding non-weighted resolutions for the reference configurations as well as the best results obtained are displayed in Figure 5-10. In this figure, configurations D and E refer to the best results obtained using the first and second objective functions, respectively. It must be noted that, while these CDF curves do not indicate how the resolution varied with respect to position, it allows for a global assessment of it across the entire system.

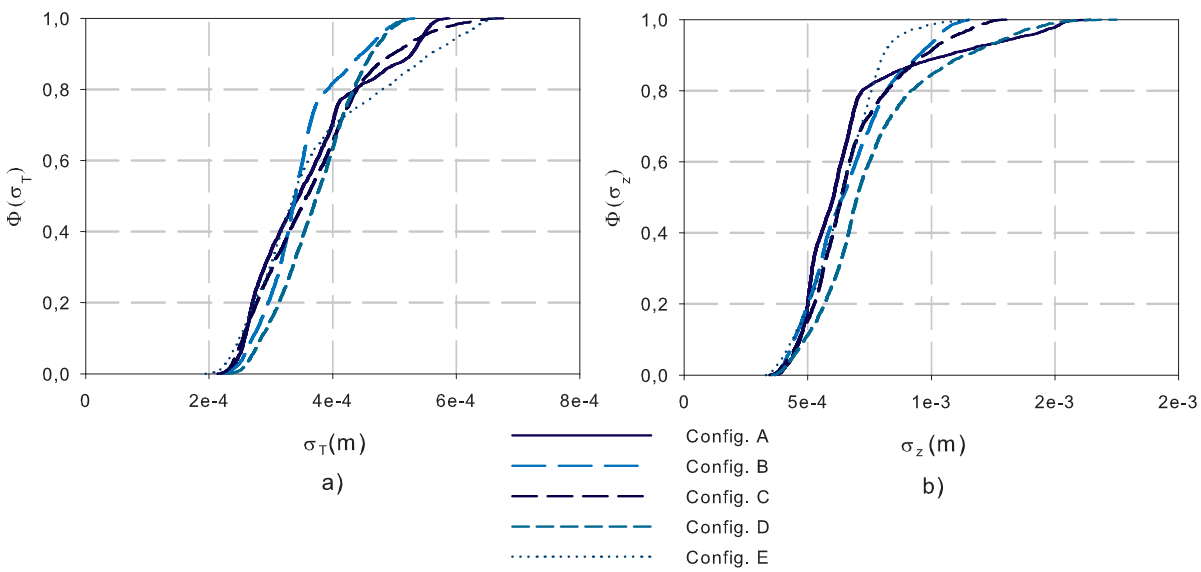

Figure 5-10 Cumulative distribution function of a) the overall radial resolution and b) the overall axial resolution.

In the case of the first objective function, it can be noticed that, even though the optimization strategy found a configuration (D) with a much lower objective function value than any of the reference cases (Figure 5-9a), the distribution of the overall radial resolution (σ_r) in the system is not significantly different from the one obtained with the reference configurations (Figure 5-10a). The maximum overall radial resolution is even similar to the one obtained using configuration B. In fact, a closer look at the three-dimensional representation of configuration D (Figure 5-8d) reveals that it is quite similar to configuration B: there are 3 planes of detectors, 2 detectors per plane, and an angle of 180° between the detectors on the same plane. The major

differences between configuration B and D are the angular step and the presence of a little gap in the height of the almost coplanar detectors. However, Figure 5-10a suggests that such small variations do not cause significant differences in the distribution of overall radial resolution in the system. B-like configurations were obtained 70% of the time when the optimization strategy was executed with the first objective function.

In the case of the second objective function, the optimization procedure found a configuration (E) that has an objective function value similar to the one obtained from configuration B (Figure 5-9b). In fact, the maximum value of the second objective function is just slightly lower than the one obtained from the reference configuration B (i.e. 1.14×10^{-3} m ± 3.2×10^{-5}m for E vs 1.33×10^{-3} m ± 3.1×10^{-5}m for B). However, it can be seen in Figure 5-10b that the overall axial resolution CDF of E diverges slightly from the one of configuration B, mainly in the higher axial resolution region. The three-dimensional representation of configuration E is presented in Figure 5-8e. Quite clearly, it cannot be associated with any single reference case; it is more a combination of configurations A and C. Furthermore, there are no co-planar detectors. In fact, it makes perfect sense to distribute the detectors over the axis of the column in order to minimize the overall axial resolution. This configuration obtained using the second objective function is significantly different from configuration D obtained using the first one. Similar configurations were obtained 40% of the time when this second objective function was used.

The results presented in this section show that the optimization strategy yields an optimal configuration that is specific to the objective function used. Moreover, even when starting with the worst possible initial configuration, the strategy is capable of finding optimal configurations that are similar to the reference configurations studied and recommended by Roy et al. (2002). Finally, the results presented here suggest that the optimization strategy should be run multiple times in order to get a good idea about an optimal configuration.

5.2.5.3 Application of the optimization strategy to a three-dimensional asymmetric system

The optimization strategy is applied here to a system consisting of a partially filled horizontal cylinder (Figure 5-11a). The radius and length of the cylinder as well as the tetrahedral mesh size used are respectively 0.127m, 0.381m and 0.015m (i.e. 4815 nodes). The cylinder has a filling fraction of 35vol% and it is assumed that the angle of the surface made by the matter is 23°, representing the cylinder in a slow rotating regime (i.e. rolling regime). This case is similar to the one studied by Alizadeh et al. (2013) and Dubé et al. (2013). The same number of detectors as in Dubé et al. (2013) is optimized (i.e. ten detectors). Since the geometry of the system consists of a horizontal cylinder, the optimization is again realized in cylindrical coordinates. As in the optimizations of Section 5.2.5.2, initially all detectors have exactly the same position and orientation; they are placed at a distance of 0.137m from the cylinder axis, an angle θ of 180° and a position z of 0m. Two types of optimization are considered. For the first optimization, the detectors are only allowed to move in z and θ (Figure 5-11b). They are not allowed to be placed at the extremities of the system. A total of 20 variables are optimized. For the second optimization, six detectors are only allowed to move in z and θ while the other four detectors, placed at the extremities, are allowed to move in R, z and θ (Figure 5-11c). These four detectors are also allowed to be inclined along the cylinder axis. To do so, an angle φ representing the angle between a detector axis and the cylinder axis is added as a variable to be optimized, leading to a total of 28 variables. For both optimization cases, a single objective function is tested: $\max_n \left(w^n \sigma_r^n \right)$, which is evaluated using only the mesh nodes inside the matter since it is only at these nodes that the tracer particle is found.

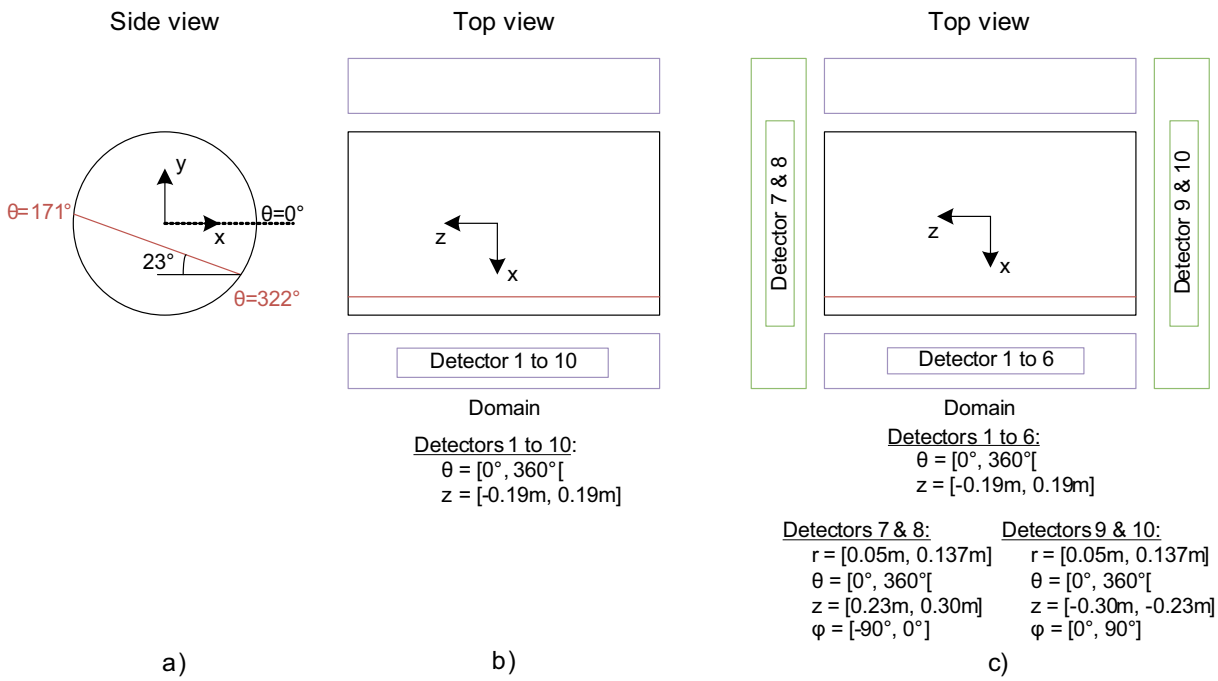

Figure 5-11 Schematic representation of the partially filled horizontal cylinder: a) side view, b) top view and variable domain for the first optimization test and c) top view and variable domain for the second optimization test.

5.2.5.3.1 Reference configuration

The results of the two optimization tests are compared to a reference configuration inspired by Alizadeh et al. (2013). In this configuration (F), presented in Figure 5-12a, eight detectors are placed at 120° from each other, six near the particle bed and two above it, and one detector is positioned at each end of the horizontal cylinder.

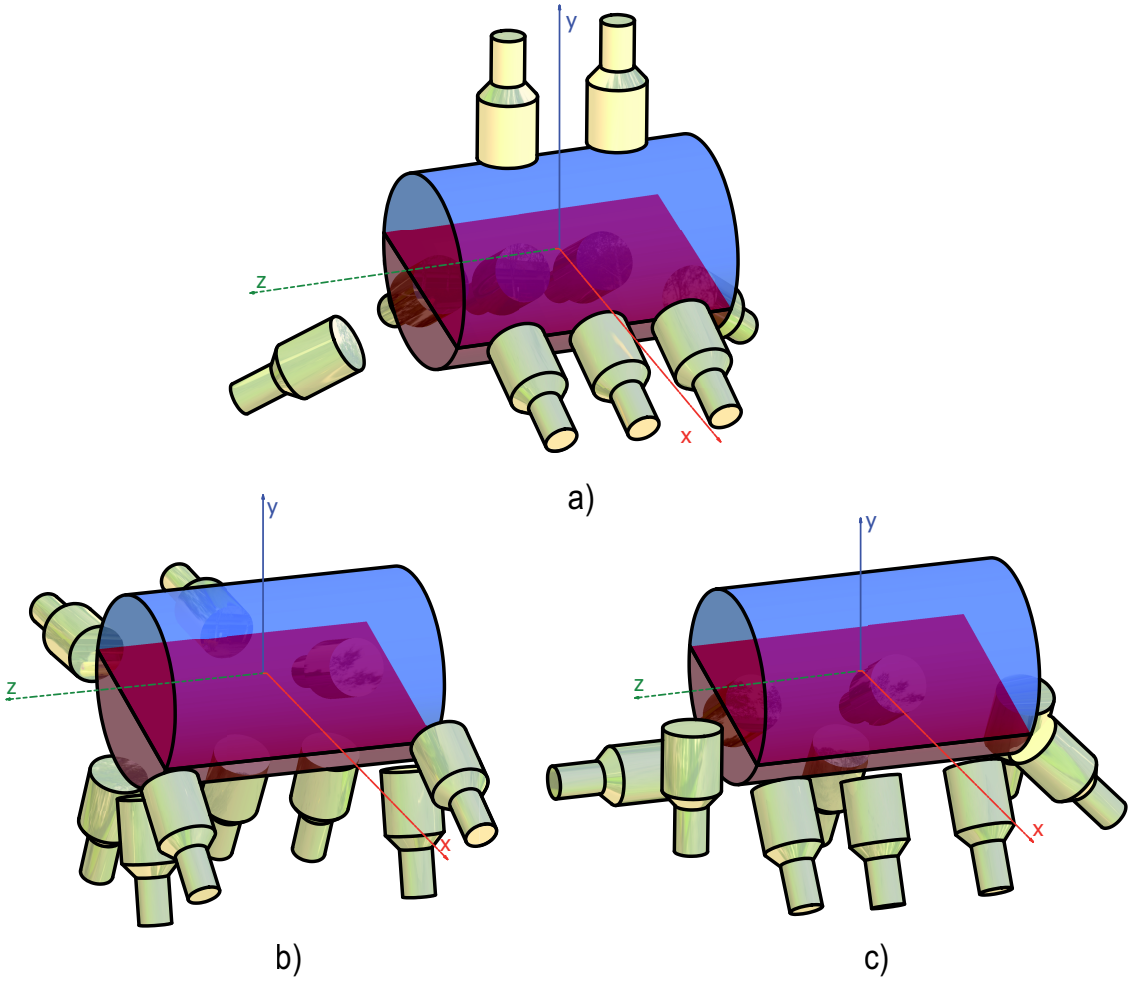

Figure 5-12 Three-dimensional representation of a) the reference configuration F, and the optimal configuration found by b) the first optimization test (configuration G) and c) the second optimization test (configuration H).

5.2.5.3.2 Optimization results

It must be noted that, since the second test is more complex and involves a greater number of variables, the CPU time required for convergence was significantly higher (Table 5-8). For this reason, the optimization procedure was successfully executed four times as opposed to ten for the first test. Moreover, it was manually stopped when the value of the objective function remained

unchanged for a relatively long period of time. The two optimization tests involved 2699 ± 522 and 3412 ± 1231 NOMAD evaluations, respectively, to either reach completion or be stopped manually. As can be seen in Table 5-7, the optimization strategy successfully found a configuration having a lower maximum overall weighted resolution than the reference configuration (F) for the first test. However, it is not the case for the second test where only two of the four trials resulted in a lower objective function value. The best configuration found in this latter case gave an objective function value of $3.21\text{x}10^{-4}$m ± $1.4\text{x}10^{-5}$m. This objective function value is not statistically different from the one that would be obtained using configuration F.

Table 5-7 Comparison of the average objective function values for the reference case and both optimization tests. Ten and four runs were performed for the first and second tests respectively.

	$\max\left(w^n \sigma_T^n\right)$
Configuration F	$3.31\text{x}10^{-4}$ m ± $4.6\text{x}10^{-6}$m
First optimization test	$2.98\text{x}10^{-4}$ m ± $2.1\text{x}10^{-5}$ m
Second optimization test	$3.48\text{x}10^{-4}$ m ± $4.1\text{x}10^{-5}$ m

The best configurations (i.e. the ones with the lowest objective function value) found by each optimization test (configuration G for the first one and H for the second one) are presented in Figure 5-12b and c. In Figure 5-12b, it can be noticed that all detectors are either placed below the surface of the bed or close to its limits. In fact, similar results were obtained for all ten runs of this first optimization test. This result is different from what was observed in Section 5.2.5.2, where the detectors were positioned all around the circumference of the vertical cylinder without any particular discrimination on θ. Figure 5-13, which presents the CDF of variable θ for all detectors of all ten trials, clearly indicates that the detectors have a uniform probability of being placed anywhere below or close to the surface of the bed. A similar conclusion can be drawn from the configurations of the second optimization test. This is expected since, for such a small fill level (35vol%), it is when the detectors are below the bed surface that the distance between them and any point inside the material is minimum, which results in a better resolution. More importantly, the results presented here show that the configuration found by the optimization strategy is specific to the experimental conditions.

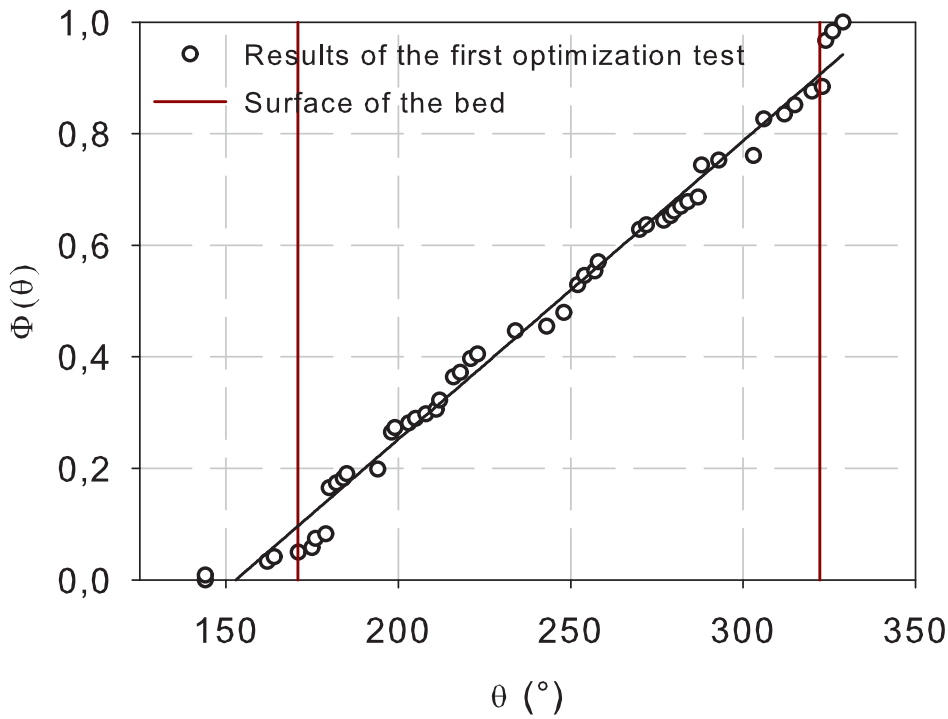

Figure 5-13 Cumulative distribution function of variable θ for the first optimization test.

Figure 5-12c shows that the second optimization test yields overlapping detectors at both extremities of the horizontal cylinder. This is a direct consequence of the decrease in sensitivity of the objective function as the number of detectors increases (see Figure 5-7). To confirm this, the database computation part of the strategy was run ten times using configuration H and a configuration identical to H but for which the overlap between the detectors was resolved. No significant differences were found between the corresponding objective function values (3.21×10^{-4}m ± 1.4×10^{-5}m for configuration H and 3.27×10^{-4}m ± 1.3×10^{-5}m for the modified configuration). It must be mentioned that the first optimization test also frequently yielded overlapping detectors. These results suggest that equally good results could be obtained using fewer detectors. To verify this, the evolution of the objective function with respect to the number of detectors was computed (Figure 5-14). Because of the computational time required to find an optimal position in this system (Table 5-8), the optimization strategy was not launched for every number of detectors tested. Instead, each point of Figure 5-14 represents the mean value obtained from ten runs of the database computation part of the algorithm when only the detectors having the best overall resolution of configuration H were kept. This means that the value for 10 detectors corresponds

to configuration H, that for 9 detectors corresponds to the 9 best detectors of configuration H, and so on. As can be observed in Figure 5-14, the maximum overall resolution stops decreasing significantly at 6 detectors, meaning that this amount of detectors should be sufficient to carry this type of experiment. Of course, this assumption would need to be verified experimentally.

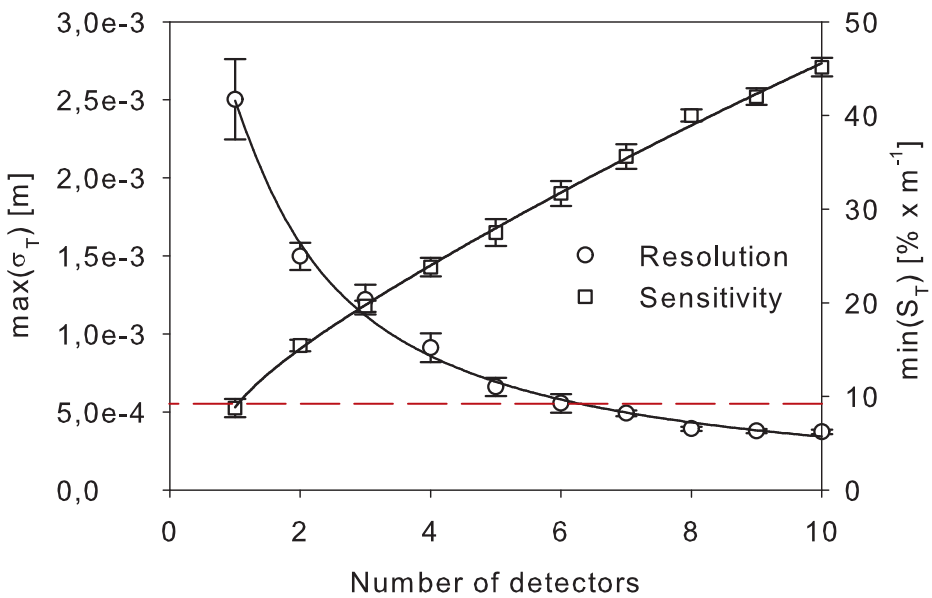

Figure 5-14 Evolution of the maximum resolution and minimum sensitivity for the partially filled horizontal cylinder as the number of detectors increases.

In order to thoroughly evaluate the two configurations (G and H) found by the optimization strategy, Figure 5-15 displays the CDF of the overall radial (σ_r) and axial (σ_z) resolutions in the system. It can be observed that both configurations result in a substantial improvement in the overall radial resolution with respect to reference configuration F (Figure 5-15a) while only configuration H yield a significant improvement in the axial resolution (Figure 5-15b). Hence, for this particular system (i.e. 35vol% filled cylindrical tumbler and ten detectors), it can be deduced that placing every detector below or close to the surface improves the overall radial resolution while placing at least two detectors at each extremity of the tumbler leads to a significant gain in overall axial resolution without causing any loss of overall radial resolution.

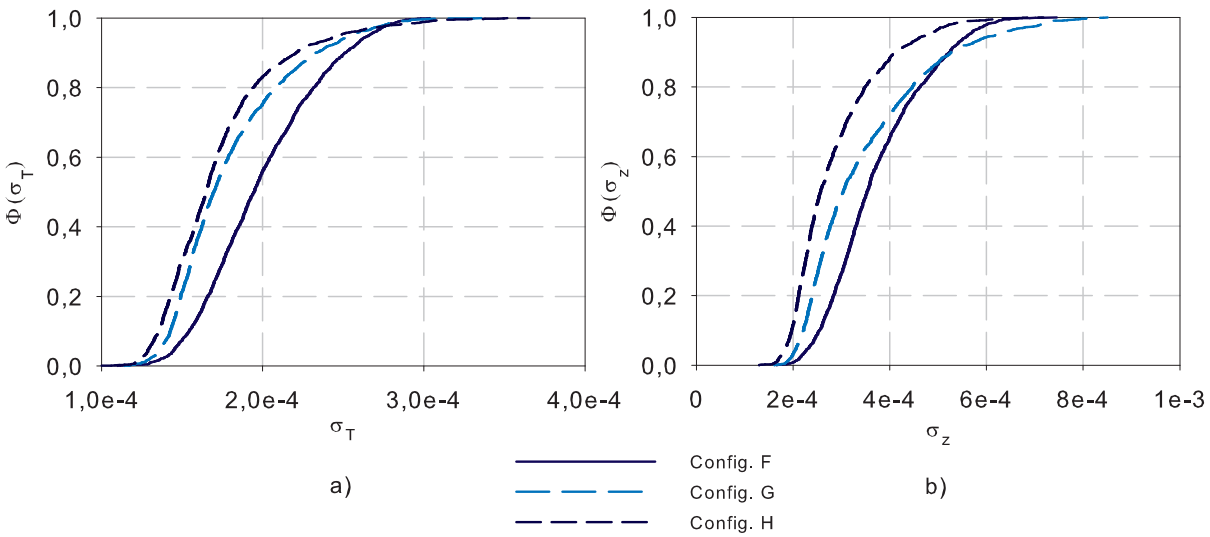

Figure 5-15 Cumulative distribution function of a) the overall radial resolution and b) the overall axial resolution.

Finally, configurations F and H were tested experimentally, with as much accuracy as possible, in order to assess the improvement obtained in the reconstruction of the tracer particle position throughout the system. It must be mentioned that the position of the two overlapping detectors of configuration H was slightly modified to remove the overlap. Two tracer particles were tested: a 3mm spherical glass bead and a large non-spherical particle, like the one presented in Figure 5-16a. These two tracer particles were used by Alizadeh et al. (2013) and Dubé et al. (2013), respectively. In each instance, the cylindrical tumbler was filled with particles identical to the tracer particle. The tracer particle was placed at five different known locations. The positions tested, which are presented in Figure 5-16b and c, were chosen to cover the whole axis of the cylinder. The error between the experimental and the reconstructed positions is simply the distance between them. Figure 5-17 presents the mean error for each configuration and both tracer particles. The error bars displayed represent the standard deviation. It can be noticed that the error is lower with the use of configuration H. The improvement is more significant in the case of the large non-spherical particle. The optimization strategy developed is then all the more useful when big tracer particles are used.

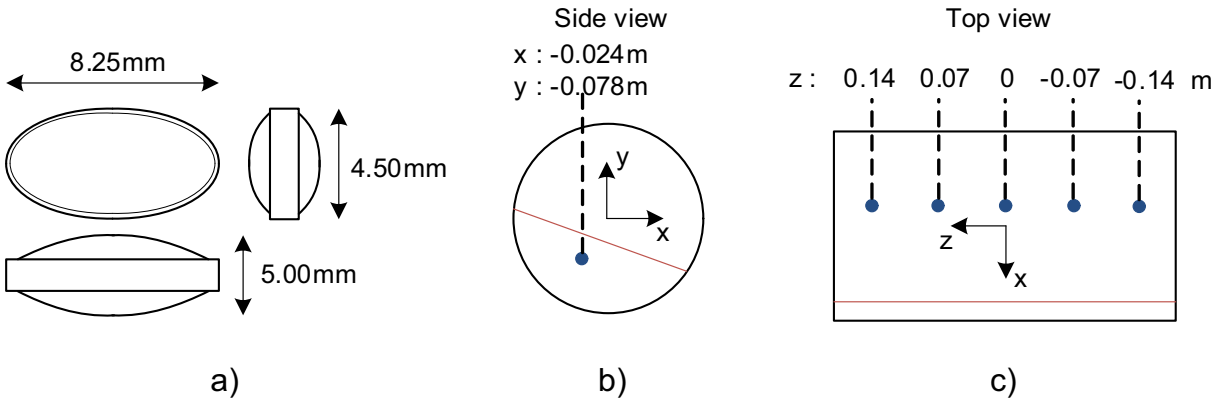

Figure 5-16 Schematic representation of a) the large non-spherical tracer particle as well as b) the side view and c) top view for the five known locations tested.

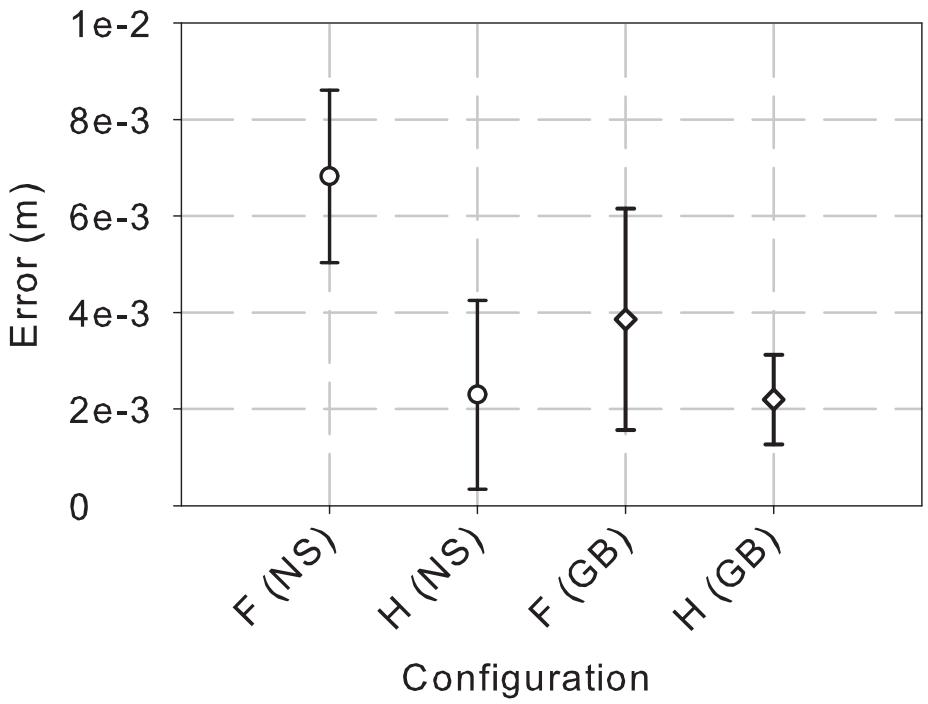

Figure 5-17 Mean error in the reconstruction of the fixed position of both tracer particle: 3mm glass bead (GB) and large non-spherical particle (NS).

5.2.5.4 Computational time

The optimizations performed for this study were done on three different computers. A summary of the computational time required to complete each optimization process is presented in Table 5-8.

Table 5-8 CPU time required to reach convergence for all the optimization tests of this study

Geometry (Number of nodes)	Number of detectors	Number of variables to optimize	CPU used for the computation	CPU time for convergence
Circle (208)	3	6	Intel® Core™ i7-2620M	3.9 ± 0.5 minutes
	4	8		6.1 ± 0.8 minutes
	6	12		12.3 ± 1.7 minutes
Vertical cylinder (3010)	6	12	Intel® Xeon® E5620	7.8 ± 1.7 hours
Horizontal cylinder (4815)	10	20	Intel® Core® i7-3820	3.3 ± 0.9 days
	10	28		10.2 ± 0.1 days

It can be noticed that the computations become increasingly expensive as the number of nodes, detectors and variables increase. The most complex case requires approximately 10 days of computational time to converge. The optimization strategy has a tremendous amount of data to process and dozens of variables to optimize. Some modifications could be made to improve the optimization strategy performance. For example, the use of a cache for detector count dictionaries would provide a substantial gain in computational time at the cost of memory usage. Further work could also be done on the data structure used to speed up the computation of the length traveled in the matter for photon the histories. Structures such as regular and non-regular space binning data constructs (grid, octree) could also be employed to speed up the computation of ray-volumetric mesh intersections.

Advances in computing technologies such as massively parallel processors (GPUs) could help further reduce the computational time. The data domain of the various steps of the optimization strategy described in Figure 5-4 is highly suitable for computational parallelization. The database

computation is essentially an embarrassingly parallel problem where each photon history used in the Monte Carlo technique can be computed independently with a minimum of intertask communication. As shown in Table 5-9, the critical path is the computation of the length traveled in the matter by the photons and the parallelization of this part of the optimization strategy would provide an interesting speedup.

While much of the computation on different parts of the data domain can be done in parallel, the use of massively parallel processors is not trivial. Indeed, many issues need to be addressed in order to implement an efficient parallel code: the amount of parallelism, the size of the parallel tasks, the frequency and nature of intertask communication, the synchronization and the appropriate use of parallel code constructs in the optimization strategy context (Hennessy, Patterson, & Arpaci-Dusseau, 2007; Kirk & Hwu, 2010). Work has already started in our group in order to overcome such issues and achieve an appropriate compromise between computational efficiency and level of parallelism.

Table 5-9 Breakdown of the computational time

Step of the optimization strategy	CPU Time per iteration (%)
Length traveled in the matter	88.3%
NOMAD	5.3%
Length traveled in the detector	3.4%
Solid angle	1.7%
Other functions	0.6%
Efficiency and count dictionary	0.5%
Resolution	<0.1%
Objective function	<0.1%

5.2.6 Conclusion

An optimization strategy was developed and applied to find an optimal set of scintillation detector positions and orientations used in the RPT technique, given many constraints and

specifications that are either related to the detectors, the tracer particle and/or the experimental setup. This strategy uses the detector overall resolution as an objective function, with the aim of minimizing the maximum overall radial or axial resolution in the system, as well as NOMAD, a C++ implementation of the MADS algorithm, as the optimization algorithm. Following its validation, the optimization strategy was applied to a three-dimensional axisymmetric system (i.e. a vertical cylinder, which could represent a fluid bed, bubble column, riser or else) and a system consisting of a partially filled cylindrical tumbler. In particular, for the first application, the strategy was observed to converge to configurations similar to the ones suggested by Roy et al. (2002), while, for the second one, the experimental application of guidelines gained by the optimization strategy was shown to lead to a significant reduction in the error made when reconstructing the fixed position of a large tracer particle.

The results of this work showed that the proposed optimization strategy is sensitive to both the type of objective function used and the experimental conditions. In fact, the lack of sensitivity of an objective function that depends only on the overall resolution can limit the application of this optimization strategy. A more sensitive objective function would be needed to overcome this issue. However, this same limitation could be used in practice to determine an optimal number of detectors for a specific RPT experiments. Moreover, it was found that the optimization strategy may have to be run multiple times in order to clearly identify an optimal configuration. It was also found that, depending on the complexity of the problem (e.g. domains of the different variables, number of variables, etc.), the technique could take up to several days to converge to an optimal configuration. Substantial improvements would be needed as regards the computational efficiency of the underlying algorithm in order to make it readily applicable to bigger and more complex systems. Work on the parallelization of the optimization strategy has already started in order to overcome this issue. Finally, for the optimizations performed in this study, all the detectors had exactly the same properties (e.g. crystal shape and crystal size, dead-time, saturation length, etc.). It must be mentioned that, even though it was not applied here, the proposed strategy could easily handle detectors having significantly different properties.

5.2.7 Acknowledgements

The financial support of PRAXAIR Inc. and the Natural Sciences and Engineering Council of Canada (NSERC) is gratefully acknowledged. The authors are thankful to Sebastian Le Digabel, assistant professor in the department of Mathematical and Industrial Engineering, for his help and support on the use of NOMAD, and to Greg Kennedy, adjunct professor in the department of Engineering Physics, for his insightful advice on RPT. The authors also thank Ebrahim Alizadeh for the images of the three-dimensional representation of the detectors configuration.

5.2.8 References

Abramson, M.A., Audet, C., Couture, G., Dennis, J.E.J., Le Digabel, S., Tribes, C.: The NOMAD Project. In. Software available at http://www.gerad.ca/nomad, (2012)

Abramson, M.A., Audet, C., Dennis, J.E., Jr., Le Digabel, S.: ORTHOMADS: a deterministic MADS instance with orthogonal directions. SIAM Journal on Optimization **20**(2), 948-966 (2009). doi:10.1137/080716980

Alizadeh, E., Dubé, O., Bertrand, F., Chaouki, J.: Characterization of Mixing and Size Segregation in a Rotating Drum by a Particle Tracking Method. AIChE Journal, n/a-n/a (2013). doi:10.1002/aic.13982

Audet, C., Bechard, V., Chaouki, J.: Spent potliner treatment process optimization using a MADS algorithm. Optimization and Engineering **9**(2), 143-160 (2008). doi:10.1007/s11081-007-9030-2

Audet, C., Dennis, J.E.J.: Mesh adaptive direct search algorithms for constrained optimization. SIAM Journal on Optimization **17**(1), 188-217 (2006). doi:10.1137/040603371

Audet, C., Dennis, J.E.J., Le Digabel, S.: Globalization strategies for mesh adaptive direct search. Computational Optimization and Applications **46**, 193-215 (2010). doi:10.1007/s10589-009-9266-1

Beam, G.B., Wielopolski, L., Gardner, R.P., Verghese, K.: Monte Carlo calculation of efficiencies of right-circular cylindrical NaI detectors for arbitrarily located point sources. Nuclear Instruments and Methods **154**(3), 501-508 (1978)

Bhusarapu, S., Al-Dahhan, M.H., Dudukovic, M.P.: Solids flow mapping in a gas-solid riser: Mean holdup and velocity fields. Powder Technology **163**(1-2), 98-123 (2006). doi:10.1016/j.powtec.2006.01.013

Cassanello, M., Larachi, F., Legros, R., Chaouki, J.: Solids dynamics from experimental trajectory time-series of a single particle motion in gas-spouted beds. Chemical Engineering Science **54**(13-14), 2545-2554 (1999). doi:10.1016/s0009-2509(98)00468-0

Cassanello, M., Larachi, F., Marie, M.-N., Guy, C., Chaouki, J.: Experimental characterization of the solid phase chaotic dynamics in three-phase fluidization. Industrial and Engineering Chemistry Research **34**(9), 2971-2980 (1995)

Cassanello, M.C., Fraguio, M.S., Larachi, F., Chaouki, J.: Flow regime transition pointers in three-phase fluidized beds inferred from a solid tracer trajectory. Chemical Engineering and Processing **45**(5), 350-358 (2006). doi:10.1016/j.cep.2005.10.001

Devanathan, N., Moslemian, D., Dudukovic, M.P.: Flow mapping in bubble columns using CARPT. Chemical Engineering Science **45**(8), 2285-2291 (1990). doi:10.1016/0009-2509(90)80107-p

Djeridane, T., Larachi, F., Roy, D., Chaouki, J., Legros, R.: Investigation of the mean and turbulent particle velocity fields in a spouted bed using radioactive particle tracking. Canadian Journal of Chemical Engineering **76**(2), 190-195 (1998)

Doucet, J., Bertrand, F., Chaouki, J.: An extended radioactive particle tracking method for systems with irregular moving boundaries. Powder Technology **181**(2), 195-204 (2008)

Dubé, O., Alizadeh, E., Chaouki, J., Bertrand, F.: Dynamics of non-spherical particles in a rotating drum. Submitted to Chemical Engineering Science (2013)

Fraguio, M.S., Cassanello, M.C., Larachi, F., Chaouki, J.: Flow regime transition pointers in three-phase fluidized beds inferred from a solid tracer trajectory. Chemical Engineering and Processing **45**(5), 350-358 (2006). doi:10.1016/j.cep.2005.10.001

Fraguio, M.S., Cassanello, M.C., Larachi, F., Limtrakul, S., Dudukovic, M.: Classifying flow regimes in three-phase fluidized beds from CARPT experiments. Chemical Engineering Science **62**(24), 7523-7529 (2007). doi:10.1016/j.ces.2007.08.039

Godfroy, L., Larachi, F., Kennedy, G., Grandjean, B., Chaouki, J.: On-line flow visualization in multiphase reactors using neural networks. Applied Radiation and Isotopes **48**(2), 225-235 (1997)

Hennessy, J.L., Patterson, D.A., Arpaci-Dusseau, A.C.: Computer architecture : a quantitative approach, 4th ed. Elsevier Morgan Kaufmann, Amsterdam (2007)

Khanna, P., Pugsley, T., Tanfara, H., Dumont, H.: Radioactive particle tracking in a lab-scale conical fluidized bed dryer containing pharmaceutical granule. Canadian Journal of Chemical Engineering **86**(3), 563-570 (2008). doi:10.1002/cjce.20073

Kiared, K., Larachi, F., Cassanello, M., Chaouki, J.: Flow structure of the solids in a three-dimensional liquid fluidized bed. Industrial and Engineering Chemistry Research **36**(11), 4695-4704 (1997a)

Kiared, K., Larachi, F., Chaouki, J., Guy, C.: Mean and turbulent particle velocity in the fully developed region of a three-phase fluidized bed. Chemical Engineering and Technology **22**(8), 683-689 (1999)

Kiared, K., Larachi, F., Guy, C., Chaouki, J.: Trajectory length and residence-time distributions of the solids in three-phase fluidized beds. Chemical Engineering Science **52**, 3931-3939 (1997b)

Kirk, D.B., Hwu, W.-m.W.: Programming massively parallel processors : hands-on with CUDA. Morgan Kaufmann Publishers : Elsevier, Amsterdam (2010)

Knoll, G.F.: Radiation detection and measurement, 3rd ed. Wiley, New York ; Toronto (2000)

Larachi, F., Cassanello, M., Chaouki, J., Guy, C.: Flow structure of the solids in a 3-D gas-liquid-solid fluidized bed. AIChE Journal **42**(9), 2439-2452 (1996)

Larachi, F., Cassanello, M., Marie, M., Chaouki, J., Guy, C.: Solids circulation patterns in three-phase fluidized beds containing binary mixtures of particles as inferred from RPT. Chemical Engineering Research and Design **73**(A3), 263-268 (1995a)

Larachi, F., Chaouki, J., Kennedy, G.: 3-D mapping of solids flow fields in multiphase reactors with RPT. AIChE Journal **41**(2), 439-443 (1995b). doi:10.1002/aic.690410226

Larachi, F., Grandjean, B.P.A., Chaouki, J.: Mixing and circulation of solids in spouted beds: Particle tracking and Monte Carlo emulation of the gross flow pattern. Chemical Engineering Science **58**(8), 1497-1507 (2003). doi:10.1016/s0009-2509(02)00676-0

Larachi, F., Kennedy, G., Chaouki, J.: A -ray detection system for 3-D particle tracking in multiphase reactors. Nuclear Instruments and Methods in Physics Research, Section A (Accelerators, Spectrometers, Detectors and Associated Equipment) **A338**(2-3), 568-576 (1994)

Le Digabel, S.: Algorithm 909: NOMAD: Nonlinear Optimization with the MADS Algorithm. ACM Transactions on Mathematical Software **37**(4), 1-15 (2011)

Lefebvre, S., Guy, C., Chaouki, J.: A convective/dispersive solid phase mixing model for three-phase fluidized bed reactors: effect of dimensionless numbers. Chemical Engineering Science **62**(18-20), 4954-4962 (2007a). doi:10.1016/j.ces.2006.12.027

Lefebvre, S., Guy, C., Chaouki, J.: Solid phase hydrodynamics of three-phase fluidized beds-a convective/dispersive mixing model. Chemical Engineering Journal **133**(1-3), 85-95 (2007b). doi:10.1016/j.cej.2007.02.004

Lewis, R.M., Torczon, V., Trosset, M.W.: Direct search methods: Then and now. Journal of Computational and Applied Mathematics **124**(1-2), 191-207 (2000). doi:10.1016/s0377-0427(00)00423-4

Lin, J.S., Chen, M.M., Chao, B.T.: A novel radioactive particle tracking facility for measurement of solids motion in gas fluidized beds. AIChE Journal **31**(3), 465-473 (1985)

Mabrouk, R., Chaouki, J., Guy, C.: Effective drag coefficient investigation in the acceleration zone of an upward gas-solid flow. Chemical Engineering Science **62**(1-2), 318-327 (2007). doi:10.1016/j.ces.2006.08.055

MCNP User Manual, Version 5. Radiation Safety Information Computational Center (RSICC). Los Alamos National Laboratory, University of California, USA. http://mcnp-green-lanl.gov (2003)

Mosorov, V., Abdullah, J.: MCNP5 code in radioactive particle tracking. Applied Radiation and Isotopes **69**(9), 1287-1293 (2011)

Mostoufi, N., Kenned, G., Chaouki, J.: Decreasing the sampling time interval in radioactive particle tracking. Canadian Journal of Chemical Engineering **81**(1), 129-133 (2003)

Roy, D., Larachi, F., Legros, R., Chaouki, J.: Study of solid behavior in spouted beds using 3-D particle tracking. Canadian Journal of Chemical Engineering **72**(6), 945-952 (1994)

Roy, S.: Quantification of two-phase flow in liquid-solid risers. Washington University (2000)

Roy, S., Chen, J., Kumar, S.B., Al-Dahhan, M.H., Dudukovic, M.P.: Tomographic and particle tracking studies in a liquid-solid riser. Industrial and Engineering Chemistry Research **36**(11), 4666-4669 (1997)

Roy, S., Kemoun, A., Al-Dahhan, M.H., Dudukovic, M.P.: Experimental investigation of the hydrodynamics in a liquid-solid riser. AIChE Journal **51**(3), 802-835 (2005). doi:10.1002/aic.10447

Roy, S., Larachi, F., Al-Dahhan, M.H., Dudukovic, M.P.: Optimal design of radioactive particle tracking experiments for flow mapping in opaque multiphase reactors. Applied Radiation and Isotopes **56**(3), 485-503 (2002)

Salierno, G.L., Fraguio, M.S., Piovano, S., Cassanello, M., Cardona, M.A., Hojman, D., Somacal, H.: Bubble columns dynamics inferred from the motion of a radioactive tracer followed by axially aligned detectors. Chemical Engineering Journal (2012). doi:10.1016/j.cej.2012.06.150

Sheritt, R.G., Chaouki, J., Mehrotra, A.K., Behie, L.A.: Axial dispersion in the three-dimensional mixing of particles in a rotating drum reactor. Chemical Engineering Science **58**(2), 401-415 (2003). doi:10.1016/s0009-2509(02)00551-1

Tamadondar, M.R., Azizpour, H., Zarghami, R., Mostoufi, N., Chaouki, J.: Using particle trajectory for determining the fluidization regime in gas-solid fluidized beds. Advanced Powder Technology **23**(3), 349-351 (2012). doi:10.1016/j.apt.2011.04.012

Tsoulfanidis, N.: Measurement and detection of radiation, 3 ed. McGraw-Hill series in nuclear engineering. Hemisphere Pub. Corp. McGraw-Hill, Washington ; New York (2011)

Upadhyay, R.K., Roy, S.: Investigation of hydrodynamics of binary fluidized beds via radioactive particle tracking and dual-source densitometry. Canadian Journal of Chemical Engineering **88**(4), 601-610 (2010). doi:10.1002/cjce.20334

CHAPITRE 6 DYNAMIQUE DE PARTICULES NON-SPHÉRIQUES DANS UN CYLINDRE ROTATIF

6.1 Présentation de l'article

Soumis à *Chemical Engineering Science* en avril 2013.

Auteurs : Olivier Dubé, Ebrahim Alizadeh, Jamal Chaouki, François Bertrand.

Ce chapitre présente la caractérisation de la dynamique de particules non-sphériques à l'intérieur d'un cylindre rotatif.

6.2 Dynamics of Non-Spherical Particles in a Rotating Drum

6.2.1 Abstract

Considerable amount of experimental work has been performed to elucidate the behavior of granular flow inside a rotating drum and it has yet to be clearly understood. However, a majority of these investigations have involved spherical or nearly spherical particles. The extent of the experiments involving non-spherical particles previously carried out was limited by the experimental technique used for the investigation or the inability to single out the effect of the particle shape. In this work, the radioactive particle tracking technique (RPT) is adapted to follow large non-spherical particles inside a rotating drum. The particles consist of pharmaceutical tablets containing a suitable compound, thus enabling their use as a tracer particle. Three crucial aspects of particle dynamics inside a rotating drum are studied: residence time in the active and passive layers, mixing and segregation, as well as axial dispersion. The results obtained for non-

spherical particles are compared to those which would be predicted using models developed for spherical of nearly spherical particles. For the different shapes studied in this work, it is found that particles having an aspect ratio greater than two can lead to significant deviations in velocity profile and residence time. In addition, the mixing of different shaped particles is observed to lead to unexpected core segregation patterns. Lastly, it is found that the non-spherical particle higher degree of spatial orientation in the active layer leads to a lower axial dispersion coefficient than the ones obtained with spherical particles.

6.2.2 Introduction

Rotating drums are widely used to process granular materials in a great variety of industries such as pharmaceutical, food processing, polymer, ceramic, chemical, metallurgical, solid waste treatment, etc. Due to their adequate mixing and heat transfer efficiency (Descoins et al., 2005) as well as their ability to handle heterogeneous feedstock (Boateng, 1998), they are used in a broad range of processes which involves, for example, size reduction, sintering, mixing, drying, heating, cooling, chemical reactions or solid thermal decomposition (e.g. incineration, pyrolysis, combustion) operations. Heat and mass transfer, determined by solid transport and particulate mixing, control and/or limit these operations (Heydenrych et al., 2002; Liu et al., 2006; Mellmann, Specht, & Liu, 2004). The rotating drums are usually operated in the so-called rolling regime since it provides superior particle mixing, resulting in enhanced heat transfer (Fantozzi et al., 2007; S. Q. Li, Yan, Li, Chi, & Cen, 2002; Liu et al., 2006). This regime is characterized by two regions: a passive layer found near the cylinder wall, where particles move as a solid body, and an active layer, where the particles avalanche and cascade downward. It is widely accepted that mixing, segregation, heat transfer or other transport phenomena mainly occur in the active layer (Cheng, Zhou, Keat Tan, & Zhao, 2011; Ding et al., 2001; Ingram et al., 2005; Liu & Specht, 2010; Liu et al., 2006). Understanding the phenomena occurring inside rotating drums on a fundamental level is essential for optimal design and operation of this equipment (Heydenrych et al., 2002; Khakhar, McCarthy, Shinbrot, et al., 1997; Mellmann, 2001). In particular, characterizing the transverse flow of particles is of primary importance. Although rotating drums represent a relatively simple geometry, the granular flow occurring inside them is rather complex

(Boateng, 1998; Ding et al., 2002a; Ndiaye et al., 2010). If the particles are reagents and/or change size or shape over the course of the process, like in incineration, pyrolysis, sintering, combustion or size reduction operations, the problem becomes much more complex as new phenomena affecting the particle dynamics may occur.

Experimental studies of granular flow are tedious mainly because of the opaque nature of such materials. Nevertheless, a considerable amount of experimental work has been performed in order to elucidate the behavior of granular flow inside a rotating drum. To perform these investigations, a wide selection of experimental techniques, such as in situ bed freeze (Wightman & Muzzio, 1998), magnetic resonance imaging (MRI) (Hill et al., 1997; Kawaguchi, 2010; Nakagawa et al., 1993), fiber optics probe (Boateng & Barr, 1997), positron emission particle tracking (PEPT) (Ding et al., 2001; Ingram et al., 2005; Parker et al., 1997), particle image velocimetry (PIV) and particle tracking velocimetry (PTV) (Alexander et al., 2002; Felix, Falk, & D'Ortona, 2002, 2007; Jain et al., 2002; Jain, Ottino, & Lueptow, 2004; Mellmann et al., 2004; Thomas, 2000) and radioactive particle tracking (RPT) (Alizadeh, Dubé, et al., 2013; Sheritt et al., 2003), have been used. However, a majority of these investigations have involved spherical or nearly spherical particles. As it was previously mentioned, one advantage of rotating drums is their ability to handle varied feedstock, i.e. granular material having a wide distribution of size, density, shape, roughness or else. It has been known for quite some time now that the particle shape affects the dynamical properties (Ridgway & Rupp, 1971). The behavior of non-spherical particles differs from that of spherical particles in terms of their compaction efficiency, resistance to shear, dilation under shear, transfer of momentum between translational and angular motions as well as their ability to form arches and block the flow (Cleary, 2010). Experimental investigations of granular flow in rotating drums involving non-spherical particles drums are rather limited: Boateng and Barr (1997) used limestone and rice grains, Van Puyvelde et al. (2000) used shale, Woodle and Munro (1993) used particles made from and with ovoid, shell and tube shapes, Henein et al. (1983; 1985) used sand, limestone and gravel, and Ingram et al. (2005) used sand. In the pharmaceutical field, the dynamics of non-spherical particles is particularly of interest for particle and tablet coating applications, which are generally conveyed in a pan coater consisting of a rotating drum. Wilson and Crossman (1997) as well as Tobiska and Kleinebudde (2003) studied the effect of the tablet shape and size on the tablet film coating uniformity and

efficiency. While useful, the results and extent of these studies involving non-spherical particles were restricted by either the experimental technique used, the inability to single out the effect of the particle shape or the objectives of the study.

This work aims at investigating three crucial aspects of the particle dynamic inside a rotating drum containing non-spherical particles: the residence time in the active and passive layers, the mixing and segregation of these particles, and the axial dispersion. To do so, the radioactive particle tracking (RPT) technique was adapted to follow the motion of non-spherical particles, which are in fact non-spherical tablets suitably built to become radioactive tracer particles. The results obtained for the non-spherical particles are compared to models previously developed for spherical or nearly spherical particles.

6.2.3 Methodology

As previously mentioned, numerous non-intrusive experimental techniques have been used to study granular flow. In particular, PIV and/or PTV can solely provide information on flow at the bed surface or, if the rotating drum has a transparent side, flow under the surface. In the latter case, the flow measured is affected by the presence of the end wall as well as the material constituting it, and may not represent what is going on inside the particle bed. Using PIV and/or PTV is then limited to two-dimensional systems and properties like axial dispersion can hardly be quantified. MRI and PEPT can also be used though they present limitations on the size and constitution of the system that can be studied, not to mention they are also expensive. On the other hand, RPT does not present any limitations on the system size and is much cheaper than these two methods. However, its extension to a system having irregular moving boundaries is not trivial (Doucet, Bertrand, et al., 2008). This technique was used to carry out the investigations of this work since the rotating drum possesses simple moving boundaries. The next section briefly describes the RPT technique and the adaptations performed to apply it to this work.

6.2.3.1 RPT

RPT is a non-invasive experimental velocimetry and tomography technique that can be used to study the hydrodynamics inside a variety of systems. In this technique, the trajectory of a single tracer particle emitting isotropic γ-rays can be reconstructed using a phenomelogical model relating the number of γ-rays received and effectively counted by an array of scintillation detectors strategically placed around the system. Assuming a nonparalyzable counting RPT setup, the phenomenological relation linking the number of γ-rays C counted by a scintillation detector to the position $\vec{r}$ of the tracer particle is given by:

$$C\left(\vec{r}\right) = \frac{T\nu A\phi\zeta\left(\vec{r}\right)}{1+\tau\nu A\phi\zeta\left(\vec{r}\right)} \tag{6.1}$$

where T is the sampling period (s), ν the number of distinct energy γ-rays emitted by the source, A the activity of the source (Bq), τ the detector dead-time (s), ζ the detector absolute efficiency and ϕ the fraction of the energy spectrum captured by the detector. ζ is rigorously evaluated using a Monte Carlo technique developed by Beam et al. (1978). Following a calibration procedure, equation (6.1) is used to compute the detector count dictionaries, corresponding to theoretical count rates associated with specific positions inside the system.

In this study, the detectors were positioned according to guidelines coming from an optimization strategy to find an optimal configuration for detectors given specific experimental conditions, as developed by Dubé et al. (2013). Further details on the traditional application of the RPT technique can be found in Larachi et al. (1994), Roy et al. (2002) and Dubé et al. (2013).

Similar to Alizadeh, Dubé et al. (2013), this work uses a tracer particle containing the isotope ^{24}Na. This isotope emits two γ-rays at energy levels of 1.368 and 2.754 MeV, and has a relatively short half-life (14.95 hours). Explanations on why this particular isotope is used are provided in Section 6.2.3.2.1. To account for the short half-life, Alizadeh, Dubé et al. (2013) suggested using a second tracer particle having the same activity as the first tracer particle, placed

outside of the vessel, to monitor the source loss of activity throughout experiments. This method yielded satisfactory results when the tracer particle consisted of a 3mm to 6mm radius glass bead. However, since the count dictionaries with this strategy are corrected according to count values obtained from an emitting sentinel having a different specific absolute efficiency because it does not take into account the particle bed, the error in the tracer particle trajectory reconstruction increases with the experimental time. In this work, the decrease in activity is instead accounted for by introducing the equation for the isotope half-life in the phenomenological model (equation (6.1)):

$$A = A(t) = A_0 \exp\left(-\frac{t \ln(2)}{t_{1/2}}\right) \tag{6.2}$$

where t is the time elapsed since the beginning of the experiment, $t_{1/2}$ the half-life of the isotope and A_0 the activity of the tracer particle at the beginning of the experiment. The quality of each RPT experiment was assessed and, under the conditions of this work, the RPT technique was shown to be able to reconstruct a given tracer particle position with an accuracy of 2.5mm and a precision of 2.0mm.

6.2.3.2 Experiments

6.2.3.2.1 Material

One of the biggest challenges encountered when applying the RPT technique is how to build a tracer particle which has the exact same physical properties (e.g. density, mass, shape, etc.) as the material under study. When studying the effect of the particle shape on the hydrodynamics, the shape of the tracer particle is all the more important. In this study, pharmaceutical tablets were used to investigate non-spherical particle dynamics in a rotating drum. Pharmaceutical tablets were chosen for three main reasons. First, their composition can be controlled to some extent. Consequently, an isotope suitable for the RPT technique can easily be introduced in the powder

mixture used for manufacturing. Second, the mass and size of a given pharmaceutical tablet can be carefully controlled during the manufacturing process, thus ensuring that tablets are nearly identical. Finally, punches and dies of a broad range of shapes and sizes are readily available for tablet manufacturing.

The composition of the pharmaceutical tablets is presented in Table 6-1. The sodium contained in the sodium bicarbonate was used as the suitable isotope for the RPT technique. More precisely, the isotope ^{24}Na was produced from the sodium bicarbonate by means of the Slowpoke reactor of Ecole Polytechnique de Montreal. Sodium bicarbonate is the ideal choice for a sodium-based compound in that it possesses adequate flow and compression properties for the tableting process. The amount of sodium bicarbonate needed inside the tablets was dictated by a single criterion: the smallest tablet produced needs to reach an activity of 60 μCi (2.22MBq) in less than 20 minutes when activated in the Slowpoke nuclear reactor. This time limit is extremely relevant in order to avoid any changes in the physical properties of the tablets during the activation process. Computations revealed that a 40% concentration of sodium bicarbonate is sufficient to respect this criterion. Ultimately, it was decided to use an activity of 45 μCi (1.665MBq) for the experiments, therefore all tablets needed less than 12 minutes to complete their activation.

Table 6-1 Tablet composition

Components	Mass %
Sodium bicarbonate ($NaHCO_3$)	40%
Mannitol 100	29.75%
Avicel PH-200	29.75%
Magnesium stearate (MgSt)	0.5%

Five different pharmaceutical tablets were produced using a fully instrumented 10-station small-scale rotary tablet press KORSCH XL100 (KORSCH America Inc., South Easton, MA). Their shapes and dimensions are shown in Figure 6-1, and their properties are presented in Table 6-2. These shapes were chosen so as to cover various sphericities and aspect ratios, but also to have tablets with similar shapes yet different sizes in order to study mixing and segregation. For the

purpose of improving the shear resistance of the pharmaceutical tablets, a 2% weight Opadry® II-red coating (Colorcon®, West Point, PA) was applied on all tablets using a Vector LDCS pan coater (Freund-Vector Corporation, Marion, IA).

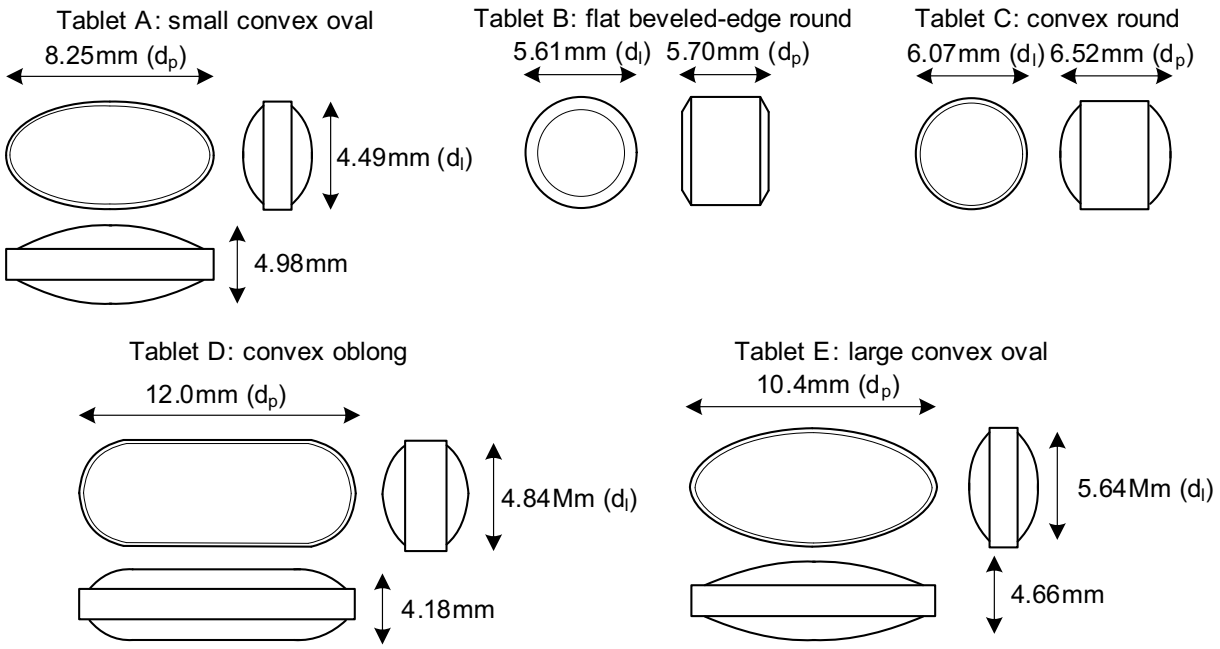

Figure 6-1 Schematic representation of the five tablets used in this study

Table 6-2 Tablet properties

Tablet	A	B	C	D	E
Mass, M (mg)	206.8 ± 2.1	219.8 ± 3.0	276.1 ± 3.7	280.1 ± 3.3	284.4 ± 3.1
Volume, V (mm^3)	147.2 ± 0.4	139.0 ± 0.8	169.0 ± 1.6	181.9 ± 1.3	220.9 ± 1.6
Surface, S (mm^2)	162.6 ± 0.5	143.2 ± 0.6	157.6 ± 1.1	176.1 ± 0.7	195.5 ± 1.3
Particle density, ρ_p (mg/mm^3)	1.40 ± 0.01	1.58 ± 0.02	1.63 ± 0.02	1.54 ± 0.02	1.29 ± 0.01
Bulk density, ρ_b (kg/m3)	1072 ± 3	1035 ± 3	1029 ± 2	968 ± 2	1031 ± 6
Sphericity	0.83	0.91	0.94	0.88	0.90
Aspect ratio	1.84	1.02	1.07	2.48	1.84

6.2.3.2.2 Design of experiments

The experiments performed for this study used a 16.8L rotating drum made from acrylic with a 0.3556m internal length and a 0.2413m internal diameter. A single filling fraction (35vol %) was used for all experiments. The mass of material put inside the rotating drum was based on the bulk density of the individual tablets. The design of experiments applied is presented in Table 6-3. The five different tablet shapes were tested individually and bi-disperse blends of tablets were also tested. The blends were chosen so as to study bi-disperse mixtures of mono-shaped tablets (i.e. mixtures made from tablets A-E and B-C), and bi-disperse mixtures of bi-shaped tablets (i.e. mixtures made from tablets C-D and C-E). These two kinds of mixture were chosen to represent cases when a varied feedstock is used or when changes in size (mono-shaped mixture) or shape (bi-shaped mixtures) occur over the course of the rotating drum operation. The blend compositions were chosen to represent situations where only a small fraction of the particle bed changes size or shape. Hence, these blends were composed of 85vol% of the bigger tablet and 15vol% of the smaller tablet. Moreover, in order to compare the non-spherical particle dynamics to the spherical one, three experiments involving spherical glass beads were performed. One

experiment involved mono-disperse 6mm glass beads (GB6 in Table 6-3) while the other two were a blend of 5mm and 6mm glass beads (GB56.5 and GB56.6 in Table 6-3). All the experiments were performed in the rolling regime given that it is the one used in most applications. Because of the tracer particle half-life (~15 hours), a 10RPM drum rotational speed was used to gather as much data as possible within one single experiment. Only one experiment was performed with at 5RPM to verify the effect of the drum rotational speed on the particle dynamics. Each experiment used a 10ms sampling period (T) and lasted at least 180 minutes, resulting in a total of 1 080 000 tracer particle positions. A total of eighteen experiments were performed.

Table 6-3 Design of experiments

Type	Experiment	Blend specification	Rotational speed (RPM)	Tracer particle
Mono-disperse	A	100vol% A	10	A
	B	100vol% B	10	B
	C	100vol% C	10	C
	D	100vol% D	10	D
	E	100vol% E	10	E
	GB6	100vol% 6mm	10	6mm
Bi-disperse	AE.A	15vol% A	10	A
	AE.E	85vol% E		E
	AE.A*	15vol% A	5	A
	AE.E*	85vol% E		E
	BC.B	15vol% B	10	B
	BC.C	85vol% C		C
	CD.C	15vol% C	10	C
	CD.D	85vol% D		D
	CE.C	15vol% C	10	C
	CE.E	85vol% E		E
	GB56.5	15vol% 5mm	10	5mm
	GB56.6	85vol% 6mm		6mm

* Indicates a rotational speed of 5 RPM.

6.2.4 Results and discussion

Three important characteristics of granular flow inside a rotating drum are presented and analyzed in this section: the residence time in the active and passive layers, the mixing and segregation of the particles and finally, the axial dispersion. The results of this study were obtained using the tracer particle trajectories acquired from the RPT experiments. Using such a trajectory, the tracer particle velocity was computed and projected onto an Eulerian grid. Given that the granular flow inside a rotating drum is essentially two-dimensional, a two-dimensional grid with a $2.5 \times 2.5\,mm^2$ cell size was used. To avoid any interference of the drum axial end walls, only the part of the tracer particle trajectory axially located in a 20cm region around the drum center was considered. It is believed that statistically reliable data was obtained since the tracer particle was found to pass anywhere between 200 and 1200 times in each cell.

Before going any further, the variables used subsequently must be defined. Figure 6-2 presents a schematic cross-section view of the drum. In this figure, it can be seen that the bed is composed of two different layers: a passive layer found near the cylinder wall, where the particles move as a solid body, and an active layer, where the particles avalanche and cascade downward. The interface between the two layers is defined as the yield line (Boateng & Barr, 1997) and is represented in Figure 6-2b by the $\delta(x)$ curve. The turning point line, found above the yield line and denoted by the $\alpha(x)$ curve in Figure 6-2b, is where the streamwise $u(x,y)$ velocity changes direction $(u(x,y)=0)$. The space between the yield and turning point lines is known as the transition region and is sometimes neglected due to its relatively small size (Khakhar, McCarthy, & Ottino, 1997). In such a case, the active layer boundary is singularly defined by the turning point line. In this work, both boundaries are considered. The depth of the active layer based on the yield or the turning point line is given by $\delta(x)$ or $\alpha(x)$, respectively, with $\delta(x=0)=\delta_0$ and $\alpha(x=0)=\alpha_0$. Table 6-4 defines the variables displayed in Figure 6-2.

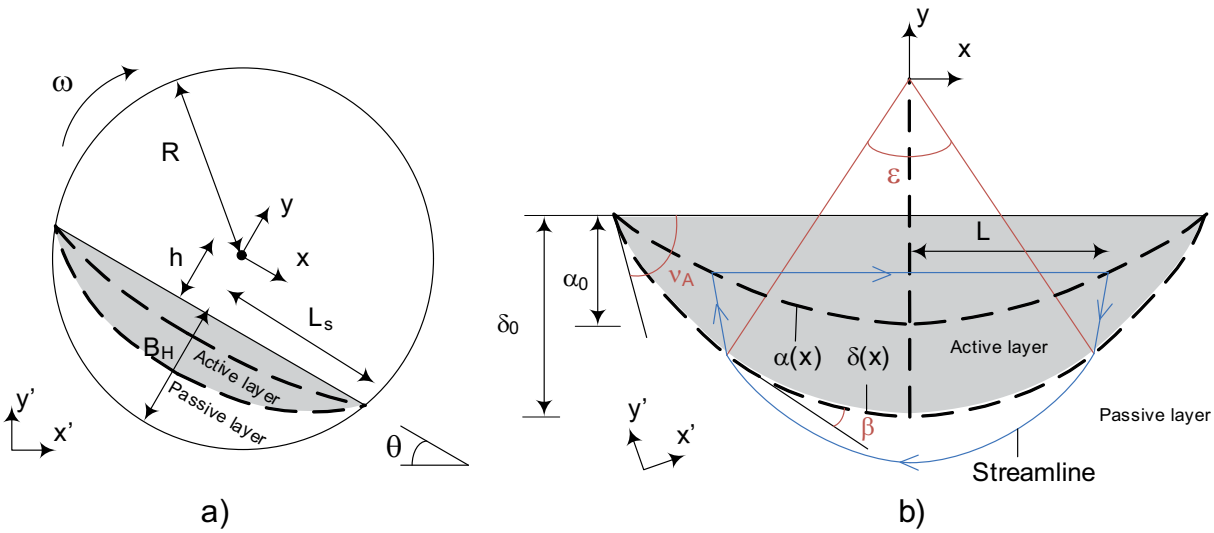

Figure 6-2 a) Cross-section view of the rotating drum and b) a close-up on the active layer

Table 6-4 Definition of the variables used

Variable	Definition
x	Streamwise direction (m)
y	Transverse direction (m)
u	Streamwise velocity (m/s)
v	Transverse velocity (m/s)
R	Drum radius
h	Normal distance between the bed surface center and the drum center of rotation (m)
L_s	Half-length of the bed surface (m)
L	Half-length of a streamline in the active layer (m)
β	Angle between the horizontal axis x' and the yield line
ν_A	Inclination angle of the yield line at the top of the material bed
θ	Dynamic repose angle
ω	Angular velocity (rad/s), $\omega < 0$ since the rotation is clockwise
B_H	Bed height

6.2.4.1 Modelling of the residence time

Much information about particle flow is needed to compute and model the residence time in the active and passive layers. In this section, primary observations related to the static and dynamic angles of repose, the bed effective rotational speed and dilation are first reported. The velocity profiles, the active layer thicknesses as well as the active and passive layer residence times obtained for all the experiments are then presented and analysed.

6.2.4.1.1 Primary observations

Significant differences can be observed between the flow of spherical particles and that of non-spherical particles. Primary observations regarding the static and dynamic repose angles, the effective particle rotational speed and the bed dilation are reported in Table 6-5. The experimental measurement of these quantities are of great importance since the models developed for the granular flow inside a rotating drum frequently use one or all of them (see Sections 6.1.4.1.2. to 6.1.4.1.4).

The static repose angle corresponds to the angle made by the stationary free surface of the particles once the cylinder operating under steady flow conditions stops rotating. The dynamic repose angles were computed using the velocity field. Figure 6-3 displays a typical velocity field obtained from the RPT experiments. The reported values of the dynamic repose angle correspond to the mean angle between the velocity vectors and the horizontal axis, for vectors belonging to the range $-0.05 \le x \le 0.05$ and $-(h+0.005) \le y \le -h$. For the bi-dispersed mixtures, the dynamic repose angles were obtained from the combination of the two tracer particle velocity fields. Note that the reported values match the visual measurements made in the laboratory but are more accurate and not affected by end wall effects. The rotational speed was computed using the mean streamwise velocity u at $x = 0$ and $-R < y < -R + 0.015$. Finally the filling fraction f was measured using the bed height at $x = 0$, as inferred by the velocity field (Figure 6-3).

Table 6-5 Primary observations

Case	Static repose angle θ_s (°)	Dynamic repose angle θ (°)	Rotational speed Ω (RPM)	Filling fraction f (%)
A	29.1 ± 4.1	32.24 ± 0.95	8.83 ± 0.38	35.9
B	32.8 ± 4.6	34.00 ± 1.72	8.82 ± 0.39	39.0
C	33.2 ± 5.0	35.01 ± 1.11	8.36 ± 0.13	40.0
D	30.6 ± 2.2	35.55 ± 1.93	8.38 ± 0.19	37.4
E	27.4 ± 4.2	29.27 ± 1.59	8.78 ± 0.15	36.9
AE	28.4 ± 2.8	30.40 ± 1.24	8.84 ± 0.17	38.5
BC	33.0 ± 3.6	34.39 ± 1.64	8.23 ± 0.18	38.5
CD	33.2 ± 1.8	35.34 ± 1.25	8.73 ± 0.05	41.6
CE	32.5 ± 2.3	35.23 ± 0.92	8.55 ± 0.13	41.6

It can be readily noticed that the use of tablets B, C and D resulted in a significantly higher dynamic repose angle than tablets A and E. This can be explained by the shape of the tablets (Figure 6-1). Tablets B, C and D all exhibit a longer straight side which enables them to form stable structures upstream, near the wall of the cylinder, thus yielding higher dynamic repose angles. It can be noticed that even if the aspect ratio of tablet D is 2.5 times greater than those of tablets B and C (Table 6-2), similar dynamic repose angles were measured. When tablets having similar dynamic repose angles are mixed, the resulting repose angle is the same as the individual ones. However, in the case of the binary mixture made from tablets C and E, even though tablets C only represent 15% of the whole volume, they nonetheless dictate the resulting dynamic repose angle.

All the experiments presented in Table 6-5 were performed at 10RPM. Even though the experimental setup encoder confirmed that the cylinder rotational speed was 10±0.5 RPM, the one experienced by the particles was approximately 1.5RPM lower. This confirms the experimental observation that the particles seemed to slip against the cylinder wall. Slipping of the particles is attributed to the friction between the bulk of the particles and the acrylic of the

cylinder. Given that the tablets were all coated using the same substance, it is not surprising that all individual tablets and blends experienced approximately the same rotational speed.

As it was specified in Section 6.2.3.2.2., all the experiments involved a 35vol% filled cylinder. From Table 6-5, it can be noticed that bed dilation occurred in all cases. More precisely, a bed dilation of more than 10% was measured in four cases (B, C, CD and CE). This phenomenon, which was not observed with the spherical glass beads used by Alizadeh, Dubé et al. (2013), is a characteristic of non-spherical granular flow (Cleary, 2010).

6.2.4.1.2 Velocity profiles

The computation of the active layer boundary essentially relies on the velocity profiles. Figure 6-3 displays the velocity fields in the case of experiments E and AE. At the exception of the bed dilation which can be appreciated by comparing these two pictures, every experiment presented a qualitatively similar velocity field.

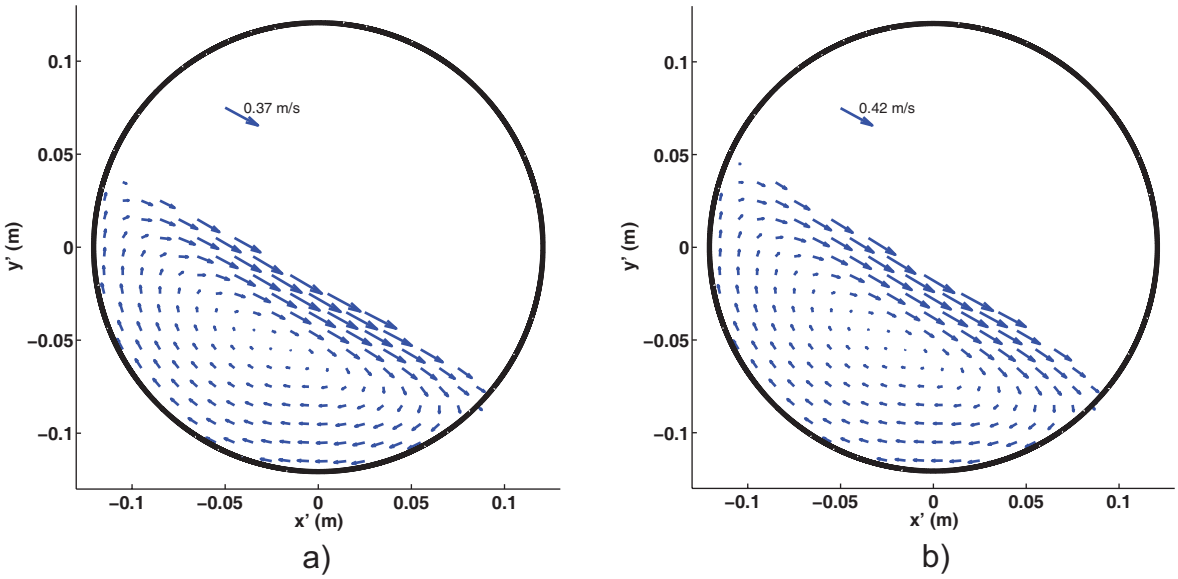

Figure 6-3 Typical velocity field for a) tablet E and b) blend AE (at 10RPM)

To make an efficient comparison and observe the effect of the shape on the velocity fields, one has to analyze the streamwise and transverse components of the velocity at specific x positions and along the surface bed.

6.2.4.1.2.1 Streamwise and transverse velocity profiles at specific x positions

Figure 6-4 shows the streamwise and transverse velocity profiles for the individual tablets as well as for the different blends, at $x = 0$. As representative examples of the individual tablets and blends, Figure 6-5 presents the same profiles for tablet C and blend AE, but at various x positions.

In the passive layer $\left(-R \le y \le -\left(\delta\left(x\right)+h\right)\right)$, since the particles are moving according to a solid body rotation (SBR), the streamwise $\left(u_{passive}\right)$ and transverse $\left(v_{passive}\right)$ velocity profiles follow:

$$u_{passive}\left(x, y\right) = \omega y \tag{6.3}$$

$$v_{passive}\left(x, y\right) = -\omega x \tag{6.4}$$

The linear variation of the streamwise and transverse velocities in the passive layer predicted by the previous equations can be appreciated in Figure 6-4 and Figure 6-5.

In the active layer $\left(-\left(\delta\left(x\right)+h\right) \le y \le -h\right)$, the streamwise and transverse velocities likewise display a linear profile except in the transition region $-\left(\delta\left(x\right)+h\right) \le y \le -\left(\alpha\left(x\right)+h\right)$, where a non-linear variation of the streamwise velocity (i.e. a non-constant shear rate $\left(\dot{\gamma} = \dot{\gamma}\left(y\right)\right)$) can be observed (Figure 6-4a and c, Figure 6-5a and c). However, most models consider a constant shear rate $\left(\dot{\gamma} \ne \dot{\gamma}\left(y\right)\right)$ in the active layer (Khakhar, Orpe, & Ottino, 2001b; Makse, 1999; Meier, Lueptow, & Ottino, 2007). Figure 6-5a and c also suggests that the shear rate depends on the

streamwise position $\left(\dot{\gamma}=\dot{\gamma}\left(x\right)\right)$. Again, for modeling purposes, it is often assumed that $\dot{\gamma}\neq\dot{\gamma}\left(x\right)$. Knowing that $u\left(x,y\right)=0$ at $y=-\left(\alpha\left(x\right)+h\right)$, the streamwise velocity in the active layer can be modeled by (Alizadeh, Dubé, et al., 2013):

$$u_{active}\left(y\right)\Big|_{x}=u_{surf}\left(x\right)\left(1+\xi\left(x,y\right)\right) \tag{6.5}$$

where $u_{surf}\left(x\right)$ is the streamwise velocity at the surface and $\xi\left(x,y\right)=\dfrac{y+h}{\alpha\left(x\right)}$ represents a dimensionless depth in the active layer based on the turning point line. An expression for $u_{surf}\left(x\right)$ will be presented in Section 6.2.4.1.2.2. Letting $v=0$ at $y=-h$ and knowing that $v=-\omega x$ at $y=-\left(\delta\left(x\right)+h\right)$, the transverse velocity in the active layer can be written as (Meier et al., 2007):

$$v_{active}\left(x,y\right)=-\frac{\omega x\left(y+h\right)}{\delta\left(x\right)} \tag{6.6}$$

As mentioned by Alizadeh, Dubé et al. (2013), the linear behaviour of the streamwise velocity profiles has been extensively reported in the literature. Furthermore, Alizadeh, Dubé et al. (2013) and Jain et al. (2004) showed that the transverse velocity profiles at $x=0$ oscillate around zero in the active layer. The same phenomenon was observed here for all the tablets and blends tested (Figure 6-4b and d). In Figure 6-5c, it can be noticed that the streamwise velocity profile near the surface seems to be more parabolic than linear. The development of a parabolic velocity profile for non-spherical particles has been observed before by Boateng and Barr (1997) for long-grain rice. This parabolic velocity profile suggests that the shear rate near the surface is close to zero, which means that the particles at the surface and a few millimeters under move together (at the same velocity). It can be observed in Figure 6-5a and c that the streamwise velocity profiles in the active layer are not symmetric with respect to the y axis. In other words, the $x=\pm0.04$ profiles are different as well as those corresponding at $x=\pm0.08$. This is more evident when looking at the streamwise velocity evolution along the bed surface. Finally, it can be observed in Figure 6-5b and d that the transverse velocity profiles in the passive layer are in agreement with what is predicted by equation (6.4). Figure 6-5 also highlights the fact that the active layer boundary as defined by the turning point line $\left(u=0\right)$ can easily be identified using the RPT results, unlike the one based on the yield line (dashed line), especially when $x\neq0$.

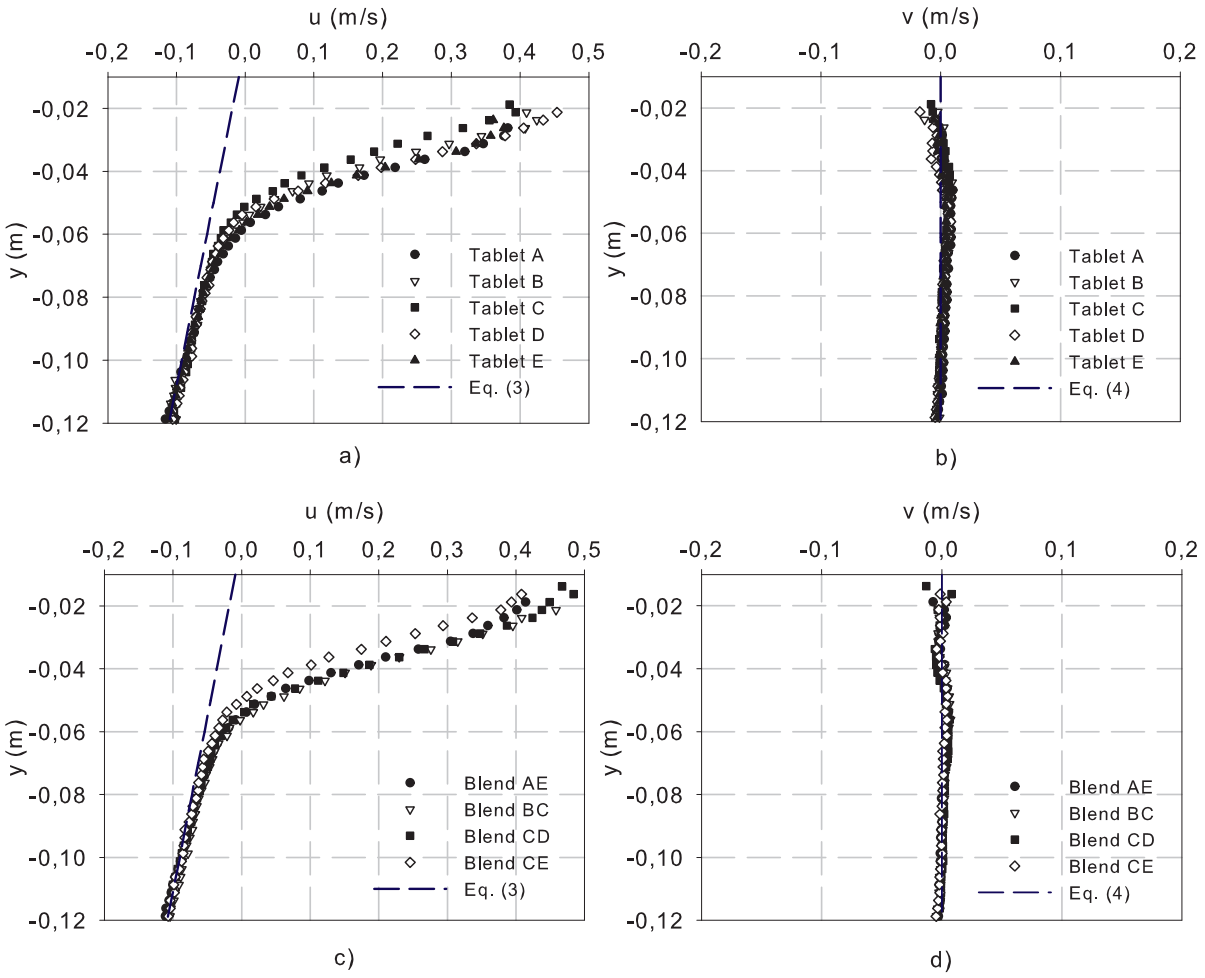

Figure 6-4 Streamwise velocity profiles at x=0 for a) the individual tablets and c) the different blends, and transverse velocity profiles at x=0 for b) the individual tablets and d) the different blends.

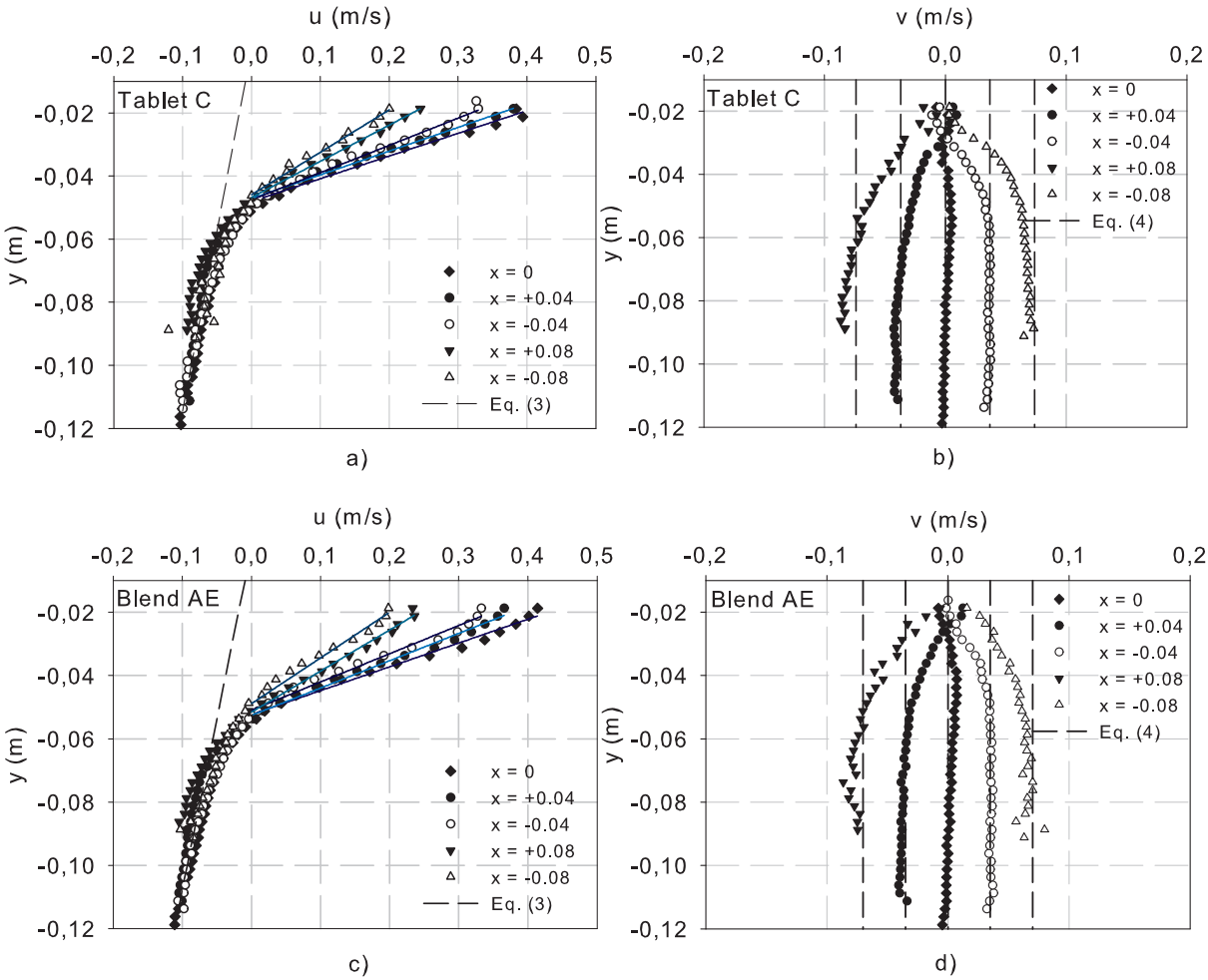

Figure 6-5 Streamwise velocity profiles for a) tablet C and c) blend AE, and transverse velocity profiles for b) tablet C and d) blend AE, at x = 0m, ±0.04m and ±0.08m

6.2.4.1.2.2 Streamwise velocity profile along the bed surface

The evolution of the streamwise velocity along the bed free surface is another significant feature of granular flow inside the rotating drum that needs to be analyzed thoroughly. This particular profile is essential to evaluate the residence time on the surface as well as in the active layer.

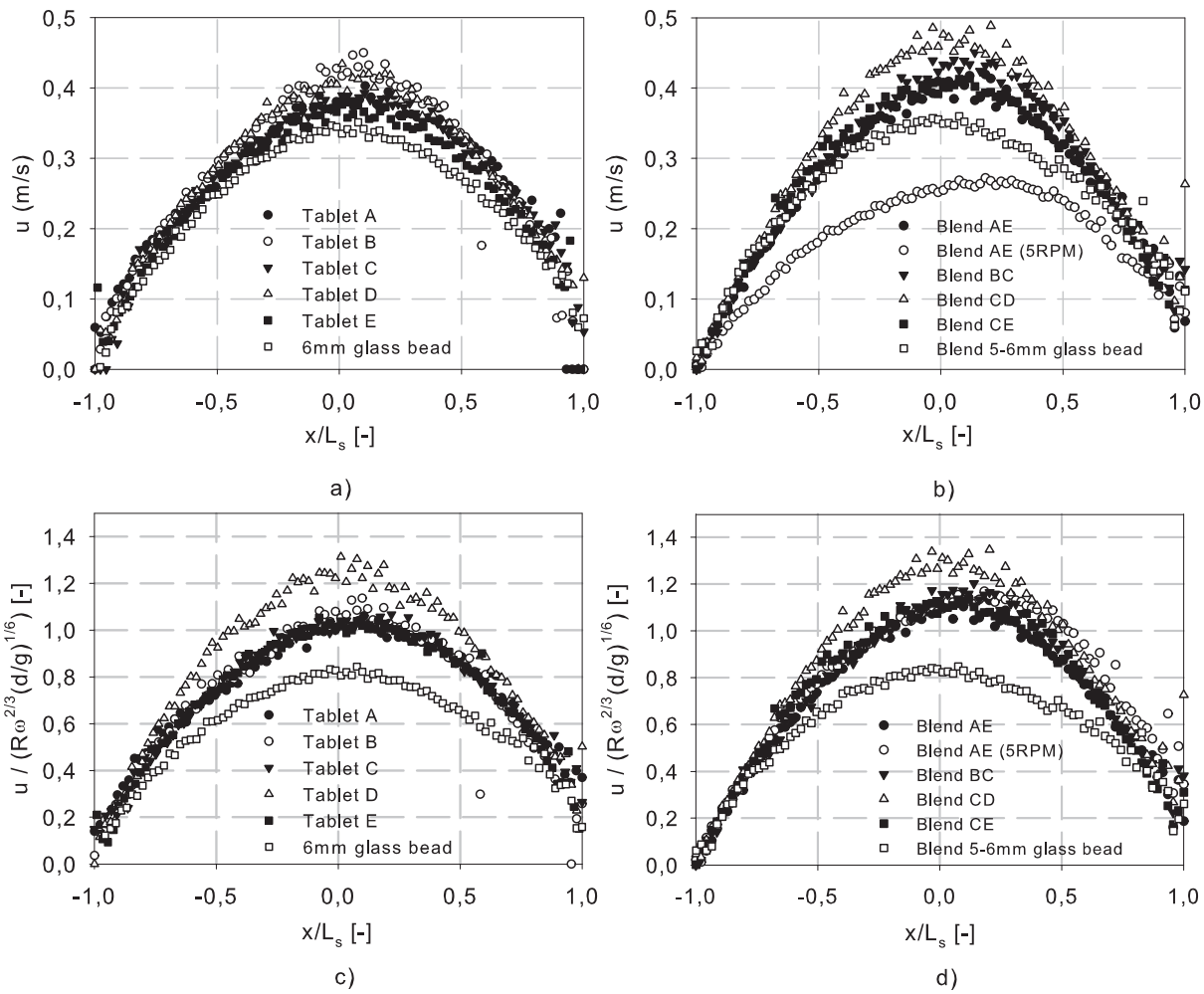

Figure 6-6 Streamwise velocity profiles along the bed free surface for a) the individual tablets and b) the different blends, and the scaled streamwise velocity profiles along the bed free surface for c) the individual tablets and d) the different blends.

Figure 6-6a and b display the streamwise velocity profiles on the bed surface for the individual tablets and all the blends. The results obtained using 6mm glass beads and a mix of 5mm (15vol%) and 6mm (85vol%) glass beads are also included to allow a comparison between spherical and non-spherical particles. It must be noted that the mass of a 6mm glass bead is approximately the same as that of tablets C, D or E (i.e. ~280mg). It can be noticed that the individual tablets B and D as well as the blends made from either of these tablets present the highest velocity peaks in comparison to the other shapes and blends. All the individual tablets and blends exhibit a higher velocity profile than the glass beads. Suzzi et al. (2012) and Wilson

and Crossman (1997) mentioned that, if the shape of a tablet is relatively flat, this tablet is likely to have a preferred spatial orientation on the surface and inside the bed, thereby causing to slide rather than rotate. Even though the RPT technique used in this study did not measure the angular velocity, the larger streamwise velocities observed in Figure 6-6a and b for the non-spherical tablets seem to corroborate these findings. Unfortunately, the comparison of these profiles cannot be made directly as each experiment used different particle sizes and resulted in different effective rotational speeds and dynamic repose angles (Table 6-5). On the one hand, the increase in the streamwise velocity peak could potentially simply be attributed to the difference in the dynamic repose angle. Indeed, the dynamic repose angle of the glass beads was measured at 27°, which is lower than those measured in involving tablets. On the one hand, the increase in the streamwise velocity peak could potentially simply be attributed to the difference in the dynamic repose angle. Indeed, the dynamic repose angle of the glass beads was measured at 27°, which is lower than those measured in involving tablets. On the other hand, the fact that no slipping between the glass beads and the wall of the cylinder was observed suggests that the glass beads have a higher velocity than the non-spherical tablets in the passive layer, which means that these spherical particles should start cascading down the bed free surface with a larger momentum. Alexander et al. (2002) found that, for a rotational speed below 30RPM, the streamwise velocity of spherical particles at the bed surface scales as:

$$u \propto R\omega^{2/3}\left(\frac{g}{d_p}\right)^{1/6} \tag{6.7}$$

where g is the gravitational acceleration and d_p is the particle diameter. Since this relation incorporates the particle diameter as well as the rotational speed, the streamwise velocity profiles were normalized by the expression on the right-hand side of equation (6.7) using for d_p the values of Figure 6-1. The new profiles are presented in Figure 6-6c and d. They indicate that tablet D and the 6mm glass bead have a behavior significantly different than that of the other tablets. The same phenomenon can be observed in Figure 6-6d, where the profiles of the mixture containing tablet D and the mixture of 5mm and 6mm glass beads differ from the other profiles. These results further confirm that tablets D, which exhibit the highest aspect ratio (Table 6-2) and the flatter shape, have a tendency to slide on the bed surface, whereas the glass beads have a

tendency to rotate. The other shapes behave somewhere in between, combining translational and rotational motion.

According to Khakhar et al. (1997), the streamwise velocity along the bed surface $u_{surf}(x)$ can be expressed as:

$$u_{surf}(x) = u_{\max}\left(1 - \frac{x^2}{L_s^2}\right) \tag{6.8}$$

with

$$u_{\max} = \frac{\omega L_s^2}{\alpha_0} \tag{6.9}$$

where the distance α_0, shown in Figure 6-2b, corresponds to $y = -\left(\alpha\left(x = 0\right) + h\right)$.

Figure 6-7a and b confirms that this equation correctly models the streamwise velocity profiles for both the individual tablets and the different blends, at the exception of the blend AE with a 5RPM rotational speed. As was observed by Ding et al. (2002b) and Alizadeh, Dubé et al. (2013), the downstream part of the flow is better modeled by adding 2/3 as an exponent to equation (6.8), which complies with the asymmetry noticed in Section 6.2.4.1.2.1 and presented in Figure 6-5.

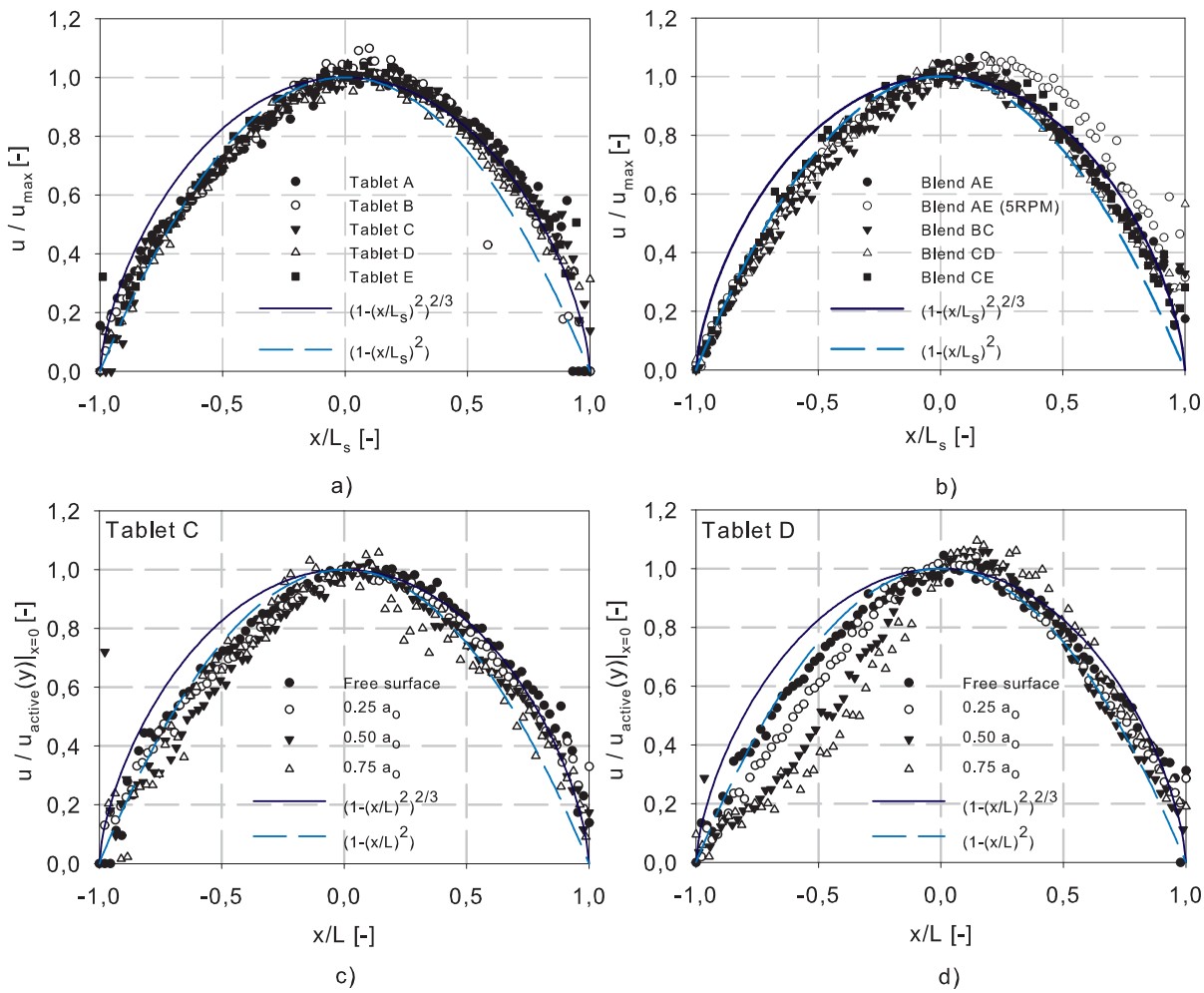

Figure 6-7 Normalized streamwise velocity profiles at the bed surface for a) the individual tablets and b) the different blends, and under the bed surface for c) tablet C and d) tablet D.

The blend AE with a rotational speed of 5RPM displays a skewed streamwise velocity profile with a peak velocity attained past the mid-chord position $\left(x/L_s = 0\right)$, whereas its profile at 10RPM is symmetric. The occurrence of an asymmetric profile for a smaller rotational speed has been observed previously by Alexander et al. (2002), Boateng and Barr (1997) and Nakagawa et al. (1993). In particular, Alexander et al. (2002) mentioned that the asymmetry in the profile may be due to the fact that the frictional/collisional losses within the cascade do not balance, before the particles reach the mid-chord position, the particle kinetic energies imparted by the rotational speed of the blender, thereby allowing these particles to accelerate beyond this point.

Finally, the streamwise velocity profile under the bed surface $u_{us}(x)$ is analyzed. For this purpose, the evolution of the profile with respect to the bed depth for tablets C and D is provided in Figure 6-7c and d, respectively. Note that tablets A, D, E as well as blends AE, BC and CE all follow the same trend as the one shown for tablet C, whereas blend CD and tablet D exhibit similar profiles. For all these cases, the velocity profile can be approximated by:

$$u_{us}(x) = u_{active}(y)\Big|_{x=0}\left(1-\frac{x^2}{L^2}\right) \tag{6.10}$$

This expression is similar to the one obtained using spherical particles by (Alizadeh, Dubé, et al., 2013). However, as can be seen in Figure 6-7d, the profile for tablet D deviates from equation (6.10) as it becomes more asymmetric as the distance under the free surface increases. Nevertheless, the downstream portion of the flow follows the profile predicted by equation (6.10) . The deviation of the upstream portion can be explained by the shape of the particles. The long flat side of tablet D enables it to form a stable structure near the cylinder wall. By doing so, only the tablets at or near the surface will easily cascade downstream. This creates an asymmetric profile under the surface, much more pronounced than for tablet C, whereby the tablets accelerate past the mid-chord position. As Weir et al. (2005) mentioned, complex repositioning within the shear layer is expected for particles having a large aspect ratio.

The results presented in this section showed that the particle shape can have a significant impact on the velocity profile. They also evidenced that more complicated structures can form within the bulk of particles. At the exception of tablet D as well as blends CD and AE (at 5RPM), the models previously developed could adequately represent the streamwise and transverse velocities of the non-spherical systems considered in this work.

6.2.4.1.3 Active layer thickness

The active layer thickness is a key parameter as mixing, segregation, heat transfer or other phenomena mainly occur in this region. Many correlations can be found in the literature to predict the thickness of the active layer, based either on the turning point or yield line. These correlations often use parameters that are difficult to measure experimentally (e.g. the surface velocity profile or the angle between the active layer boundary at its extremities and the horizontal plane (ν_A in Figure 6-2b), operating conditions, material properties, geometrical characteristics of the rotating drum, fitting parameters, or a combination of any of these). In this section, some of these correlations are compared to evaluate their performance in predicting the active layer thickness for the non-spherical particles and blends used in this study.

6.2.4.1.3.1 Active layer thickness based on the turning point line

The active layer thickness based on the turning point line can easily be identified using the results from the RPT experiments. The profiles for tablets D, E, and for the 6mm glass beads are displayed in Figure 6-8. Note that tablets A, B and C, and blends AE, CB and CE all present profiles similar to that of tablet E, while the profile for the blend CD is similar to that of tablet D.

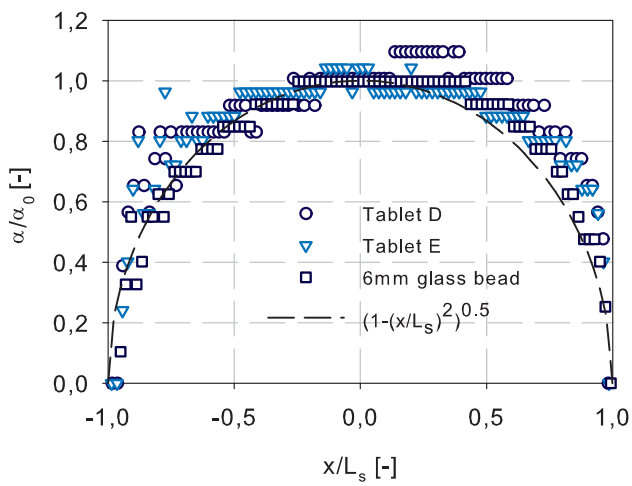

Figure 6-8 Normalized active layer depth profile $\alpha(x)/\alpha_0$ for tablets D and E, and 6mm glass bead

It can be observed that, at the exception of tablet D (look at the results downstream from $x=0$), the active layer can be properly modeled by:

$$\alpha(x)=\alpha_0\sqrt{1-\left(\frac{x}{L_s}\right)^2} \tag{6.11}$$

This equation is different from that reported by Alizadeh, Dubé et al. (2013) for spherical glass beads. As noted by Sturman et al. (2008), although the square root in equation (6.11) appears in some models and not in others, both forms yield comparable results. However, as will be discussed in Section 6.2.4.1.4, the model used for $\alpha(x)$ has an impact on the prediction of the residence time along streamlines in the active layer. The asymmetric active layer profile of tablet D is compliant with the corresponding streamwise velocity profiles under the bed surface (Figure 6-7d).

The experimental values obtained for α_0 are presented in Table 6-6 and are compared to those which would be obtained using the models developed by Liu et al. (2006), Weir et al. (2005) and

Ding et al. (2001). The reader is referred to these references for the detailed description of these models.

The model derived by Liu et al. (2006) is based on a previous one developed by Mellmann et al. (2004), which uses mass and momentum balances to evaluate the transverse solids motion in a rotating drum. In order to compute the active layer thickness, this model requires the particle diameter d_p (identified in Figure 6-1), the drum diameter D, the dynamic angle of repose θ as well as the inclination angle of the active layer boundary line at the top of the material bed (i.e. the angle ν_A in Figure 6-2). This angle is difficult to measure (Mellmann et al., 2004) and could not be backed out with adequate accuracy from the RPT data. To overcome this limitation, a correlation between ν_A and θ, developed by Mellmann et al. (2004), was used. This correlation was experimentally derived using 15 different materials, including both spherical and non-spherical particles, with $25° < \theta < 50°$, which matches the properties of the tablets used for the current work. The correlation needs θ, f, R as well as ω to compute ν_A.

Weir et al. (2005) developed a regression model using experimental results obtained by various authors. Their model requires d_p, R, ω, f as well as an author- and particle-dependent fitting parameter λ. This parameter depends on particle properties, geometrical characteristics of the rotating drum and operating conditions.

Finally, Ding et al. (2002b; 2001) proposed a model based on mass and momentum balances. They also considered a quadratic polynomial to model the streamwise velocity in the active layer along the axis perpendicular to the bed surface, $u_{active}(y)\big|_x$. Let us recall that this velocity was introduced as a linear polynomial in y for a given x in equation (6.5). Their model, which can be used to compute both active layer boundaries ($\alpha(x)$ and $\delta(x)$), requires the knowledge of ω, f and the streamwise velocity along the bed surface, $u_{surf}(x)$. Note that only $u_{active}(0)\big|_{x=0}$ is needed to compute α_0 and δ_0. Ding et al. (2002a) provided a correlation to evaluate this value

for nearly spherically shaped particles having high restitution coefficients, yet it was found to be inadequate for the tablets used in this work. In fact, the use of this correlation resulted in values for $u_{active}(0)\big|_{x=0}$ that are 40% lower than the experimental ones. For this reason, experimental values measured by the RPT technique were used instead.

Table 6-6 Values of the active layer thickness α_0 based on the turning point line

Case	Measured α_0 [cm (%)$^{\pm}$]	Liu et al. (2006) [cm (%)$^{\pm}$]	Weir et al. (2005) [cm (%)$^{\pm}$]	Ding et al. (2001) [cm (%)$^{\pm}$]
A	3.1 (33)	2.2 (24)	3.1 (33)	2.2 (23)
B	3.4 (34)	2.3 (23)	3.5 (35)	2.1 (21)
C	3.2 (31)	2.4 (23)	3.3 (33)	2.1 (21)
D	2.8 (29)	2.6 (27)	2.8 (29)	1.8 (19)
E	3.1 (33)	2.2 (23)	3.0 (32)	2.2 (23)
Average error (%)	-	25	2	33
AE	3.3 (33)	2.2 (23)	3.2 (32)	2.1 (22)
AE*	3.3 (33)	2.0 (20)	2.7 (26)	1.8 (18)
BC	3.3 (34)	2.3 (23)	3.3 (34)	1.8 (18)
CD	3.8 (36)	2.6 (25)	3.3 (31)	1.9 (18)
CE	3.4 (32)	2.5 (24)	3.3 (32)	2.1 (20)
Average error (%)	-	32	8	43

$^{\pm}$Percentage of bed depth

Previous studies reported an increase in the active layer thickness with an increase of the drum rotational speed and polydispersity (Alizadeh, Dubé, et al., 2013; Boateng & Barr, 1997; Henein et al., 1983; Van Puyvelde et al., 2000; Woodle & Munro, 1993). From Table 6-6, it can be noticed that the polydispersity does not increase α_0 except in the case of blend CD. In addition, no change in α_0 can be noticed when the drum rotational speed is increased in the case of blend AE. The model from Liu et al. (2006) invariably underpredicts α_0 and presents a high average errors. This model best predicts the α_0 value of tablet D yet it fails to predict the high increase in α_0 observed in blend CD. The errors may be attributed to the angle ν_A, which was obtained using a correlation, as explained above. In fact, it was found that, to adequately predict α_0 using this

model, ν_A has to be 6° higher than that predicted by the correlation. The model proposed by Ding et al. (2001) also underpredicts α_0 and presents an even higher average errors than the previous model. It is believed that the errors may be partially attributed to the quadratic polynomial used to model $u_{active}(y)\big|_x$. A closer look at the results presented in Ding et al. (2001) reveals that their model does underpredict $\alpha(x)$ and that a linear approximation model for $u_{active}(y)\big|_x$ would reduce this under-prediction. Moreover, the results presented in Section 6.2.4.1.2.1, indicate that, for the solid particles of this work, a linear profile can accurately model $u_{active}(y)\big|_x$. Finally, the model of Weir et al. (2005) results in the smallest average errors. This is not surprising as this model uses a particle-dependent fitting parameter λ. Its value had to be set at 1 for tablets B and C (just as for spherical particles), 0.8 for tablets A and E, and 0.7 for tablet D. In other words, rather close values for λ were found for tablets of similar shapes.

6.2.4.1.3.2 Active layer thickness based on the yield line

The experimental values for δ_0 are presented in Table 6-7 and are compared to those obtained using the models of Orpe and Khakhar (2001), Alizadeh, Dubé et al. (2013) and Ding et al. (2001).

The model proposed by Orpe and Khakhar (2001) is based on a model developed by Makse (1999), and obtained using a mass balance and the assumption of constant shear rate $(\dot{\gamma})$ along the y direction in the active layer. In this model, the active layer thickness based on the yield line is expressed as:

$$\delta(x) = \sqrt{\frac{\omega}{\dot{\gamma}(x)}\left(L_s^2 - x^2\right)} \tag{6.12}$$

with $\dot{\gamma}(x)$ given by (Khakhar, Orpe, Andresen, et al., 2001; Khakhar, Orpe, et al., 2001b; Meier et al., 2007; Orpe & Khakhar, 2001):

$$\dot{\gamma}(x) = \sqrt{\frac{g\cos\beta(x)\sin(\theta-\theta_s)}{cd_p\cos\theta\cos\theta_s}} \tag{6.13}$$

where g is the gravitational acceleration, θ_s the static angle of repose, $\beta(x)$ the angle between the horizontal and the boundary of the active layer, and c a fitting parameter. It can be noticed that $\dot{\gamma}(x)$ depends mainly on particle properties. Previous studies reported a value of $c \approx 1.5$ for two-dimensional systems (Khakhar, Orpe, et al., 2001b; Meier et al., 2007; Orpe & Khakhar, 2001).

Alizadeh, Dubé et al. (2013) proposed a model based on the intersection between the linear streamwise velocity profiles in the passive and active layers. This model gives a relation between α_0 and δ_0. They suggested using it to compute α_0 using the value of δ_0 obtained from equation (6.12). Since this equation requires an a priori unknown fitting parameter c and $\delta(x)$ is harder to identify experimentally, it was instead decided to use the experimental value of α_0 to obtain δ_0. Aside from α_0, this model only requires f to compute δ_0.

Table 6-7 Values of the active layer thickness δ_0 based on the yield line

Case	Measured δ_0 [cm (%)$^{\pm}$]	Orpe and Khakhar (2001) [cm (%)$^{\pm}$]	Alizadeh, Dubé et al. (2013) [cm (%)$^{\pm}$]	Ding et al. (2001) [cm (%)$^{\pm}$]
A	3.8 (40)	3.8 (41)	3.5 (37)	2.3 (25)
B	4.4 (44)	4.4 (45)	3.9 (39)	2.2 (22)
C	4.2 (41)	4.1 (40)	3.6 (35)	2.2 (22)
D	3.7 (39)	3.7 (38)	3.1 (33)	1.9 (20)
E	4.2 (44)	4.6 (48)	3.5 (37)	2.4 (25)
Average error (%)	-	4	13	45
AE	4.6 (46)	4.5 (46)	3.7 (38)	2.2 (23)
AE*	4.4 (44)	4.5 (45)	3.8 (38)	1.8 (18)
BC	4.1 (41)	4.2 (43)	3.8 (38)	1.9 (19)
CD	4.7 (45)	4.4 (42)	4.4 (42)	1.9 (19)
CE	4.5 (43)	4.4 (42)	3.8 (27)	2.2 (21)
Average error (%)	-	3	12	55

$^{\pm}$Percentage of bed depth

Table 6-7 shows a slight increase of the experimental values of δ_0 with an increasing drum rotational speed for blend AE. Furthermore, polydispersity seems to increase δ_0 in the case of blends AE and CD. The model from Orpe and Khakhar (2001) adequately predicts δ_0 in all cases, with a very low average error. However, it must be mentioned that, as in Alizadeh, Dubé et al. (2013), $c = 1$ was used to match the experimental results. Moreover, it was noticed that this model is strongly dependent on the values of θ and θ_s. As can be seen in Table 6-5, the θ_s values present an uncertainty of approximately 4°. Interestingly, a different value of θ_s, lying in the range of uncertainty, used in combination with $c = 1.5$, could be found in each case so that the model matches the experimental results. Thus, it is believed that a more precise value of θ_s should be obtained before concluding on the value of c. The model of Alizadeh, Dubé et al. (2013) always underpredicts δ_0. The underprediction is due to the fact that this model computes δ_0 as the intersection between the two linear velocity profiles of the active and passive layers and does not consider the varying shear rate characteristic of the transition region. Nevertheless, its application results in acceptable discrepancies, presenting average errors of 13% and 12% for

individual tablets and blends, respectively. Unfortunately, the model does not capture the increase in δ_0 with an increasing drum rotational speed. This can be attributed to the experimental data used for α_0. Finally, the results obtained using the model of Ding et al. (2001) are completely off the mark, presenting average errors between 45% and 55%. Reasons for these large discrepancies have already been provided in Section 6.2.4.1.3.1.

The results of this work indicate that there does not seem to be a significant effect of the tablet shape on the values of α_0 and δ_0, contrary to what has been previously reported, for other non-spherical particles. At the exception of the models by Ding et al. (2001) and Liu et al. (2006), most of them could predict with reasonable accuracy the size of the active layer depth. However, they all needed at some point a fitting parameter, the value of which is a priori unknown.

6.2.4.1.4 Residence time

Knowing the residence time in the active layer of a rotation drum is important for many applications such as those involving rotary kilns since the material renewal occurs mainly in this region. Figure 6-9 presents the mean residence time spent by the tracer particle in each cell of the Eulerian grid, for tablets B and D. It can be readily observed that the shape of tablet D disrupts the expected profile symmetry observed for spherical particles.

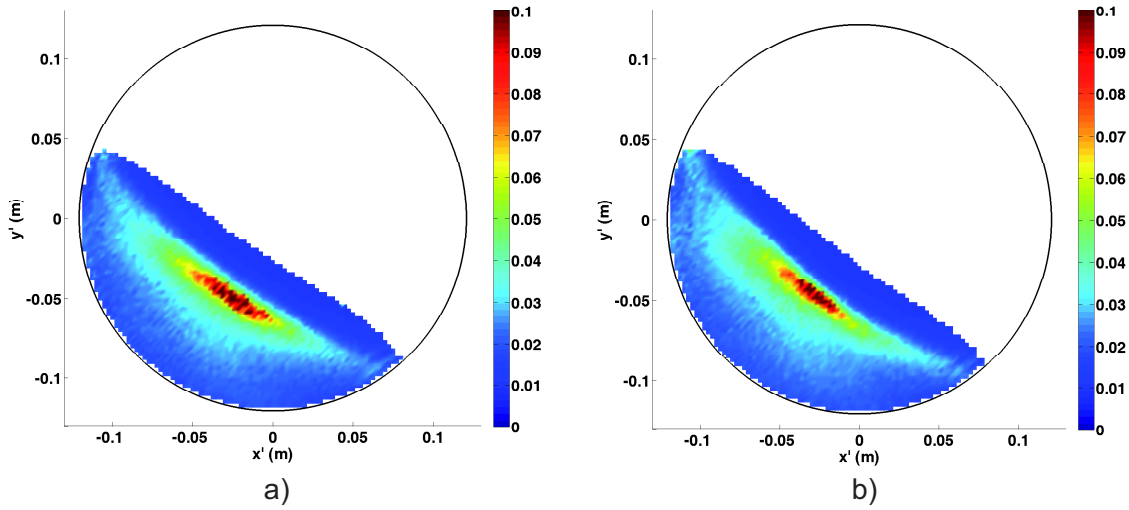

Figure 6-9 Mean residence time in cells of the Eulerian grid used for a) tablet B and b) tablet D.

Using the results presented in Sections 6.2.4.1 to 6.2.4.3, it is possible to compute the residence times spent by the particles in the active and passive layers. In order to extract these residence times from the RPT results, streamlines must be identified. To do so, massless tracers are launched in the velocity fields of each experiment, along the line $x = 0$ and $-(\alpha_0 + h) < y < -h$. The time spent in the active and passive layers can then be computed using these massless tracer trajectories. Two criteria can be used to define the boundary between the active and passive layers: the turning point and yield line. As was previously mentioned, the former can easily be identified through the RPT data whereas the latter cannot be identified with enough accuracy. To overcome this limitation, it is assumed that the ratio $\Lambda(x) = \alpha(x)/\delta(x)$ is constant, even though the velocity profiles from Figure 6-5 and Ding et al. (2001) suggest it does vary. Consequently, the yield line is defined as:

$$\Lambda = \frac{\alpha_0}{\delta_0} \Rightarrow \delta(x) = \frac{\alpha(x)}{\Lambda} \tag{6.14}$$

The residence time in the passive layer (t_p) is modeled using the angle of the streamlines (ε, see Figure 6-2) and the angular velocity (ω) (Alizadeh, Dubé, et al., 2013):

$$t_p = \frac{\varepsilon}{\omega} \tag{6.15}$$

For this equation to hold, the angle of the streamline must be associated with the yield line boundary and not the turning point boundary. Alizadeh, Dubé et al. (2013) modeled the residence time in the active layer (t_a) by neglecting the curvature at the beginning and the end of the streamlines and assuming that:

- the streamlines in the active layer are parallel to the bed surface;
- the streamwise velocity profile in the active layer obeys equations (6.5) and (6.10);
- the active layer boundary $\alpha(x)$ is symmetric and follows:

$$\alpha(x) = \alpha_0 \left(1 - \left(\frac{x}{L_s} \right)^2 \right) \tag{6.16}$$

Given that it was shown in Section 6.2.4.1.3.1 that equation (6.11) adequately models $\alpha(x)$, the model proposed by Alizadeh, Dubé et al. (2013) can be adapted to yield:

$$t_a = \frac{3\alpha_0}{\omega L_s} \frac{\sqrt{1-\xi_0^{\,2}}}{(1+\xi_0)} \tag{6.17}$$

where $\xi_0 = \frac{y+h}{\alpha_0}$, and y represents the height of the streamline in the active layer. Equation (6.17) holds only when the active layer is defined by the turning point line. It is proposed here to modify this model so that it takes into account the transition region and thus brings into play the yield line. Since Λ is assumed constant, it then comes from equation (6.11) and (6.14) that :

$$\delta(x) = \frac{\alpha(x)}{\Lambda} = \frac{\alpha_0}{\Lambda} \sqrt{1 - \left(\frac{x}{L_s} \right)^2} \tag{6.18}$$

It is also assumed that, in the transition region (i.e. for $-(\delta(x)+h) < y < -(\alpha(x)+h)$), the streamlines are oriented along the *y* axis. It can then be deduced from Figure 6-2b that the time spent by a streamline in the transition region $(t_{\alpha-\delta})$ can be approximated by:

$$t_{\alpha-\delta} = 2\frac{\left(\delta(x)-\alpha(x)\right)}{\left|\overline{v(x,y)}\right|} \tag{6.19}$$

where $\overline{v(x,y)}$ is the mean transverse velocity between $\alpha(x)$ and $\delta(x)$ which can be obtained by equation (6.6). By letting $x = L$, it can be shown that:

$$\left|\overline{v(x,y)}\right| = \frac{1}{2}\omega(\Lambda+1)L \tag{6.20}$$

where, from equation (6.11),

$$L = L_s\sqrt{1-\xi_0^{\,2}} \tag{6.21}$$

Finally, using the fact that the numerator of equation (6.19) can be expressed as:

$$\delta(x)-\alpha(x) = \xi_0(\alpha_0-\delta_0) \tag{6.22}$$

It comes from equations (6.19), (6.20) and (6.21) that:

$$t_{\alpha-\delta} = \frac{4\xi_0(\alpha_0-\delta_0)}{\omega(\Lambda+1)L_s\sqrt{1+\xi_0}} \tag{6.23}$$

The total residence time in the active layer is then given by summing equations (6.17) and (6.23):

$$t_a = \frac{3\alpha_0}{\omega L_s}\frac{\sqrt{1-\xi_0^2}}{(1+\xi_0)} + \frac{4\xi_0(\alpha_0-\delta_0)}{\omega(\Lambda+1)L_s\sqrt{1+\xi_0}} \tag{6.24}$$

and the total residence time along a specific streamline $(t_a + t_p)$ is simply the sum of equations (6.15) and (6.24). Figure 6-10 displays the experimental and predicted residence times in the active and passive layers as well as the total residence time along streamlines for all tablets and blends tested in this work. It must be mentioned that the model developed for the residence time in the active layer is not expected to work in the case of tablet D and blends AE (at 5RPM) and CD as their velocity profiles were shown in Figure 6-7 to deviate from equation (6.10). This is confirmed in Figure 6-10, where a large deviation between the model and the experimental data can be noticed.

In all cases, a good agreement is found between the values of t_p predicted by equation (6.15) and the experimental data. The small discrepancies that can be observed for $\xi_0 < -0.4$ can be attributed to the way $\delta(x)$ was defined (i.e. equation (6.14)) for the experimental data. As was already mentioned, only $\alpha(x)$ could be identified experimentally. A constant Λ was assumed in order to evaluate $\delta(x)$. Since the experimental values of t_p are greater than the ones predicted by equation (6.15), it seems that equation (6.14) underestimates $\delta(x)$, thus confirming the findings of Ding et al. (2001) who observed that Λ decreases as the distance from the center of the flow increases. As for the residence time in the active layer, a good agreement is obtained between the experimental results and equation (6.24), except for the three cases previously mentioned. In fact, it can be readily noticed that the model generally overestimates t_a. Again, this can be attributed to the identification of $\delta(x)$ through equation (6.14). An even better agreement is obtained for the total residence time along the streamline. This is expected as the total experimental time does not neeed the identification of $\delta(x)$. Finally, a comparison of the curves of Figure 6-10 for all tablets and blends with a rotational speed of 10RPM reveals that the tablet shape has little effect on the residence times in both layers with the exception of tablet D that shows slight differences.

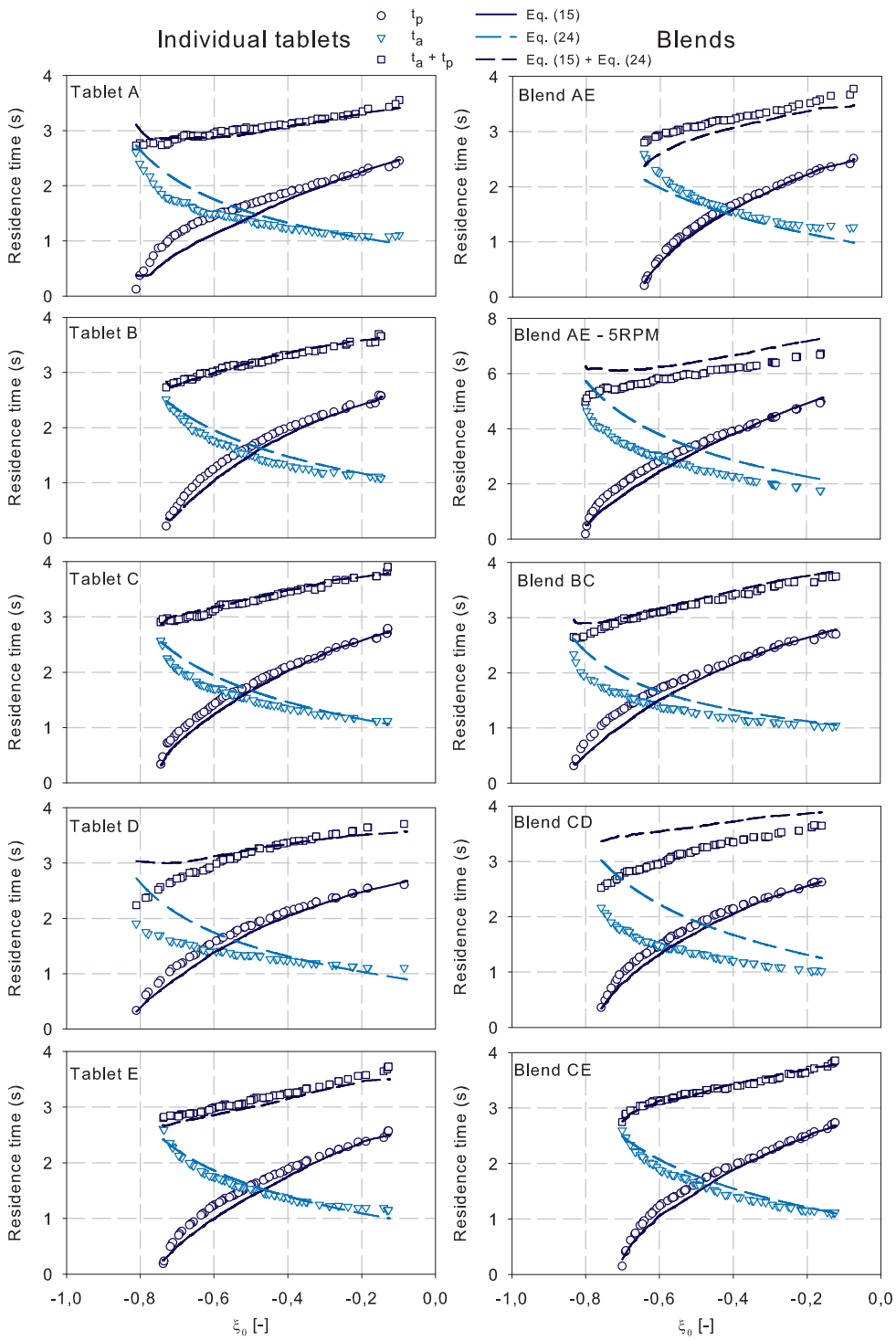

Figure 6-10 Residence times in the active and passive layers for all the tablets and blends tested. The symbols correspond to experimental data.

The good quality of the model developed here means that it could be used to predict the total residence time along streamlines for any situations. It simply needs the filling fraction f to compute L_s, the drum rotational speed ω, equation (6.12) to evaluate δ_0, the model of Alizadeh, Dubé et al. (2013) to evaluate α_0 from δ_0, and finally, equation (6.11) to link L to ε.

6.2.4.2 Mixing and segregation

The mixing and segregation of non-spherical particles were investigated using the tablet blends presented in Table 6-3. As already discussed, the mixtures were chosen to represent cases when a varied feedstock is used or when changes in size (mono-shaped mixture) or shape (bi-shaped mixtures) occur over the course of the rotating drum operation. The study of segregation inside rotating drums is important as it can greatly affect the heat and mass transfer efficiency occurring in the active layer. In order to compare the segregation of non-spherical particles to that of spherical particles, an experiment using 5mm (15vol%) and 6mm (85vol%) glass beads with a 10RPM drum rotational speed was realized. The volume, density as well as the particle diameter ratios of each blend are presented in Table 6-8.

Table 6-8 Blend characteristic ratios

Blend (ratio)	V ratio	ρ_p ratio	d_p ratio	d_l ratio
AE (E/A)	1.5	0.92	1.26	1.26
BC (C/B)	1.2	1.02	1.14	1.08
CD (D/C)	1.1	0.94	1.84	0.80
CE (E/C)	1.3	0.79	1.60	0.87
5-6mm glass beads	1.7	1	1.2	-

Jain et al. (2005) conducted an impressive and thorough study of the combined size and density effect on mixing and segregation inside a rotating drum. They limited their study to cohesionless spherical particles. Depending on the size or density ratios of the mixtures, percolation (i.e. size) and/or buoyancy (i.e. density) driven segregation could be observed. In the case where buoyancy

and percolation acted in the same direction, the smaller/denser particles were always found in the center of the bed (core segregation), unless the size ratio of the small particle to the large particle was lower than 0.5, in which case radial streaks of particles of the same size would be observed. In this work, it can be seen from Table 6-8 that both percolation and buoyancy are expected to act in the same direction: the particle with the smaller volume, invariably has a higher (or nearly equal) density. Thus, traditional core segregation is expected in all cases.

To quantify the extent of segregation, the occupancy and the location probability were computed. The occupancy is simply the ratio of the number of times the tracer particle was found in a specific cell of the Eulerian grid to the maximum number of times it was detected in a single cell. The location probability is computed as the number of times a tracer particle was found in a specific cell to the total number of times that both tracer particles (one for each tablet type) were found in that same specific cell. The occupancy and location probability for blends AE, AE*, BC and the 5-6mm glass beads are presented as a function of the normalized bed depth $\left(\left|y+h\right|/B_H\right)$ in Figure 6-11, while those for blends CD and CE can be found in Figure 6-12. It must be noted that only the values of the occupancy and location probability along the y axis at $x=0$ are presented. In these two figures, the notation AB.C signifies blend AB and the use of Tablet C as a tracer in the experiments.

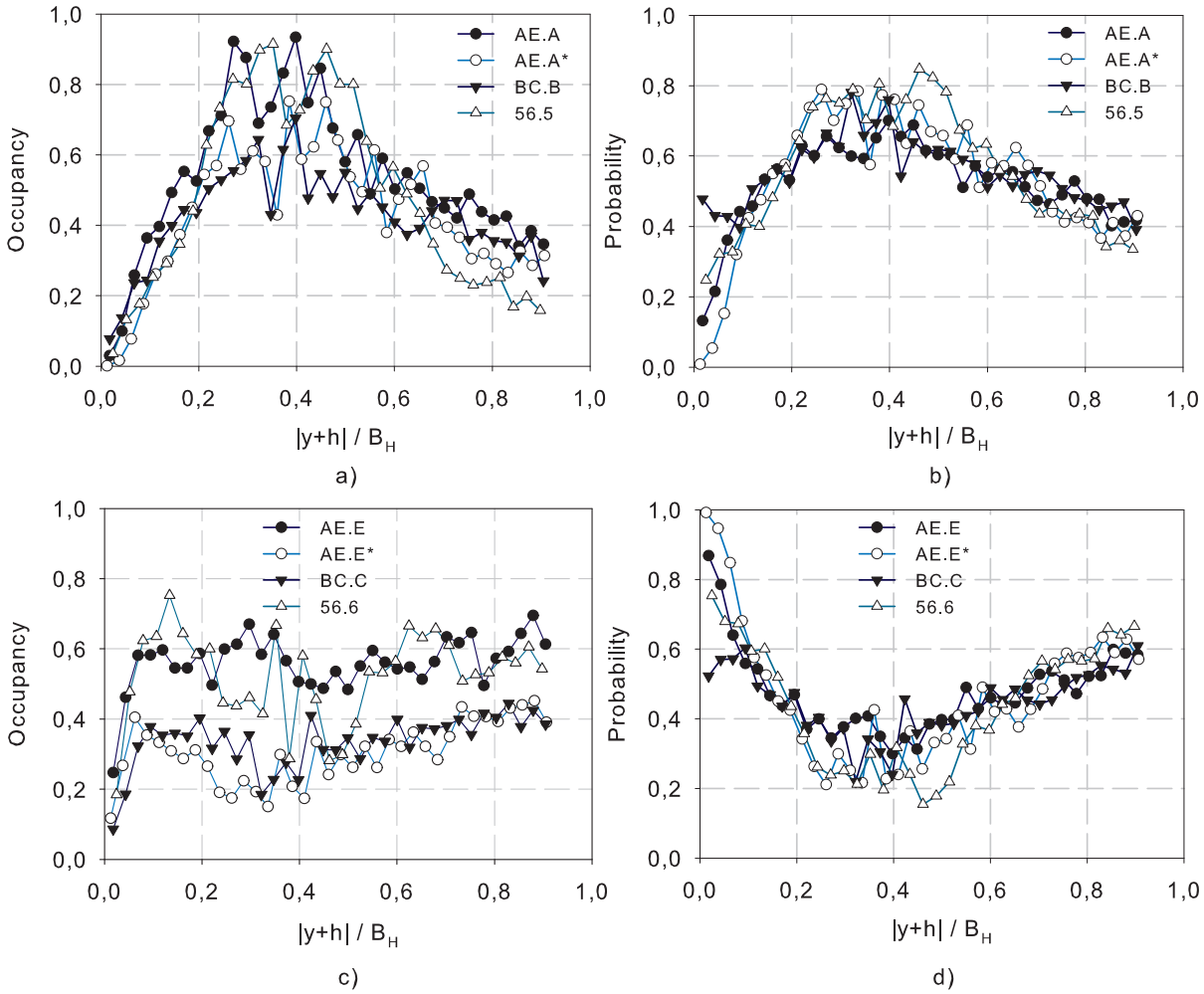

Figure 6-11 Values of (a and c) the occupancy and (b and d) the location probability for blends AE, AE*, BC and the 5-6 mm glass beads. For a) and b), the smaller particle was used as a tracer. For c) and d), the larger particle was used as a tracer.

The location probabilities of Figure 6-11b show that the smaller particles (i.e. tablets A, B and the 5mm glass bead) have a higher probability of being found in the center of the bed rather than on the outside. The occupancy plot for the smaller particles (Figure 6-11a) also confirms this trend. These results indicate the occurrence of traditional core segregation. However, one may notice that the occupancy curves of the larger particles (Figure 6-11c) are nearly uniform in all cases. Similar occupancy profiles were obtained in mono-disperse experiments (not shown here), suggesting that even though the core of the bed is more likely to contain a greater concentration of smaller particles, this does not seem to affect the flow pattern of larger particles. A similar

result was obtained for a 4mm glass tracer in a blend of 3, 4, 5 and 6mm glass beads (Alizadeh, Dubé, et al., 2013). From Figure 6-12, it can be seen that completely different results were obtained for blends CD and CE. The smaller and denser particle (i.e. tablet C) is never found in the core of the bed as its occupancy and location probability both approach zero in this zone. This is an indication of a counter-intuitive phenomenon.

Two points of view can be provided to explain these results. First, it is probable that the buoyancy and percolation mechanisms are hampered by the effect of the particle shape. The preferred orientation taken by tablets D and E when flowing in the active layer may result in a lack of the space required for tablet C to segregate between them. In fact, it was observed experimentally that the preferred orientation taken by tablets D and E enabled them to slide along their longest edge. Second, perhaps the volume ratio does not dictate the observed segregation patterns. Indeed, given that tablets D and E slide along their longest edge (d_p in Figure 6-1), it is plausible that the width (d_l in Figure 6-1) or the height of the tablets would be a better criterion. For instance, tablet C has a smaller volume but a bigger width (d_l ratio) than tablets D and E, which may explain the reverse core segregation phenomenon described above. Further investigations would be required to fully understand the segregation mechanisms observed in this work. Nevertheless, the results presented here are of interest in that they highlight for the first time the effect that the shape of a particle may have on mixing and segregation inside a rotating drum.

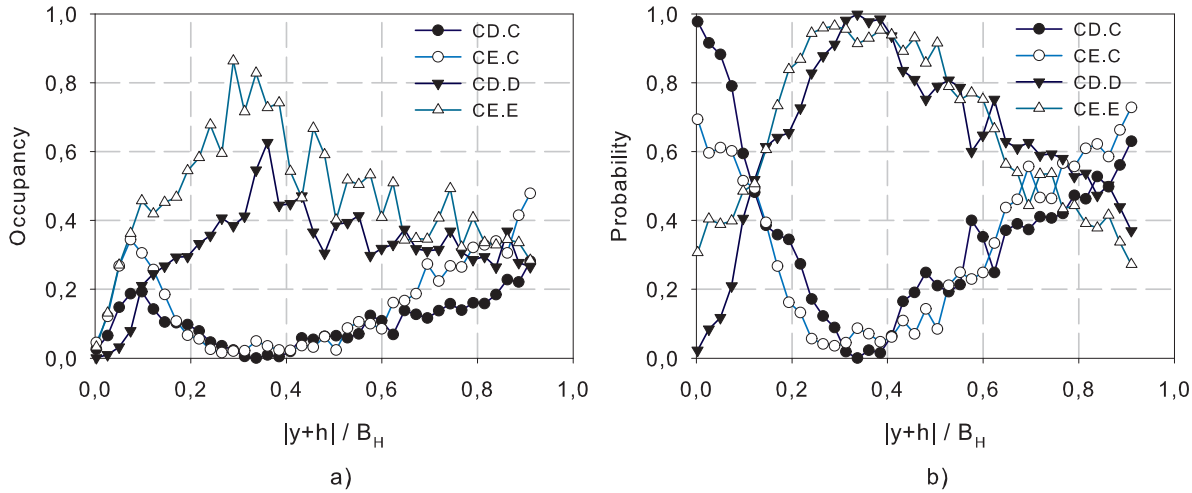

Figure 6-12 Values of a) the occupancy and b) the location probability for blends CD and CE.

6.2.4.3 Axial dispersion

It is well known that tumbling blenders used without intensifier bars or baffles suffer from weak axial mixing (Alizadeh, Hajhashemi, Bertrand, & Chaouki, 2013; Lemieux et al., 2007). Nevertheless, it is best to have efficient mixing in both the radial and axial directions. In this section, a comparison of the axial motion of the non-spherical tablets and the spherical glass beads is performed. To quantify the extent of axial displacement occurring in each experiment, the axial dispersion coefficient was computed using Einstein's law (Einstein, 1905):

$$D_{axial} = \frac{\sum_{i=1}^{N}\left(\Delta z_i - \overline{\Delta z}\right)^2 \Big/ \Delta t_i}{2\left(N-1\right)} \tag{6.25}$$

where Δz_i is the axial displacement of the tracer particle during the ith cycle, $\overline{\Delta z}$ the mean axial displacement of the tracer particle for the N cycles and Δt_i the time interval. To reduce the effect of the measurement error on the computation of the dispersion coefficient, the time interval for cycle i was taken as the residence time of the tracer particle along the corresponding streamline (Alizadeh, Dubé, et al., 2013; Sheritt et al., 2003). The residence time was approximated using the model presented in Section 6.2.4.1.4 (i.e. equation (6.24) and (6.15)).

Figure 6-13 displays the evolution of D_{axial} with respect to the active layer depth (ξ_0) and Table 6-9 contains the value of D_{axial} measured for all experiments.

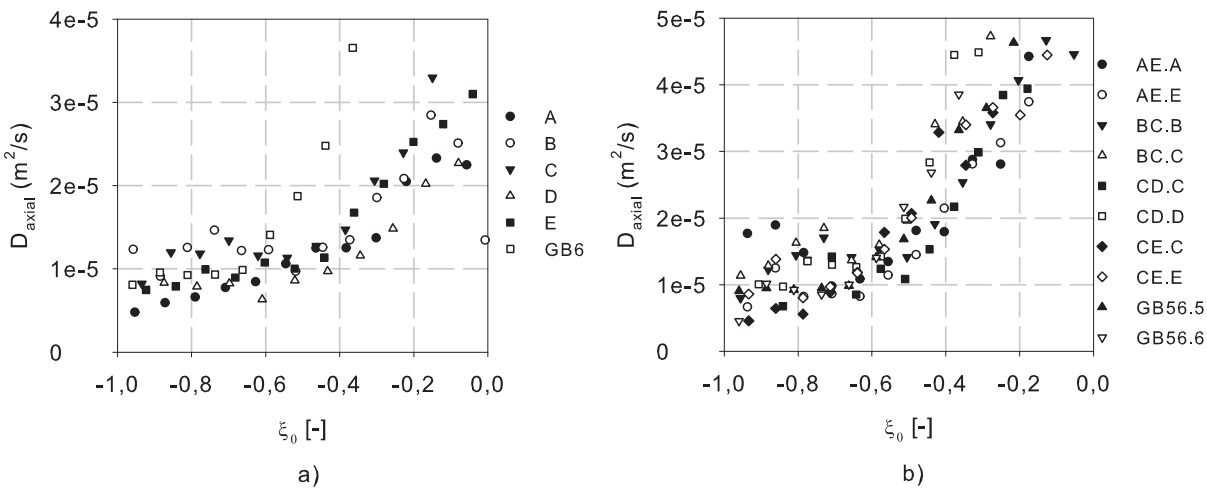

Figure 6-13 Evolution of D_{axial} with respect to the active layer depth (ξ_0).

As was reported by Alizadeh, Dubé et al. (2013), Figure 6-13 shows an increase in the axial dispersion coefficient as the depth in the active layer decreases. This behavior is expected as the particles found at or near the bed surface have more freedom to move and are in fact more likely to move axially. There does not seem to be a noteworthy difference between the D_{axial} profiles of the blends tested (Figure 6-13b), but a significant difference can be noticed between the D_{axial} profile of the 6mm glass beads and the ones obtained for the non-spherical tablets (Figure 6-13a).

Previous studies using polydisperse mixtures of particles have reported an increase in the dispersion coefficient with the increase of the particle size, except when large particles occupy the center of the bed (Alizadeh, Dubé, et al., 2013; Ingram et al., 2005). A similar trend is expected here for the non-spherical tablets composing a specific blend. In other words, a higher axial dispersion should be obtained for the particles most likely to be at or near the surface of the bed: $D_{axial,AE.A} < D_{axial,AE.E}$, $D_{axial,BC.B} < D_{axial,BC.C}$, $D_{axial,CD.D} < D_{axial,CD.C}$, $D_{axial,CE.E} < D_{axial,CE.C}$ and

$D_{axial,GB56.5} < D_{axial,GB56.6}$). In the case of the mono-disperse experiments, when comparing similar shapes, it is expected that the largest tablet should present a slightly higher dispersion coefficient: $D_{axial,A} < D_{axial,E}$ and $D_{axial,B} < D_{axial,C}$). Moreover, it is likely that a higher degree of preferred spatial orientation in the active layer will lead to a lower axial dispersion coefficient. This means that a higher dispersion coefficient for the glass bead is expected. For the same reason, tablet D should present a slightly lower coefficient than the other shapes. The results presented in Table 6-9 confirm all these expectations. However, the differences in axial dispersion are not significant in all cases. Experiments E, BC.B, and CD.C were repeated. The results obtained suggest that the uncertainty on D_{axial} is approximately 5×10^{-6} m^2/s. It must be noted that the values reported for the 6mm glass beads and the blend containing 5mm and 6mm glass beads are comparable to those reported by Alizadeh, Dubé et al. (2013).

Table 6-9 Axial dispersion coefficient

Type	Experiment ID	$D_{axial}\times10^{-6}\left[m^2/s\right]$
Mono-disperse	A	15.3
	B	15.9
	C	20.0
	D	12.9
	E	17.4
	GB6	34.2
Bi-disperse	AE.A	13.4
	AE.E	27.6
	AE.A*	8.0
	AE.E*	20.8
	BC.B	17.8
	BC.C	19.5
	CD.C	25.2
	CD.D	17.9
	CE.C	27.1
	CE.E	13.0
	GB56.5	14.3
	GB56.6	45.3

6.2.5 Conclusion

In this work, the dynamics of non-spherical particles in a rotating drum was investigated using pharmaceutical tablets. The tablets were composed of sodium bicarbonate, making them suitable tracer particles for the radioactive particle tracking (RPT) technique. Three important aspects of the particle dynamics in rotating drums were investigated: the active and passive layer residence times, the mixing and segregation as well as the axial dispersion. It was shown that models previously developed using spherical or nearly spherical particles could adequately predict the velocity profile and the active layer thickness, except when the non-spherical particles have a high aspect ratio (i.e. greater than two). In this case, significant deviations in the velocity profile were found under the bed surface. A model for the residence times in the active and passive layers was developed and good agreement was obtained with the RPT experimental data for most of the non-spherical tablets tested. It was observed that the mixing of non-spherical particles having different shapes led to unexpected reverse core segregation where the smaller and denser tablets were found on the outside of the bed and larger and lighter tablets in the bed core. Lastly, the non-spherical tablets displayed a lower axial dispersion coefficient than the spherical particles which can partially be attributed to the higher degree of spatial orientation of these non-spherical tablets in the active and passive layers.

6.2.6 Acknowledgements

The financial support of the Natural Sciences and Engineering Council of Canada (NSERC), the Research and Development Center of Teva (Mirabel, Quebec) and PRAXAIR Inc. is gratefully acknowledged. The authors are thankful to Cornelia Chilian and Rahma Kada from the SLOWPOKE Neutron Activation Analysis laboratory for the precise activations of the tracer particles.

6.2.7 References

Alexander, A., Shinbrot, T., Muzzio, F.J.: Scaling surface velocities in rotating cylinders as a function of vessel radius, rotation rate, and particle size. Powder Technology 126(2), 174-190 (2002)

Alizadeh, E., Dubé, O., Bertrand, F., Chaouki, J.: Characterization of Mixing and Size Segregation in a Rotating Drum by a Particle Tracking Method. AIChE Journal, n/a-n/a (2013a)

Alizadeh, E., Hajhashemi, H., Bertrand, F., Chaouki, J.: Experimental Investigation of Solid Mixing and Segregation in a Tetrapodal Blender. Submitted to Chemical Engineering Science, n/a-n/a (2013b)

Beam, G.B., Wielopolski, L., Gardner, R.P., Verghese, K.: Monte Carlo calculation of efficiencies of right-circular cylindrical NaI detectors for arbitrarily located point sources. Nuclear Instruments and Methods 154(3), 501-508 (1978)

Boateng, A.A.: Boundary layer modeling of granular flow in the transverse plane of a partially filled rotating cylinder. International Journal of Multiphase Flow 24(3), 499-521 (1998)

Boateng, A.A., Barr, P.V.: Granular flow behaviour in the transverse plane of a partially filled rotating cylinder. Journal of Fluid Mechanics 330, 233-249 (1997)

Cheng, N.-S., Zhou, Q., Keat Tan, S., Zhao, K.: Application of incomplete similarity theory for estimating maximum shear layer thickness of granular flows in rotating drums. Chemical Engineering Science 66(12), 2872-2878 (2011)

Cleary, P.W.: DEM prediction of industrial and geophysical particle flows. Particuology 8(2), 106-118 (2010)

Descoins, N., Dirion, J.L., Howes, T.: Solid transport in a pyrolysis pilot-scale rotary kiln: Preliminary results - Stationary and dynamic results. Chemical Engineering and Processing 44, 315-321 (2005)

Ding, Y.L., Forster, R., Seville, J.P.K., Parker, D.J.: Granular motion in rotating drums: bed turnover time and slumping-rolling transition. Powder Technology 124(1-2), 18-27 (2002a)

Ding, Y.L., Forster, R., Seville, J.P.K., Parker, D.J.: Segregation of granular flow in the transverse plane of a rolling mode rotating drum. International Journal of Multiphase Flow 28(4), 635-663 (2002b)

Ding, Y.L., Seville, J.P.K., Forster, R., Parker, D.J.: Solids motion in rolling mode rotating drums operated at low to medium rotational speeds. Chemical Engineering Science 56(5), 1769-1780 (2001)

Doucet, J., Bertrand, F., Chaouki, J.: An extended radioactive particle tracking method for systems with irregular moving boundaries. Powder Technology 181(2), 195-204 (2008)

Dubé, O., Dubé, D., Chaouki, J., Bertrand, F.: Optimization of detector positioning in the radioactive particle tracking technique. Submitted to Applied Radiation and Isotopes (2013)

Einstein, A.: Motion of suspended particles on the kinetic theory. Annalen der Physik 17(3), 549-560 (1905)

Fantozzi, F., Colantoni, S., Bartocci, P., Desideri, U.: Rotary kiln slow pyrolysis for syngas and char production from biomass and waste - Part I: Working envelope of the reactor. Journal of Engineering for Gas Turbines and Power 129(4), 901-907 (2007)

Felix, G., Falk, V., D'Ortona, U.: Segregation of dry granular material in rotating drum: Experimental study of the flowing zone thickness. Powder Technology 128(2-3), 314-319 (2002)

Felix, G., Falk, V., D'Ortona, U.: Granular flows in a rotating drum: The scaling law between velocity and thickness of the flow. European Physical Journal E 22(1), 25-31 (2007)

Henein, H., Brimacombe, J.K., Watkinson, A.P.: Experimental Study of Transverse Bed Motion in Rotary Kilns. Metallurgical Transactions B (Process Metallurgy) 14 B(2), 191-205 (1983)

Henein, H., Brimacombe, J.K., Watkinson, A.P.: Experimental Study of Segregation in Rotary Kilns. Metallurgical transactions. B (Process metallurgy) 16 B(4), 763-774 (1985)

Heydenrych, M.D., Greeff, P., Heesink, A.B.M., Versteeg, G.F.: Mass transfer in rolling rotary kilns: A novel approach. Chemical Engineering Science 57(18), 3851-3859 (2002)

Hill, K.M., Caprihan, A., Kakalios, J.: Bulk segregation in rotated granular material measured by magnetic resonance imaging. Physical Review Letters 78(1), 50-53 (1997)

Ingram, A., Seville, J.P.K., Parker, D.J., Fan, X., Forster, R.G.: Axial and radial dispersion in rolling mode rotating drums. Powder Technology 158(1-3), 76-91 (2005)

Jain, N., Ottino, J.M., Lueptow, R.M.: An experimental study of the flowing granular layer in a rotating tumbler. Physics of Fluids 14(2), 572-582 (2002)

Jain, N., Ottino, J.M., Lueptow, R.M.: Effect of interstitial fluid on a granular flowing layer. Journal of Fluid Mechanics 508, 23-44 (2004)

Jain, N., Ottino, J.M., Lueptow, R.M.: Regimes of segregation and mixing in combined size and density granular systems: An experimental study. Granular Matter 7(2-3), 69-81 (2005)

Kawaguchi, T.: MRI measurement of granular flows and fluid-particle flows. Advanced Powder Technology 21(3), 235-241 (2010)

Khakhar, D.V., McCarthy, J.J., Ottino, J.M.: Radial segregation of granular mixtures in rotating cylinders. Physics of Fluids 9(12), 3600-3614 (1997a)

Khakhar, D.V., McCarthy, J.J., Shinbrot, T., Ottino, J.M.: Transverse flow and mixing of granular materials in a rotating cylinder. Physics of Fluids 9(1), 31-43 (1997b)

Khakhar, D.V., Orpe, A.V., Andresen, P., Ottino, J.M.: Surface flow of granular materials: model and experiments in heap formation. Journal of Fluid Mechanics 441, 255-264 (2001a)

Khakhar, D.V., Orpe, A.V., Ottino, J.M.: Surface Granular Flows: Two related Examples. Advances in Complex Systems 04(04), 407-417 (2001b)

Larachi, F., Kennedy, G., Chaouki, J.: A -ray detection system for 3-D particle tracking in multiphase reactors. Nuclear Instruments and Methods in Physics Research, Section A (Accelerators, Spectrometers, Detectors and Associated Equipment) A338(2-3), 568-576 (1994)

Lemieux, M., Bertrand, F., Chaouki, J., Gosselin, P.: Comparative study of the mixing of free-flowing particles in a V-blender and a bin-blender. Chemical Engineering Science 62(6), 1783-1802 (2007)

Li, S.Q., Yan, J.H., Li, R.D., Chi, Y., Cen, K.F.: Axial transport and residence time of MSW in rotary kilns - Part I. Experimental. Powder Technology 126(3), 217-227 (2002)

Liu, X.Y., Specht, E.: Predicting the fraction of the mixing zone of a rolling bed in rotary kilns. Chemical Engineering Science 65(10), 3059-3063 (2010)

Liu, X.Y., Specht, E., Gonzalez, O.G., Walzel, P.: Analytical solution for the rolling-mode granular motion in rotary kilns. Chemical Engineering and Processing 45(6), 515-521 (2006)

Makse, H.A.: Continuous Avalanche Segregation of Granular Mixtures in Thin Rotating Drums. Physical Review Letters 83(16), 3186-3189 (1999)

Meier, S.W., Lueptow, R.M., Ottino, J.M.: A dynamical systems approach to mixing and segregation of granular materials in tumblers. Advances in Physics 56(5), 757-827 (2007)

Mellmann, J.: The transverse motion of solids in rotating cylinders-forms of motion and transition behavior. Powder Technology 118(3), 251-270 (2001)

Mellmann, J., Specht, E., Liu, X.: Prediction of rolling bed motion in rotating cylinders. AIChE Journal 50(11), 2783-2793 (2004)

Nakagawa, M., Altobelli, S.A., Caprihan, A., Fukushima, E., Jeong, E.K.: Non-invasive measurements of granular flows by magnetic resonance imaging. Experiments in Fluids 16(1), 54-60 (1993)

Ndiaye, L.G., Caillat, S., Chinnayya, A., Gambier, D., Baudoin, B.: Application of the dynamic model of Saeman to an industrial rotary kiln incinerator: Numerical and experimental results. Waste Management 30(7), 1188-1195 (2010)

Orpe, A.V., Khakhar, D.V.: Scaling relations for granular flow in quasi-two-dimensional rotating cylinders. Physical Review E - Statistical, Nonlinear, and Soft Matter Physics 64(3 I), 313021-3130213 (2001)

Parker, D.J., Dijkstra, A.E., Martin, T.W., Seville, J.P.K.: Positron emission particle tracking studies of spherical particle motion in rotating drums. Chemical Engineering Science 52(13), 2011-2022 (1997)

Ridgway, K., Rupp, R.: Mixing of powder layers on a chute. The effect of particle size and shape. Powder Technology 4(4), 195-202 (1971)

Roy, S., Larachi, F., Al-Dahhan, M.H., Dudukovic, M.P.: Optimal design of radioactive particle tracking experiments for flow mapping in opaque multiphase reactors. Applied Radiation and Isotopes 56(3), 485-503 (2002)

Sheritt, R.G., Chaouki, J., Mehrotra, A.K., Behie, L.A.: Axial dispersion in the three-dimensional mixing of particles in a rotating drum reactor. Chemical Engineering Science 58(2), 401-415 (2003)

Sturman, R., Meier, S.W., Ottino, J.M., Wiggins, S.: Linked twist map formalism in two and three dimensions applied to mixing in tumbled granular flows. Journal of Fluid Mechanics 602, 129-174 (2008)

Suzzi, D., Toschkoff, G., Radl, S., Machold, D., Fraser, S.D., Glasser, B.J., Khinast, J.G.: DEM simulation of continuous tablet coating: Effects of tablet shape and fill level on inter-tablet coating variability. Chemical Engineering Science 69(1), 107-121 (2012)

Thomas, N.: Reverse and intermediate segregation of large beads in dry granular media. Physical Review E - Statistical Physics, Plasmas, Fluids, and Related Interdisciplinary Topics 62(1 B), 961-974 (2000)

Tobiska, S., Kleinebudde, P.: Coating uniformity and coating efficiency in a Bohle Lab-Coaterusing oval tablets. European Journal of Pharmaceutics and Biopharmaceutics 56(1), 3-9 (2003)

Van Puyvelde, D.R., Young, B.R., Wilson, M.A., Schmidt, S.J.: Modelling transverse segregation of particulate solids in a rolling drum. Chemical Engineering Research and Design 78(4), 643-650 (2000)

Weir, G., Krouse, D., McGavin, P.: The maximum thickness of upper shear layers of granular materials in rotating cylinders. Chemical Engineering Science 60(7), 2027-2035 (2005)

Wightman, C., Muzzio, F.J.: Mixing of granular material in a drum mixer undergoing rotational and rocking motions II. Segregating particles. Powder Technology 98(2), 125-134 (1998)

Wilson, K.E., Crossman, E.: The Influence of Tablet Shape and Pan Speed on Intra-tablet Film Coating Uniformity. Drug Development and Industrial Pharmacy 23(12), 1239-1243 (1997)

Woodle, G.R., Munro, J.M.: Particle motion and mixing in a rotary kiln. Powder Technology 76(3), 241-245 (1993)

CHAPITRE 7 DISCUSSION GÉNÉRALE

L'objectif principal de la thèse comporte deux volets traités ici séparément, soit les écoulements particulaires denses dans un lit fixe et ceux dans un lit rotatif.

7.1 Écoulements particulaires denses dans un lit fixe

L'écoulement particulaire se produisant à l'intérieur d'un lit fixe suite à une expansion et contraction thermique cyclique des murs d'un réacteur à flux radial (RFR) a été étudié à l'aide de simulations utilisant la méthode des éléments discrets (DEM). Ces simulations ont démontré que si le modèle DEM est adéquatement calibré à l'aide de mesures expérimentales directes des propriétés particulaires et par le biais d'expériences auxiliaires simples, celui-ci est capable de reproduire la phénoménologie de l'écoulement particulaire à l'intérieur d'un lit fixe. La précision du modèle DEM a été évaluée en utilisant les valeurs expérimentales de porosité d'un lit fixe, les valeurs analytiques de pression prédites par la théorie de Janssen ainsi que les valeurs expérimentales de pression mesurées aux parois du lit fixe d'une unité commerciale de pré-purification de l'air réalisée à l'aide d'un procédé d'adsorption par oscillations thermiques (TSA).

Lors de la comparaison des résultats de pression DEM à ceux prédits par la théorie de Janssen, il ressort que la DEM surestime la pression normale lorsque la hauteur du lit particulaire est grande. Deux explications ont été avancées pour tenter d'expliquer ce phénomène. La première concerne les hypothèses utilisées par Janssen lors de l'élaboration de sa théorie alors que la seconde concerne le lien existant entre les propriétés microscopiques, utilisées par la DEM, et les propriétés macroscopiques, utilisées par la théorie de Janssen. Aucune de ces deux explications ne peuvent à elles seules expliquer l'écart obtenu entre la théorie de Janssen et les résultats DEM. Une étude plus approfondie est nécessaire pour connaître la cause des déviations observées. Cependant, l'accord quantitatif obtenu entre les pressions mesurées par la DEM et celles prédites par la théorie de Janssen pour les lits fixes de plus petite hauteur permet quand même une

vérification du modèle DEM. Le modèle DEM a aussi été vérifié en comparant la pression obtenue à l'aide de simulations DEM lorsque les murs du lit fixe se déplacent à celle mesurée sur une unité d'adsorption commerciale en opération. La pression maximale mesurée à chaque cycle DEM a présenté un comportement asymptotique se stabilisant à une valeur comparable à celle mesurée sur l'unité commerciale. De plus, l'évolution de la pression obtenue par les simulations DEM a affiché un comportement qualitativement et quantitativement similaire à celui mesuré sur l'unité commerciale, confirmant ainsi que le modèle DEM est capable de reproduire la phénoménologie de ce type d'écoulement. Il est important de noter que la vérification du modèle DEM n'a été possible que parce que les véritables propriétés particulaires et qu'un pas de temps extrêmement faible ont été utilisés pour les simulations. L'utilisation d'un module de Young de l'ordre du MPa plutôt que du GPa aurait permis l'utilisation d'un pas de temps significativement plus grand mais le modèle DEM n'aurait pas pu être vérifié à l'aide de mesures de pression.

La vérification du modèle DEM à l'aide des pressions mesurées sur une unité commerciale en opération a permis d'identifier la fréquence de cycle à utiliser pour étudier la dispersion survenant à l'interface des adsorbants. Ainsi, des coefficients de dispersions radiaux relativement similaires ont été obtenus pour les deux types d'adsorbants. Ces coefficients de dispersion ont semblé se stabiliser rapidement, soient après seulement quatre cycles. Ceux-ci peuvent être utilisés pour résoudre une équation de diffusion transitoire et ainsi prédire l'état du mélange à l'interface après plusieurs années d'opération.

Il est possible de croire que l'étude DEM réalisée pour caractériser l'écoulement particulaire à l'intérieur d'un lit fixe a permis d'évaluer l'écoulement maximal pouvant survenir. Tout d'abord, les simulations réalisées ont considéré les parois du RFR comme étant rigides alors qu'elles sont élastiques. Le mouvement simulé des parois est donc plus grand que ce qui est susceptible de se produire en réalité. De plus, les mêmes déplacements de murs ont été reproduits à chaque cycle alors qu'il est plutôt fort probable que ceux-ci s'amenuisent avec le temps. Cependant, il ne faut pas oublier que les propriétés des particules ont été considérées constantes alors qu'il est possible que ces dernières changent en cours de cycle, étant donné que la composition à la surface des particules est modifiée due à l'adsorption de contaminants. De surcroît, l'effet de la circulation de

l'air à travers le lit fixe n'a pas été pris en compte non plus. Il est possible que dans ces circonstances, le passage du gaz amplifie ou diminue la dispersion particulaire mesurée.

7.2 Écoulements particulaires non-sphériques denses dans un cylindre rotatif

L'écoulement de particules non-sphériques à l'intérieur d'un cylindre rotatif a été caractérisé à l'aide de la technique de suivi de particules radioactives (RPT) et de comprimés pharmaceutiques. Cependant, pour que la RPT puisse être utilisée pour suivre la trajectoire des comprimés, il a été nécessaire de développer une stratégie d'optimisation permettant d'identifier un positionnement optimal des détecteurs à scintillation.

La stratégie d'optimisation qui a été développée utilise une méthode de recherche directe à maillage adaptatif (MADS) comme algorithme d'optimisation ainsi que la résolution des détecteurs comme fonction-objectif. La stratégie a été validée à l'aide d'un système où le positionnement optimal des détecteurs est connu. Elle a ensuite été appliquée à un cas fréquemment étudié à l'aide de la RPT (i.e. une colonne verticale pouvant représenter un lit d'air fluidisé ou autre) ainsi qu'au cas concerné par cette thèse, soit un cylindre rotatif partiellement rempli. La stratégie développée permet d'identifier un positionnement optimal qui est spécifique à l'objectif de l'étude de même qu'aux conditions expérimentales dans lesquelles l'expérience RPT est réalisée. Par contre, le temps calcul nécessaire à la réalisation d'une seule optimisation augmente rapidement avec le nombre de variables à optimiser. De plus, les résultats obtenus avec la stratégie d'optimisation ont démontré que cette dernière doit, dans la plupart des cas, être lancée plusieurs fois afin d'avoir une bonne idée de la configuration optimale des détecteurs. Il a aussi été démontré que le nombre de détecteurs dont le positionnement peut être optimisé est limité par le choix de la fonction-objectif. Ce nombre dépend essentiellement de la taille du système auquel la RPT est appliquée. Si un trop grand nombre de détecteurs est utilisé, la fonction-objectif n'est plus assez sensible pour pouvoir réaliser une optimisation adéquate. Cependant, la démonstration a été faite que cette limitation de la fonction-objectif pourrait servir à identifier un nombre optimal de détecteurs à utiliser pour réaliser une expérience.

L’application en laboratoire d’une configuration optimale identifiée par la stratégie d’optimisation a permis de réduire significativement l’erreur commise lors de la reconstruction de la position d’un comprimé pharmaceutique immobile (comprimé A présenté à la Figure 3-7) utilisé comme traceur radioactif. Afin d’apprécier davantage l’impact du positionnement sur les résultats recueillis par la technique RPT, la Figure 7-1 compare le champ de vitesse de ce même comprimé obtenu à l’aide d’un positionnement non-optimal et optimal. Il est possible de remarquer que le positionnement optimal a permis d’éliminer le « bruit » mesuré à la surface du lit particulaire ainsi qu’aux extrémités de l’écoulement et d’améliorer significativement la qualité des résultats.

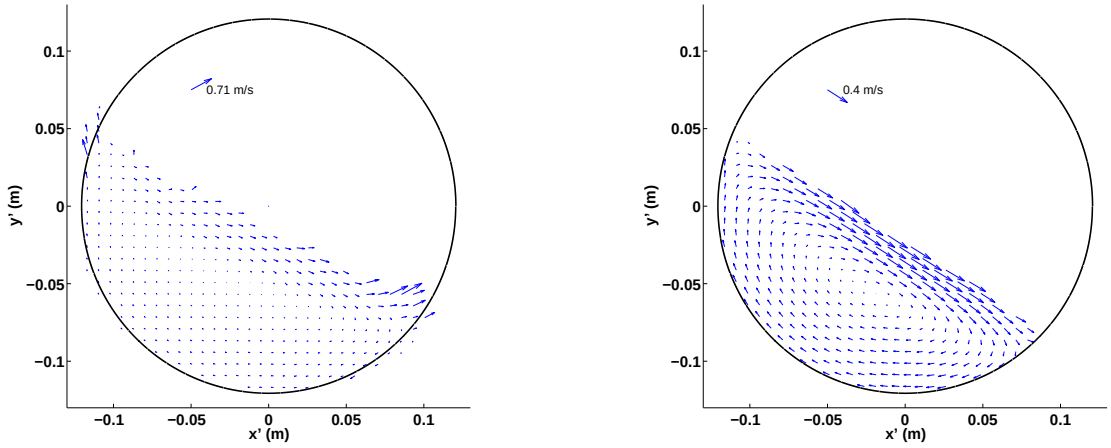

a) b)

Figure 7-1 Comparaison des champs de vitesse obtenus à l'aide d'un positionnement a) non-optimal et b) optimal pour le comprimé A.

Grâce aux connaissances acquises avec la stratégie d’optimisation, la dynamique d’écoulement de particules non-sphériques à l’intérieur d’un cylindre rotatif a pu être quantifiée à l’aide de la technique RPT. Pour ce faire, des comprimés de tailles et de formes variées ont été employés. Il a été constaté que les formes ayant un côté droit présentent généralement un angle de repos

dynamique plus élevé que celui des autres formes. Le côté droit permet de former des structures stables en amont de l'écoulement. Dans le cas où le côté droit d'une particule est long, il appert que les structures formées affectent significativement les profils de vitesse ainsi que la position de l'interface séparant la couche passive de la couche active. L'analyse des profils de vitesse le long de la surface de l'écoulement des particules non-sphériques et des particules sphériques a permis de constater que les particules non-sphériques ont tendance à glisser plutôt que de rouler. De plus, les particules non-sphériques testées ont toutes présenté un coefficient de dispersion axiale plus faible que celui des particules sphériques. La technique RPT employée pour caractériser la dynamique particulaire n'a pas permis de suivre l'orientation prise par les particules lors de leur écoulement. Cependant, les données recueillies ainsi que les observations réalisées en laboratoire permettent de supposer que les particules non-sphériques s'écoulent selon une orientation spatiale préférentielle. Cette dernière semble être une des raisons pouvant expliquer les différences observées entre certaines particules non-sphériques et les particules sphériques.

À l'aide des données recueillies sur les profils de vitesse, il a été possible de modéliser le temps de résidence des particules dans les couches active et passive du cylindre. Le modèle peut être utilisé de manière prédictive en autant que l'écoulement particulaire considéré est en accord avec les hypothèses qui ont servi à créer le modèle.

Pour la première fois, le mélange et la ségrégation à l'intérieur d'un cylindre rotatif de particules de formes similaires mais de tailles différentes ainsi que de masses similaires mais de formes différentes a aussi été étudié. Une ségrégation radiale traditionnelle, où les particules petites ou denses se retrouvent au centre de l'écoulement alors que les grosses et légères se retrouvent en périphérie, a été observée dans la plupart des cas. Une ségrégation radiale inverse a toutefois été constatée dans le cas où de grosses particules longues et plates étaient mélangées à de petites particules denses. Dans ce cas-ci, les petites particules denses se sont retrouvées en périphérie de l'écoulement plutôt que dans le centre. Davantage d'études sont nécessaires pour identifier la cause de ce phénomène mais celui-ci permet néanmoins d'exposer l'effet que la forme particulaire peut avoir sur le mélange et la ségrégation.

CONCLUSION ET RECOMMANDATIONS

L'objectif principal de la présente thèse était de caractériser la dynamique particulaire des écoulements denses, en lits fixes pour l'écoulement de particules sphériques résultant d'un phénomène de transfert thermique, et en lits rotatifs pour des particules non-sphériques.

L'effet sur un lit particulaire fixe d'une contraction et d'une expansion thermique cyclique des murs d'un réacteur à flux radial utilisé pour la pré-purification de gaz a pour la première fois été évalué à l'aide de la méthode des éléments discrets (DEM). L'incorporation des véritables propriétés particulaires au modèle DEM de même que l'utilisation d'un pas de temps excessivement faible ont permis de vérifier le modèle numérique établi. L'utilisation de la DEM dans le cadre de cette étude a permis d'évaluer la dispersion particulaire pouvant survenir à l'interface des adsorbants composant le lit fixe. Cette mesure peut permettre d'évaluer la qualité du lit fixe après plusieurs années d'utilisation. Il est important de noter que le modèle DEM développé ne considère pas l'effet du gaz circulant à travers le lit fixe de même que les changements au niveau des propriétés particulaires pouvant survenir en cours de cycle. Néanmoins, les résultats obtenus avec le modèle montrent que la DEM est un outil utile pour l'étude de ce type de dynamique lente, à condition qu'une calibration minutieuse ait été préalablement réalisée.

La dynamique, le mélange et la ségrégation de particules non-sphériques à l'intérieur d'un cylindre rotatif ont été caractérisés à l'aide de la technique de suivi de particules radioactives (RPT). Des comprimés pharmaceutiques de tailles et de formes variées ont été utilisés. Les résultats obtenus ont permis pour la première fois de mettre en évidence l'effet que peut avoir la forme de la particule sur la dynamique, le mélange et la ségrégation de celle-ci dans le cadre d'écoulements particulaires denses dans un cylindre rotatif. Un modèle, prédisant le temps de résidence des particules dans les différentes zones de l'écoulement, applicable aux cas de particules sphériques et non-sphériques dont le comportement est similaire à celui de particules sphériques, a été développé. Étant donné les formes restreintes testées, les conclusions tirées de

cette étude sont difficilement généralisables. Cependant, l'orientation préférentielle prise par les particules non-sphériques lorsqu'elles s'écoulent peut expliquer les comportements observés. Davantage de formes doivent être testées pour véritablement identifier les effets de la forme particulaire sur les écoulements denses dans des lits rotatifs.

Pour que la technique RPT puisse être appliquée au cas des particules non-sphériques considérées dans cette thèse, une stratégie d'optimisation permettant d'identifier un positionnement optimal des détecteurs à scintillation utilisés a d'abord été développée. Cette stratégie présente comme avantage de pouvoir identifier une configuration optimale des détecteurs qui est propre à l'objectif de l'étude ainsi qu'aux conditions expérimentales. Elle peut donc facilement être appliquée à d'autres types d'études que celle réalisée dans le cadre de cette thèse. L'application de la stratégie a montré que le nombre de détecteurs dont le positionnement optimal peut être identifié par cette stratégie est limité par la sensibilité de la fonction-objectif employée pour l'optimisation. Cette limitation peut cependant servir à identifier un nombre optimal de détecteurs à utiliser pour réaliser une étude à l'aide de la technique RPT.

À la suite de cette thèse, les recommandations suivantes peuvent être faites :

1. Développer une approche multi-échelle DEM-CFD pour quantifier l'effet combiné de la circulation du gaz et de la contraction/expansion cyclique des parois du lit fixe sur la dispersion des particules ainsi que sur l'uniformité de l'écoulement du gaz selon la hauteur du lit fixe.
2. Identifier et tester une fonction-objectif équivalente (« surrogate function ») dans le but d'accélérer significativement la stratégie d'optimisation et ainsi permettre l'optimisation d'un plus grand nombre de variables.
3. Développer une stratégie d'optimisation permettant d'identifier à la fois le nombre optimal de détecteurs à utiliser pour une expérience RPT et le positionnement de ceux-ci.
4. Étudier l'orientation préférentielle prise par les particules non-sphériques lorsqu'elles s'écoulent.

5. Identifier la raison du phénomène de ségrégation radiale non-traditionnelle observé à l’aide des particules non-sphériques utilisées.
6. Développer, améliorer et valider des modèles de non-sphéricité pour la DEM à l’aide des résultats expérimentaux recueillis avec la technique RPT et les comprimés pharmaceutiques. D’ailleurs, les formes utilisées dans le cadre de cette thèse présentent l’avantage de pouvoir être facilement reproduites par un assemblage de sphères, soit la méthode la plus fréquemment utilisée pour représenter des formes non-sphériques en DEM.

BIBLIOGRAPHIE

Abramson, M. A., Audet, C., Couture, G., Dennis, J. E. J., Le Digabel, S., & Tribes, C. (2012). The NOMAD Project (Version 3.5.1): Software available at http://www.gerad.ca/nomad. Tiré de http://www.gerad.ca/nomad

Abramson, M. A., Audet, C., Dennis, J. E., Jr., & Le Digabel, S. (2009). ORTHOMADS: a deterministic MADS instance with orthogonal directions. *SIAM Journal on Optimization, 20*(2), 948-966.

Ackley, M. W., Celik, C. E., Nowobilski, J. J., & Schneider, J. S. (2011). US 8,216,343 B2.

Ackley, M. W., Celik, C. E., Nowobilski, J. J., & Schneider, J. S. (2012). US 8,101,133 B2.

Akseli, I., & Cetinkaya, C. (2008). Drug tablet thickness estimations using air-coupled acoustics. *International Journal of Pharmaceutics, 351*(1–2), 165-173.

Alexander, A., Shinbrot, T., & Muzzio, F. J. (2002). Scaling surface velocities in rotating cylinders as a function of vessel radius, rotation rate, and particle size. *Powder Technology, 126*(2), 174-190.

Alizadeh, E., Bertrand, F., & Chaouki, J. (2013). Comparison of DEM results and lagrangian experimental data for the mixing and segregation of granules in a rotating drum. *Submitted to AIChE Journal*, n/a-n/a.

Alizadeh, E., Dubé, O., Bertrand, F., & Chaouki, J. (2013). Characterization of Mixing and Size Segregation in a Rotating Drum by a Particle Tracking Method. *AIChE Journal*, n/a-n/a.

Alizadeh, E., Hajhashemi, H., Bertrand, F., & Chaouki, J. (2013). Experimental Investigation of Solid Mixing and Segregation in a Tetrapodal Blender. *Submitted to Chemical Engineering Science*, n/a-n/a.

Arratia, P. E., Duong, N.-H., Muzzio, F. J., Godbole, P., Lange, A., & Reynolds, S. (2006). Characterizing mixing and lubrication in the Bohle Bin blender. *Powder Technology, 161*(3), 202-208.

Audet, C., Bechard, V., & Chaouki, J. (2008). Spent potliner treatment process optimization using a MADS algorithm. *Optimization and Engineering, 9*(2), 143-160.

Audet, C., & Dennis, J. E. J. (2006). Mesh adaptive direct search algorithms for constrained optimization. *SIAM Journal on Optimization, 17*(1), 188-217.

Audet, C., Dennis, J. E. J., & Le Digabel, S. (2010). Globalization strategies for mesh adaptive direct search. *Computational Optimization and Applications, 46*, 193-215.

Balevicius, R., Sielamowicz, I., Mroz, Z., & Kacianauskas, R. (2011). Investigation of wall stress and outflow rate in a flat-bottomed bin: A comparison of the DEM model results with the experimental measurements. *Powder Technology, 214*(3), 322-336.

Beam, G. B., Wielopolski, L., Gardner, R. P., & Verghese, K. (1978). Monte Carlo calculation of efficiencies of right-circular cylindrical NaI detectors for arbitrarily located point sources. *Nuclear Instruments and Methods, 154*(3), 501-508.

Berthiaux, H. (2002). Mélange et homogénéisation des solides divisés. *Techniques de l'ingénieur Principes de formulation, base documentaire : TIB489DUO*(ref. article : j3397).

Bertrand, F., Gange, T., Desaulniers, E., Vidal, D., & Hayes, R. E. (2004). Simulation of the consolidation of paper coating structures: Probabilistic versus deterministic models. *Computers and Chemical Engineering, 28*(12), 2595-2604.

Bertrand, F., Leclaire, L. A., & Levecque, G. (2005). DEM-based models for the mixing of granular materials. *Chemical Engineering Science, 60*, 2517-2531.

Bhusarapu, S., Al-Dahhan, M. H., & Dudukovic, M. P. (2006). Solids flow mapping in a gas-solid riser: Mean holdup and velocity fields. *Powder Technology, 163*(1-2), 98-123.

Boateng, A. A. (1998). Boundary layer modeling of granular flow in the transverse plane of a partially filled rotating cylinder. *International Journal of Multiphase Flow, 24*(3), 499-521.

Boateng, A. A., & Barr, P. V. (1997). Granular flow behaviour in the transverse plane of a partially filled rotating cylinder. *Journal of Fluid Mechanics, 330*, 233-249.

Bouffard, J. (2012). *Dynamique d'écoulement et pellétisation dans un granulateur à rotor* (Ph.D.), Ecole Polytechnique, Montreal (Canada), Canada. Tiré de ProQuest Dissertations & Theses Full Text.

Bouffard, J., Bertrand, F., & Chaouki, J. (2012). A multiscale model for the simulation of granulation in rotor-based equipment. *Chemical Engineering Science, 81*, 106-117.

Bridgwater, J. (1995). Particle technology. *Chemical Engineering Science, 50*(24 pt B), 4081-4089.

Brone, D., Alexander, A., & Muzzio, F. J. (1998). Quantitative characterization of mixing of dry powders in V-blenders. *AIChE Journal, 44*(2), 271-278.

Brucks, A., Arndt, T., Ottino, J. M., & Lueptow, R. M. (2007). Behavior of flowing granular materials under variable g. *Physical Review E - Statistical, Nonlinear, and Soft Matter Physics, 75*(3).

Campbell, C. S. (1990). Rapid Granular Flows. *Annual Review of Fluid Mechanics, 22*(1), 57-90.

Campbell, C. S. (2006). Granular material flows - An overview. *Powder Technology, 162*(3), 208-229.

Cassanello, M., Larachi, F., Legros, R., & Chaouki, J. (1999). Solids dynamics from experimental trajectory time-series of a single particle motion in gas-spouted beds. *Chemical Engineering Science, 54*(13-14), 2545-2554.

Cassanello, M., Larachi, F., Marie, M.-N., Guy, C., & Chaouki, J. (1995). Experimental characterization of the solid phase chaotic dynamics in three-phase fluidization. *Industrial and Engineering Chemistry Research, 34*(9), 2971-2980.

Cassanello, M. C., Fraguio, M. S., Larachi, F., & Chaouki, J. (2006). Flow regime transition pointers in three-phase fluidized beds inferred from a solid tracer trajectory. *Chemical Engineering and Processing, 45*(5), 350-358.

Celik, C. E., & Ackley, M. W. (2012). US 8,313,561 B2.

Cetinkaya, C. (2009). *Accoustic Measurement of Young's Modulus and Poisson's Ratio for Adsorbents Beads*.

Chaouki, J., Larachi, F., & Dudukovic, M. P. (1997). Noninvasive tomographic and velocimetric monitoring of multiphase flows. *Industrial and Engineering Chemistry Research, 36*(11), 4476-4503.

Chaudhuri, B., Muzzio, F. J., & Tomassone, M. S. (2010). Experimentally validated computations of heat transfer in granular materials in rotary calciners. *Powder Technology, 198*(1), 6-15.

Chen, P., Ottino, J. M., & Lueptow, R. M. (2010). Onset mechanism for granular axial band formation in rotating tumblers. *Physical Review Letters, 104*(18).

Cheng, N.-S., Zhou, Q., Keat Tan, S., & Zhao, K. (2011). Application of incomplete similarity theory for estimating maximum shear layer thickness of granular flows in rotating drums. *Chemical Engineering Science, 66*(12), 2872-2878.

Chung, Y. C., Hsiau, S. S., Liao, H. H., & Ooi, J. Y. (2010). An improved PTV technique to evaluate the velocity field of non-spherical particles. *Powder Technology, 202*(1-3), 151-161.

Cleary, P. W. (2008). The effect of particle shape on simple shear flows. *Powder Technology, 179*(3), 144-163.

Cleary, P. W. (2010). DEM prediction of industrial and geophysical particle flows. *Particuology, 8*(2), 106-118.

Collection of authors. (2005). So Much More to Know. *Science, 309*(5731), 78-102.

Couroyer, C., Ning, Z., Ghadiri, M., Brunard, N., Kolenda, F., Bortzmeyer, D., & Laval, P. (1999). Breakage of macroporous alumina beads under compressive loading: Simulation and experimental validation. *Powder Technology, 105*, 57-65.

Cundall, P. A., & Strack, O. D. L. (1979). Discrete Numerical Model for Granular Assemblies. *Geotechnique, 29*(1), 47-65.

Das, G. S., Khakhar, D. V., & Bhatia, S. K. (1991). Axial segregation of particles in a horizontal rotating cylinder. *Chemical Engineering Science, 46*(5-6), 1513-1513.

Descoins, N., Dirion, J. L., & Howes, T. (2005). Solid transport in a pyrolysis pilot-scale rotary kiln: Preliminary results - Stationary and dynamic results. *Chemical Engineering and Processing, 44*, 315-321.

Devanathan, N., Moslemian, D., & Dudukovic, M. P. (1990). Flow mapping in bubble columns using CARPT. *Chemical Engineering Science, 45*(8), 2285-2291.

Di Renzo, A., & Di Maio, F. P. (2004). Comparison of contact-force models for the simulation of collisions in DEM-based granular flow codes. *Chemical Engineering Science, 59*(3), 525-541.

Ding, Y. L., Forster, R., Seville, J. P. K., & Parker, D. J. (2002a). Granular motion in rotating drums: bed turnover time and slumping-rolling transition. *Powder Technology, 124*(1-2), 18-27.

Ding, Y. L., Forster, R., Seville, J. P. K., & Parker, D. J. (2002b). Segregation of granular flow in the transverse plane of a rolling mode rotating drum. *International Journal of Multiphase Flow, 28*(4), 635-663.

Ding, Y. L., Seville, J. P. K., Forster, R., & Parker, D. J. (2001). Solids motion in rolling mode rotating drums operated at low to medium rotational speeds. *Chemical Engineering Science, 56*(5), 1769-1780.

Djeridane, T., Larachi, F., Roy, D., Chaouki, J., & Legros, R. (1998). Investigation of the mean and turbulent particle velocity fields in a spouted bed using radioactive particle tracking. *Canadian Journal of Chemical Engineering, 76*(2), 190-195.

Doucet, J. (2008). *Mesure et caracterisation du melange dans les systemes granulaires denses.* NR41746 (Ph.D.), Ecole Polytechnique, Montreal (Canada), Canada. Tiré de ProQuest Dissertations & Theses Full Text.

Doucet, J., Bertrand, F., & Chaouki, J. (2008). An extended radioactive particle tracking method for systems with irregular moving boundaries. *Powder Technology, 181*(2), 195-204.

Doucet, J., Hudon, N., Bertrand, F., & Chaouki, J. (2008). Modeling of the mixing of monodisperse particles using a stationary DEM-based Markov process. *Computers and Chemical Engineering, 32*(6), 1342-1349.

Dubé, O., Alizadeh, E., Chaouki, J., & Bertrand, F. (2013). Dynamics of non-spherical particles in a rotating drum. *Submitted to Chemical Engineering Science*.

Dubé, O., Bouffard, J., Legros, R., Bertrand, F., & Chaouki, J. (2009). *Dynamics of Mono-Shaped Non-Spherical Particles in a Cylindrical Tumbler*. 8th World Congress of Chemical Engineering, Montréal, Québec, Canada.

Dubé, O., Chaouki, J., & Bertrand, F. (2012). A Fast and Robust Method for the Discrete Element Simulation of Non-Spherical Granular Flows. *14th Asia Pacific Confederation of Chemical Engineering Congress, Singapore*.

Dubé, O., Dubé, D., Chaouki, J., & Bertrand, F. (2013). Optimization of detector positioning in the radioactive particle tracking technique. *Submitted to Applied Radiation and Isotopes*.

Einstein, A. (1905). Motion of suspended particles on the kinetic theory. *Annalen der Physik, 17*(3), 549-560.

Elperin, T., & Vikhansky, A. (1998). Kinematics of the mixing of granular material in slowly rotating containers. *Europhysics Letters, 43*(1), 17-22.

Fantozzi, F., Colantoni, S., Bartocci, P., & Desideri, U. (2007). Rotary kiln slow pyrolysis for syngas and char production from biomass and waste - Part I: Working envelope of the reactor. *Journal of Engineering for Gas Turbines and Power, 129*(4), 901-907.

Felix, G., Falk, V., & D'Ortona, U. (2002). Segregation of dry granular material in rotating drum: Experimental study of the flowing zone thickness. *Powder Technology, 128*(2-3), 314-319.

Felix, G., Falk, V., & D'Ortona, U. (2007). Granular flows in a rotating drum: The scaling law between velocity and thickness of the flow. *European Physical Journal E, 22*(1), 25-31.

Feng, Y. T., Han, K., & Owen, D. R. J. (2010). Combined three-dimensional lattice Boltzmann method and discrete element method for modelling fluid-particle interactions with experimental assessment. *International Journal for Numerical Methods in Engineering, 81*(2), 229-245.

Figueroa, I., Vargas, W. L., & McCarthy, J. J. (2010). Mixing and heat conduction in rotating tumblers. *Chemical Engineering Science, 65*(2), 1045-1054.

Fraguio, M. S., Cassanello, M. C., Larachi, F., & Chaouki, J. (2006). Flow regime transition pointers in three-phase fluidized beds inferred from a solid tracer trajectory. *Chemical Engineering and Processing, 45*(5), 350-358.

Fraguio, M. S., Cassanello, M. C., Larachi, F., Limtrakul, S., & Dudukovic, M. (2007). Classifying flow regimes in three-phase fluidized beds from CARPT experiments. *Chemical Engineering Science, 62*(24), 7523-7529.

Fraige, F. Y., & Langston, P. A. (2004). Integration schemes and damping algorithms in distinct element models. *Advanced Powder Technology, 15*(2), 227-245.

Fraige, F. Y., Langston, P. A., & Chen, G. Z. (2008). Distinct element modelling of cubic particle packing and flow. *Powder Technology, 186*(3), 224-240.

Freireich, B., Li, J., Litster, J., & Wassgren, C. (2011). Incorporating particle flow information from discrete element simulations in population balance models of mixer-coaters. *Chemical Engineering Science, 66*(16), 3592-3604.

Fries, L., Antonyuk, S., Heinrich, S., Dopfer, D., & Palzer, S. (2013). Collision dynamics in fluidised bed granulators: A DEM-CFD study. *Chemical Engineering Science, 86*, 108-123.

GDR MiDi. (2004). On dense granular flows. *The European Physical Journal E, 14*(4), 341-365.

Goda, T. J., & Ebert, F. (2005). Three-dimensional discrete element simulations in hoppers and silos. *Powder Technology, 158*(1-3), 58-68.

Godfroy, L., Larachi, F., Kennedy, G., Grandjean, B., & Chaouki, J. (1997). On-line flow visualization in multiphase reactors using neural networks. *Applied Radiation and Isotopes, 48*(2), 225-235.

Gonzalez-Montellano, C., Gallego, E., Ramirez-Gomez, A., & Ayuga, F. (2012). Three dimensional discrete element models for simulating the filling and emptying of silos: Analysis of numerical results. *Computers and Chemical Engineering, 40*, 22-32.

Gonzalez-Montellano, C., Ramirez, A., Fuentes, J. M., & Ayuga, F. (2012). Numerical effects derived from en masse filling of agricultural silos in DEM simulations. *Computers and Electronics in Agriculture, 81*, 113-123.

Gonzalez-Montellano, C., Ramirez, A., Gallego, E., & Ayuga, F. (2011). Validation and experimental calibration of 3D discrete element models for the simulation of the discharge flow in silos. *Chemical Engineering Science, 66*(21), 5116-5126.

Gray, J. M. N. T. (2001). Granular flow in partially filled slowly rotating drums. *Journal of Fluid Mechanics, 441*, 1-29.

Harnby, N., Edwards, M. F., & Nienow, A. W. (1992). *Mixing in the process industries* (2nd[e] éd.). Oxford: Butterworth-Heinemann.

Hart, R., Cundall, P. A., & Lemos, J. (1988). Formulation of a Three-Dimensional Distinct Element Model-Part II. Mechanical Calculations for Motion and Interaction of a System Composed of Many Polyhedral Blocks. *International journal of rock mechanics and mining sciences & geomechanics abstracts, 25*(3), 117-125.

Hartl, J., & Ooi, J. Y. (2008). Experiments and simulations of direct shear tests: Porosity, contact friction and bulk friction. *Granular Matter, 10*(4), 263-271.

Heggs, P. J., Ellis, D. I., & Ismail, M. S. (1994). Modelling of fluid-flow distributions in annular packed beds. *Gas Separation & Purification, 8*(4), 257-264.

Heggs, P. J., Ellis, D. I., & Ismail, M. S. (1995a). Evaluation of pressure profiles and overall pressure drop for flow through annular packed bed configurations. *Gas Separation & Purification, 9*(3), 171-171.

Heggs, P. J., Ellis, D. I., & Ismail, M. S. (1995b). Prediction of flow distributions and pressure changes in multi-layered annular packed beds. *Gas Separation & Purification, 9*(4), 243-243.

Henein, H., Brimacombe, J. K., & Watkinson, A. P. (1983). Experimental Study of Transverse Bed Motion in Rotary Kilns. *Metallurgical Transactions B (Process Metallurgy), 14 B*(2), 191-205.

Henein, H., Brimacombe, J. K., & Watkinson, A. P. (1985). Experimental Study of Segregation in Rotary Kilns. *Metallurgical transactions. B (Process metallurgy), 16 B*(4), 763-774.

Hennessy, J. L., Patterson, D. A., & Arpaci-Dusseau, A. C. (2007). *Computer architecture : a quantitative approach* (4th[e] éd.). Amsterdam: Elsevier Morgan Kaufmann.

Herminghaus, S. (2005). Dynamics of wet granular matter. *Advances in Physics, 54*(3), 221-261.

Heydenrych, M. D., Greeff, P., Heesink, A. B. M., & Versteeg, G. F. (2002). Mass transfer in rolling rotary kilns: A novel approach. *Chemical Engineering Science, 57*(18), 3851-3859.

Hidano, T., Nakamura, M., & Kawai, M. (2011). US 7,931,736 B2.

Hill, K. M., Caprihan, A., & Kakalios, J. (1997). Bulk segregation in rotated granular material measured by magnetic resonance imaging. *Physical Review Letters, 78*(1), 50-53.

Hill, K. M., & Kakalios, J. (1994). Reversible axial segregation of binary mixtures of granular materials. *Physical Review E (Statistical Physics, Plasmas, Fluids, and Related Interdisciplinary Topics), 49*(5), 3610-3613.

Hill, K. M., & Kakalios, J. (1995). Reversible axial segregation of rotating granular media. *Physical Review E (Statistical Physics, Plasmas, Fluids, and Related Interdisciplinary Topics), 52*(4), 4393-4400.

Hogue, C. (1998). Shape representation and contact detection for discrete element simulations of arbitrary geometries. *Engineering Computations, 15*(3), 374-390.

Ingram, A., Seville, J. P. K., Parker, D. J., Fan, X., & Forster, R. G. (2005). Axial and radial dispersion in rolling mode rotating drums. *Powder Technology, 158*(1-3), 76-91.

Jain, N., Ottino, J. M., & Lueptow, R. M. (2002). An experimental study of the flowing granular layer in a rotating tumbler. *Physics of Fluids, 14*(2), 572-582.

Jain, N., Ottino, J. M., & Lueptow, R. M. (2004). Effect of interstitial fluid on a granular flowing layer. *Journal of Fluid Mechanics, 508*, 23-44.

Jain, N., Ottino, J. M., & Lueptow, R. M. (2005). Regimes of segregation and mixing in combined size and density granular systems: An experimental study. *Granular Matter, 7*(2-3), 69-81.

Jia, X., & Williams, R. A. (2001). A packing algorithm for particles of arbitrary shapes. *Powder Technology, 120*(3), 175-186.

Jin, F., Xin, H., Zhang, C., & Sun, Q. (2011). Probability-based contact algorithm for non-spherical particles in DEM. *Powder Technology, 212*(1), 134-144.

Johnson, K. L. (1985). *Contact mechanics*. Cambridge [Cambridgeshire] ; New York: Cambridge University Press.

Jop, P., Forterre, Y., & Pouliquen, O. (2006). A constitutive law for dense granular flows. *Nature, 441*(7094), 727-730.

Juarez, G. (2009). *Mixing and segregation dynamics of granular mixtures in rotating tumblers.* 3386525 (Ph.D.), Northwestern University, United States -- Illinois. Tiré de ProQuest Dissertations & Theses Full Text.

Kalbassi, M. A., & Golden, T. C. (1999). US 5,855,650.

Kareeri, A. A., Zughbi, H. D., & Al-Ali, H. H. (2006). Simulation of flow distribution in radial flow reactors. *Industrial and Engineering Chemistry Research, 45*, 2862-2874.

Kawaguchi, T. (2010). MRI measurement of granular flows and fluid-particle flows. *Advanced Powder Technology, 21*(3), 235-241.

Kawaguchi, T., Tsutsumi, K., & Tsuji, Y. (2006). MRI measurement of granular motion in a rotating drum. *Particle and Particle Systems Characterization, 23*, 266-271.

Ketterhagen, W. R., Curtis, J. S., Wassgren, C. R., & Hancock, B. C. (2009). Predicting the flow mode from hoppers using the discrete element method. *Powder Technology, 195*(1), 1-10.

Khakhar, D. V. (2011). Rheology and mixing of granular materials. *Macromolecular Materials and Engineering, 296*(3-4), 278-289.

Khakhar, D. V., McCarthy, J. J., & Ottino, J. M. (1997). Radial segregation of granular mixtures in rotating cylinders. *Physics of Fluids, 9*(12), 3600-3614.

Khakhar, D. V., McCarthy, J. J., Shinbrot, T., & Ottino, J. M. (1997). Transverse flow and mixing of granular materials in a rotating cylinder. *Physics of Fluids, 9*(1), 31-43.

Khakhar, D. V., Orpe, A. V., Andresen, P., & Ottino, J. M. (2001). Surface flow of granular materials: model and experiments in heap formation. *Journal of Fluid Mechanics, 441*, 255-264.

Khakhar, D. V., Orpe, A. V., & Hajra, S. K. (2003). Segregation of granular materials in rotating cylinders. *Physica A: Statistical Mechanics and its Applications, 318*, 129-136.

Khakhar, D. V., Orpe, A. V., & Ottino, J. M. (2001a). Continuum model of mixing and size segregation in a rotating cylinder: Concentration-flow coupling and streak formation. *Powder Technology, 116*(2-3), 232-245.

Khakhar, D. V., Orpe, A. V., & Ottino, J. M. (2001b). Surface Granular Flows: Two related Examples. *Advances in Complex Systems, 04*(04), 407-417.

Khanna, P., Pugsley, T., Tanfara, H., & Dumont, H. (2008). Radioactive particle tracking in a lab-scale conical fluidized bed dryer containing pharmaceutical granule. *Canadian Journal of Chemical Engineering, 86*(3), 563-570.

Kiared, K., Larachi, F., Cassanello, M., & Chaouki, J. (1997). Flow structure of the solids in a three-dimensional liquid fluidized bed. *Industrial and Engineering Chemistry Research, 36*(11), 4695-4704.

Kiared, K., Larachi, F., Chaouki, J., & Guy, C. (1999). Mean and turbulent particle velocity in the fully developed region of a three-phase fluidized bed. *Chemical Engineering and Technology, 22*(8), 683-689.

Kiared, K., Larachi, F., Guy, C., & Chaouki, J. (1997). Trajectory length and residence-time distributions of the solids in three-phase fluidized beds. *Chemical Engineering Science, 52*, 3931-3939.

Kirk, D. B., & Hwu, W.-m. W. (2010). *Programming massively parallel processors : hands-on with CUDA*. Amsterdam: Morgan Kaufmann Publishers : Elsevier.

Knoll, G. F. (2000). *Radiation detection and measurement* (3rd^{e} éd.). New York ; Toronto: Wiley.

Ko, D., Kim, M., Moon, I., & Choi, D. (2002). Analysis of purge gas temperature in cyclic TSA process. *Chemical Engineering Science, 57*(1), 179-195.

Kodam, M., Bharadwaj, R., Curtis, J., Hancock, B., & Wassgren, C. (2010). Cylindrical object contact detection for use in discrete element method simulations, Part II—Experimental validation. *Chemical Engineering Science, 65*(22), 5863-5871.

Kruggel-Emden, H., Stepanek, F., & Munjiza, A. (2011). Performance of integration schemes in discrete element simulations of particle systems involving consecutive contacts. *Computers and Chemical Engineering, 35*(10), 2152-2157.

Kruggel-Emden, H., Sturm, M., Wirtz, S., & Scherer, V. (2008). Selection of an appropriate time integration scheme for the discrete element method (DEM). *Computers and Chemical Engineering, 32*(10), 2263-2279.

Kumar, R., & Deng, S. (2006). Trace carbon monoxide and hydrogen conversion prior to cryogenic distillation of air. *Adsorption, 12*(5-6), 361-373.

Kumar, R., & Dissinger, G. R. (1986). Nonequilibrium, Nonisothermal Desorption of Single Adsorbate by Purge. *Industrial & Engineering Chemistry, Process Design and Development, 25*(2), 456-464.

Kumar, R., Huggahalli, M., & Bülow, M. (2002). US 6,432,171 B1.

Kuo, H. P., Knight, P. C., Parker, D. J., & Seville, J. P. K. (2005). Solids circulation and axial dispersion of cohesionless particles in a V-mixer. *Powder Technology, 152*(1-3), 133-140.

Lacey, P. M. C. (1954). Developments in the theory of particle mixing. *Journal of Applied Chemistry, 4*(5), 257-268.

Lai, C.-K., Holt, D., Leung, J. C., Cooney, C. L., Raju, G. K., & Hansen, P. (2001). Real time and noninvasive monitoring of dry powder blend homogeneity. *AIChE Journal, 47*(11), 2618-2622.

Landry, J. W., Grest, G. S., & Plimpton, S. J. (2004). Discrete element simulations of stress distributions in silos: Crossover from two to three dimensions. *Powder Technology, 139*(3), 233-239.

Landry, J. W., Grest, G. S., Silbert, L. E., & Plimpton, S. J. (2003). Confined granular packings: structure, stress, and forces. *Physical Review E (Statistical, Nonlinear, and Soft Matter Physics), 67*(4), 41303-41301.

Langston, P. A., Al-Awamleh, M. A., Fraige, F. Y., & Asmar, B. N. (2004). Distinct element modelling of non-spherical frictionless particle flow. *Chemical Engineering Science, 59*(2), 425-435.

Larachi, F., Cassanello, M., Chaouki, J., & Guy, C. (1996). Flow structure of the solids in a 3-D gas-liquid-solid fluidized bed. *AIChE Journal, 42*(9), 2439-2452.

Larachi, F., Cassanello, M., Marie, M., Chaouki, J., & Guy, C. (1995). Solids circulation patterns in three-phase fluidized beds containing binary mixtures of particles as inferred from RPT. *Chemical Engineering Research and Design, 73*(A3), 263-268.

Larachi, F., Chaouki, J., & Kennedy, G. (1995). 3-D mapping of solids flow fields in multiphase reactors with RPT. *AIChE Journal, 41*(2), 439-443.

Larachi, F., Grandjean, B. P. A., & Chaouki, J. (2003). Mixing and circulation of solids in spouted beds: Particle tracking and Monte Carlo emulation of the gross flow pattern. *Chemical Engineering Science, 58*(8), 1497-1507.

Larachi, F., Kennedy, G., & Chaouki, J. (1994). A -ray detection system for 3-D particle tracking in multiphase reactors. *Nuclear Instruments and Methods in Physics Research, Section A (Accelerators, Spectrometers, Detectors and Associated Equipment), A338*(2-3), 568-576.

Le Digabel, S. (2011). Algorithm 909: NOMAD: Nonlinear Optimization with the MADS Algorithm. *ACM Transactions on Mathematical Software, 37*(4), 1-15.

Leadbeater, T. W., Parker, D. J., & Gargiuli, J. (2011). Characterization of the latest Birmingham modular positron camera. *Measurement Science and Technology, 22*(10).

Leclaire, L.-A. (2004). *Parallélisation de la méthode des éléments discrets appliquée aux écoulements granulaires (Parallelization of the discrete element method applied to granular flows).*

Lefebvre, S., Guy, C., & Chaouki, J. (2007a). A convective/dispersive solid phase mixing model for three-phase fluidized bed reactors: effect of dimensionless numbers. *Chemical Engineering Science, 62*(18-20), 4954-4962.

Lefebvre, S., Guy, C., & Chaouki, J. (2007b). Solid phase hydrodynamics of three-phase fluidized beds-a convective/dispersive mixing model. *Chemical Engineering Journal, 133*(1-3), 85-95.

Lemieux, M. (2006). *Etude comparative du melange granulaire a ecoulement libre dans un melangeur en V et un melangeur simple cone.* MR19313 (M.Sc.A.), Ecole Polytechnique, Montreal (Canada), Canada. Tiré de Dissertations & Theses @ Ecole Polytechnique de Montreal; ProQuest Dissertations & Theses Full Text.

Lemieux, M., Bertrand, F., Chaouki, J., & Gosselin, P. (2007). Comparative study of the mixing of free-flowing particles in a V-blender and a bin-blender. *Chemical Engineering Science, 62*(6), 1783-1802.

Leonard, G. (2005). *Caracterisation du melange de poudres dans les procedes pharmaceutiques a l'aide de mesures d'effusivite.* MR16808 (M.Sc.A.), Ecole Polytechnique, Montreal (Canada), Canada. Tiré de Dissertations & Theses @ Ecole Polytechnique de Montreal; ProQuest Dissertations & Theses Full Text.

Leonard, G., Bertrand, F., Chaouki, J., & Gosselin, P. M. (2008). An experimental investigation of effusivity as an indicator of powder blend uniformity. *Powder Technology, 181*(2), 149-159.

Lewis, R. M., Torczon, V., & Trosset, M. W. (2000). Direct search methods: Then and now. *Journal of Computational and Applied Mathematics, 124*(1-2), 191-207.

Li, C., & Cetinkaya, C. (2006). Frequency domain thickness measurement approach for microscale multilayered structures. *IEEE Transactions on Instrumentation and Measurement, 55*(1), 206-211.

Li, J., Langston, P. A., Webb, C., & Dyakowski, T. (2004). Flow of sphero-disc particles in rectangular hoppers - A DEM and experimental comparison in 3D. *Chemical Engineering Science, 59*(24), 5917-5929.

Li, S., Marshall, J. S., Liu, G., & Yao, Q. (2011). Adhesive particulate flow: The discrete-element method and its application in energy and environmental engineering. *Progress in Energy and Combustion Science, 37*(6), 633-668.

Li, S. Q., Chi, Y., Li, R. D., Yan, J. H., & Cen, K. F. (2002). Axial transport and residence time of MSW in rotary kilns: Part II. Theoretical and optimal analyses. *Powder Technology, 126*(3), 228-240.

Li, S. Q., Yan, J. H., Li, R. D., Chi, Y., & Cen, K. F. (2002). Axial transport and residence time of MSW in rotary kilns - Part I. Experimental. *Powder Technology, 126*(3), 217-227.

Li, Y., Xu, Y., & Thornton, C. (2005). A comparison of discrete element simulations and experiments for 'sandpiles' composed of spherical particles. *Powder Technology, 160*(3), 219-228.

Libal, K., Fierlbeck, W., & Von Gemmingen, U. (1998). US 5,827,485.

Lin, J. S., Chen, M. M., & Chao, B. T. (1985). A novel radioactive particle tracking facility for measurement of solids motion in gas fluidized beds. *AIChE Journal, 31*(3), 465-473.

Lin, X., & Ng, T.-T. (1995). Contact detection algorithms for three-dimensional ellipsoids in discrete element modelling. *International Journal for Numerical and Analytical Methods in Geomechanics, 19*(9), 653-659.

Liu, X. Y., & Specht, E. (2010). Predicting the fraction of the mixing zone of a rolling bed in rotary kilns. *Chemical Engineering Science, 65*(10), 3059-3063.

Liu, X. Y., Specht, E., Gonzalez, O. G., & Walzel, P. (2006). Analytical solution for the rolling-mode granular motion in rotary kilns. *Chemical Engineering and Processing, 45*(6), 515-521.

Lobanov, E. L., & Skipin, Y. A. (1986). Increasing the Operating Efficiency of Radial Reactors in Reforming. *Chemistry and Technology of Fuels and Oils, 22*(5-6), 275-278.

Longmore, J.-P., Marais, P., & Kuttel, M. M. (2013). Towards realistic and interactive sand simulation: A GPU-based framework. *Powder Technology, 235*, 983-1000.

Mabrouk, R., Chaouki, J., & Guy, C. (2007). Effective drag coefficient investigation in the acceleration zone of an upward gas-solid flow. *Chemical Engineering Science, 62*(1-2), 318-327.

Mack, S., Langston, P., Webb, C., & York, T. (2011). Experimental validation of polyhedral discrete element model. *Powder Technology, 214*(3), 431-442.

Makse, H. A. (1999). Continuous Avalanche Segregation of Granular Mixtures in Thin Rotating Drums. *Physical Review Letters, 83*(16), 3186-3189.

Makse, H. A., Havlin, S., King, P. R., & Stanley, H. E. (1997). Spontaneous stratification in granular mixtures. *Nature, 386*(6623), 379-382.

Masson, S., & Martinez, J. (2000). Effect of particle mechanical properties on silo flow and stresses from distinct element simulations. *Powder Technology, 109*(1-3), 164-178.

McCarthy, J. J., Khakhar, D. V., & Ottino, J. M. (2000). Computational studies of granular mixing. *Powder Technology, 109*(1-3), 72-82.

MCNP User Manual, Version 5. (2003). http://mcnp-green-lanl.gov

Meier, S. W. (2007). *Mixing and segregation of granular materials: A dynamical systems approach.* 3278068 (Ph.D.), Northwestern University, United States -- Illinois. Tiré de ProQuest Dissertations & Theses Full Text.

Meier, S. W., Lueptow, R. M., & Ottino, J. M. (2007). A dynamical systems approach to mixing and segregation of granular materials in tumblers. *Advances in Physics, 56*(5), 757-827.

Mellmann, J. (2001). The transverse motion of solids in rotating cylinders-forms of motion and transition behavior. *Powder Technology, 118*(3), 251-270.

Mellmann, J., Specht, E., & Liu, X. (2004). Prediction of rolling bed motion in rotating cylinders. *AIChE Journal, 50*(11), 2783-2793.

Mishra, B. K., Thornton, C., & Bhimji, D. (2002). A preliminary numerical investigation of agglomeration in a rotary drum. *Minerals Engineering, 15*(1-2), 27-33.

Monitzer, A. (2012). Combining lattice Boltzmann and discrete element methods on a graphics processor. *International Journal of High Performance Computing Applications, 26*, 215-226.

Mosorov, V., & Abdullah, J. (2011). MCNP5 code in radioactive particle tracking. *Applied Radiation and Isotopes, 69*(9), 1287-1293.

Mostoufi, N., Kenned, G., & Chaouki, J. (2003). Decreasing the sampling time interval in radioactive particle tracking. *Canadian Journal of Chemical Engineering, 81*(1), 129-133.

Munjiza, A., Latham, J. P., & John, N. W. M. (2003). 3D dynamics of discrete element systems comprising irregular discrete elements-Integration solution for finite rotations in 3D. *International Journal for Numerical Methods in Engineering, 56*(1), 35-55.

Muzzio, F. J., Robinson, P., Wightman, C., & Dean, B. (1997). Sampling practices in powder blending. *International Journal of Pharmaceutics, 155*(2), 153-178.

Nakagawa, M., Altobelli, S. A., Caprihan, A., Fukushima, E., & Jeong, E. K. (1993). Non-invasive measurements of granular flows by magnetic resonance imaging. *Experiments in Fluids, 16*(1), 54-60.

Ndiaye, L. G., Caillat, S., Chinnayya, A., Gambier, D., & Baudoin, B. (2010). Application of the dynamic model of Saeman to an industrial rotary kiln incinerator: Numerical and experimental results. *Waste Management, 30*(7), 1188-1195.

Nedderman, R. M. (2005). *Statics and kinematics of granular materials* (Digitally printed 1st pbk.[e] éd.). Cambridge, UK ; New York: Cambridge University Press.

Nityanand, N., Manley, B., & Henein, H. (1986). Analysis of Radial Segregation for Different Sized Spherical Solids in Rotary Cylinders *Metallurgical transactions. B (Process metallurgy), 17 B*(2), 247-257.

O'Sullivan, C., & Bray, J. D. (2004). Selecting a suitable time step for discrete element simulations that use the central difference time integration scheme. *Engineering Computations 21*, 278-303.

Orpe, A. V., & Khakhar, D. V. (2001). Scaling relations for granular flow in quasi-two-dimensional rotating cylinders. *Physical Review E - Statistical, Nonlinear, and Soft Matter Physics, 64*(3 I), 313021-3130213.

Orpe, A. V., & Khakhar, D. V. (2007). Rheology of surface granular flows. *Journal of Fluid Mechanics, 571*, 1-32.

Ottino, J. M., & Khakhar, D. V. (2000). Mixing and segregation of granular materials. *Annual Review of Fluid Mechanics, 32*, 55-91.

Parker, D. J., Dijkstra, A. E., Martin, T. W., & Seville, J. P. K. (1997). Positron emission particle tracking studies of spherical particle motion in rotating drums. *Chemical Engineering Science, 52*(13), 2011-2022.

Parker, D. J., & Fan, X. (2008). Positron emission particle tracking-Application and labelling techniques. *Particuology, 6*(1), 16-23.

Parker, D. J., Leadbeater, T. W., Fan, X., Hausard, M. N., Ingram, A., & Yang, Z. (2008). Positron imaging techniques for process engineering: Recent developments at Birmingham. *Measurement Science and Technology, 19*(9).

Perkins, E., & Williams, J. R. (2001). A fast contact detection algorithm insensitive to object sizes. *Engineering Computations, 18*(1-2), 48-61.

Perrault, M., Bertrand, F., & Chaouki, J. (2010). An investigation of magnesium stearate mixing in a V-blender through gamma-ray detection. *Powder Technology, 200*(3), 234-245.

Peters, B., & Dziugys, A. (2002). Numerical simulation of the motion of granular material using object-oriented techniques. *Computer Methods in Applied Mechanics and Engineering, 191*(17-18), 1983-2007.

Ponzi, P. R., & Kaye, L. A. (1979). Effect of Flow Maldistribution on Conversion and Selectivity in Radial Flow Fixed-Bed Reactors. *AIChE Journal, 25*(1), 100-108.

Pugsley, T., Tanfara, H., Malcus, S., Cui, H., Chaouki, J., & Winters, C. (2003). Verification of fluidized bed electrical capacitance tomography measurements with a fibre optic probe. *Chemical Engineering Science, 58*(17), 3923-3934.

Radeke, C. A., Glasser, B. J., & Khinast, J. G. (2010). Large-scale powder mixer simulations using massively parallel GPUarchitectures. *Chemical Engineering Science, 65*(24), 6435-6442.

Rao, S. J., Bhatia, S. K., & Khakhar, D. V. (1991). Axial transport of granular solids in rotating cylinders. Part 2. Experiments in a non-flow system. *Powder Technology, 67*(2), 153-162.

Rapaport, D. C. (2007). Radial and axial segregation of granular matter in a rotating cylinder: a simulation study. *Physical Review E (Statistical, Nonlinear, and Soft Matter Physics), 75*(3), 31301-31301.

Ridgway, K., & Rupp, R. (1971). Mixing of powder layers on a chute. The effect of particle size and shape. *Powder Technology, 4*(4), 195-202.

Rougier, E., Munjiza, A., & John, N. W. M. (2004). Numerical comparison of some explicit time integration schemes used in DEM, FEM/DEM and molecular dynamics. *International Journal for Numerical Methods in Engineering, 61*(6), 856-879.

Roy, D., Larachi, F., Legros, R., & Chaouki, J. (1994). Study of solid behavior in spouted beds using 3-D particle tracking. *Canadian Journal of Chemical Engineering, 72*(6), 945-952.

Roy, S. (2000). *Quantification of two-phase flow in liquid-solid risers.* Ph.D., Washington University, United States -- Missouri. Tiré de ProQuest Dissertations & Theses (PQDT).

Roy, S., Chen, J., Kumar, S. B., Al-Dahhan, M. H., & Dudukovic, M. P. (1997). Tomographic and particle tracking studies in a liquid-solid riser. *Industrial and Engineering Chemistry Research, 36*(11), 4666-4669.

Roy, S., Kemoun, A., Al-Dahhan, M. H., & Dudukovic, M. P. (2005). Experimental investigation of the hydrodynamics in a liquid-solid riser. *AIChE Journal, 51*(3), 802-835.

Roy, S., Larachi, F., Al-Dahhan, M. H., & Dudukovic, M. P. (2002). Optimal design of radioactive particle tracking experiments for flow mapping in opaque multiphase reactors. *Applied Radiation and Isotopes, 56*(3), 485-503.

Ruthven, D. M. (1984). *Principles of adsorption and adsorption processes*. New York: Wiley.

Salierno, G. L., Fraguio, M. S., Piovano, S., Cassanello, M., Cardona, M. A., Hojman, D., & Somacal, H. (2012). Bubble columns dynamics inferred from the motion of a radioactive tracer followed by axially aligned detectors. *Chemical Engineering Journal*.

Savage, S. B. (1984). The Mechanics of Rapid Granular Flows. *Advances in Applied Mechanics, 24*(C), 289-366.

Savage, S. B., & Hutter, K. (1989). Motion of a finite mass of granular material down a rough incline. *Journal of Fluid Mechanics, 199*, 177-215.

Schneider, J. S., Smolarek, J., Ackley, M. W., & Nowobilski, J. J. (1999). US 5,836,362-A.

Seader, J. D., & Henley, E. J. (1998). *Separation process principles*. New York ; Toronto: John Wiley & Sons.

Sheritt, R. G., Chaouki, J., Mehrotra, A. K., & Behie, L. A. (2003). Axial dispersion in the three-dimensional mixing of particles in a rotating drum reactor. *Chemical Engineering Science, 58*(2), 401-415.

Shi, D., Vargas, W. L., & McCarthy, J. J. (2008). Heat transfer in rotary kilns with interstitial gases. *Chemical Engineering Science, 63*(18), 4506-4516.

Sondergaard, R., Chaney, K., & Brennen, C. E. (1990). Measurements of solid spheres bouncing off flat plates. *Journal of Applied Mechanics, Transactions ASME, 57*(3), 694-699.

Song, Y., Turton, R., & Kayihan, F. (2006). Contact detection algorithms for DEM simulations of tablet-shaped particles. *Powder Technology, 161*(1), 32-40.

Sturman, R., Meier, S. W., Ottino, J. M., & Wiggins, S. (2008). Linked twist map formalism in two and three dimensions applied to mixing in tumbled granular flows. *Journal of Fluid Mechanics, 602*, 129-174.

Sudah, O. S., Arratia, P. E., Alexander, A., & Muzzio, F. J. (2005). Simulation and experiments of mixing and segregation in a tote blender. *AIChE Journal, 51*(3), 836-844.

Suzzi, D., Toschkoff, G., Radl, S., Machold, D., Fraser, S. D., Glasser, B. J., & Khinast, J. G. (2012). DEM simulation of continuous tablet coating: Effects of tablet shape and fill level on inter-tablet coating variability. *Chemical Engineering Science, 69*(1), 107-121.

Tamadondar, M. R., Azizpour, H., Zarghami, R., Mostoufi, N., & Chaouki, J. (2012). Using particle trajectory for determining the fluidization regime in gas-solid fluidized beds. *Advanced Powder Technology, 23*(3), 349-351.

Thomas, N. (2000). Reverse and intermediate segregation of large beads in dry granular media. *Physical Review E - Statistical Physics, Plasmas, Fluids, and Related Interdisciplinary Topics, 62*(1 B), 961-974.

Thornton, C., Cummins, S. J., & Cleary, P. W. (2011). An investigation of the comparative behaviour of alternative contact force models during elastic collisions. *Powder Technology, 210*(3), 189-197.

Thornton, C., Cummins, S. J., & Cleary, P. W. (2013). An investigation of the comparative behaviour of alternative contact force models during inelastic collisions. *Powder Technology, 233*, 30-46.

Tjakra, J. D., Bao, J., Hudon, N., & Yang, R. (2013). Modeling collective dynamics of particulate systems under time-varying operating conditions based on Markov chains.

Tobiska, S., & Kleinebudde, P. (2003). Coating uniformity and coating efficiency in a Bohle Lab-Coaterusing oval tablets. *European Journal of Pharmaceutics and Biopharmaceutics, 56*(1), 3-9.

Tsoulfanidis, N. (2011). *Measurement and detection of radiation* (3e éd.). Washington ; New York: Hemisphere Pub. Corp. McGraw-Hill.

Tsuji, Y., Tanaka, T., & Ishida, T. (1992). Lagrangian numerical simulation of plug flow of cohesionless particles in a horizontal pipe. *Powder Technology, 71*(3), 239-250.

Upadhyay, R. K., & Roy, S. (2010). Investigation of hydrodynamics of binary fluidized beds via radioactive particle tracking and dual-source densitometry. *Canadian Journal of Chemical Engineering, 88*(4), 601-610.

Van de Velden, M., Baeyens, J., Seville, J. P. K., & Fan, X. (2008). The solids flow in the riser of a Circulating Fluidised Bed (CFB) viewed by Positron Emission Particle Tracking (PEPT). *Powder Technology, 183*(2), 290-296.

Van Puyvelde, D. R., Young, B. R., Wilson, M. A., & Schmidt, S. J. (2000). Modelling transverse segregation of particulate solids in a rolling drum. *Chemical Engineering Research and Design, 78*(4), 643-650.

Wachs, A., Girolami, L., Vinay, G., & Ferrer, G. (2012). Grains3D, a flexible DEM approach for particles of arbitrary convex shape - Part I: Numerical model and validations. *Powder Technology, 224*, 374-389.

Weir, G., Krouse, D., & McGavin, P. (2005). The maximum thickness of upper shear layers of granular materials in rotating cylinders. *Chemical Engineering Science, 60*(7), 2027-2035.

Wightman, C., & Muzzio, F. J. (1998). Mixing of granular material in a drum mixer undergoing rotational and rocking motions II. Segregating particles. *Powder Technology, 98*(2), 125-134.

Williams, J. R., & O'Connor, R. (1995). A linear complexity intersection algorithm for discrete element simulation of arbitrary geometries. *Engineering Computations, 12*(2), 185-201.

Williams, J. R., Perkins, E., & Cook, B. (2004). A contact algorithm for partitioning N arbitrary sized objects. *Engineering Computations, 21*, 235-248.

Wilson, K. E., & Crossman, E. (1997). The Influence of Tablet Shape and Pan Speed on Intra-tablet Film Coating Uniformity. *Drug Development and Industrial Pharmacy, 23*(12), 1239-1243.

Woodle, G. R., & Munro, J. M. (1993). Particle motion and mixing in a rotary kiln. *Powder Technology, 76*(3), 241-245.

Yang, Z., Fan, X., Bakalis, S., Parker, D. J., & Fryer, P. J. (2008). A method for characterising solids translational and rotational motions using Multiple-Positron Emission Particle Tracking (Multiple-PEPT). *International Journal of Multiphase Flow, 34*(12), 1152-1160.

Yang, Z., Fryer, P. J., Bakalis, S., Fan, X., Parker, D. J., & Seville, J. P. K. (2007). An improved algorithm for tracking multiple, freely moving particles in a Positron Emission Particle Tracking system. *Nuclear Instruments and Methods in Physics Research, Section A: Accelerators, Spectrometers, Detectors and Associated Equipment, 577*(3), 585-594.

Zhang, H. W., Zhou, Q., Xing, H. L., & Muhlhaus, H. (2011). A DEM study on the effective thermal conductivity of granular assemblies. *Powder Technology, 205*(1-3), 172-183.

Zhou, Y. C., Wright, B. D., Yang, R. Y., Xu, B. H., & Yu, A. B. (1999). Rolling friction in the dynamic simulation of sandpile formation. *Physica A: Statistical Mechanics and its Applications, 269*(2), 536-553.

Zhou, Y. C., Xu, B. H., Yu, A. B., & Zulli, P. (2001). Numerical investigation of the angle of repose of monosized spheres. *Physical Review E - Statistical, Nonlinear, and Soft Matter Physics, 64*(2 I), 213011-213018.

Zhou, Y. C., Xu, B. H., Yu, A. B., & Zulli, P. (2002). An experimental and numerical study of the angle of repose of coarse spheres. *Powder Technology, 125*(1), 45-54.

Zhu, H. P., & Yu, A. B. (2006). A theoretical analysis of the force models in discrete element method. *Powder Technology, 161*(2), 122-129.

Zik, O., Levine, D., Lipson, S. G., Shtrikman, S., & Stavans, J. (1994). Rotationally induced segregation of granular materials. *Physical Review Letters, 73*(5), 644-647.